

PERFECT GAS NAVIER-STOKES SOLUTIONS OF HYPERSONIC  
BOUNDARY LAYER AND COMPRESSION CORNER FLOWS

A THESIS SUBMITTED TO  
THE GRADUATE SCHOOL OF NATURAL AND APPLIED SCIENCES  
OF  
MIDDLE EAST TECHNICAL UNIVERSITY

BY

ŞADUMAN AZİZ

IN PARTIAL FULFILLMENT OF THE REQUIREMENTS  
FOR  
THE DEGREE OF DOCTOR OF PHILOSOPHY  
IN  
AEROSPACE ENGINEERING

SEPTEMBER 2005

Approval of the Graduate School of Natural and Applied Sciences.

---

Prof. Dr. Canan Özgen

Director

I certify that thesis satisfies all the requirements as a thesis for the degree of Doctor of Philosophy.

---

Prof. Dr. Nafiz Alemdaroğlu

Head of Department

This is to certify that we have read this thesis and that in our opinion it is fully adequate, in scope and quality, as a thesis for the degree of Doctor of Philosophy.

---

Prof. Dr. Mehmet Ş. Kavsaçoğlu  
Co-Supervisor

---

Prof. Dr. Cevdet Çelenligil  
Supervisor

Examining Committee Members

Prof. Dr. Sinan Akmandor	(METU, AEE)	_____
Prof. Dr. Cevdet Çelenligil	(METU, AEE)	_____
Prof. Dr. Mehmet Ş. Kavsaçoğlu	(Ist. Tech. Univ., AEE)	_____
Prof. Dr. Kahraman Albayrak	(METU, ME)	_____
Assoc. Prof. Dr. Sinan Eyi	(METU, AEE)	_____

**I hereby declare that all information in this document has been obtained and presented in accordance with academic rules and ethical conduct. I also declare that, as required by these rules and conduct, I have fully cited and referenced all material and results that are not original to this work.**

Name, Last name : Şaduman AZİZ

Signature :

## ABSTRACT

### PERFECT GAS NAVIER-STOKES SOLUTIONS OF HYPERSONIC BOUNDARY LAYER AND COMPRESSION CORNER FLOWS

Aziz, Şaduman

Ph.D., Department of Aerospace Engineering

Supervisor : Prof. Dr. Cevdet Çelenligil

Co-Supervisor: Prof .Dr. Mehmet Ş. Kavsaoğlu

September 2005, 227 pages

The purpose of this thesis is to perform numerical solutions of hypersonic, high temperature, perfect gas flows over various geometries. Three dimensional, thin layer, compressible, Navier-Stokes equations are solved. An upwind finite difference approach with Lower Upper-Alternating Direction Implicit (LU-ADI) decomposition is used.

Solutions of laminar, hypersonic, high temperature, perfect gas flows over flat plate and compression corners ( $\theta_w=5^\circ, 10^\circ, 14^\circ, 15^\circ, 16^\circ, 18^\circ$  and  $24^\circ$ ) with eight different free-stream and wall conditions are presented and discussed. During the analysis, air viscosity is calculated from the Sutherland formula up to 1000°K, for the temperature range between 1000 °K and 5000 °K a curve fit to the estimations of Svehla is applied.

The effects of  $T_w/T_0$  on heat transfer rates, surface pressure distributions and boundary layer characteristics are studied. The effects of corner angle ( $\theta_w$ ) on strong shock wave/boundary layer interactions with extended separated regions are investigated. The obtained results are compared with the available experimental data, computational results, and theory.

Keywords: CFD, Navier-Stokes, Laminar, Hypersonic Flow, Shock Wave, Boundary Layer, Viscous Interaction, Flat Plate, Compression Corner.

## ÖZ

### HİPERSONİK SINIR TABAKA VE KÖŞE AKIMLARININ MÜKEMMEL GAZ NAVIER-STOKES ÇÖZÜMÜ

Aziz, Şaduman

Doktora, Havacılık ve Uzay Mühendisliği Bölümü

Tez Yöneticisi : Prof. Dr. Cevdet Çelenligil

Yardımcı Tez Yöneticisi : Prof .Dr. Mehmet Ş. Kavsaoglu

Eylül 2005, 227 sayfa

Bu tezin amacı, yüksek sıcaklıkta olan laminer, hipersonik özelliklerdeki mükemmel gaz akımlarının sayısal çözümlerinin yapılmasıdır. Üç boyutlu Reynolds ortalamalı, ince tabaka sıkıştırılabilir Navier-Stokes denklemleri çözülmüştür. Alt Üst - Değişken Doğrultulu Kapalı (LU-ADI) adı verilen ayrıştırmalı akış yönlü sonlu fark yaklaşımı kullanılmıştır.

Sekiz değişik akım ve duvar şartları kullanılarak düz plaka ve değişik açılı sıkıştırma köşelerinde ( $\theta_w=5^\circ, 10^\circ, 14^\circ, 15^\circ, 16^\circ, 18^\circ$  ve  $24^\circ$ ) laminer, hipersonik, yüksek sıcaklık özelliklerindeki mükemmel gazların sayısal çözümü sunulmuştur. Çözümler sırasında, havanın akışmazlığı (viskozitesi)  $1000^\circ\text{K}$ 'e kadar olan sıcaklıklar için Sutherland formülü ile,  $1000^\circ\text{K}$  ile  $5000^\circ\text{K}$  arasındaki sıcaklık bölgesi için ise Svehla'nın hesaplamalarına uyarlanan bir eğri yardımı ile hesaplanmıştır.

$T_w/T_0$  oranının ısı transferi, yüzey basınç dağılımı ve sınır tabakası değişkenleri üzerindeki etkileri incelenmiştir. Ayrıca, sıkıştırma köşesi açısının ( $\theta_w$ ), geniş ayrılma bölgelerini de ihtiva eden kuvvetli şok dalgası / sınır tabakası etkileşimleri üzerindeki etkileri de incelenmiştir. Elde edilen sonuçlar mevcut deneysel veriler, sayısal sonuçlar ve teoriler ile karşılaştırılmıştır.

Anahtar Kelimeler: SAD, Navier-Sokes, Laminer, Hipersonik Akım, Şok Dalgası, Sınır Tabaka, Akışmazlık Etkileşimi, Düz Levha, Sıkıştırma Köşesi.

To My Family

## **ACKNOWLEDGMENTS**

The author wishes to express her deepest gratitude to her supervisor Prof. Dr. Mehmet Ş. Kavsaoğlu for his guidance, advice, criticism, encouragements and insight throughout the research. After he moved to İstanbul Technical University, he was attendant as co-supervisor and left his supervisory job to Prof. Dr. Cevdet Çelenligil for last one year period.

The author would also like to thank Prof. Dr. Cevdet Çelenligil, Prof. Dr. Kahraman Albayrak and Prof. Dr. Ünver KAYNAK for their valuable comments, assistance and suggestions.

The entire staff of the Aerospace Engineering Department of Middle East Technical University are gratefully acknowledged.

The author is grateful to her family for their kind support and tolerance they have provided.

## TABLE OF CONTENTS

PLAGIARISM.....	iii
ABSTRACT .....	iv
ÖZ.....	v
ACKNOWLEDGMENTS .....	vii
TABLE OF CONTENTS.....	viii
LIST OF TABLES .....	x
LIST OF FIGURES .....	xi
LIST OF SYMBOLS.....	xxii
CHAPTER	
1. INTRODUCTION.....	1
1.1 General Information about Hypersonic Flows .....	2
1.2 Literature Survey .....	3
1.3 Scope and Overview of the thesis.....	6
2. HYPERSONIC BOUNDARY LAYER .....	10
2.1 Physical Characteristic of Hypersonic Flows.....	10
2.2 Physical Characteristic of Hypersonic Boundary Layers .....	14
3. HYPERSONIC COMPRESSION CORNERS.....	18
4. NAVIER STOKES EQUATIONS.....	21
4.1 Navier-Stokes Equations .....	21
4.2 Thin Layer Navier-Stokes Equations (TLNS) .....	22
4.3 Coordinate Transformation .....	23

4.4	Modelling of Laminar Viscosity .....	27
5.	NUMERICAL METHOD AND FLOW SOLVER .....	29
5.1	Description of the Solution Algorithm .....	29
5.2	Subprograms and Computational Flow Structure of the Code .....	32
5.3	Dimensionless Forms of Variables Used in the Code .....	33
6.	TEST PROBLEMS.....	37
6.1	Description of the Test Problem I: Hypersonic Flow Over Flat Plate ...	37
6.2	Description of the Test Problem II: Hypersonic Flow Over Compression Corners.....	41
7.	GRID GENERATION AND BOUNDARY CONDITIONS .....	43
7.1	Grid Generation for the Flat Plate .....	43
7.2	Grid Generation for the Compression Corners.....	50
7.3	Initial and Boundary Conditions.....	54
8.	RESULTS AND DISCUSSIONS .....	56
8.1	Hypersonic Boundary Layer Flows Over A Flat Plate.....	57
8.2	Hypersonic Compression Corner Flows .....	121
9.	CONCLUSION.....	197
	REFERENCES .....	201
	APPENDICES	
A.	GENERALIZED COORDINATE TRANSFORMATION AND NONDIMENSIONALIZATION .....	208
B.	BOUNDARY LAYER POST PROCESSING .....	212
C.	SKIN FRICTION COEFFICIENT POST PROCESSING .....	221
D.	STANTON NUMBER POST PROCESSING .....	224

## LIST OF TABLES

Table 1.1 Navier-Stokes Calculations of Two-Dimensional Laminar Interactions .....	8
Table 1.2 Experimental and Numerical Studies.....	9
Table 6.1 Reservoir and Freestream Properties of Test Cases.....	40

## LIST OF FIGURES

Figure 2.1 Temperature profile in a hypersonic boundary layer.....	16
Figure 2.2 Illustration of strong and weak viscous interactions.....	16
Figure 2.3 Illustration of pressure distributions over a flat plate.....	17
Figure 3.1 Schematic of the flow field over a compression corner.....	20
Figure 4.1 Transformation and body coordinate [Ref 37]. ....	24
Figure 4.2 Air viscosity Models.....	28
Figure 6.1 Schematic of the flat plate model (Not to scale). Dimensions are in.....	38
Figure 6.2 Schematic of the compression corner model (side plate not shown) Dimensions are in mm.....	42
Figure 7.1 Flat Plate Grid I.....	45
Figure 7.2 Flat Plate Grid II.....	46
Figure 7.3 Flat Plate Grid III.....	47
Figure 7.4 Flat Plate Grid IV.....	48
Figure 7.5 Flat Plate Grid V (The final grid used to obtain solutions).....	49
Figure 7.6 5° compression corner grid. ....	51
Figure 7.7 10° compression corner grid. ....	51
Figure 7.8 14° compression corner grid. ....	52
Figure 7.9 15° compression corner grid. ....	52
Figure 7.10 16° compression corner grid. ....	53
Figure 7.11 18° compression corner grid. ....	53
Figure 7.12 24° compression corner grid. ....	54
Figure 8.1 Convergence and iteration history, Case B. ....	62

Figure 8.2 Mach contours, Case B.....	65
Figure 8.3 Streamlines distribution over flat plate, Case B.....	65
Figure 8.4 Boundary layer thicknesses, Case B.....	66
Figure 8.5 Number of grid points in the boundary layer, Case B.....	66
Figure 8.6 Boundary layer flow variables at $x/L=1.0$ , (Mid-point of the flat plate), Case B.....	67
Figure 8.7 Boundary layer edge variables, Case B.....	68
Figure 8.8 Temperature distributions along the boundary layer, Case B.....	68
Figure 8.9 Boundary layer thicknesses, Case B.....	71
Figure 8.10 Boundary layer thicknesses, Case D.....	71
Figure 8.11 Boundary layer thicknesses, Case Modified D.....	72
Figure 8.12 Boundary layer thicknesses, Case G.....	72
Figure 8.13 Boundary layer thicknesses, Case Modified G.....	73
Figure 8.14 Boundary layer thicknesses, Case X1.....	73
Figure 8.15 Boundary layer thicknesses, Case X2.....	74
Figure 8.16 Boundary layer thicknesses, Case X3.....	74
Figure 8.17 Comparison of boundary layer thickness with theory, Case B.....	75
Figure 8.18 Comparison of boundary layer thickness with theory, Case D.....	75
Figure 8.19 Comparison of boundary layer thickness with theory, Case Modified D.....	76
Figure 8.20 Comparison of boundary layer thickness with theory, Case G.....	76
Figure 8.21 Comparison of boundary layer thickness with theory, Case Modified G.....	77
Figure 8.22 Comparison of boundary layer thickness with theory, Case X1.....	77
Figure 8.23 Comparison of boundary layer thickness with theory, Case X2.....	78
Figure 8.24 Comparison of boundary layer thickness with theory, Case X3.....	78
Figure 8. 25 Density profile through the boundary layer, Case D. (Distance from the leading egde $x=74$ mm) .....	79

Figure 8.26 Density profile through the boundary layer. Case G. (Distance from the leading edge $x=33$ mm) .....	79
Figure 8.27 Temperature profiles over a cold flat plate, $M_e=7.04$ , Case B.....	80
Figure 8. 28 Temperature profiles over a cold flat plate, $M_e=7.1$ , Case D. ....	80
Figure 8. 29 Temperature profiles over a cold flat plate, $M_e=8.8$ , Case G. ....	81
Figure 8.30 Velocity profiles over a cold flat plate, $M_e=7.04$ , Case B.....	81
Figure 8.31 Velocity profiles over a cold flat plate, $M_e=7.1$ , Case D. ....	82
Figure 8.32 Velocity profiles over a cold flat plate, $M_e=8.8$ , Case G. ....	82
Figure 8.33 Surface pressure distribution, Case B. ....	83
Figure 8.34 Surface pressure distribution, Case D. ....	83
Figure 8.35 Surface pressure distribution, Case Modified D.....	84
Figure 8.36 Surface pressure distribution, Case G.....	84
Figure 8.37 Surface pressure distribution, Case Modified G. ....	85
Figure 8.38 Surface pressure distribution, Case X1. ....	85
Figure 8.39 Surface pressure distribution, Case X2. ....	86
Figure 8.40 Surface pressure distribution, Case X3. ....	86
Figure 8.41 Surface pressure distribution, Case B. ....	87
Figure 8.42 Surface pressure distribution, Case D. ....	87
Figure 8.43 Surface pressure distribution, Case Modified D.....	88
Figure 8.44 Surface pressure distribution, Case G.....	88
Figure 8.45 Surface pressure distribution, Case Modified G. ....	89
Figure 8.46 Surface pressure distribution, Case X1. ....	89
Figure 8.47 Surface pressure distribution, Case X2. ....	90
Figure 8.48 Surface pressure distribution, Case X3. ....	90
Figure 8.49 Stanton number distribution, Case B. ....	91
Figure 8.50 Stanton number distribution, Case D.....	91

Figure 8.51 Stanton number distribution, Case Modified D. ....	92
Figure 8.52 Stanton number distribution, Case G. ....	92
Figure 8.53 Stanton number distribution, Case Modified G. ....	93
Figure 8.54 Stanton number distribution, Case X1. ....	93
Figure 8.55 Stanton number distribution, Case X2. ....	94
Figure 8.56 Stanton number distribution, Case X3. ....	94
Figure 8.57 $St\sqrt{Re_{x,e}}$ distribution, Case B. ....	95
Figure 8.58 $St\sqrt{Re_{x,e}}$ distribution, Case D. ....	95
Figure 8.59 $St\sqrt{Re_{x,e}}$ distribution, Case Modified D. ....	96
Figure 8.60 $St\sqrt{Re_{x,e}}$ distribution, Case G. ....	96
Figure 8.61 $St\sqrt{Re_{x,e}}$ distribution, Case Modified G. ....	97
Figure 8.62 $St\sqrt{Re_{x,e}}$ distribution, Case X1. ....	97
Figure 8.63 $St\sqrt{Re_{x,e}}$ distribution, Case X2. ....	98
Figure 8.64 $St\sqrt{Re_{x,e}}$ distribution, Case X3. ....	98
Figure 8.65 Skin friction coefficient distribution, Case B. ....	99
Figure 8.66 Skin friction coefficient distribution, Case D. ....	99
Figure 8.67 Skin friction coefficient distribution, Case Modified D. ....	100
Figure 8.68 Skin friction coefficient distribution, Case G. ....	100
Figure 8.69 Skin friction coefficient distribution, Case Modified G. ....	101
Figure 8.70 Skin friction coefficient distribution, Case X1. ....	101
Figure 8.71 Skin friction coefficient distribution, Case X2. ....	102
Figure 8.72 Skin friction coefficient distribution, Case X3. ....	102
Figure 8.73 Effect of $T_w/T_0$ on convergence history. ....	105

Figure 8.74 Effect of $T_w/T_0$ on number of grid points. ....	105
Figure 8.75 Effect of $T_w/T_0$ on temperature profiles at $x/L=1.0$ . ....	106
Figure 8.76 Effect of $T_w/T_0$ on velocity profiles at $x/L=1.0$ . ....	106
Figure 8.77 Effect of $T_w/T_0$ on heat transfer parameter at $x/L=1.0$ . ....	107
Figure 8.78 Effect of $T_w/T_0$ on $T_e$ distribution along the boundary layer. ....	107
Figure 8.79 Effect of $T_w/T_0$ on $T_{max}$ distribution along the boundary layer. ....	108
Figure 8.80 Effect of $T_w/T_0$ on $T^*$ distribution along the boundary layer. ....	108
Figure 8.81 Mach contours, Case B. ....	109
Figure 8.82 Mach contours, Case Modified D. ....	109
Figure 8.83 Mach contours, Case Modified G. ....	110
Figure 8.84 Mach contours, Case X1. ....	110
Figure 8.85 Mach contours, Case X2. ....	111
Figure 8.86 Mach contours, Case X3. ....	111
Figure 8.87 Effect of $T_w/T_0$ on streamlines, Case B. ....	112
Figure 8.88 Effect of $T_w/T_0$ on streamlines, Case Modified D. ....	112
Figure 8.89 Effect of $T_w/T_0$ on streamlines, Case Modified G. ....	113
Figure 8.90 Effect of $T_w/T_0$ on streamlines, Case X1. ....	113
Figure 8.91 Effect of $T_w/T_0$ on streamlines, Case X2. ....	114
Figure 8.92 Effect of $T_w/T_0$ on streamlines, Case X3. ....	114
Figure 8.93 Effect of $T_w/T_0$ on pressure distribution. ....	115
Figure 8.94 Effect of $T_w/T_0$ on pressure distribution. ....	115
Figure 8.95 Effect of $T_w/T_0$ on skin friction, $C_f$ , distribution. ....	116
Figure 8.96 Effect of $T_w/T_0$ on skin friction, $C_f$ , distribution. ....	116
Figure 8.97 Effect of $T_w/T_0$ on skin friction coefficient. ....	117
Figure 8.98 Effect of $T_w/T_0$ on skin friction coefficient. ....	117
Figure 8.99 Effect of $T_w/T_0$ on skin friction coefficient. ....	118

Figure 8.100 Effect of $T_w/T_0$ on skin friction coefficient.....	118
Figure 8.101 Effect of $T_w/T_0$ on heat transfer distribution. ....	119
Figure 8.102 Effect of $T_w/T_0$ on heat transfer distribution. ....	119
Figure 8.103 Effect of $T_w/T_0$ on heat transfer distribution. ....	120
Figure 8.104 Effect of $T_w/T_0$ on heat transfer distribution. ....	120
Figure 8.105 Convergence and iteration history, $\theta_w=14^\circ$ , Case B. ....	124
Figure 8.106 Mach contours, $\theta_w=14^\circ$ , Case B. ....	127
Figure 8.107 Streamlines distribution over corner region, $\theta_w=14^\circ$ , Case B.....	127
Figure 8.108 Boundary layer thicknesses, $\theta_w=14^\circ$ , Case B. ....	128
Figure 8.109 Number of grid points in the boundary layer, $\theta_w=14^\circ$ , Case B. ....	128
Figure 8.110 Boundary layer flow variables at $x/L=0.5$ , $\theta_w=14^\circ$ , Case B.....	129
Figure 8.111 Boundary layer flow variables at $x/L=1.0$ , $\theta_w=14^\circ$ , Case B.....	130
Figure 8.112 Boundary layer flow variables at $x/L=2.0$ , $\theta_w=14^\circ$ , Case B.....	131
Figure 8.113 Boundary layer edge variables, $\theta_w=14^\circ$ , Case B.....	132
Figure 8.114 Temperature distributions along the boundary layer, $\theta_w=14^\circ$ , Case B.....	132
Figure 8.115 Surface pressure distribution, $\theta_w=5^\circ$ , Case B. ....	135
Figure 8.116 Surface pressure distribution, $\theta_w=5^\circ$ , Case D. ....	135
Figure 8.117 Surface pressure distribution, $\theta_w=5^\circ$ , Case G.....	136
Figure 8.118 Surface pressure distribution, $\theta_w=10^\circ$ , Case B. ....	136
Figure 8.119 Surface pressure distribution, $\theta_w=10^\circ$ , Case D. ....	137
Figure 8.120 Surface pressure distribution, $\theta_w=10^\circ$ , Case G.....	137
Figure 8.121 Surface pressure distribution, $\theta_w=14^\circ$ , Case B. ....	138
Figure 8.122 Surface pressure distribution, $\theta_w=14^\circ$ , Case D. ....	138
Figure 8.123 Surface pressure distribution, $\theta_w=14^\circ$ , Case Modified D.....	139
Figure 8.124 Surface pressure distribution, $\theta_w=14^\circ$ , Case G.....	139
Figure 8.125 Surface pressure distribution, $\theta_w=14^\circ$ , Case Modified G. ....	140

Figure 8.126 Surface pressure distribution, $\theta_w=14^\circ$ , Case X1. ....	140
Figure 8.127 Surface pressure distribution, $\theta_w=14^\circ$ , Case X2. ....	141
Figure 8.128 Surface pressure distribution, $\theta_w=14^\circ$ , Case X3. ....	141
Figure 8.129 Surface pressure distribution, $\theta_w=15^\circ$ , Case B. ....	142
Figure 8.130 Surface pressure distribution, $\theta_w=15^\circ$ , Case D. ....	142
Figure 8.131 Surface pressure distribution, $\theta_w=15^\circ$ , Case G. ....	143
Figure 8.132 Surface pressure distribution, $\theta_w=16^\circ$ , Case B. ....	143
Figure 8.133 Surface pressure distribution, $\theta_w=16^\circ$ , Case D. ....	144
Figure 8.134 Surface pressure distribution, $\theta_w=16^\circ$ , Case G. ....	144
Figure 8.135 Surface pressure distribution, $\theta_w=18^\circ$ , Case B. ....	145
Figure 8.136 Surface pressure distribution, $\theta_w=18^\circ$ , Case D. ....	145
Figure 8.137 Surface pressure distribution, $\theta_w=18^\circ$ , Case Modified D. ....	146
Figure 8.138 Surface pressure distribution, $\theta_w=18^\circ$ , Case G. ....	146
Figure 8.139 Surface pressure distribution, $\theta_w=18^\circ$ , Case Modified G. ....	147
Figure 8.140 Surface pressure distribution, $\theta_w=18^\circ$ , Case X1. ....	147
Figure 8.141 Surface pressure distribution, $\theta_w=18^\circ$ , Case X2. ....	148
Figure 8.142 Surface pressure distribution, $\theta_w=18^\circ$ , Case X3. ....	148
Figure 8.143 Surface pressure distribution, $\theta_w=24^\circ$ , Case B. ....	149
Figure 8.144 Surface pressure distribution, $\theta_w=24^\circ$ , Case D. ....	149
Figure 8.145 Surface pressure distribution, $\theta_w=24^\circ$ , Case Modified D. ....	150
Figure 8.146 Surface pressure distribution, $\theta_w=24^\circ$ , Case G. ....	150
Figure 8.147 Surface pressure distribution, $\theta_w=24^\circ$ , Case Modified G. ....	151
Figure 8.148 Surface pressure distribution, $\theta_w=24^\circ$ , Case X1. ....	151
Figure 8.149 Surface pressure distribution, $\theta_w=24^\circ$ , Case X2. ....	152
Figure 8.150 Surface pressure distribution, $\theta_w=24^\circ$ , Case X3. ....	152
Figure 8.151 Effect of corner angle ( $\theta_w$ ) on surface pressures, Case B. ....	153

Figure 8.152 Effect of corner angle ( $\theta_w$ ) on surface pressures, Case D. ....	153
Figure 8.153 Effect of corner angle ( $\theta_w$ ) on surface pressures, Case G. ....	154
Figure 8.154 Stanton number distribution, $\theta_w=5^\circ$ , Case B. ....	154
Figure 8.155 Stanton number distribution, $\theta_w=5^\circ$ , Case D. ....	155
Figure 8.156 Stanton number distribution, $\theta_w=5^\circ$ , Case G. ....	155
Figure 8.157 Stanton number distribution, $\theta_w=10^\circ$ , Case B. ....	156
Figure 8.158 Stanton number distribution, $\theta_w=10^\circ$ , Case D. ....	156
Figure 8.159 Stanton number distribution, $\theta_w=10^\circ$ , Case G. ....	157
Figure 8.160 Stanton number distribution, $\theta_w=14^\circ$ , Case B. ....	157
Figure 8.161 Stanton number distribution, $\theta_w=14^\circ$ , Case D. ....	158
Figure 8.162 Stanton number distribution, $\theta_w=14^\circ$ , Case G. ....	158
Figure 8.163 Stanton number distribution, $\theta_w=15^\circ$ , Case B. ....	159
Figure 8.164 Stanton number distribution, $\theta_w=15^\circ$ , Case D. ....	159
Figure 8.165 Stanton number distribution, $\theta_w=16^\circ$ , Case B. ....	160
Figure 8.166 Stanton number distribution, $\theta_w=16^\circ$ , Case D. ....	160
Figure 8.167 Stanton number distribution, $\theta_w=16^\circ$ , Case G. ....	161
Figure 8.168 Stanton number distribution, $\theta_w=18^\circ$ , Case B. ....	161
Figure 8.169 Stanton number distribution, $\theta_w=18^\circ$ , Case D. ....	162
Figure 8.170 Stanton number distribution, $\theta_w=18^\circ$ , Case G. ....	162
Figure 8.171 Stanton number distribution, $\theta_w=24^\circ$ , Case B. ....	163
Figure 8.172 Stanton number distribution, $\theta_w=24^\circ$ , Case D. ....	163
Figure 8.173 Stanton number distribution, $\theta_w=24^\circ$ , Case G. ....	164
Figure 8.174 Effect of $T_w/T_0$ on convergence histories, $\theta_w=14^\circ$ .....	167
Figure 8.175 Effect of $T_w/T_0$ on number of grid points in boundary layer, $\theta_w=14^\circ$ .	167
Figure 8.176 Mach contours, $\theta_w=14^\circ$ , Case B. ....	168
Figure 8.177 Mach contours, $\theta_w=14^\circ$ , Case Modified D. ....	168

Figure 8.178 Mach contours, $\theta_w=14^\circ$ , Case Modified G. ....	169
Figure 8.179 Mach contours, $\theta_w=14^\circ$ , Case X1. ....	169
Figure 8.180 Mach contours, $\theta_w=14^\circ$ , Case X2. ....	170
Figure 8.181 Mach contours, $\theta_w=14^\circ$ , Case X3. ....	170
Figure 8.182 Mach contours, $\theta_w=18^\circ$ , Case B. ....	171
Figure 8.183 Mach contours, $\theta_w=18^\circ$ , Case Modified D. ....	171
Figure 8.184 Mach contours, $\theta_w=18^\circ$ , Case Modified G. ....	172
Figure 8.185 Mach contours, $\theta_w=18^\circ$ , Case X1. ....	172
Figure 8.186 Mach contours, $\theta_w=18^\circ$ , Case X2. ....	173
Figure 8.187 Mach contours, $\theta_w=18^\circ$ , Case X3. ....	173
Figure 8.188 Mach contours, $\theta_w=24^\circ$ , Case B. ....	174
Figure 8.189 Mach contours, $\theta_w=24^\circ$ , Case Modified D. ....	174
Figure 8.190 Mach contours, $\theta_w=24^\circ$ , Case Modified G. ....	175
Figure 8.191 Mach contours, $\theta_w=24^\circ$ , Case X1. ....	175
Figure 8.192 Mach contours, $\theta_w=24^\circ$ , Case X2. ....	176
Figure 8.193 Mach contours, $\theta_w=24^\circ$ , Case X3. ....	176
Figure 8.194 Effect of $T_w/T_0$ on streamlines, $\theta_w=14^\circ$ , Case B. ....	177
Figure 8.195 Effect of $T_w/T_0$ on streamlines, $\theta_w=14^\circ$ , Case Modified D. ....	177
Figure 8.196 Effect of $T_w/T_0$ on streamlines, $\theta_w=14^\circ$ , Case Modified G. ....	178
Figure 8.197 Effect of $T_w/T_0$ on streamlines, $\theta_w=14^\circ$ , Case X1. ....	178
Figure 8.198 Effect of $T_w/T_0$ on streamlines, $\theta_w=14^\circ$ , Case X2. ....	179
Figure 8.199 Effect of $T_w/T_0$ on streamlines, $\theta_w=14^\circ$ , Case X3. ....	179
Figure 8.200 Effect of $T_w/T_0$ on streamlines, $\theta_w=18^\circ$ , Case B. ....	180
Figure 8.201 Effect of $T_w/T_0$ on streamlines, $\theta_w=18^\circ$ , Case Modified D. ....	180
Figure 8.202 Effect of $T_w/T_0$ on streamlines, $\theta_w=18^\circ$ , Case Modified G. ....	181
Figure 8.203 Effect of $T_w/T_0$ on streamlines, $\theta_w=18^\circ$ , Case X1. ....	181

Figure 8.204 Effect of $T_w/T_0$ on streamlines, $\theta_w=18^\circ$ , Case X2.....	182
Figure 8.205 Effect of $T_w/T_0$ on streamlines, $\theta_w=18^\circ$ , Case X3.....	182
Figure 8.206 Effect of $T_w/T_0$ on streamlines, $\theta_w=24^\circ$ , Case B.....	183
Figure 8.207 Effect of $T_w/T_0$ on streamlines, $\theta_w=24^\circ$ , Case Modified D. ....	183
Figure 8.208 Effect of $T_w/T_0$ on streamlines, $\theta_w=24^\circ$ , Case Modified G. ....	184
Figure 8.209 Effect of $T_w/T_0$ on streamlines, $\theta_w=24^\circ$ , Case X1.....	184
Figure 8.210 Effect of $T_w/T_0$ on streamlines, $\theta_w=24^\circ$ , Case X2.....	185
Figure 8.211 Effect of $T_w/T_0$ on streamlines, $\theta_w=24^\circ$ , Case X3.....	185
Figure 8.212 Effect of $T_w/T_0$ on pressures contours, $\theta_w=14^\circ$ Case X2.....	186
Figure 8. 213 Effect of $T_w/T_0$ on pressures contours, $\theta_w=14^\circ$ Case X3.....	186
Figure 8. 214 Effect of $T_w/T_0$ on pressures contours, $\theta_w=18^\circ$ Case X2.....	187
Figure 8.215 Effect of $T_w/T_0$ on pressures contours, $\theta_w=18^\circ$ Case X3.....	187
Figure 8. 216 Effect of $T_w/T_0$ on pressures contours, $\theta_w=24^\circ$ Case X2.....	188
Figure 8. 217 Effect of $T_w/T_0$ on pressures contours, $\theta_w=24^\circ$ Case X3.....	188
Figure 8. 218 Effect of $T_w/T_0$ on temperature contours, $\theta_w=14^\circ$ Case X2. ....	189
Figure 8. 219 Effect of $T_w/T_0$ on temperature contours, $\theta_w=14^\circ$ Case X3. ....	189
Figure 8. 220 Effect of $T_w/T_0$ on temperature contours, $\theta_w=18^\circ$ Case X2. ....	190
Figure 8. 221 Effect of $T_w/T_0$ on temperature contours, $\theta_w=18^\circ$ Case X3. ....	190
Figure 8. 222 Effect of $T_w/T_0$ on temperature contours, $\theta_w=24^\circ$ Case X2. ....	191
Figure 8. 223 Effect of $T_w/T_0$ on temperature contours, $\theta_w=24^\circ$ Case X3. ....	191
Figure 8.224 Effect of $T_w/T_0$ on surface pressures, $\theta_w=14^\circ$ .....	192
Figure 8.225 Effect of $T_w/T_0$ on surface pressures, $\theta_w=18^\circ$ . ....	192
Figure 8.226 Effect of $T_w/T_0$ on surface pressures, $\theta_w=24^\circ$ .....	193
Figure 8.227 Effect of $T_w/T_0$ on heat transfer, $\theta_w=14^\circ$ .....	193
Figure 8.228 Effect of $T_w/T_0$ on heat transfer, $\theta_w=14^\circ$ .....	194
Figure 8.229 Effect of $T_w/T_0$ on heat transfer, $\theta_w=18^\circ$ .....	194

Figure 8.230 Effect of $T_w/T_0$ on heat transfer, $\theta_w=18^\circ$ .....	195
Figure 8.231 Effect of $T_w/T_0$ on heat transfer, $\theta_w=24^\circ$ .....	195
Figure 8.232 Effect of $T_w/T_0$ on heat transfer, $\theta_w=24^\circ$ .....	196
Figure B.1 Estimation of distance normal to the surface .....	217

## LIST OF SYMBOLS

$a$	Speed of sound
$a_1$	Ratio of Reynolds shear stress to turbulent kinetic energy
$C$	Chapman-Rubesin constant ( $C = (\mu / \mu_\infty) / (T_\infty / T)$ )
$C_f$	Skin friction coefficient
$C_p$	Pressure coefficient
$e_t$	Total energy per unit volume
$\hat{e}_t$	Total energy per unit mass
$E$	Inviscid flux in x-direction
$E_v$	Viscous flux in x-direction
$\bar{E}$	Inviscid flux in $\xi$ -direction
$\bar{E}_v$	Viscous flux in $\xi$ -direction
$f_{qw}$	Heat transfer parameter
$F$	Inviscid flux in y-direction
$F_v$	Viscous flux in y-direction
$\bar{F}$	Inviscid flux in $\eta$ -direction
$\bar{F}_v$	Viscous flux in $\eta$ -direction
$G$	Inviscid flux in z-direction
$G_v$	Viscous flux in z-direction
$\bar{G}$	Inviscid flux in $\zeta$ -direction
$\bar{G}_v$	Viscous flux in $\zeta$ -direction
$h$	Enthalpy
$h_r$	Recovery enthalpy
$J$	Jacobian of the transformation from Cartesian co-ordinate to the generalised curvilinear co-ordinates
$k$	Thermal conductivity

$\ell$	Mixing length
l	Left hand-side
M	Mach number
P	Pressure
$P_t$	Total pressure
Pr	Prandtl Number
r	Right hand-side
R	Gas constant
$Re_{x,e}$	Local Reynolds number ( $U_e \rho_e x / \mu_e$ )
$Re_{x,\infty}$	Local Reynolds number ( $U_\infty \rho_\infty x / \mu_\infty$ )
$Re_\infty$	Reynolds number ( $U_\infty \rho_\infty L / \mu_\infty$ )
Ru	Universal gas constant
q	Component of velocity perpendicular to the separation line
$q_x, q_y, q_z$	Heat conduction terms in x, y, and z directions
$\dot{q}$	Total heat flux
Q	Vector of dependent flow variables in Cartesian co-ordinate system
$\bar{Q}$	Vector of dependent flow variables in generalised curvilinear co-ordinate system
S	Surface of the cell
St	Stanton number
t	Time
T	Temperature
$T_0$	Stagnation temperature
$T_{aw}$	Adiabatic wall temperature
$T^*$	Reference temperature
$U_{DIF}$	Difference between maximum and minimum total velocity at a constant x-station
U	Velocity
u, v, w	Velocity components in Cartesian co-ordinate system
$U^c, V^c, W^c$	Contravariant velocity components
x	Distance from leading edge
$y^+$	Non-dimensional wall distance
x,y,z	Spatial co-ordinates in Cartesian co-ordinate system
$\xi, \eta, \zeta$	Components of the generalised curvilinear co-ordinate system

$\delta$	Boundary layer thickness, Central difference operator
$\delta_T$	Thermal boundary layer thickness
$\delta^*$	Displacement thickness
$\delta_{T,\max}$	Location of maximum temperature inside the boundary layer
$\bar{\delta}^2$	Pressure averaging operator
$\partial$	Partial differentiation operator
$\gamma$	Ratio of specific heats
$\rho$	Density
$\mu$	Kinematic viscosity
$\nu_t$	Eddy viscosity
$\sigma(s)$	Modelling parameter in J-K turbulence model
$\tau$	Shear stress, Reynolds shear stress, Time in generalised curvilinear co-ordinate system
$\theta$	Momentum thickness.
$\theta_w$	Compression ramp angle
$\beta$	Wave angle
$\omega$	Mean vorticity
$\bar{\kappa}$	Hypersonic viscous interaction parameter
$\varepsilon_i$	Implicit smoothing constant
$\varepsilon_e$	Explicit smoothing constant
$\kappa^{(2)}, \kappa^{(4)}$	Second-and fourth-order dissipation terms
$\nabla$	Total derivatives

### Subscripts

$x, y, z, t$	Differentiation with respect to $x, y, z, t$
$\xi, \eta, \zeta, \tau$	Differentiation with respect to $\xi, \eta, \zeta, \tau$
$\infty$	Free-stream property
$e$	Boundary layer edge property
$w$	Wall property
$\max$	Maximum value
$\min$	Minimum value
$\text{tot}$	Total

### Superscripts

$\wedge$	Property scaled by Jacobian
$-$	Non-dimensional property

## **CHAPTER 1**

### **INTRODUCTION**

Since hypersonic flight has been started on 22 September 1963 with the flight of an aircraft named North American X-15 at Mach number 6.7, large number of scientist and engineers accomplished intensive research and development to understand this harsh and unforgiving phenomenon.

The flow field characteristics change towards characteristics of hypersonic flow drastically when the Mach number is five or greater.

Generally, the external contours, control surfaces and propulsion systems of the advanced hypersonic vehicles use compression and expansion surfaces for inlet and nozzle respectively. It is well known that, the shock/shock, and shock/boundary layer interactions take place on those surfaces during hypersonic flights and those interactions play vital role on the performance of the air vehicle. As a result of those features of advanced hypersonic vehicles, the integration of engine and airframe is an important design consideration [1].

The phenomenon of hypersonic flow over compression ramps can be naturally observed in control surfaces of reentry vehicles. The flow passing a compression ramp is a classical example of shock-boundary layer interactions.

High Mach number and high enthalpy flow conditions of a hypersonic vehicle which may be encountered in flight can not be materialized in ground-based test facilities. Thus, computer codes are used with appropriate geometric flexibility and physical models. Much works has been performed both experimentally and numerically to gain an accurate capability to describe the physics of hypersonic flows around compression corners.

## 1.1 General Information about Hypersonic Flows

The term “hypersonic” (or hypervelocity) implies that the flight speed is much greater than the ambient speed of sound. There is a conventional rule of thumb that defines hypersonic aerodynamics as those flows where the Mach number,  $M$ , is greater than 5. Rather, hypersonic flow is best defined as that regime where certain physical flow phenomena become progressively more important as the Mach number is increased to higher values [2]. For the hypersonic flow the kinetic energy of the free stream particles is very high when compared with internal thermodynamic energy of the free stream fluid particles.

The flow past a vehicle flying at hypersonic speed is the source of strong shock waves formed ahead of the vehicle nose, the rounded leading edge of wings and tails, at the compression ramp of air-intakes, and at the control surfaces. These shock waves are the origin of interference phenomena resulting, first from the intersection of two shocks, and second from their interaction with the boundary layers developing on the vehicle surface.

Shock-wave/boundary layer interactions occur at the impingement of a bow shock, at a deflected flap, along axial corners in wing-body and fin-wing junctions, etc. These interactions are also present in the air intake of an air-breathing propulsion system and in the vicinity of an afterbody where the nozzle jet meets the outer flow. Such interactions can induce separation of the boundary layer which causes loss of control effectiveness or flow degradation in an engine jet. Also, in high-enthalpy hypersonic flows, the subsequent reattachment on a surface of the separated shear layer gives rise to heat transfer which can be far in excess of an attached boundary layer [3].

Thomas et al. [4] identified critical aerothermodynamics design issues for a hypersonic aircraft powered by an air-breathing propulsion system. The flow around a hypersonic aircraft is predominantly three-dimensional and is dominated by viscous effects.

## 1.2 Literature Survey

In the last decades there have been many studies dealing with the shock wave/boundary layer interaction phenomena. Most of the experimental and computational research have been performed on a configuration to simulate a deflected control surface in which a two-dimensional flat plate is followed by a compression corner. This type of geometry has been the cornerstone of many investigations to understand the phenomena associated with shock/shock and shock wave/boundary layer interactions. However, very few experimental studies have proven to be sufficiently well documented to satisfy the requirements for CFD code validation. Besides, success of these studies has been limited due to measurement uncertainties on the experimental side.

Holden [5] and Hankey and Holden [6] have performed experimental studies to characterize both laminar and turbulent shock wave /boundary layer interactions, from supersonic through hypersonic regime, by investigating the influence of the Mach and Reynolds numbers, the wedge angle and the leading edge bluntness on the flow field.

Detailed measurements of density profiles of a hypervelocity flat plate boundary layer flow have been studied experimentally and compared with theory that includes real gas effects by Mallinson et al. [7].

Mallinson et al. [8] has focused on high enthalpy laminar hypersonic flow over a compression corner including real gas effects in another experimental study. The shock wave/boundary layer interaction has been examined both experimentally and theoretically.

An experimental and computational study of two-dimensional hypersonic flow field over flat plate/compression corner configurations at Mach 14 and wall-to-total-temperature ratio ( $T_w/T_0$ ) of 0.12 with Reynolds numbers to hinge line varying between  $4.5 \times 10^5$  and  $2.6 \times 10^6$  have been performed by Simeonides and Haase [9] for fully laminar and perfect gas to investigate strong shock wave/boundary layer interactions with extensive separation and transitional interactions with transition occurring near the reattachment point. Experimental

studies have been performed in the VKI Longshot hypersonic wind tunnel. Numerical analysis have been done by using Navier-Stokes equations.

Schutle et al. [10] has focused on the boundary layer separation caused by an impingement shock and the boundary layer separation at compression corners by performing experimental and numerical studies. The experiments have been done in the German Aerospace Research Center hypersonic wind tunnel at Mach 6 and laminar flow conditions. The objective of the study was to improve the inlet efficiency by finding effective measures to manipulate shock wave/boundary layer interactions.

Another important parameter to effect the aerothermal characteristics of the control surface is, in a typical reentry flight regime, a high angle of attack. In the literature, the works are mainly for cases with zero angle of attack, only a few basic experiments have been conducted for cases with higher angles of attack. One of these studies has been performed by Hozumi et al. [11] experimentally and numerically. The experimental study has been obtained in the National Aerospace Laboratory and ONERA S4MA hypersonic wind tunnels. The effects of nose bluntness and angle of attack on the corner heating pattern has been investigated by examining the relations between hypersonic aerodynamic heating characteristics at a high angle of attack, such as 15°, 30° and 35°.

Another experimental and computational study of two-dimensional hypersonic laminar flow field over flat plate/compression corner configurations has been done by Chanetz et al. [12]. Experiments have been carried out in the ONERA R5Ch wind tunnel on a hollow cylinder flare. Classical Navier-Stokes solutions and Direct Simulation Monte-Carlo have been used as numerical approach. The aim of the study was to improve the capacity of the Navier-Stokes codes to predict high Mach number shock wave/boundary layer interactions.

A code validation study has been conducted by using four different codes for solving the compressible Navier-Stokes equations by Rudy et al. [13]. The solution of two-dimensional high speed laminar separated flows at Mach 14.1 for 15°, 18° and 24° compression corners have been compared with experimental shock tunnel results.

Brenner et al. [14] have focused on the numerical simulation of the flow of perfect gases through the inlet of airbreathing, hypersonic vehicles based on a model problem. Shock wave and turbulent boundary layer interaction, shock/shock interaction and highly three-dimensional separation have been investigated in a blunt-fin configuration with a downstream compression ramp. The three-dimensional, time dependent Navier-Stokes equations in conservative form for a reacting, multicomponent mixture of perfect gases have been considered.

Grasso and Marini [15] have numerically studied the two- and three-dimensional laminar hypersonic flows dominated by strong shock wave/boundary layer interactions with rather extended separated regions to evaluate the influence of some geometrical and flow parameters such as corner angle, leading edge bluntness, Mach number, and viscous interaction parameter. A cell centered finite volume formulation has been used for the solution of the compressible Navier-Stokes equations.

D'Ambrosio [16] has carried out a numerical study for the purpose of verification and validation of a CFD code. The numerical results have been compared with the experiments conducted at the ONERA Chalais-Meudon Research Center and at the Chalspan-University, Buffalo Research Center on shock/shock interactions.

Another numerical analysis has been performed by Martinez et al. [17] over a three-dimensional  $15^\circ$  compression corner in a laminar hypersonic flow at Mach 6.85 and at a Reynolds number per unit length of  $2.45 \times 10^6 \text{ m}^{-1}$ .

Laminar and turbulent hypersonic flows over  $24^\circ$  compression corner and curved compression corner have been analyzed numerically by Dogrusoz [18] solving three dimensional, thin layer, compressible, Navier-Stokes equations. The heat transfer and pressure distributions, skin friction coefficient and boundary layer surveys have been performed.

Tables 1.1-1.2 list the most representative calculations of hypersonic compression corner by solutions of the Navier-Stokes equations and experimental studies.

### **1.3 Scope and Overview of the thesis**

The purpose of this thesis is to perform numerical solutions of hypersonic, high temperature, perfect gas flows over various geometries. Three dimensional, thin layer, compressible, Navier-Stokes equations are solved. An upwind finite difference approach with Lower Upper-Alternating Direction Implicit (LU-ADI) decomposition is used.

During the analysis, two different geometries are used: A flat plate at zero incidence and compression corners with angles of 5°, 10°, 14°, 15°, 16°, 18°, and 24°.

Hypersonic flows over compression ramps, for example, as used for control purposes on re-entry vehicles, feature a complex structure of interacting shock waves and include shock-wave/boundary-layer interactions, which are known to induce flow separation. Subsequent flow reattachment on the ramp causes high heat fluxes, which must be predicted accurately to preserve the thermal and structural integrity of the vehicle.

Three dimensional, compressible, Reynolds averaged, thin layer Navier-Stokes equations are solved numerically.

The shock /shock wave, the shock wave/boundary layer interactions, the heat transfer rates, local skin friction coefficients, the effect of wall-to stagnation temperature ratio ( $T_w/T_0$ ) on the flow and boundary layer variables, the effect of corner angle ( $\theta_w$ ) and the other boundary layer properties are studied and obtained numerical results are compared with available numerical and experimental data.

In the thesis, chapters are presented in the following order:

Physical characteristics of hypersonic boundary layer, and hypersonic compression corner flows are presented in Chapter 2 and Chapter 3, respectively.

General Navier-Stokes equations and their thin layer formulation, the general Cartesian coordinate formulation and transformation of equations from Cartesian to curvilinear coordinates are given in Chapter 4.

In Chapter 5, a description of the code and the solution algorithm are presented. Each subprogram is described with their function in the code by the help of the computational flow structure of the code. Also, non-dimensional forms of the variables used in the code are given in this chapter.

In Chapter 6, a description of the test cases is given with their flow conditions. In Chapter 7, the grids used for the solutions are described and the initial and boundary conditions are explained.

In Chapter 8, Computational details obtained numerical results are compared with available numerical, experimental and theoretical data. Especially, the effect of  $T_w/T_0$  on the heat transfer rate, the surface pressure distribution and the boundary layer flow variables, the effect of corner angle ( $\theta_w$ ), strong shock wave boundary layer interactions with extended separated regions are presented. Note that, all the obtained results are not presented in this chapter. The results not presented in Chapter 8 are published in Ref. [33].

Also, in Appendix A, details of the transformation of the solution domain from Cartesian coordinates to curvilinear coordinates and non-dimensionalization of the governing equations are given. Details of the boundary layer post processing are presented in Appendix B. In Appendix C and D, the details for skin friction and Stanton number post processing are given, respectively.

**Table 1.1** Navier-Stokes Calculations of Two-Dimensional Laminar Interactions

<b>Author</b>	<b>Computed Cases</b>	<b>Numerical Method</b>
Carter (1972), [19]	Corner Flow at $M_0=6$	Brailovskaya Explicit
Hung & MacCormack (1976), [20]	Corner Flow at $M_0=14.4$	MacCormack Explicit
Lawrence et al.(1986), [21]	Corner Flow at $M_0=14.1$	Forward Marching
Ray et al. (1987), [22]	Corner Flow, $M_0=14.1$ &18.9	MacCormack Explicit
Hollanders & Marmignon (1989), [23]	Corner Flow at $M_0=14.1$	Upwind
Rudy et al. (1989), [24]	Corner Flow at $M_0=14.1$	Several
Thajera et al. (1990), [25]	Corner Flow at $M_0=14.1$	Unstructured Grid
Antibes Workshops (1990, 1991, 1993)	Corner Flow at $M_0=10$ and 11.68	Several
Simeonides (1992), [26]	Corner Flow at $M_0=14.1$	Runge-Kutta with central and upwind
Grasso & Leone (1992), [27]	Corner Flow at $M_0=7.4, 11.7$ and 17.4	Runge-Kutta with central differences
Joulot (1992)	Corner Flow at $M_0=10$ & 11.7	Upwind
Leyland (1993), [28]	Corner Flow at $M_0=14.1$	Upwind

**Table 1.2** Experimental and Numerical Studies

<b>Author</b>	<b>Computed Cases</b>	<b>Method</b>
Lewis et al. (1968), [29]	Corner Flow with 10.25 degree corner at $M_0=6$ & 4	Experimental
Erengil & Dolling (1991), [30]	Corner Flow with 28 deg. corner at $M_0=5$	Experimental
Rudy et al. (1991), [13]	Corner Flow with 15,18 degree corner at $M_0=14.1$	Experimental and Numerical
Simeonides et al., (1992,1993), [9]	Corner Flow with 7.5, 15 degree corner at $M_0=6$ & 14.1	Experimental and Numerical
Galassi et al. (1993), [31]	Corner Flow with curved corner at $M_0=5.71-5.77$	Experimental and Numerical
Mallinson et al. (1996), [8]	Corner Flow with 0, 15, 18, 24 deg. corner with diff. L.E. conf. at $M_0=7.5$ and 9.1	Experimental
Paciorri et al. (1998), [32]	Hollow cylinder flare with 35 deg. corner at $M_0=5$	Experimental and Numerical

## CHAPTER 2

### HYPERSONIC BOUNDARY LAYER

With reference to hypersonic lifting re-entry vehicles, attention is drawn to control surfaces such as body flaps, elevons and rudders. Deflections of a control surface is anticipated to cause a severe interaction between the oncoming boundary layer and the resulting shock wave, which may yield significant flow separation linked to significant losses in control effectiveness and excessive heating of the surface.

In this chapter, the physical characteristics of hypersonic flow and hypersonic laminar boundary layer flow are explained in detail, respectively.

#### 2.1 Physical Characteristic of Hypersonic Flows

##### Thin Shock Layers

The oblique shock theory states that, for a given flow deflection angle, the density increase across the shock wave becomes progressively large as the Mach number is increased. At higher densities, the mass flow behind the shock can more easily squeeze through smaller areas. For flow over a hypersonic body, this means that the distance between the shock wave and the body is defined as the shock layer, and for hypersonic speeds this shock layer can be quite thin [2].

##### Entropy Layer

At hypersonic Mach numbers, the shock layer over the blunt nose is also very thin, with a small shock-detachment distance. In the nose region, the shock wave is highly curved. The entropy of the flow increases across a shock wave, and as

the shock gets stronger, the entropy increase becomes larger. A streamline passing through the strong, nearly normal portion of the curved shock near the centerline of the flow will experience a larger entropy increase than a neighboring streamline which passes through a weaker portion of the shock further away from the centerline. Hence, there are strong entropy gradients generated in the nose region; this “entropy layer” flows downstream, and essentially wets the body for large distance from the nose. The boundary layer along the surface grows inside this entropy layer, and is affected by it. This entropy layer causes analytical problems when we wish to perform a standard boundary layer calculation on the surface, because there is a question as to what the proper edge conditions should be for the boundary layer [2].

### **Viscous Interaction**

The local severe heating rates produced by viscous interaction and shock/shock interactions can cause catastrophic failures on hypersonic vehicles.

Consider a boundary layer on a flat plate in a hypersonic flow, as sketched in Figure 2.2 [2]. A high-velocity, hypersonic flow contains a large amount of kinetic energy, which is partly dissipated within the boundary layer, causing large temperature increases as indicated in Figure 2.2. In turn, the viscosity within the boundary layer is increased, and the density greatly decreases. This causes the boundary layer thickness to grow more rapidly. The thick boundary layer in hypersonic flow can exert a major displacement effect on the inviscid flow outside the boundary layer, causing a given body shape to appear much thicker than it really is. Due to the extreme thickness of the boundary-layer flow, the outer inviscid flow is greatly changed; the changes in the inviscid flow in turn feed back to affect the growth of the boundary layer. This major interaction between the boundary layer and the outer inviscid flow is called as viscous interaction. Viscous interaction can have important effects on the surface pressure distribution, hence lift, drag and stability on hypersonic vehicles. Moreover, skin friction and heat transfer are increased by viscous interaction.

The boundary layer on a hypersonic vehicle can become so thick that it essentially merges with the shock wave - a merged shock layer. When this

happens the shock layer must be treated as fully viscous, and the conventional boundary layer analysis must be completely abandoned [2].

For all practical purposes, the strong and weak viscous interaction regions appear to be described by

$$\text{Strong interaction} \quad \bar{\chi} > 3,$$

$$\text{Weak interaction} \quad \bar{\chi} < 3,$$

where hypersonic laminar viscous interaction parameter,  $\bar{\chi}$ , is defined as [2]

$$\bar{\chi} = \frac{M_\infty^2}{\sqrt{\text{Re}}} \sqrt{C} \quad \text{and} \quad C = \frac{\rho_w \mu_w}{\rho_e \mu_e}.$$

Figure 2.3 illustrates the hypersonic viscous flow over a flat plate, and illustrates the strong interaction immediately downstream of the leading edge, and the weak interaction region further downstream.

In the strong interaction region the following physical effects occur:

1. In the leading edge region, the growth rate of the boundary layer displacement thickness is large, that is,  $d\delta^*/dx$  is large.
2. Hence, the incoming freestream “sees” an effective body with rapidly growing thickness; the inviscid streamlines are deflected upward, into the incoming flow, and a shock wave is consequently generated at the leading edge of the flat plate, i.e., the inviscid flow is strongly affected by the rapid boundary layer growth.
3. In turn, the substantial changes in the outer inviscid flow feedback to the boundary layer, affecting its growth and properties.

In the weak interaction region the following physical effects occur:

1. The rate of growth of the boundary layer is moderate, that is,  $d\delta^*/dx$  is reasonably small.
2. In turn, the outer inviscid flow is only weakly affected.
3. As a result, the changes in the inviscid flow result in a negligible feedback on the boundary layer, and this is ignored.

### **High-Temperature Flows**

The extreme viscous dissipation within hypersonic boundary layers can create high temperatures, leading to vibrational excitation, dissociation and ionization of the gas. Both boundary layer and the entire shock layer can be dominated by chemically reacting flow.

High temperature chemically reacting flows can have an influence on lift, drag and moments on a hypersonic vehicle. For example, such effects have been found to be very important for estimating the body flap deflection necessary to trim the space shuttle during the high-speed re-entry. However, by far the most dominant aspect of high temperatures in hypersonics is the resultant high heat transfer rate to the surface. Aerodynamic heating takes the form of heat transfer from the hot boundary layer to the cooler surface- called convective heating. Moreover, if the shock layer temperature is high enough, the thermal radiation emitted by the gas itself can become important, giving rise to a radiative flux to the surface- called radiative heating [2].

### **Low Density Flows**

Low density flows are not an inherent part of the definition of hypersonic flow, and therefore this discussion is not legitimately part of the definition of hypersonic flow. However, hypersonic vehicles frequently fly at very high altitudes, and therefore will encounter low density conditions. Hence, the design and analysis of hypersonic vehicles will sometimes require the consideration of low density flow. There are certain hypersonic applications which involve low-density flow, generally involving flight at high altitudes. For any given flight vehicle, as the

altitude progressively increases, hence the density decreases, the assumption of continuum flow becomes tenuous. As the altitude increases, the normal viscous flow no-slip assumptions at the wall of (1) zero velocity, (2) gas temperature equals the wall temperature, begin to fail. They are replaced by slip effects, in which a velocity and temperature jump at the wall must be assumed. Finally, when the air density becomes rarefied enough, the mean distance a molecule moves between collisions (the molecular free path,  $\lambda$ ) can become much larger than the scale of the body itself. This is the regime of free molecular flow, where the aerodynamic characteristics of the vehicle are determined by individual, scattered molecular impacts, and must be analyzed on the basis of kinetic theory [2].

## 2.2 Physical Characteristic of Hypersonic Boundary Layers

There are two important flow problems in the viscous boundary layer changes the nature of the outer inviscid flow, and turn these inviscid changes feedback as changes in the boundary layer structure. This phenomenon is called as viscous interaction detailed in Section 2.1.1 of this chapter. Those problems are:

1. Pressure interaction, due to the exceptionally thick boundary layers on faces under some hypersonic conditions.
2. Shock wave/boundary layer interaction, due to impingement of a strong shock wave on a boundary layer.

The classical hypersonic interaction between the outer inviscid flow and the boundary layer is due to very large boundary layer thicknesses which can occur at high hypersonic speeds.

For a flat plate laminar boundary layer thickness,  $\delta$ , grows as

$$\delta \propto \frac{M_e^2}{\sqrt{\text{Re}}}$$

Clearly, the thickness grows as the square of the Mach number, and therefore hypersonic boundary layers can be orders of magnitude thicker than low speed boundary layers at the same Reynolds number.

This thick hypersonic boundary layer displaces the outer inviscid flow, changing the nature of the inviscid flow. For example, inviscid flow over a flat plate is shown in Figure 2.4a, the streamlines are straight and parallel, and the pressure on the surface is constant. In contrast, for hypersonic viscous flow with a thick boundary layer, the inviscid streamlines are displaced upward, creating a shock wave at the leading edge as shown in Figure 2.4b. Moreover, the pressure varies over the surface of the flat plate. This is the source of the viscous interaction. The increased pressure (hence increased density) tends to make the boundary layer thinner than would be expected, and hence the velocity and temperature gradients at the wall are increased. In turn, the skin friction and heat transfer are increased over their values that would exist if a constant pressure equal to  $p_\infty$  are assumed [2, 34].

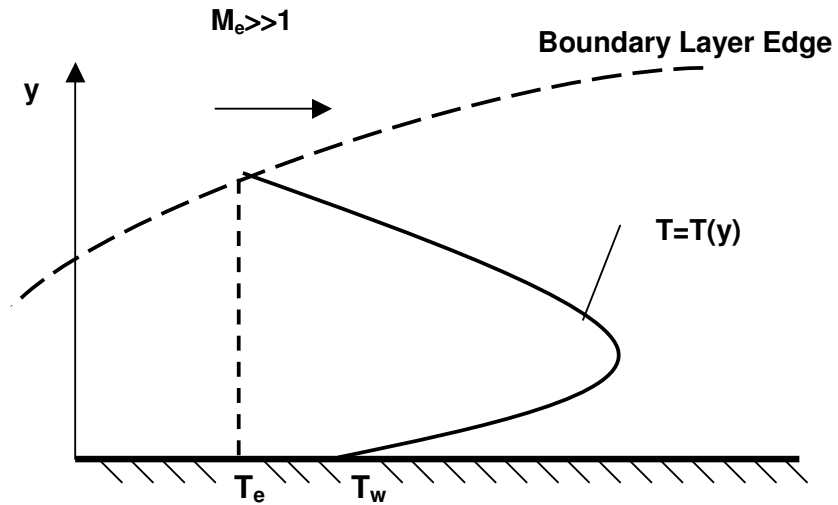


Figure 2.1 Temperature profile in a hypersonic boundary layer.

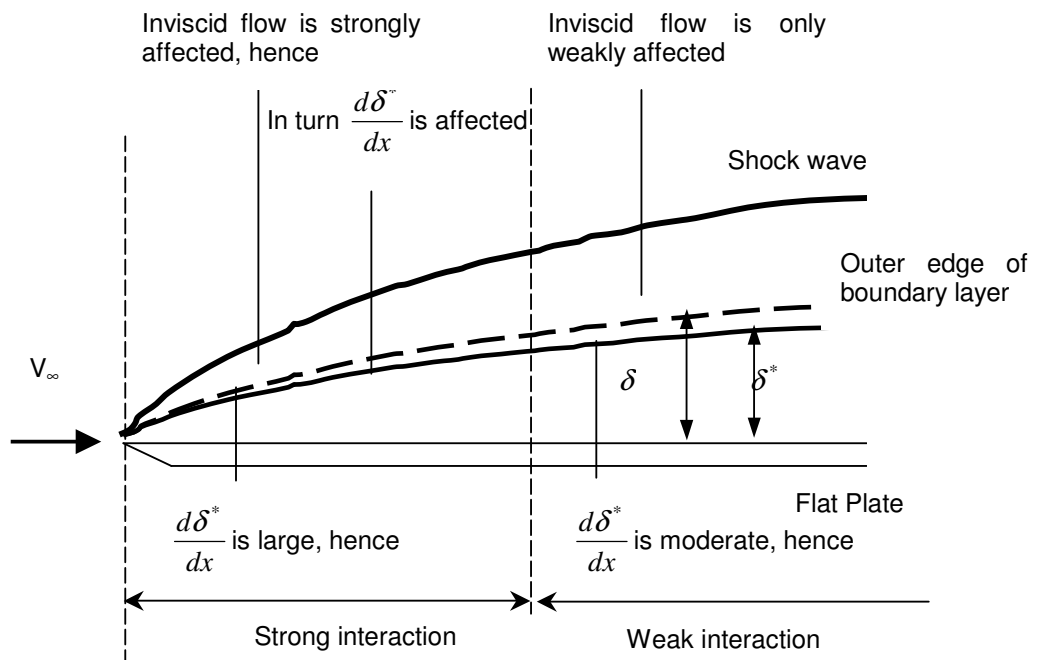
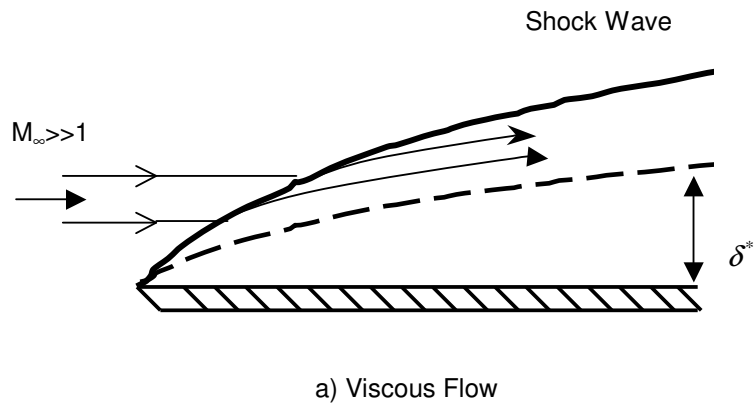
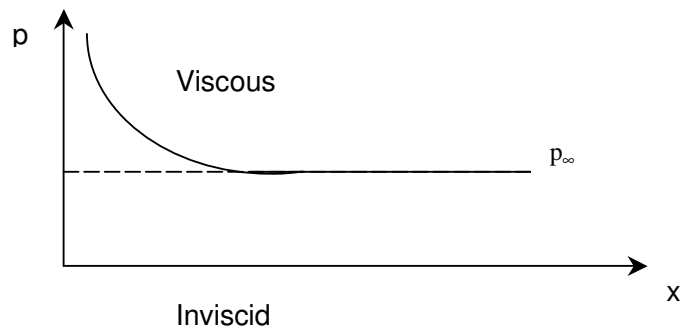
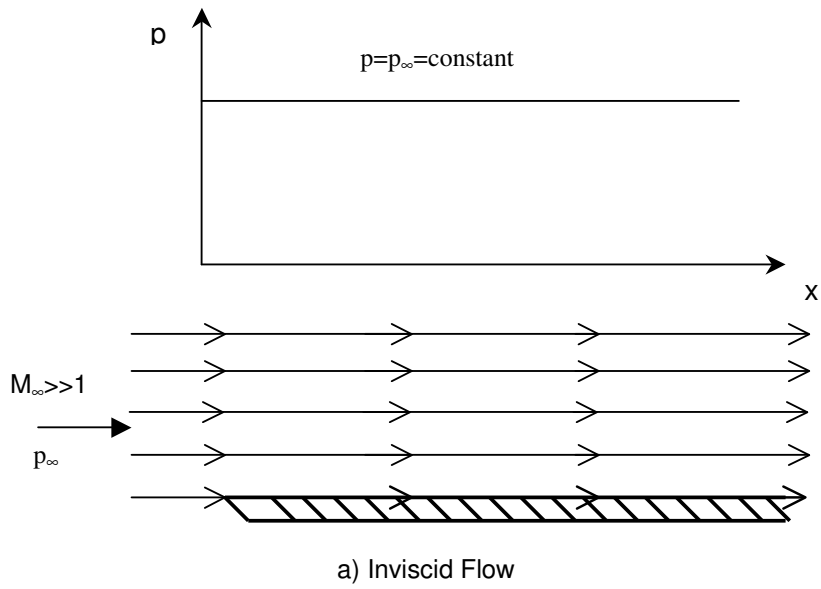


Figure 2.2 Illustration of strong and weak viscous interactions.



**Figure 2.3** Illustration of pressure distributions over a flat plate. (a) inviscid flow; (b) viscous flow [Ref. 2].

## CHAPTER 3

### HYPERSONIC COMPRESSION CORNERS

The viscous interactions can cause boundary layers to separate, can produce locally high pressures and high heat transfer rates as described in Chapter 2.

Flow separation can result in a loss of control effectiveness, or flow degradation in an engine inlet. The heating rates and pressure in the interaction regions can be locally severe, being orders of magnitude greater than the stagnation-point values. Large gradients exist in the heat transfer and in the pressure distribution, with locally severe values affecting extremely small areas.

The designers of vehicles that are to fly at hypersonic speeds have long recognized that the locally severe heating rates produced by viscous interactions and by shock/shock interactions can cause catastrophic failures.

Shock waves that are generated when there is a compressive turning of the local flow create shock/boundary layer interactions. The canopy and deflected control surfaces can produce the required flow deflections.

Axial corners formed by compression surfaces, such as those occurring in air breathing engine inlets and at wing/body or at fin/wing junctions can produce complex flow patterns, which contain vortices and embedded shock waves.

The parameters, which influence the extent of the shock wave/boundary layer interactions, are:

1. whether the approaching boundary layer is laminar or turbulent,
2. the Mach number of the approaching flow,

3. the Reynolds number of the approaching flow,
4. the surface temperature
5. the deflection angle of the corner, and
6. the chemical state of the gases.

The schematic of the flow field over a compression corner is illustrated in Figure 3.1. A relatively weak shock forms at the sharp leading edge of the plate. The shock induced by the corner interacts with the flat plate boundary layer. The shock inside the boundary layer is first seen to be a curved, lambda shock. The curvature of this shock is being due to its propagations through a rotational layer in which the Mach number changes from one streamline to another. Outside of the boundary layer, the shock wave is linear since the incoming flow is uniform. Due to the upstream propagation of pressure disturbances across the subsonic portion of the boundary layer, flow separation may occur depending upon the value of the viscous interaction parameter,  $\overline{\chi}$ , which is explained in Chapter 2, the Mach number  $M_\infty$  and corner angle  $\theta_w$ . The presence of the separation bubble causes the formation of the separation and reattachment shocks, the interaction of which generates a transmitted shock, a shear layer, and depending upon the Mach number, either a shock wave or an expansion fan that interacts with the boundary layer on the corner. The skin friction and heat transfer rapidly increase downstream of reattachment due to the recompression of the flow, and have a peak immediately past reattachment in the proximity of the location where the boundary layer thickness is minimum. Down-stream of the reattachment point, the boundary layer thins rapidly due to compression, resulting in large increases in skin friction and heat transfer on the wedge surface. Furthermore, the compression waves produced by the corner coalesce into a shock wave that intersects with the leading edge shock, producing an expansion fan and a shear layer, both of which affect the flow on the corner [34, 13, 14, 15].

At relatively large deflection angles, i.e., when appreciable separation of the boundary layer occurs, the pressure distributions exhibit three inflection points. These three inflection points are:

1. that is associated with the separation of the boundary layer,
2. that is associated with onset of reattachment, and
3. that is associated with the reattachment compression.

As noted by Delery [35], at very large deflection angles, the pressure distribution exhibits a decrease following the rise corresponding to reattachment. Then it tends to the constant level of the inviscid solution, with the tendency that the pressure overshoot increases as the deflection angle increases.

The peak measured heating rate usually occurs in the vicinity of reattachment where the boundary layer is the thinnest or, if separation does not occur, immediately downstream of the shock interaction [36].

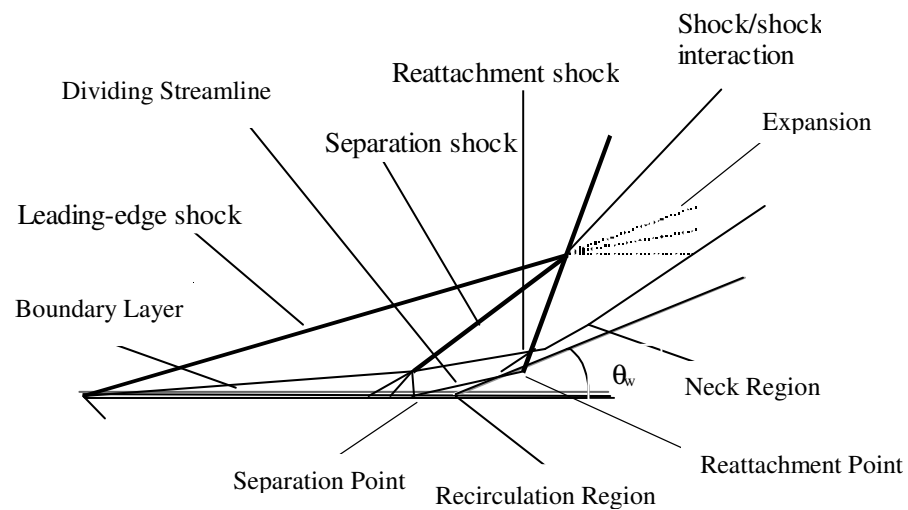


**Figure 3.1** Schematic of the flow field over a compression corner.

## CHAPTER 4

### NAVIER STOKES EQUATIONS

#### 4.1 Navier-Stokes Equations

The equations of fluid motion in complete form which include the conservation of mass, conservation of momentum and conservation of energy are referred to as the Navier-Stokes equations for Newtonian fluids in continuum. One of the most commonly used version of this equation set for CFD applications is the compact, conservative form written in Cartesian coordinates [37, 38] as

$$\frac{\partial Q}{\partial t} + \frac{\partial E}{\partial x} + \frac{\partial F}{\partial y} + \frac{\partial G}{\partial z} = \frac{\partial E_v}{\partial x} + \frac{\partial F_v}{\partial y} + \frac{\partial G_v}{\partial z} \quad (4.1)$$

where  $Q$  is the dependent variable vector,  $E, F$  and  $G$  are the inviscid momentum and energy flux vectors;  $E_v, F_v, G_v$  are the viscous flux vectors. The open forms of these vectors are as follows:

$$Q = \begin{bmatrix} \rho \\ \rho u \\ \rho v \\ \rho w \\ \rho e_t \end{bmatrix}, E = \begin{bmatrix} \rho u \\ \rho u^2 + p \\ \rho uv \\ \rho uw \\ u(\rho e_t + p) \end{bmatrix}, F = \begin{bmatrix} \rho v \\ \rho vu \\ \rho v^2 + p \\ \rho vw \\ v(\rho e_t + p) \end{bmatrix}, G = \begin{bmatrix} \rho w \\ \rho wu \\ \rho wv \\ \rho w^2 + p \\ w(\rho e_t + p) \end{bmatrix} \quad (4.2)$$

$$(4.3)$$

$$(4.4)$$

$$(4.5)$$

$$E_v = \begin{bmatrix} 0 \\ \tau_{xx} \\ \tau_{xy} \\ \tau_{xz} \\ u\tau_{xx} + v\tau_{xy} + w\tau_{xz} - q_x \end{bmatrix}, F_v = \begin{bmatrix} 0 \\ \tau_{yx} \\ \tau_{yy} \\ \tau_{yz} \\ u\tau_{yx} + v\tau_{yy} + w\tau_{yz} - q_y \end{bmatrix}, G_v = \begin{bmatrix} 0 \\ \tau_{zx} \\ \tau_{zy} \\ \tau_{zz} \\ u\tau_{zx} + v\tau_{zy} + w\tau_{zz} - q_z \end{bmatrix} \quad (4.6), (4.7), (4.8)$$

where;

$$\begin{aligned} \tau_{xx} &= -\frac{2}{3}\mu\nabla \cdot \mathbf{V} + 2\mu \frac{\partial u}{\partial x} & \tau_{xy} &= \tau_{yx} = \mu \left( \frac{\partial u}{\partial y} + \frac{\partial v}{\partial x} \right) \\ \tau_{yy} &= -\frac{2}{3}\mu\nabla \cdot \mathbf{V} + 2\mu \frac{\partial v}{\partial y} & \tau_{xz} &= \tau_{zx} = \mu \left( \frac{\partial u}{\partial z} + \frac{\partial w}{\partial x} \right) \\ \tau_{zz} &= -\frac{2}{3}\mu\nabla \cdot \mathbf{V} + 2\mu \frac{\partial w}{\partial z} & \tau_{yz} &= \tau_{zy} = \mu \left( \frac{\partial v}{\partial z} + \frac{\partial w}{\partial y} \right) \end{aligned}$$

$$q_x = -k \frac{\partial T}{\partial x}, \quad q_y = -k \frac{\partial T}{\partial y}, \quad q_z = -k \frac{\partial T}{\partial z} \quad (4.9)$$

The first component of each column vector is associated with the mass conservation equation, the next three components are associated with momentum equation, and the last component is associated with the energy equation.

## 4.2 Thin Layer Navier-Stokes Equations (TLNS)

The full Navier-Stokes equations can be simplified by neglecting the circumferential and streamwise gradient of stresses while retaining only the normal gradient of the stresses to reduce computational time and required storage.

According to this statement, all viscous terms in  $G_v$ , containing derivatives with respect to the direction along or parallel to the no-slip surface, are neglected. The resultant equations are called the thin layer Navier-Stokes equations (TLNS) and written in Cartesian coordinates as follow:

$$\frac{\partial Q}{\partial t} + \frac{\partial E}{\partial x} + \frac{\partial F}{\partial y} + \frac{\partial G}{\partial z} = \frac{\partial G_{TL}}{\partial z} \quad (4.10)$$

where Q, E, F, and G are defined in equations (4.2), (4.3), (4.4), and (4.5) respectively,  $G_{TL}$  is defined as

$$G_{TL} = \begin{bmatrix} 0 \\ \mu \frac{\partial u}{\partial z} \\ \mu \frac{\partial v}{\partial z} \\ \frac{4}{3} \mu \frac{\partial w}{\partial z} \\ u \tau_{zx} + v \tau_{zy} + w \tau_{zz} - q_z \end{bmatrix} \quad (4.11)$$

where  $\tau_{zx}$ ,  $\tau_{zy}$ ,  $\tau_{zz}$  and  $q_z$  are defined in equation (4.9).

### 4.3 Coordinate Transformation

Coordinate transformation is a technique used to convert the equations in the physical domain  $(x, y, z)$  to the computational domain  $(\xi, \eta, \zeta)$  as shown in Figure 4.1.

The relations between the Cartesian coordinates and the generalized curvilinear coordinates are given in the following way:

$$\{\tau = t, \xi = \xi(x, y, z, t), \eta = \eta(x, y, z, t), \zeta = \zeta(x, y, z, t)\} \quad (4.13)$$

where  $\tau$  is time, and  $\xi, \eta, \zeta$  are components of coordinates in the computational domain. Details of the transformation and non-dimensionalization are given in Appendix A.

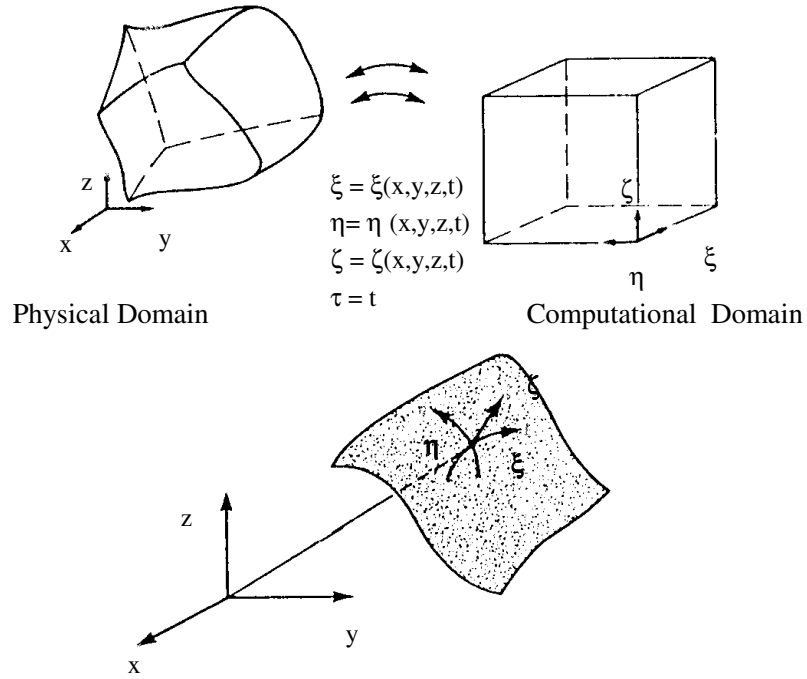


**Figure 4.1** Transformation and body coordinate [Ref 37].

#### 4.3.1 Transformed Form of The Full Navier-Stokes Equations

The nondimensional and transformed form of the full Navier-Stokes equations from the Cartesian coordinates to the generalized curvilinear coordinates is

$$\frac{\partial \hat{Q}}{\partial \tau} + \frac{\partial \hat{E}}{\partial \xi} + \frac{\partial \hat{F}}{\partial \eta} + \frac{\partial \hat{G}}{\partial \zeta} = \frac{\partial \hat{E}_v}{\partial \xi} + \frac{\partial \hat{F}_v}{\partial \eta} + \frac{\partial \hat{G}_v}{\partial \zeta} \quad (4.14)$$

where;

$$\hat{Q} = \frac{1}{J} \begin{bmatrix} \rho \\ \rho u \\ \rho v \\ \rho w \\ \rho e_t \end{bmatrix}, \quad \hat{E} = \frac{1}{J} \begin{bmatrix} \rho U^c \\ \rho u U^c + \xi_x p \\ \rho v U^c + \xi_y p \\ \rho w U^c + \xi_z p \\ U^c (\rho e_t + p) - \xi_t p \end{bmatrix}, \quad \hat{F} = \frac{1}{J} \begin{bmatrix} \rho V^c \\ \rho u V^c + \eta_x p \\ \rho v V^c + \eta_y p \\ \rho w V^c + \eta_z p \\ V^c (\rho e_t + p) - \eta_t p \end{bmatrix}$$

(4.15), (4.16), (4.17)

$$\hat{G} = \frac{1}{J} \begin{bmatrix} \rho W^c \\ \rho u W^c + \zeta_x p \\ \rho v W^c + \zeta_y p \\ \rho w W^c + \zeta_z p \\ W^c (\rho e_t + p) - \zeta_t p \end{bmatrix}, \quad \hat{E}_v = \frac{1}{J} \begin{bmatrix} 0 \\ \xi_x \tau_{xx} + \xi_y \tau_{xy} + \xi_z \tau_{xz} \\ \xi_x \tau_{xy} + \xi_y \tau_{yy} + \xi_z \tau_{yz} \\ \xi_x \tau_{zx} + \xi_y \tau_{zy} + \xi_z \tau_{zz} \\ \xi_x \beta_x + \xi_y \beta_y + \xi_z \beta_z \end{bmatrix} \quad (4.18), (4.19)$$

$$\hat{F}_v = \frac{1}{J} \begin{bmatrix} 0 \\ \eta_x \tau_{xx} + \eta_y \tau_{xy} + \eta_z \tau_{xz} \\ \eta_x \tau_{xy} + \eta_y \tau_{yy} + \eta_z \tau_{yz} \\ \eta_x \tau_{zx} + \eta_y \tau_{zy} + \eta_z \tau_{zz} \\ \eta_x \beta_x + \eta_y \beta_y + \eta_z \beta_z \end{bmatrix}, \quad \hat{G}_v = \frac{1}{J} \begin{bmatrix} 0 \\ \zeta_x \tau_{xx} + \zeta_y \tau_{xy} + \zeta_z \tau_{xz} \\ \zeta_x \tau_{xy} + \zeta_y \tau_{yy} + \zeta_z \tau_{yz} \\ \zeta_x \tau_{zx} + \zeta_y \tau_{zy} + \zeta_z \tau_{zz} \\ \zeta_x \beta_x + \zeta_y \beta_y + \zeta_z \beta_z \end{bmatrix} \quad (4.20), (4.21)$$

where;

$$\begin{aligned} \tau_{xx} &= \frac{\mu}{\text{Re}_\infty} \left[ \frac{4}{3} (\xi_x u_\xi + \eta_x u_\eta + \zeta_x u_\zeta) - \frac{2}{3} (\xi_y v_\xi + \eta_y v_\eta + \zeta_y v_\zeta) \right] - \frac{\mu}{\text{Re}_\infty} \left[ \frac{2}{3} (\xi_z w_\xi + \eta_z w_\eta + \zeta_z w_\zeta) \right] \\ \tau_{yy} &= \frac{\mu}{\text{Re}_\infty} \left[ -\frac{2}{3} (\xi_x u_\xi + \eta_x u_\eta + \zeta_x u_\zeta) + \frac{4}{3} (\xi_y v_\xi + \eta_y v_\eta + \zeta_y v_\zeta) \right] - \frac{\mu}{\text{Re}_\infty} \left[ -\frac{2}{3} (\xi_z w_\xi + \eta_z w_\eta + \zeta_z w_\zeta) \right] \\ \tau_{zz} &= \frac{\mu}{\text{Re}_\infty} \left[ -\frac{2}{3} (\xi_x u_\xi + \eta_x u_\eta + \zeta_x u_\zeta) - \frac{2}{3} (\xi_y v_\xi + \eta_y v_\eta + \zeta_y v_\zeta) \right] + \frac{\mu}{\text{Re}_\infty} \left[ \frac{4}{3} (\xi_z w_\xi + \eta_z w_\eta + \zeta_z w_\zeta) \right] \end{aligned} \quad (4.22)$$

$$\begin{aligned}
\tau_{xy} = \tau_{yx} &= \frac{\mu}{\text{Re}_\infty} (\xi_y u_\xi + \eta_y u_\eta + \zeta_y u_\zeta + \xi_x v_\xi + \eta_x v_\eta + \zeta_x v_\zeta) \\
\tau_{xz} = \tau_{zx} &= \frac{\mu}{\text{Re}_\infty} (\xi_z u_\xi + \eta_z u_\eta + \zeta_z u_\zeta + \xi_x v_\xi + \eta_x v_\eta + \zeta_x v_\zeta) \\
\tau_{yz} = \tau_{zy} &= \frac{\mu}{\text{Re}_\infty} (\xi_z v_\xi + \eta_z v_\eta + \zeta_z v_\zeta + \xi_y w_\xi + \eta_y w_\eta + \zeta_y w_\zeta)
\end{aligned} \tag{4.23}$$

$$\begin{aligned}
\beta_x = u\tau_{xx} + v\tau_{xy} + w\tau_{xz} - q_x, \quad q_x &= -\frac{\mu}{\text{Pr Re}(\gamma-1)M_\infty^2} (\xi_x T_\xi + \eta_x T_\eta + \zeta_x T_\zeta) \\
\beta_y = u\tau_{yx} + v\tau_{yy} + w\tau_{yz} - q_y, \quad q_y &= -\frac{\mu}{\text{Pr Re}(\gamma-1)M_\infty^2} (\xi_y T_\xi + \eta_y T_\eta + \zeta_y T_\zeta) \\
\beta_z = u\tau_{zx} + v\tau_{zy} + w\tau_{zz} - q_z, \quad q_z &= -\frac{\mu}{\text{Pr Re}(\gamma-1)M_\infty^2} (\xi_z T_\xi + \eta_z T_\eta + \zeta_z T_\zeta).
\end{aligned} \tag{4.24}$$

The Jacobian of the transformation,  $J$ , is interpreted as the ratio of volume in physical space to that of computational space. It is defined as,

$$J = \frac{\partial(\xi, \eta, \zeta)}{\partial(x, y, z)} = \frac{1}{x_\xi(z_\zeta y_\eta - z_\eta y_\zeta) - x_\eta(y_\xi z_\zeta - y_\zeta z_\xi) + x_\zeta(y_\xi z_\eta - y_\eta z_\xi)} \tag{4.25}$$

Transformed components of velocity are given as,

$$\begin{aligned}
U^C &= \xi_t + \xi_x u + \xi_y v + \xi_z w, \\
V^C &= \eta_t + \eta_x u + \eta_y v + \eta_z w, \\
W^C &= \zeta_t + \zeta_x u + \zeta_y v + \zeta_z w.
\end{aligned} \tag{4.26}$$

### 4.3.2 Transformed Form of the Thin Layer Navier-Stokes Equations

The gradients of the viscous stress in the direction parallel to the surface ( $\xi$  and  $\eta$ ) are neglected. The thin layer Navier-Stokes equations are expressed in curvilinear coordinate system as follow:

$$\frac{\partial \hat{Q}}{\partial \tau} + \frac{\partial \hat{E}}{\partial \xi} + \frac{\partial \hat{F}}{\partial \eta} + \frac{\partial \hat{G}}{\partial \zeta} = \frac{1}{\text{Re}} \frac{\partial \hat{G}_v}{\partial \zeta} \quad (4..27)$$

where  $\hat{Q}, \hat{E}, \hat{F}, \hat{G}$  are given in equations (4.15), (4.16), (4.17), (4.18) respectively, and  $\hat{G}_v$  is defined as,

$$\hat{G}_v = \frac{1}{J} \begin{bmatrix} 0 \\ \mu m_1 u_\zeta + \frac{\mu}{3} m_2 \zeta_x \\ \mu m_1 v_\zeta + \frac{\mu}{3} m_2 \zeta_y \\ \mu m_1 w_\zeta + \frac{\mu}{3} m_2 \zeta_z \\ \mu m_1 m_2 + \frac{\mu}{3} m_2 (\zeta_x u + \zeta_y v + \zeta_z w) \end{bmatrix} \quad (4.28)$$

where

$$\begin{aligned} m_1 &= \zeta_x^2 + \zeta_y^2 + \zeta_z^2 \\ m_2 &= \zeta_x u_\zeta + \zeta_y v_\zeta + \zeta_z w_\zeta \\ m_3 &= \frac{1}{2} \frac{\partial}{\partial \zeta} (u^2 + v^2 + w^2) + \frac{1}{\text{Pr}(\gamma - 1)} (a^2)_\zeta. \end{aligned}$$

Pressure is related to the conservative flow variables as follows:

$$P = (\gamma - 1) \left[ e_t - \frac{1}{2} \rho (u^2 + v^2 + w^2) \right]$$

$e_t$  is total energy per unit volume.

#### 4.4 Modelling of Laminar Viscosity

There can be local peaks of heat transfer, such as 5,000°K, in the hypersonic shock-wave/boundary layer. Viscosity directly depends on temperature and can no longer be constant in high temperature regions so viscosity should be modelled in accordance to temperature variations.

In the scope of this thesis, two different viscosity models are used to consider the high temperature influence on viscosity during the analysis.

In temperature region  $0^{\circ}\text{K} < T < 1000^{\circ}\text{K}$ , air viscosity is calculated from Sutherland formula [39].

$$\mu(T) = 1.458 * 10^{-6} * \left( \frac{T^{1.5}}{T + 110.4} \right) \quad [\text{kg}/(\text{ms})] \quad (4.29)$$

In this equation  $T$  is in Kelvin. In temperature region  $1000 \text{ K} < T < 5000 \text{ K}$  a curve fit to the estimations of Svehla [40], given in Figure 4.2, is used.

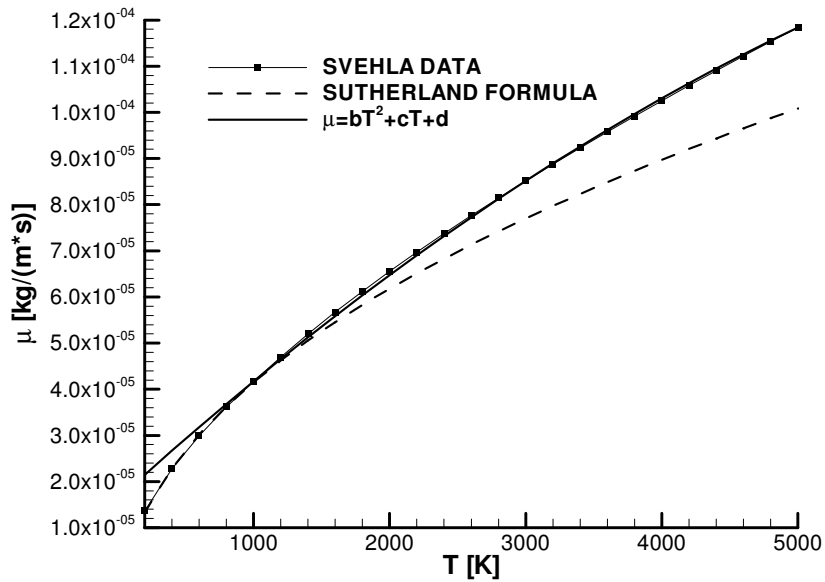


**Figure 4.2** Air viscosity Models

## CHAPTER 5

### NUMERICAL METHOD AND FLOW SOLVER

In the present study; three-dimensional, Reynolds averaged thin layer Navier Stokes equations are solved in generalized curvilinear coordinates. Finite differencing approach and LU - ADI (Lower Upper-Alternating Direction Implicit) [41] splitting technique are used. The accuracy of the scheme is improved by the application of an artificial dissipation model which uses the simplified idea of TVD upwind schemes.

The LU-ADI factorization algorithm used in this code was developed by Obayashi and Kuwahara et.al. [42]. The flux Jacobian matrices which appear in the left-hand side operators in the Beam and Warming method are decomposed as the product of the lower and upper bi-diagonal matrices with the LU factorization based on the idea of the flux vector splitting [43] and the implicit MacCormack scheme [44].

#### 5.1 Description of the Solution Algorithm

The space discretized form of equation (4.27) can be written as

$$\frac{\partial \hat{Q}}{\partial \tau} = - \frac{\hat{E}_{i+1/2} - \hat{E}_{i-1/2}}{\Delta \xi} - \frac{\hat{F}_{j+1/2} - \hat{F}_{j-1/2}}{\Delta \eta} - \frac{\hat{G}_{k+1/2} - \hat{G}_{k-1/2}}{\Delta \zeta} + \text{Re}^{-1} \frac{\hat{G}_{v,i+1/2} - \hat{G}_{v,i-1/2}}{\Delta \zeta} \quad (5.1)$$

In this equation, the viscous term is discretized by using second-order central difference formulation. The evaluation of the inviscid fluxes is based on a finite-

volume-cell-centered scheme. Discretization of the inviscid fluxes at cell interfaces is performed in a central or upwind fashion [45].

### 5.1.1 Central Difference Method

The second-order accurate central-difference scheme with the artificial dissipation terms can be given by

$$\hat{F}(Q_j, Q_{j+1}, S_{j+1/2}) = \frac{1}{2} \left\{ \hat{F}(Q_j, S_j) + \hat{F}(Q_{j+1}, S_{j+1}) \right\} - \left( \frac{\sigma}{J} \right)_{j+1/2} \left\{ \kappa^{(2)} (Q_{j+1} - Q_j) - \kappa^{(4)} (\delta^2 Q_{j+1} - \delta^2 Q_j) \right\} \quad (5.2)$$

where  $\delta$  is a second-order accurate central difference operator,  $S$  is the surface of the cell,  $\sigma$  is a sum of spectral radii of the Jacobian matrices of the inviscid fluxes, and the mid-point operator is  $()_{j+1/2} = \{ ()_j + ()_{j+1} \} / 2$ . The parameters,  $\kappa^{(2)}$  and  $\kappa^{(4)}$  control the strength of the second-and fourth-order dissipation terms

$$\kappa^{(2)} = \frac{\epsilon^{(2)}}{4} \left( \left| \delta^2 p_{j-1} \right| + 2 \left| \delta^2 p_j \right| + \left| \delta^2 p_{j+1} \right| \right) \quad (5.3)$$

and

$$\bar{\delta}^2 p_j = \frac{p_{j+1} - p_j + p_{j-1}}{p_{j+1} + p_j + p_{j-1}} \quad (5.4)$$

where  $\delta^2$  is a “pressure averaging operator” and  $\kappa^{(4)} = \epsilon^{(4)} - \min(\epsilon^{(4)}, \kappa^{(2)})$ . Typical values for dissipation coefficients,  $\epsilon^{(2)}$ ,  $\epsilon^{(4)}$  are 0.25 and 0.01 respectively. [45].

### 5.1.2 Streamwise Upwind Method

The present streamwise upwind algorithm uses a combination of differences such as total mass flux, pressure and contravariant velocity. The upwind representation of an inviscid flux at a cell interface can be given as

$$\hat{F}(Q_j, Q_{j+1}, S_{j+1/2}) = \frac{|\nabla\eta|}{J} \left( \frac{1}{2} [F_l^+ + F_r^-] - k_t \hat{Q}_\infty \right) \quad (5.5)$$

where

$$F_{l,r}^\mp = \begin{bmatrix} f_{l,r}^\mp \\ f_{l,r}^\mp u_{l,r} + k_x p_{l,r}^\mp \\ f_{l,r}^\mp v_{l,r} + k_y p_{l,r}^\mp \\ f_{l,r}^\mp w_{l,r} + k_z p_{l,r}^\mp \\ f_{l,r}^\mp H_{l,r} + k_t p_{l,r} \left( \tilde{V}_m \Delta p - \tilde{V}_m \Delta_2 \right) \sin^2 \theta \end{bmatrix} \quad (5.6)$$

The subscripts  $l$  and  $r$  represent the left and right states of the variables, respectively. The basic scheme is first-order accurate with  $l=j$  and  $r=j+1$ . The term subtracts the freestream for time metrics. A third-order upwind scheme is presently used in the numerical method. The present streamwise upwind method uses the local stream direction, flow velocity and pressure gradient to construct the upwinding [46].

### 5.1.3 Time-Marching Method

Time marching-method used in the LU-ADI factorization method was proposed by Obayashi and Fuji [38]. The LU-ADI method is a compromise of ADI and LU factorization. After the application of this method Equation (5.1) is written as

$$(T_\xi L_A D_A U_A T_\xi^{-1})(T_\eta L_B D_B U_B T_\eta^{-1})(T_\zeta L_C D_C U_C T_\zeta^{-1}) \Delta \hat{Q}^n = \Delta t R^n \quad (5.7)$$

Where L, D, U are the lower, diagonal and upper matrices respectively. A first-order finite-difference upwind formulation is used for numerical efficiency. The left hand side is obtained by rewriting diagonal algorithm of Pulliam and Chaussee [47] and the flux vector splitting technique of Steger and Warming [43].

## 5.2 Subprograms and Computational Flow Structure of the Code

Flow structure of the code is given as Figure 5.1. The MAIN program first calls a subroutine named INITIA. This subroutine initializes the flow field for the first iteration by assigning the values of the unknowns at every point of the computational grid. These unknowns are the density, three components of the velocity and the total energy. INITIA also calls the subroutines named IOALL(2), IOALL(3), JACN, MET3D, IOALL(4), IOALL(9), EIGEN. The subroutine IOALL(2) and IOALL(3) read the initial values of the unknowns and the coordinates of the grid points from relevant file, respectively. The subroutines JACN, MET3D calculate the Jacobian and the metrics of the grid in  $\xi$ ,  $\eta$ ,  $\zeta$  directions in the computational domain respectively. The subroutine EIGEN computes the eigenvalue of the equation (4.27) for determination of time step  $\Delta t$  in order to guarantee stability of numerical discretization scheme used in the code. Although Courant Number ( $u \Delta t / \Delta x$ ) is given as input by the user, EIGEN updates it by considering the clustering or stretching in the grid points and the freestream velocity. The subroutine IOALL(4) contains restart option and IOALL(9) reads turbulence data from relevant file.

Iteration starts for the numerical solution and continues until NMAX number of iterations is completed which is given by the user. Next, subroutine STEP, which acts as a main program for solving the flow variables in each iteration, starts calling the subroutines BC1, VISCOSITY, RHSR or RHS and SMOOTH, LHS3D2. Air viscosity is calculated in VISCOSITY subroutine according to temperature value. The subroutines RHSR and RHS are called by the subroutine STEP depending on a variable called as IRHS.

In BC1, boundary conditions are given. In the subroutines RHSR and RHS, the right hand side of the Navier-Stokes equations is updated. If the variable IRHS is taken as greater than zero, the code calculates the right hand side of the Navier-Stokes equations by the central-difference method else the streamwise upwind method is applied to compute these equations. The subroutine RHSR calls MUSCL and ROEFLX. The MUSCL approach, this acronym standing for Monotone Upstream-centered Schemes for Conservation Laws [49], is applied in

the subroutine MUSCL. The subroutine ROEFLX computes the generalized Roe fluxes based on conservative variables or based on primitive variables. When viscous solution is required, VISRHS is called by the subroutines RHSR and RHS. VISRHS calculates the viscous terms at the right hand side for laminar flow. But, if the flow is turbulent, VISRHS updates the viscous right hand side terms by calling one of the following turbulence subroutines depending on the will of the user: MUTUR, which applies the Baldwin-Lomax turbulence model or NTM3D, which applies the Cebeci-Smith or the Johnson King turbulence model. Other subroutine related to the turbulence algorithm in the code is VORTCTY which calculates the vorticity needed for the subroutine NTM3D.

After the right hand side calculations is completed by the subroutine RHS, SMOOTH is called which smoothes the corrections and applies to the right hand side array. The speed of sound has to be calculated before SMOOTH returns, because the solution of complete equation takes place in the next subroutine.

For the left hand side of the Navier-Stokes equations, in accordance with the Lower-Upper Alternating Direction Implicit (LU-ADI) method, the subroutine LHS3D2 sweeps in  $\xi$ ,  $\eta$ ,  $\zeta$  directions. At the end of these subroutines, STEP calculates the residuals and writes them in a file for the convergence history.

After each iteration level, the flow field solution is written in to a file as a restart data by the subroutine IOALL(5), the output variables are computed by IOALL(6) and pressure data are written on a file by IOALL(7). The turbulence data are refreshed by IOALL(8) which is called FORMOM. In FORMOM, force and moment coefficients are computed.

Afterwards, this iteration step ends and the loop continues until the NMAX iterations are completed. At the end of NMAX iterations, the subroutines IOALL(5), IOALL(6), IOALL(7), IOALL(8) to refresh the related data.

### **5.3 Dimensionless Forms of Variables Used in the Code**

In the code, dimensionless forms of density, three components of velocity, pressure and energy per unit volume (or per unit mass) are used [50].

### 5.3.1 Density

Density can be brought into dimensionless form by using the freestream density, and thus dimensionless value of the freestream density is 1.

$$\bar{\rho} = \frac{\rho}{\rho_{\infty}} \quad \text{and} \quad \bar{\rho}_{\infty} = 1 \quad (5.8)$$

### 5.3.2 Velocity Components

Freestream speed of sound is used obtaining the dimensionless form of the velocity components,

$$\bar{u} = \frac{u}{a_{\infty}}, \quad \bar{v} = \frac{v}{a_{\infty}}, \quad \bar{w} = \frac{w}{a_{\infty}} \quad (5.9)$$

and using the following relations,  $u_{\infty} = U_{\infty}$  and  $v_{\infty} = w_{\infty} = 0$

$$\bar{U}_{\infty} = M_{\infty} \quad \text{and} \quad \bar{a}_{\infty} = 1 \quad (5.10)$$

### 5.3.3 Pressure

Dimensionless form of pressure can be obtained dividing it by  $(\rho_{\infty} a_{\infty}^2)$ , then,

$$\bar{P} = \frac{P}{\rho_{\infty} a_{\infty}^2} \quad \text{and} \quad \bar{P}_{\infty} = \frac{P_{\infty}}{\rho_{\infty} a_{\infty}^2} = \frac{\rho_{\infty} R T_{\infty}}{\rho_{\infty} \gamma R T_{\infty}} = \frac{1}{\gamma} \quad (5.11)$$

### 5.3.4 Total Energy Per Unit Volume

To obtain dimensionless forms of total energy per unit mass and total energy per unit volume, they are divided by  $a_{\infty}^2$  and  $(\rho_{\infty} a_{\infty}^2)$  respectively.

$$\bar{\hat{e}} = \frac{\hat{e}_t}{a_{\infty}^2} \quad (5.12)$$

$$\bar{e}_t = \frac{e_t}{\rho_\infty a_\infty^2} \quad (5.13)$$

Using the definition of the energy per unit volume,

$$e_t = \frac{P}{\gamma - 1} + \frac{1}{2} \rho U_{TOT}^2 \quad (5.14)$$

Dimensionless form of it can be found as in the following.

$$\bar{e}_t = \frac{\bar{P}}{\gamma - 1} + \frac{1}{2} (\bar{\rho} \bar{U}_{TOT}^2) \quad (5.15)$$

Thus at  $\infty$

$$\bar{e}_{t_\infty} = \frac{1}{\gamma(\gamma - 1)} + \frac{1}{2} M_\infty^2 \quad (5.16)$$

### 5.3.5 Viscosity

Viscosity can be brought into dimensionless form by using the freestream viscosity.

$$\bar{\mu} = \frac{\mu}{\mu_\infty} \quad (5.17)$$

Up to 1000 °K viscosity is calculated from the Sutherland formula:

$$\mu_\infty = 1.458 * 10^{-6} * \left( \frac{T_\infty^{1.5}}{T_\infty + 110.4} \right) \text{ and } \mu(T) = 1.458 * 10^{-6} * \left( \frac{T^{1.5}}{T + 110.4} \right) \text{ [kg/(ms)]} \quad (5.18)$$

where,  $T$  is in °K. For the region between 1000 °K and 5000 °K a curve fit to estimations of Svehla is used as described in Chapter 4.

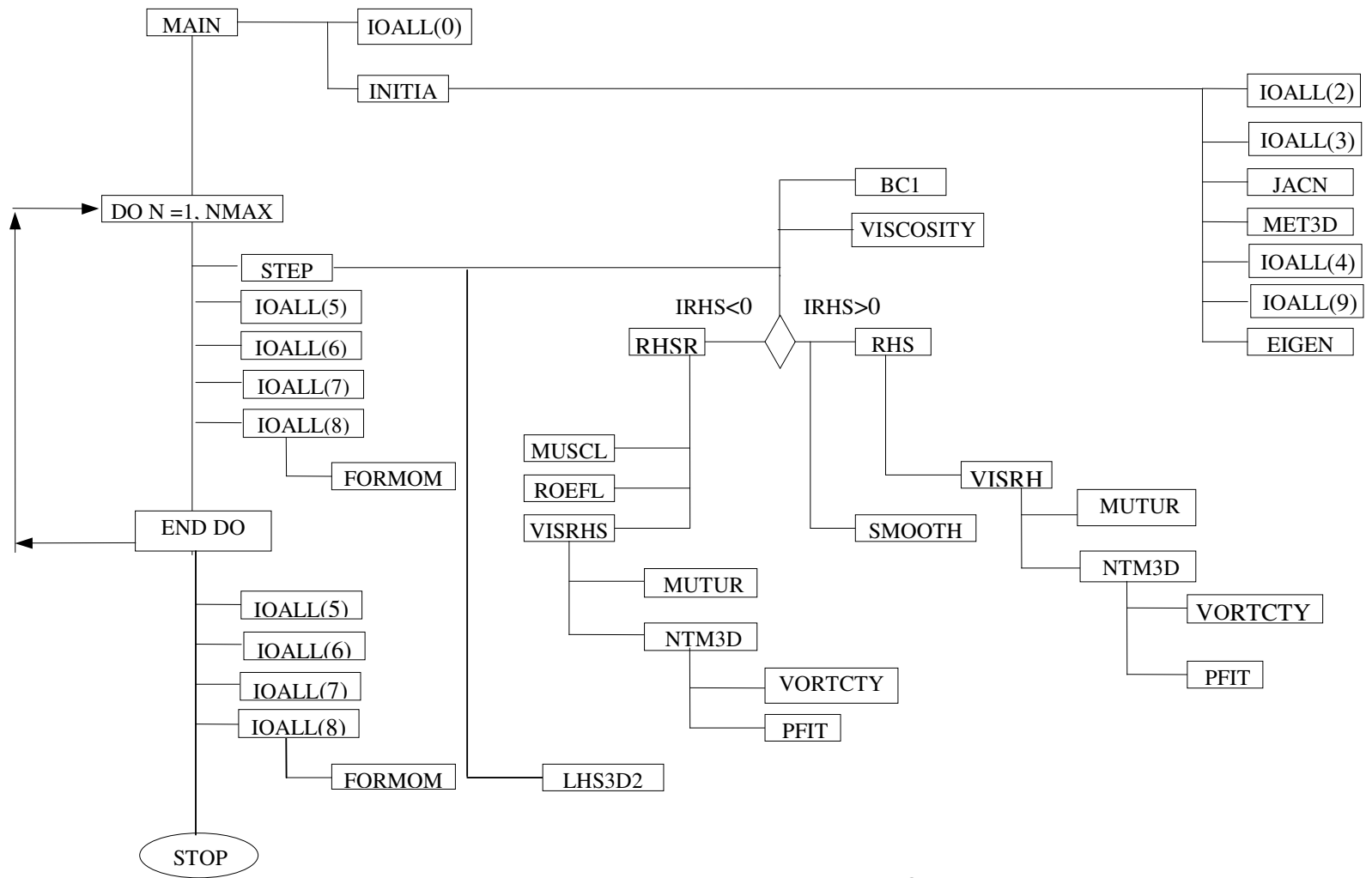


**Figure 5.1** The flowchart of the Code.

## CHAPTER 6

### TEST PROBLEMS

During the study, two different geometries are analysed: A flat plate at zero incidence angle with the flow and compression corners with seven different corner angles ( $\theta_w=5^\circ, 10^\circ, 14^\circ, 15^\circ, 16^\circ, 18^\circ$  and  $24^\circ$ ). The test geometries and the flow conditions of some of the test cases are selected to correspond to the experimental work of Mallinson et al. [7, 8] for comparison purposes. Those experiments were performed in the Australian National University T3 free-piston shock tunnel facility [51]. In Mallinson et al. [7, 8] study, flow was assumed as a two dimensional laminar flow.

#### **6.1 Description of the Test Problem I: Hypersonic Flow Over Flat Plate**

In the present study, eight different flow conditions, wall and freestream conditions which will be named as test cases, are examined. The reservoir, freestream and wall properties of those cases are shown in Table 6.1.

The three of those test cases correspond to the experiments and numerical studies of Mallinson et al. [7] and these conditions are referred to as B, D, G by Mallinson. The test gas is air. Test Cases B, D and G correspond to high level of oxygen dissociation, moderate level of oxygen dissociation and no oxygen dissociation in the freestream, respectively. The level of nitrogen dissociation was negligible for all the test cases. The flow was reported as laminar throughout the experiment. In the calculation of Reynolds Number, the viscosity,  $\mu$ , was obtained from a curve fit assuming a Lenard-Jones potential [52]. The Prandtl Number

does not vary appreciably over the range of conditions tested [53] and was assumed to have a constant value of 0.72.

The model is consisted of a flat plate with a detachable leading edge. The plate rested upon a gauge housing which, in turn, has been attached to a support plate. Upwash from the undersurface of the model has been prevented by side-skirts. A sketch of the model is shown is Figure 6.1. A model width of 180 mm has been chosen to fit within the inviscid core of the nozzle of the wind tunnel. The sides of the plate have been inclined  $4.3^\circ$  to match the source flow from the nozzle virtual origin. The model length of 180 mm ensured that it has been within the nozzle exit Mach cone and also that it has satisfied the aspect ratio requirements for two-dimensional flow [54]. Note that a length equal to that of the flat-plate sections (85 mm) of the compression corner geometries is used as the nondimensionalizing distance.

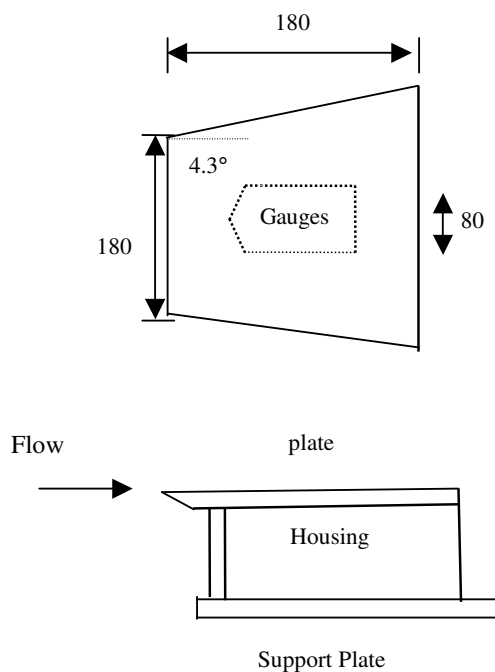


**Figure 6.1** Schematic of the flat plate model (Not to scale). Dimensions are in mm.

The Cases X1, X2 and X3, are chosen according to the  $T_w/T_0$  values to investigate the effect of the  $T_w/T_0$  on the flow variables, boundary layer variables etc. The Cases Modified D and Modified G correspond to Case D and G of Mallinson et al. [7] with differences in  $M_\infty$  and  $Re_\infty$ .

**Table 6.1** Reservoir and Freestream Properties of the Test Cases

<b>CASE</b>	<b><math>M_\infty</math></b>	<b><math>Re_\infty</math> (1/m)</b>	<b><math>Re_{\infty, L}</math></b>	<b><math>T_w/T_0</math></b>	<b><math>T_w/T_\infty</math></b>	<b><math>T_{aw}/T_0</math></b>	<b><math>T_w</math> (° K)</b>	<b><math>T_\infty</math> (° K)</b>	<b><math>T_0</math> (° K) Present Solution</b>	<b><math>T_0</math> (° K) Mallinson et al. (1997)</b>
B	7.5	$3.1 \cdot 10^5$	26350	0.0211	0.2586	0.86	300	1160	14210	8400
D	7.5	$4.08 \cdot 10^5$	34680	0.0260	0.3191	0.86	300	940	11515	7200
Modified D	7.5	$3.1 \cdot 10^5$	26350	0.0260	0.3191	0.86	300	940	11515	7200
G	9.1	$32.2 \cdot 10^5$	273700	0.1068	1.875	0.86	300	160	2810	2400
Modified G	7.5	$3.1 \cdot 10^5$	26350	0.1068	1.53	0.86	300	195.92	2810	2400
X1	7.5	$3.1 \cdot 10^5$	26350	0.2	2.45	0.86	2450	1000	12250	---
X2	7.5	$3.1 \cdot 10^5$	26350	0.8	9.8	0.86	3000	306.12	3750	---
X3	7.5	$3.1 \cdot 10^5$	26350	1.0	12.25	0.86	3000	244.89	3000	---

## 6.2 Description of the Test Problem II: Hypersonic Flow Over Compression Corners

During the present study, eight different test cases are examined. The reservoir and freestream properties of those cases are the same as the flat plate problems solved and are given in Table 6.1. The Cases B, D and G corresponds to the experiments and numerical studies of Mallinson et al. [8]. The Case X1, X2 and X3 are chosen according to the  $T_w/T_0$  values to investigate the effect of the  $T_w/T_0$  on the flow variables, boundary layer variables etc. The Cases Modified D and Modified G correspond to Case D and G of Mallinson et al. [8] with differences in  $M_\infty$  and  $Re_\infty$ .

For the Cases B, D and G, the flat plate / compression corner model shown in Figure 6.2 has been used by Mallinson during the experimental analysis. A flat plate and a ramp plate that rest upon gauge housings, which, in turn, have been attached to a support plate. By inserting wedges beneath the housing for the ramp plate, the corner angle can be varied from  $5^\circ$  to  $24^\circ$ . Seven different corner angles are used during the experiments. ( $\theta_w = 5^\circ, 10^\circ, 14^\circ, 15^\circ, 16^\circ, 18^\circ, \text{ and } 24^\circ$ ). The flat plate model was achieved by removal of the wedge altogether. The heat transfer and pressure measurements have been made using separate models. Upwash from the undersurface of the model has been prevented by side-skirts extending below the flat plate and ramp plate upper surfaces. The model width was 180 mm. The sides of the plates are inclined so as to be parallel to the source-like flow produced by the conical nozzle. The model length was 180 mm. Note that a length equal to that of the flat-plate sections (85 mm) is used as for nondimensionalizing distance.

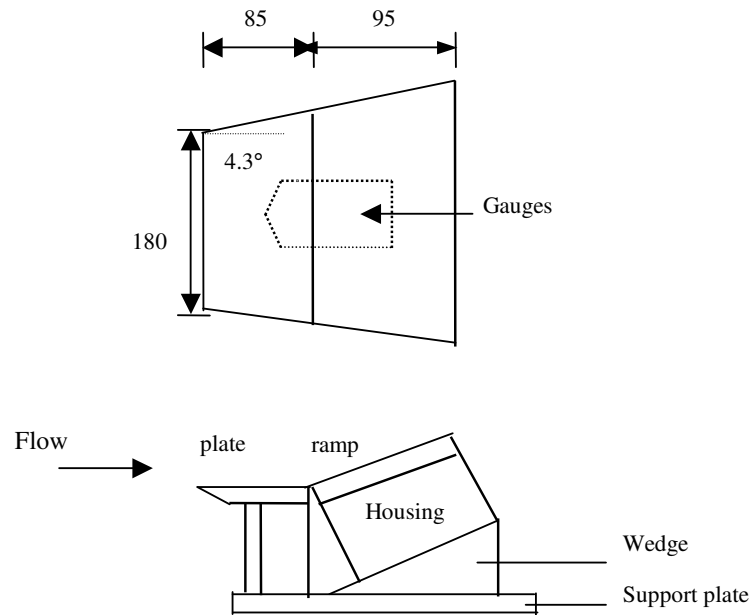


**Figure 6.2** Schematic of the compression corner model (side plate not shown)  
Dimensions are in mm.

The pressure and heat transfer distributions were measured using PCB 113M165 pressure transducers and in-house manufactured coaxial chromel-alumel (type K) surface junction thermocouples.

## CHAPTER 7

### GRID GENERATION AND BOUNDARY CONDITIONS

It is obvious that accurate grid generations should capture flow features during the numerical analysis. Due to the small shock wave angle with the surface, special care should be given to the grid generation during the analysis of the high temperature hypersonic flows. Large gradients in the hypersonic boundary layer require fine grids near the model surface in order for CFD codes to accurately predict the surface heat transfer rate and the local skin friction coefficient.

As a general rule, the wall spacing (the distance between the first grid point above the wall and the grid point on the wall,  $\frac{\Delta z}{L}$ ) should be equal to  $\frac{1}{\sqrt{\text{Re}_L}}$  at least. In the present study the length used for nondimensionalisation is  $L = 0.85$  cm. This is the length of the flat plate sections of the compression corner geometries of Mallinson et al. [7, 8].

#### 7.1 Grid Generation for the Flat Plate

During the analysis of the flow over a flat plate, a grid refinement study has been performed to obtain the most suitable grid for the solution of this problem. The first four grids produced within this study are presented in Figures 7.1 to 7.4. These grids are not used to obtain the results presented in Chapter 8.

The grid used during the numerical calculation of the flat plate test cases is given in Figure 7.5. This is a single block grid, but in generation of this final grid, initially 4 different algebraic grid blocks are produced. Then, these blocks are joined together to make the final grid, which is presented in Figure 7.5. Those 4 different

initial grid blocks are also presented in Figure 7.5 with different colours. The number of grid points of these blocks in  $\xi$ ,  $\eta$ ,  $\zeta$  directions are given below:

First Block : 37\*3\*160

Second Block : 183\*3\*160

Third Block : 37\*3\*29

Fourth Block : 183\*3\*29

The final grid which is obtained by joining these four blocks has 220\*3\*189 points in  $\xi$ ,  $\eta$ ,  $\zeta$  directions, respectively. The distance from the wall in the normal direction between the first and the second grid points is  $2.24*10^{-4}$ . In generation of this grid the following are considered:

- to capture boundary layer properties near the surface, accurately,
- to capture boundary layer properties near the edge of the boundary layer, accurately,
- to capture the leading edge shock, accurately.

(Not to scale)

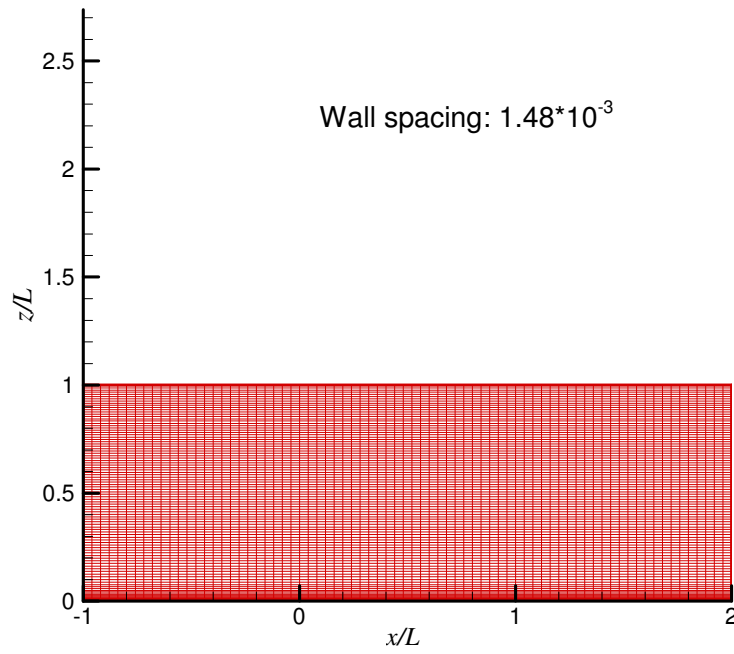
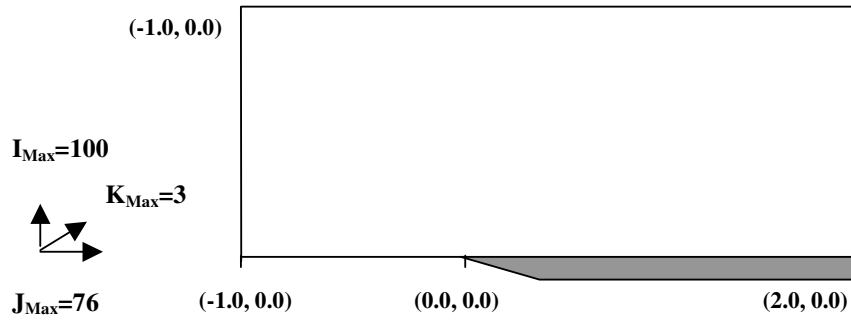


Figure 7.1 Flat Plate Grid I

(Not to scale)

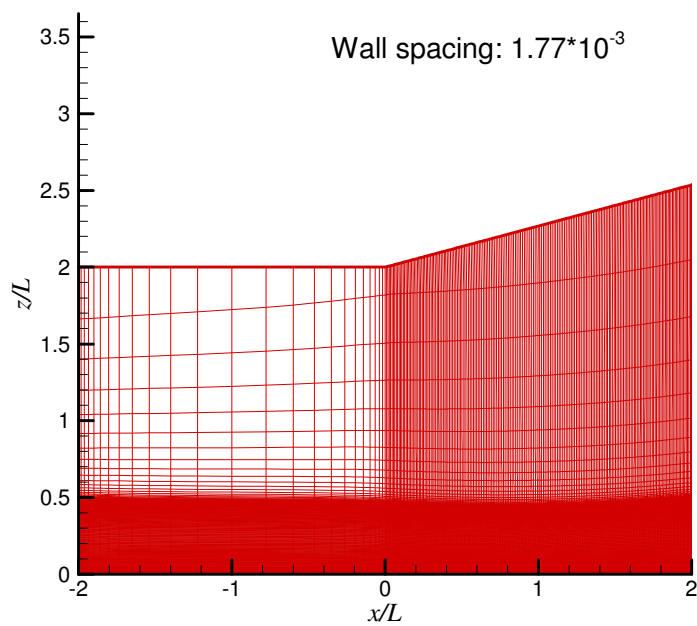
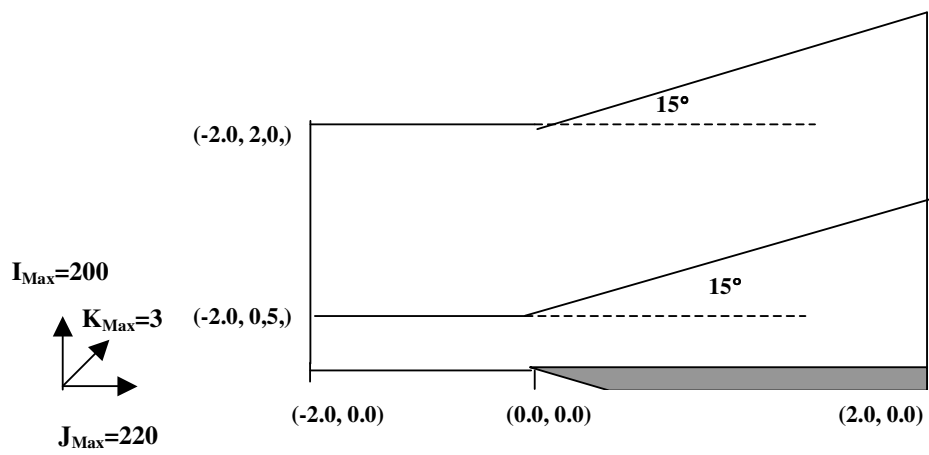


Figure 7.2 Flat Plate Grid II

(Not to scale)

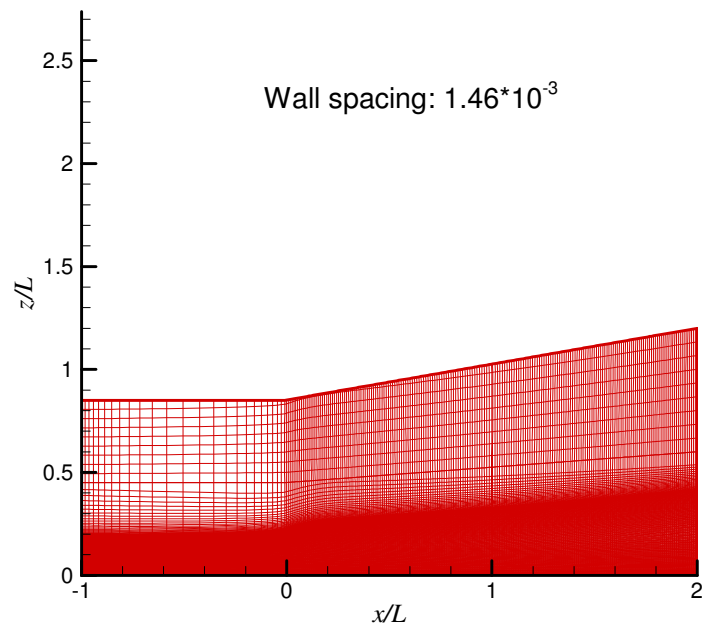
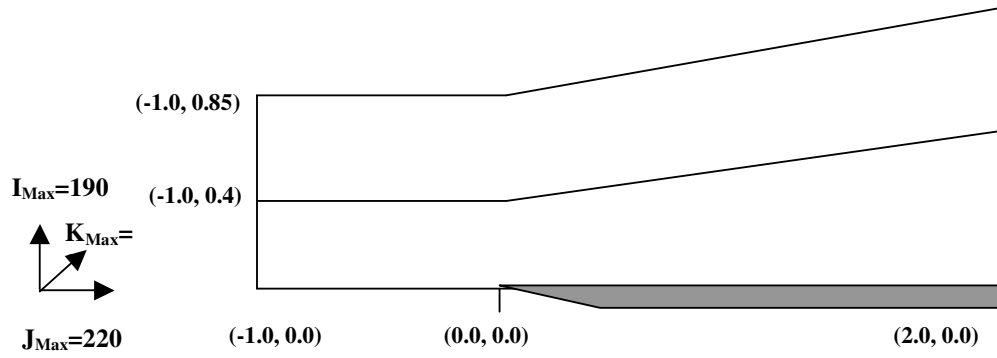


Figure 7.3 Flat Plate Grid III

(Not to scale)

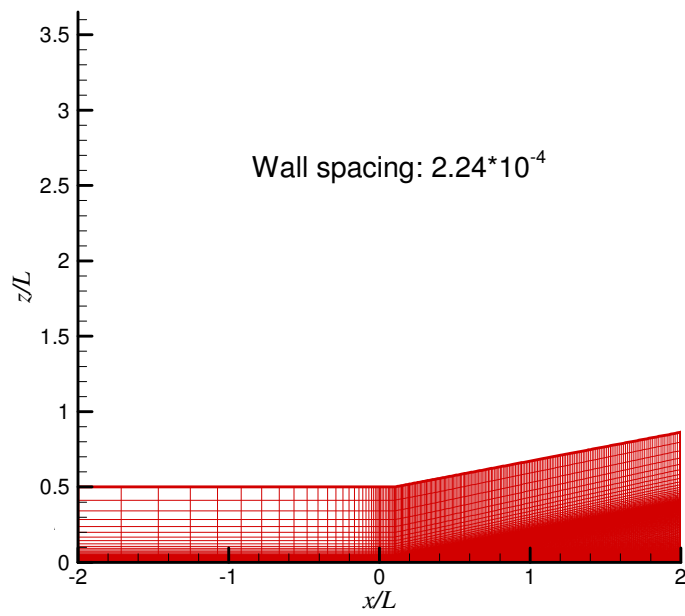
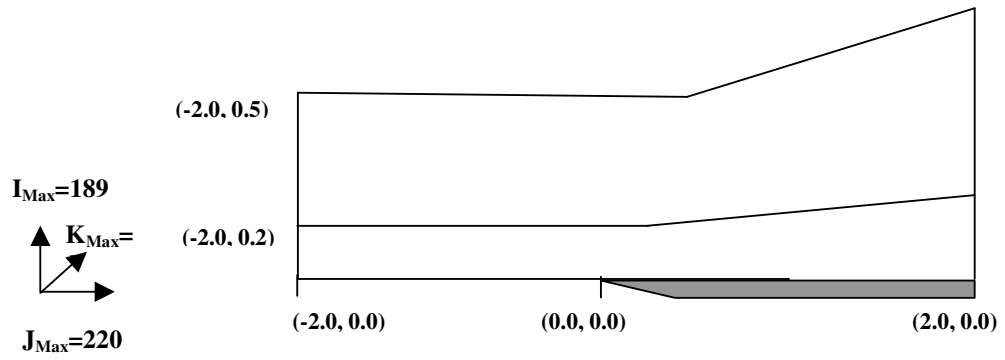
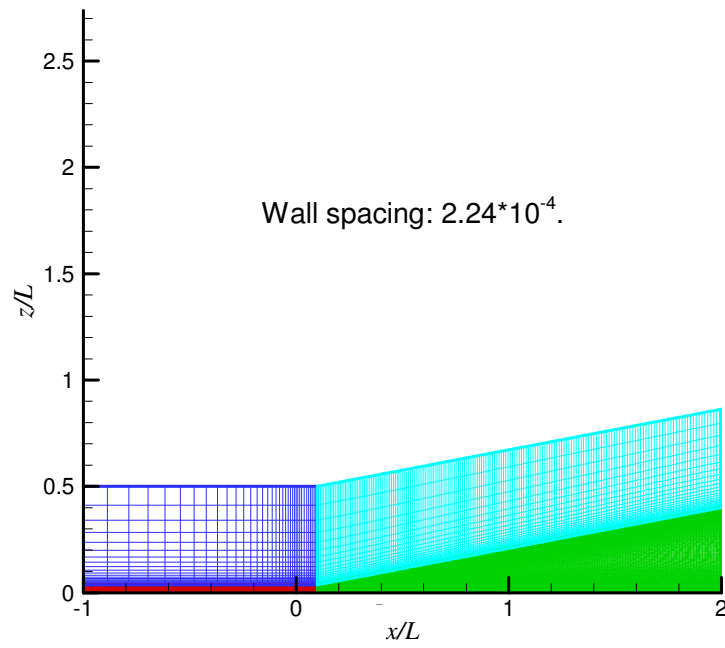
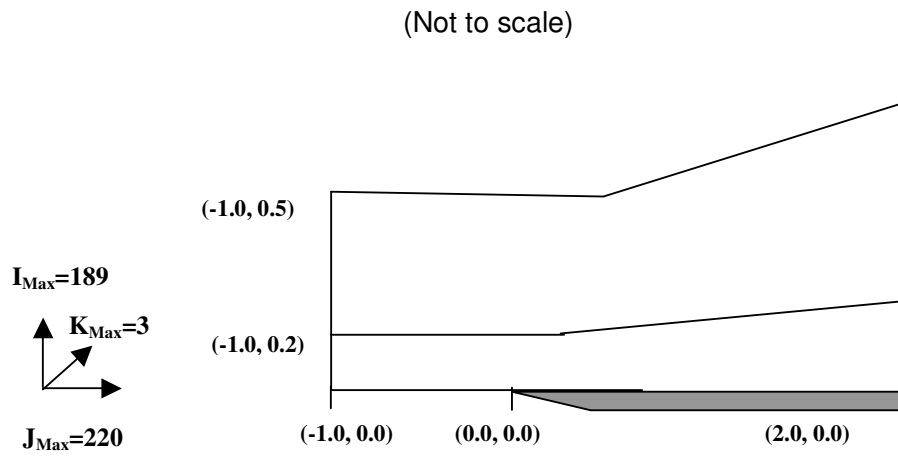


Figure 7.4 Flat Plate Grid IV



**Figure 7.5** Flat Plate Grid V (The final grid used to obtain solutions).

## 7.2 Grid Generation for the Compression Corners

Seven different grids are produced for the seven different corner angles ( $5^\circ$ ,  $10^\circ$ ,  $14^\circ$ ,  $15^\circ$ ,  $16^\circ$ ,  $18^\circ$  and  $24^\circ$ ). These corner angles are the same as those of Mallinson et al. [8]. Each grid had  $230 \times 3 \times 200$  points in  $\xi$ ,  $\eta$ ,  $\zeta$  directions, respectively. Before producing each of these grids, initially two sub blocks are produced algebraically. Then these blocks are joined together to form the final single block grid. The number of grid points of the sub blocks in  $\xi$ ,  $\eta$ ,  $\zeta$  directions are given below:

First Block :  $105 \times 200$

Second Block :  $125 \times 200$

In the normal direction, the  $J=1$  and  $J=JMAX$  planes are divided into two segments: The first segment, which is more clustered, starts from the base and its height is adjusted by the point at which the shock impinges the  $JMAX$  plane. The second segment is the region between the first segment and the  $LMAX$  plane. In the stream-wise direction, the  $L=1$  plane and  $L=LMAX$  plane are divided into three segments: Two of them are placed on the  $L=1$  plane that corresponds to the flat plate region of the model. The other segment lies on the ramp region of the model. The grid was clustered around the corner region. At the  $L=LMAX$  plane, the grid points are adjusted according to the grid points at the  $L=1$  plane.

Figures 7.6 to 7.12 show grids for  $5^\circ$ ,  $10^\circ$ ,  $14^\circ$ ,  $15^\circ$ ,  $16^\circ$ ,  $18^\circ$  and  $24^\circ$  compression corners used in this study. Note that a length equal to that of the flat-plate section (85 mm) is used as for non-dimensionalizing distance. The wall distance,  $\frac{\Delta z}{L}$ , is  $2 \times 10^{-4}$  for each grid. In generation of these grids the following are considered:

- to capture boundary layer properties near the surface, accurately,
- to capture boundary layer properties near the edge of the boundary layer, accurately,
- to capture the leading edge shock, accurately,
- to capture flow properties around the corner, accurately.

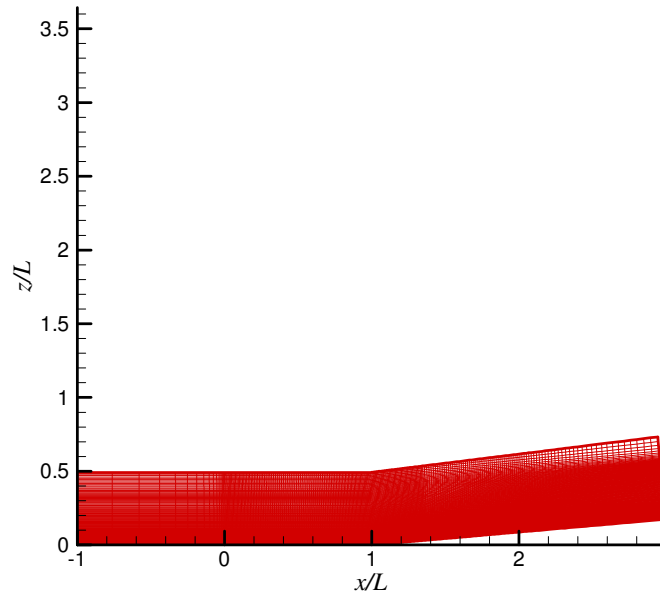


**Figure 7.6** 5° compression corner grid.

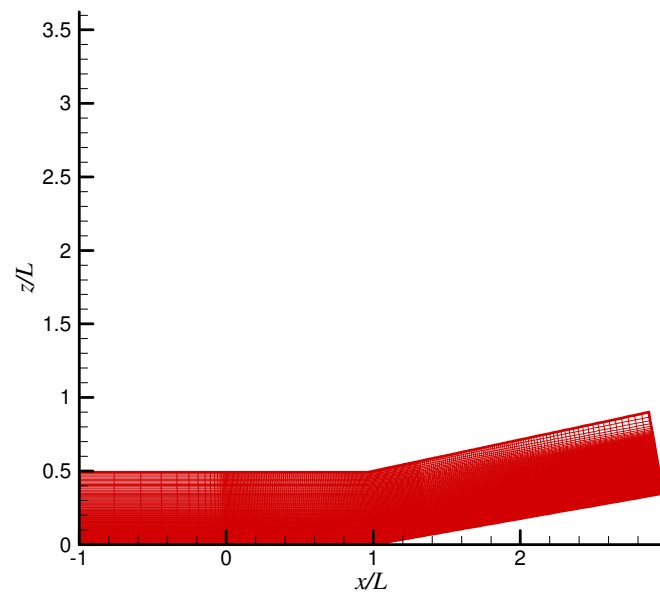


**Figure 7.7** 10° compression corner grid.

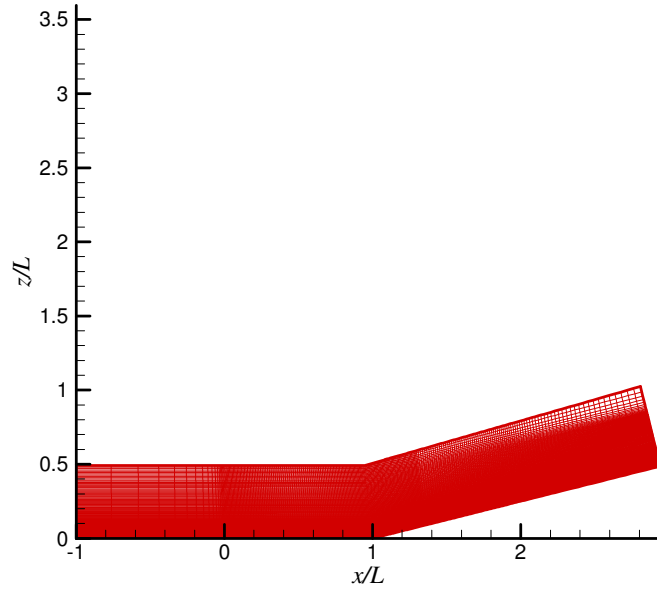


**Figure 7.8** 14° compression corner grid.

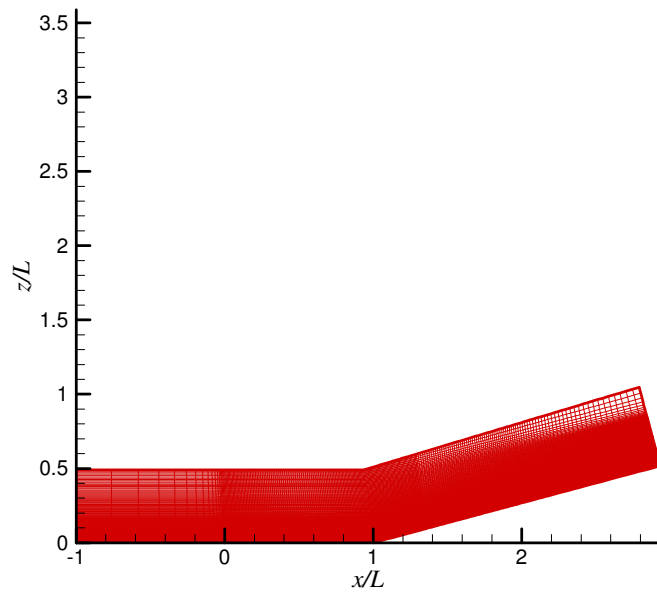


**Figure 7.9** 15° compression corner grid.

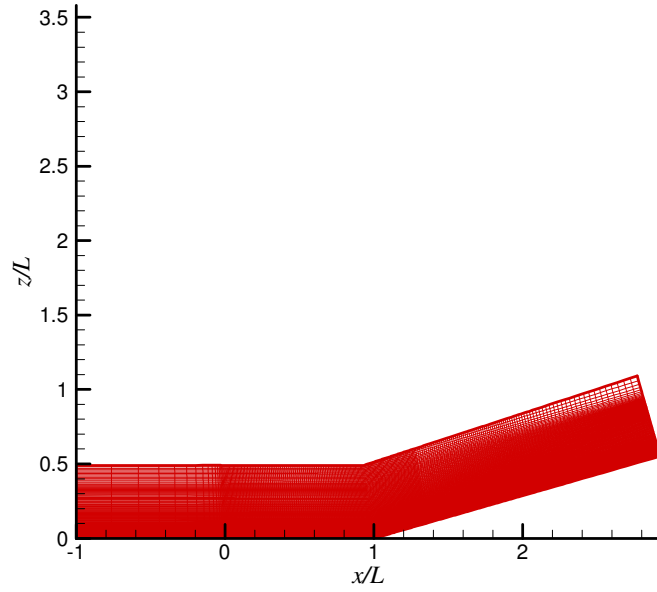


**Figure 7.10** 16° compression corner grid.

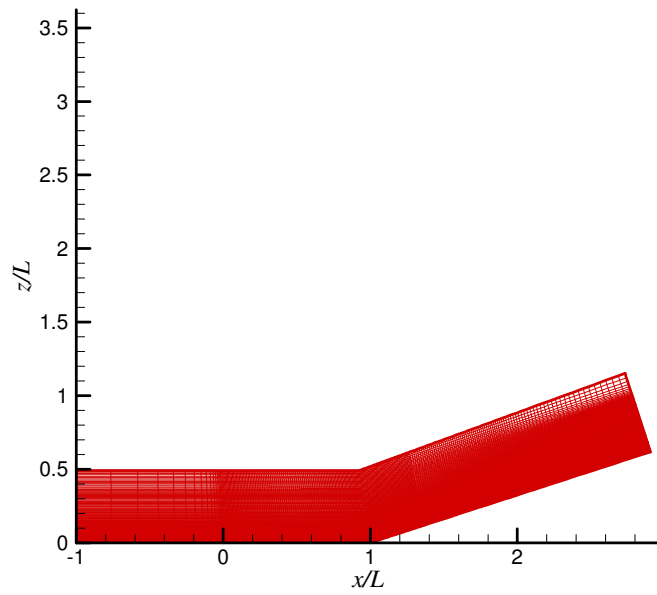


**Figure 7.11** 18° compression corner grid.

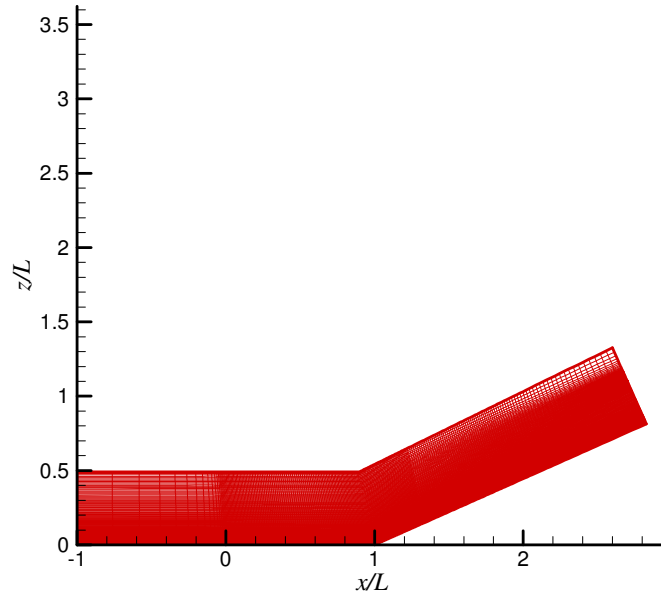


**Figure 7.12** 24° compression corner grid.

### 7.3 Initial and Boundary Conditions

Freestream values of the variables at the start of the iterations are assigned as the initial conditions everywhere.

At the left surface (flow in plane,  $J=1$  plane), freestream values of the variables are assigned as follows:

$$\rho = \rho_{\infty}, u = U_{\infty}, v = 0, w = 0, \text{ and } P = P_{\infty}$$

Total energy per unit volume can be calculated from:

$$e_t = \frac{P}{\gamma - 1} + \frac{1}{2} \rho (u^2 + v^2 + w^2)$$

At the lower surface up to the leading edge of the flat plate ( $L=1$  plane,  $-1.0 \leq x/L < 0.0$ ) normally symmetry boundary conditions should be

applied. But, in the present study, considering the flow is hypersonic and the disturbances should not propagate upstream, and to speed up the convergence, freestream values of the variables are assigned. At this boundary, there are 25 grid points ahead of the leading edge of the flat plate and 15 grid points ahead of the leading edge part of the compression corners.

At the lower surface starting from the leading edge of the flat plate ( $L=1$  plane,  $0.0 \leq x/L$ ) constant temperature wall with the no slip condition is applied. At this surface, pressure is extrapolated from the interior points. Density is calculated using the extrapolated pressure and the specified temperature from the equation of state as follows:

$$\rho = \frac{P}{RT}$$

or in nondimensional form;

$$\frac{\rho}{\rho_{\infty}} = \gamma \frac{\frac{P}{T}}{\frac{\rho_{\infty} a_{\infty}^2}{T_{\infty}}}$$

At the right surface (flow out plane,  $J=JMAX$  plane), values of the flow variables are extrapolated from the  $J=JMAX-1$  plane. At this surface more sophisticated boundary conditions could be used considering the angular expansion of the flow between the shock and the surface. However, the present application was considered to be satisfactory for our purpose.

At the top surface ( $L=LMAX$  plane) Flow variables are extrapolated from the  $L=LMAX-1$  surface. This is an appropriate boundary condition for this surface. In fact, for hypersonic flow the freestream conditions can also be assigned at this surface as an alternative way of specifying the boundary conditions.

## CHAPTER 8

### RESULTS AND DISCUSSIONS

In this chapter the results of the thin layer Navier–Stokes solutions of laminar, hypersonic, high temperature, perfect gas flows over two different geometries will be presented. The first geometry is a flat plate at zero angle of incidence with the flow direction. The second geometry is a compression corner with 7 different corner angles,  $\theta_w = 5^\circ, 10^\circ, 14^\circ, 15^\circ, 16^\circ, 18^\circ, 24^\circ$ .

The shock/shock wave, shock wave/boundary layer interactions are studied. Surface heat transfer rates, local skin friction coefficients are obtained. The effects of wall-to stagnation temperature ratio ( $T_w/T_0$ ) on the flow and boundary layer characteristics are obtained. The effects of corner angle ( $\theta_w$ ) on the main features of the flow field are studied. Results are compared with the available experimental, theoretical and/or numerical results.

The effects of  $T_w/T_0$  on the heat transfer rate, the surface pressure distribution and the boundary layer flow variables are presented. The effects of corner angle ( $\theta_w$ ), on strong shock wave boundary layer interactions with extended separated regions are investigated.

All obtained results are not given in this chapter, in Part 8.1 Section 8.1.1-8.1.3 the results regarding Case B and in Part 8.2, Section 8.2.1-8.2.4 the results regarding  $\theta_w=14^\circ$  Case B are presented, only. However, the other results for flat plate and compression corners are published in Numerical Solution of Hypersonic Boundary Layer and Compression Corner Flows (Extensive Research Results of the Ph.D. study) [33].

## 8.1 HYPERSONIC BOUNDARY LAYER FLOWS OVER A FLAT PLATE

The computed results of laminar, hypersonic flows over flat plate are presented and discussed in this section. During the analysis, eight different free-stream and wall conditions (flow conditions or test cases) are selected: three of those test cases correspond to the experiments and numerical studies of Mallinson et al. [8] and these test conditions are referred as B, D and G by Mallinson et al.. The Cases X1, X2 and X3, are chosen according to the  $T_w/T_0$  values to investigate the effect of the  $T_w/T_0$  on the flow variables, boundary layer variables etc. The Cases Modified D and Modified G correspond to Case D and G of Mallinson et al. [8] with the differences in  $M_\infty$  and  $Re_\infty$ .

### 8.1.1. Post Processing and Theoretical Knowledge for Comparisons

After getting the numerical results by solving Navier-Stokes equations over flat plate for eight different test cases, post processing are applied on the obtained solution vector of dependent flow variables to obtain heat transfer rate, skin friction coefficient and boundary layer flow variables such as boundary layer thickness, velocity, temperature and pressure distributions inside the boundary layer, heat transfer parameters inside the boundary layer etc.

Details of applied post processing are given in Appendix B, C and D.

During the analyses, the heat transfer parameter ( $f_{qw}$ ) distributions inside the boundary layer are obtained at the different flat plate stations.

Integral energy equation is defined as

$$q_w = \frac{d}{dx} \left( \int f_{qw} dy \right) \quad (1)$$

where  $f_{qw}$  is

$$f_{q_w} = \left[ \int_0^\infty \bar{\rho} \bar{U} \left\{ \left( \frac{\gamma}{\gamma-1} \right) \left( \frac{\bar{p}}{\bar{\rho}} - \frac{\bar{p}_\infty}{\bar{\rho}_\infty} \right) + \frac{1}{2} (\bar{U}^2 - \bar{M}_\infty^2) \right\} dy \right] \quad (2)$$

In these non-dimensional equations,  $q_w$  is normalised by  $\rho_\infty a_\infty^3$ , velocity by  $a_\infty$  pressure by  $\rho_\infty a_\infty^2$  and density by  $\rho_\infty$ . From figures, it can be seen that  $f_{q_w}$  makes a small maximum before it goes to zero asymptotically at the edge of the thermal boundary layer. This small maximum is used as a criterion to locate the edge of the thermal boundary layer, thus the edge conditions, in the present study.

The distribution of various temperatures ( $T_{aw}$ ,  $T^*$  and  $T_0$ ) along the flat plate are calculated from formulas given below:

$$T_{aw} = T_e \left[ 1 + \sqrt{\text{Pr}} * \left( \frac{\gamma-1}{2} \right) M_e^2 \right] \text{ White [56]} \quad (3)$$

$$T^* = T_e \left[ 0.5 + 0.039 * M_e^2 + 0.5 \frac{T_w}{T_e} \right] \text{ Eckert [57]} \quad (4)$$

$$T_0 = \left[ 1 + \left( \frac{\gamma-1}{2} \right) M_\infty^2 \right] T_\infty \quad (5)$$

During the comparison of the boundary layer thicknesses ( $x$  vs  $\delta$  plots) with available experimental data and theory the following formulas are applied.

White [56] derived the following expression for a perfect gas boundary layer thickness.

$$\delta = x \left[ 5.0 + \left( 0.2 + 0.9 \frac{T_w}{T_{aw}} \right) (\gamma-1) M_e^2 \right] \left( \frac{C_w}{\text{Re}_x} \right)^{1/2} \quad (6)$$

Mallinson, Gai, Mudford (1996) [7] results given in the figures are obtained from:

$$\delta = 1.721 \frac{x}{\sqrt{\text{Re}_x}} \left[ 2.397 + \frac{T_w}{T_e} + 0.193 \text{Pr}^{1/2} (\gamma - 1) M_e^2 \right]. \quad (7)$$

Mallinson, Gai, Mudford (1996)\* [7] results are obtained from the formula given below and it is based on infinity variables:

$$\delta = 1.721 \frac{x}{\sqrt{\text{Re}_\infty}} \left[ 2.397 + \frac{T_w}{T_e} + 0.193 \text{Pr}^{1/2} (\gamma - 1) M_\infty^2 \right]. \quad (8)$$

Mallinson, Gai, Mudford (1996)\*\* results are directly taken from Mallinson et al [7].

The obtained pressure distributions over flat plate are compared with Mallinson et al.[8] results. The hypersonic viscous interaction parameter,  $\bar{\chi}$ , is defined as [8]

$$\bar{\chi} = M_\infty^3 \left( \frac{C^*}{\text{Re}_{x,e}} \right)^{1/2} \quad (9)$$

where

$$C^* = \left( \frac{\mu^*}{\mu_\infty} \right) \left( \frac{T_\infty}{T^*} \right) \text{ and } A' = 0.322(\gamma - 1) \left( 1 + 2.6 \frac{T_w}{T_0} \right). \quad (10)$$

The value of  $\bar{\chi}$  can be used to ascertain whether an interaction is strong or weak; large values of  $\bar{\chi}$  correspond to the strong interaction region, and small values of  $\bar{\chi}$  denote a weak interaction region.

The obtained pressure distributions are compared with Bertram and Blackstock Theory [58], also. The hypersonic viscous interaction parameter is defined by Lees and Probstein [59] as:

$$\chi = Ma_\infty^3 \left( \frac{C_w}{\text{Re}_{x,\infty}} \right)^{1/2} \quad (11)$$

where

$$C_w = \left( \frac{\rho_w}{\rho_\infty} \right) \left( \frac{\mu_w}{\mu_\infty} \right). \quad (12)$$

Bertram and Blackstock Theory [58] is

$$\frac{p}{p_\infty} = 1 + a\chi \left( \frac{9\gamma(\gamma+1)}{8} \right)^{0.5} \quad (13)$$

where

$$a = 0.425 \left( \frac{T_w}{T_{aw}} + 0.35 \right) (\gamma - 1). \quad (14)$$

The Stanton number is defined as [8]:

$$St = \frac{q_w}{\rho_e U_e (h_r - h_w)}. \quad (15)$$

The Eckert theory [57] is  $St' = 0.332 \text{Re}_{x,e}^{-0.5}$  (16)

where

$$St = St' (\text{Pr}^*)^{-2/3} (C^*)^{1/2}. \quad (17)$$

Differential and integral post processing details of skin friction coefficient and heat transfer rate are given in Appendix C and D, respectively.

### 8.1.2. Computational Details

The computations are carried out on the Nautilus System at METU. Rorqual machine was used as host and cases are given as jobs to various Nautilus Central Processing Units (CPU).

Nautilus is IBM Scalable POWER parallel 2 (SP2). SP2 system frame houses 8 wide nodes. The each wide node has 67 MHZ CPU with Power2 processors and 128 MB memory.

In the present study, 124,740 points ( $220 \times 3 \times 189$ ) are used for the flat plate grid.

The computations are started from the freestream conditions. A slow start of boundary conditions is implemented for 30 iterations from the starting point. The calculations are continued until a steady state solution is obtained.

For 20,000 iterations:

**Table 8.1** Computational Details of Flat Plate

Test Case	Real Time	CPU Time	Memory
B	29 h. 50 min.	30 h. 33 min.	16 M
D	30 h. 19 min.	30 h. 58 min.	16 M
Modified D	15 h. 45 min.	15 h. 44 min.	16 M
G	31 h. 53 min.	32 h. 42 min.	16 M
Modified G	15 h. 58 min.	15 h. 57 min.	16 M
X1	15 h. 4 min.	15 h. 5 min.	16 M
X2	15 h. 20 min.	15 h. 57 min.	16 M
X3	15 h. 15 min.	15 h. 23 min.	16 M

An Implicit smoothing constant,  $\varepsilon_i$ , of 1.0 and an explicit smoothing constant,  $\varepsilon_e$ , of 1.0 are used, respectively. Courant number is 1.0 and Prandtl number is 0.72 for a laminar solution. The reservoir and freestream flow conditions of the test cases are shown in Table 6.1.

Air composition was assumed to be 21% oxygen and 79% nitrogen. The high level of atomic Oxygen which existed in the experimental case was ignored.

A decrease by at least three orders of magnitude in residual error is a criterion for convergence. A typical convergence and iteration history is shown in Figure 8.1 for Case B as an example. The iterations are continued until the number of iterations reached to 20,000.

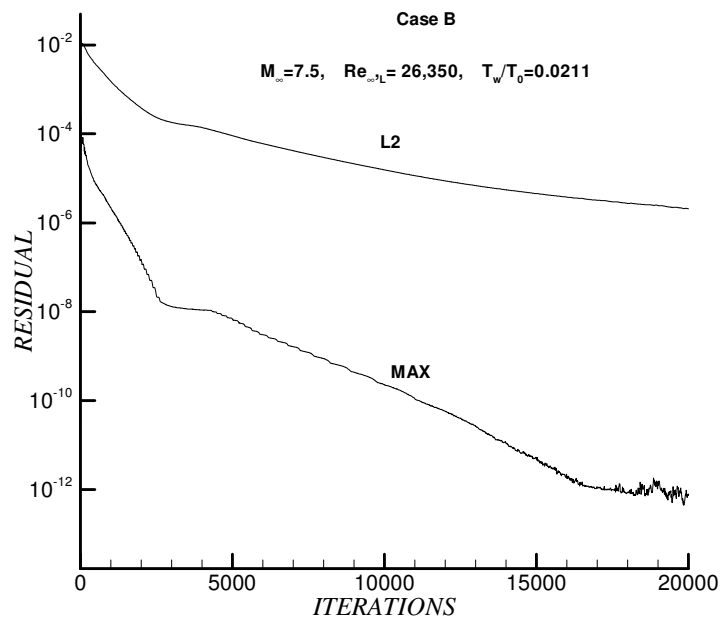


**Figure 8.1** Convergence and iteration history, Case B.

### 8.1.3. General Results

In this part of the chapter, the general results for Case B, with flow parameters  $M_\infty=7.5$ ,  $Re_{\infty,L}=26,350$  and  $T_w/T_0=0.0211$ , are presented.

The Mach contours and streamline distributions for the selected case are shown in Figure 8.2. and Figure 8.3, respectively. It can be seen from Mach contours that there is strong interaction between boundary layer and leading edge shock along the flat plate in accordance with oblique shock theory. Between the separation and reattachment shocks, expansion waves are generated where the boundary layer is turning back toward to surface. At the point of reattachment, the boundary layer has become relatively thin, the pressure is high, and consequently this becomes a region of high local aerodynamic heating. It was predicted that the flow is attached flow.

In Figure 8.4, boundary layer thicknesses are shown for Case B. In this figure, the leading edge shock due to the boundary layer displacement thickness effect is seen.  $\delta_T$ , is the thermal boundary layer thickness,  $\delta$ , is the boundary layer thickness,  $\delta^*$ , is the displacement thickness,  $\delta_{T,max}$ , is the location of maximum temperature inside the boundary layer, and  $\theta$  is the momentum thickness. In a direction normal to surface, between the leading edge shock and the thermal boundary layer thickness, the flow properties are not constant due to a slight expansion. This expansion is again a result of the boundary layer displacement thickness. In this region, the flow turns upwards as can, clearly, be seen from Figure 8.3. Since, the flow variables are not constant between the edge of the boundary layer and the shock, determination of the boundary layer edge requires special care. Thermal boundary layer is thicker than the momentum boundary layer and edge variables ( $U_e$ ,  $T_e$ , etc.) are obtained at the thermal boundary layer edge.

The number of grid points in the boundary layer during the numerical solution is very important to get reliable results. In Figure 8.5, number of grid points distribution for Case B is shown. For this case at the average, there are about 70 grid points in the boundary layer.

Typical velocity, temperature, Mach number and a heat transfer parameter ( $f_{qw}$ ), distributions inside the boundary layer are shown for Case B in Figure 8.6. It can be seen that  $f_{qw}$  makes a small maximum before it goes to zero asymptotically at the edge of the thermal boundary layer. This small maximum is used as criteria to locate the edge of the thermal boundary layer, thus the edge conditions, in the present study.

The boundary layer edge variables; distributions of Reynolds number, Mach number, temperature, density, velocity and viscosity at the edge of the boundary layer along the flat plate are shown in Figure 8.7 for Case B. It can be seen clearly that the boundary layer variables do not converge to a constant value due to slight expansion as mentioned above.

In Figure 8.8 shows the distribution of various temperatures along the boundary layer for Case B. The formulas for  $T_{aw}$ ,  $T^*$  and  $T_0$  are given in Section 8.1.1.

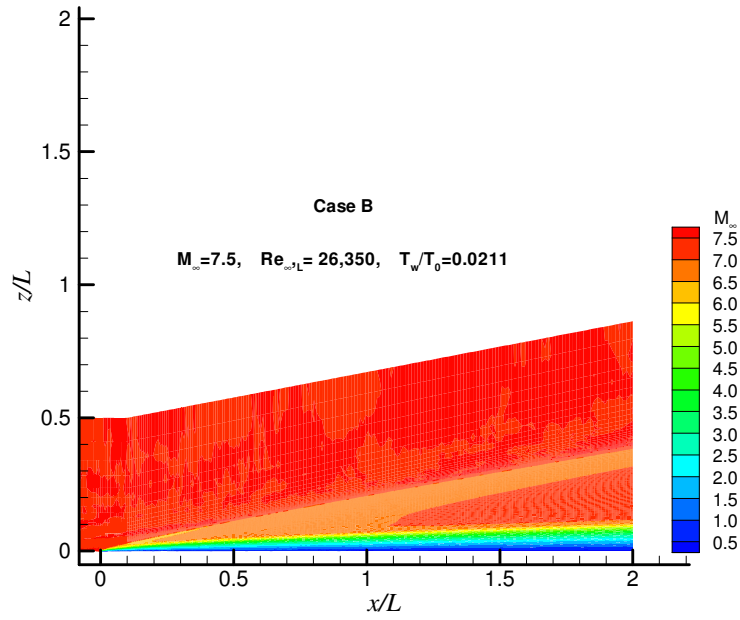


Figure 8.2 Mach contours, Case B.

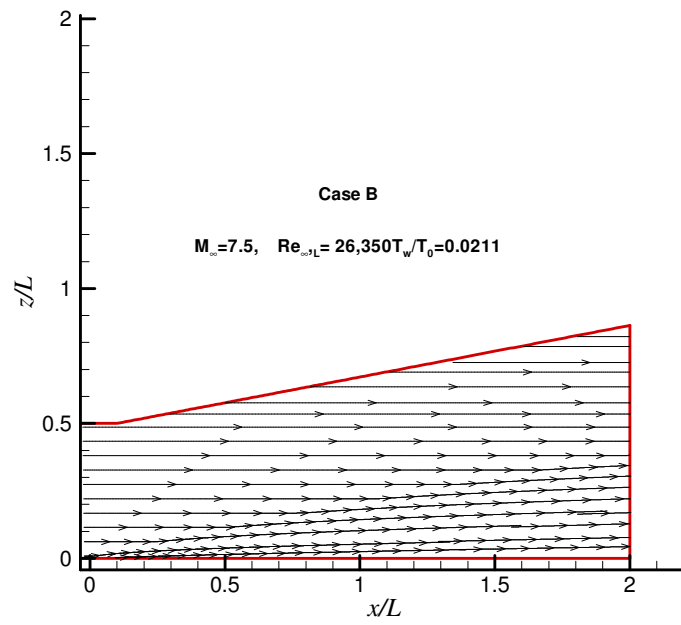
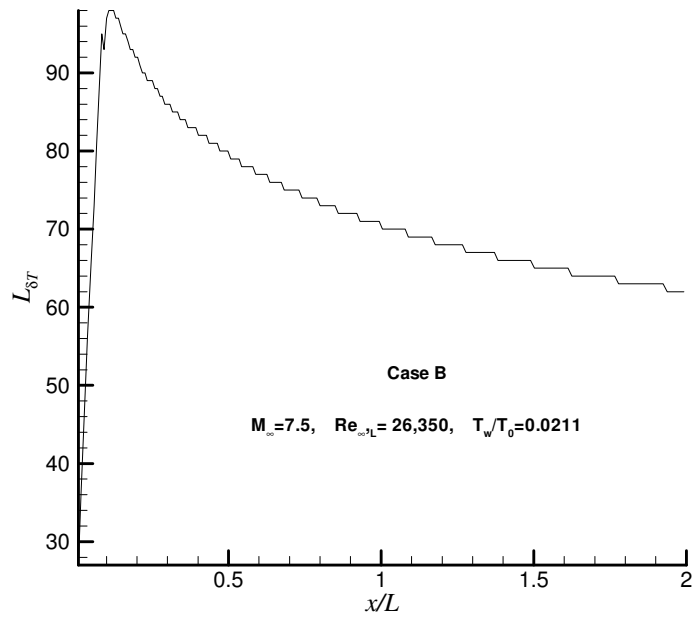
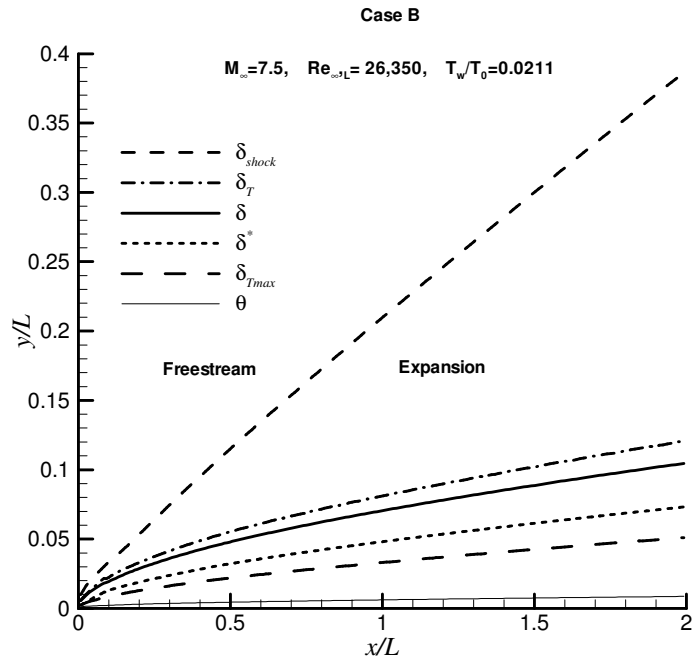
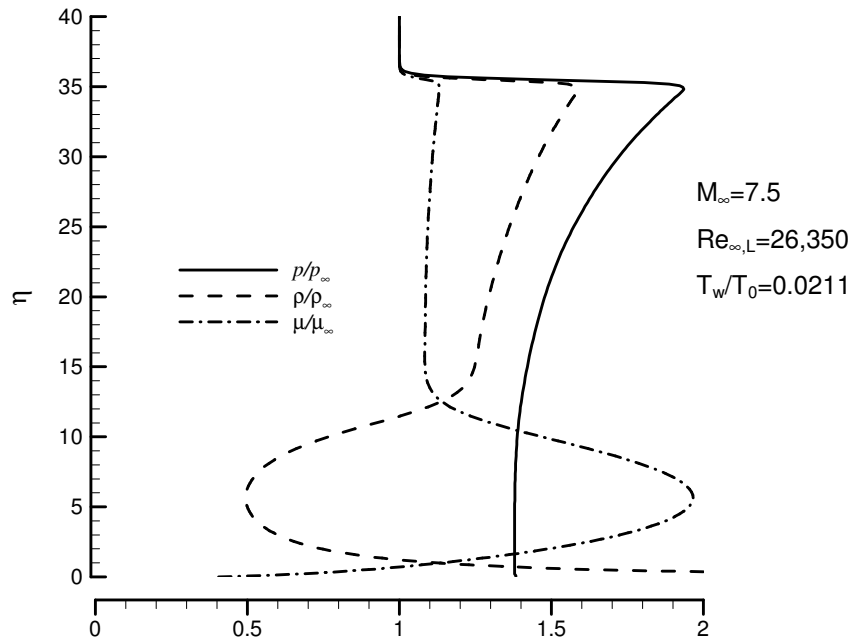
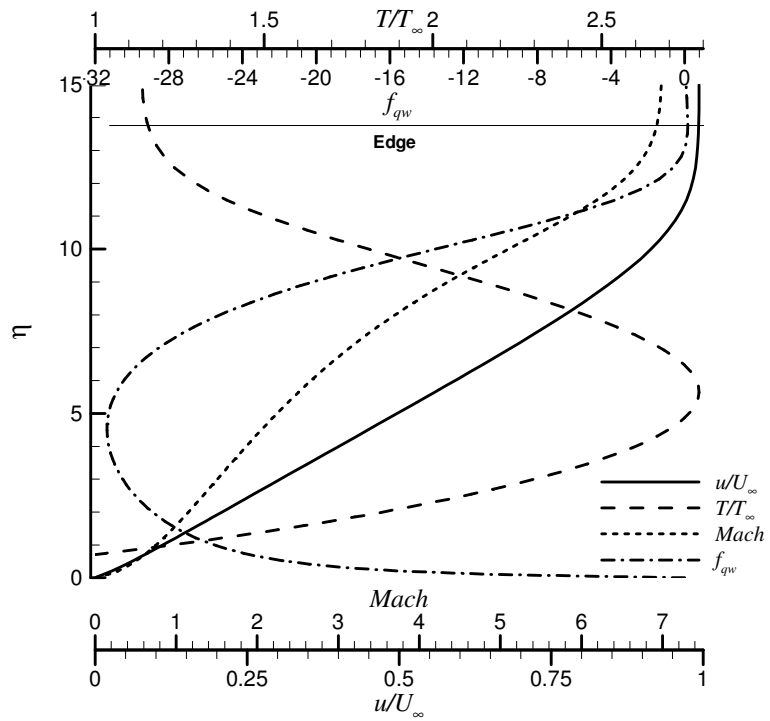


Figure 8.3 Streamlines distribution over flat plate, Case B.





**Figure 8.6** Boundary layer flow variables at  $x/L=1.0$ , (Mid-point of the flat plate), Case B.

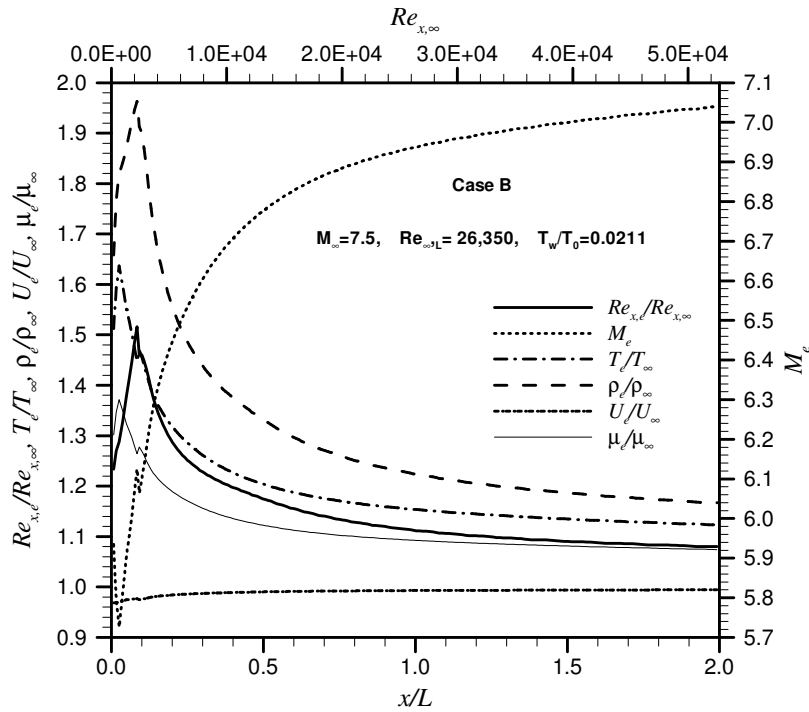


Figure 8.7 Boundary layer edge variables, Case B.

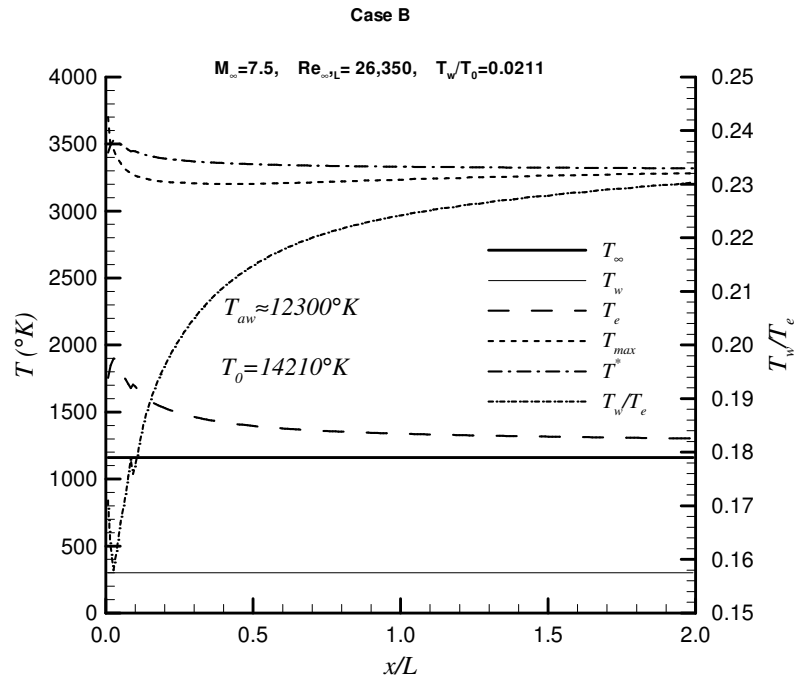


Figure 8.8 Temperature distributions along the boundary layer, Case B.

#### 8.1.4. Results of the Code Validation Study

In this section of the chapter, the obtained numerical results are compared with available numerical, experimental and theoretical data.

The comparisons of the obtained boundary layer thicknesses ( $x$  vs  $\delta$  plots) and available experimental data and theory are given in Figures 8.9 to 8.16 for all eight cases; Case B, Case D, Case Modified D, Case G, Case Modified G, Case X1, Case X2 and Case X3. The expression derived by White [56] for a perfect gas boundary layer thickness is given in Section 8.1.1. As can be seen, the present computations compare well with the other theories in the literature. Another way of presentation of the boundary layer thicknesses ( $x$  vs  $\left(\frac{\delta}{x}\right)\sqrt{Re_{x,e}}$ ) are given in Figures 8.17 to 8.24. The present results and results obtained from theory are compared for all cases.

In Figures 8.25 and 8.26 for Case D and Case G, respectively, the present predictions of the density profiles inside the boundary layer are compared with the available results from the literature [7]. The calculations for a perfect gas and for a real gas lie upon one another. It is meant that the effect of chemical and vibrational nonequilibrium upon the boundary layer profile is negligible for the present conditions. The thermal boundary layer thickness is seen to compare well with the theoretical prediction.

In Figures 8.27 to 8.29 the temperature profiles and in Figures 8.30 to 8.33 the velocity profiles for Case B, Case D and Case G are compared with the calculations of Van Driest [60] for a cold flat plate for the selected cases.

Figures 8.33 to 8.40 show the pressure distributions over the flat plate for the eight cases. The hypersonic viscous interaction parameter,  $\bar{\chi}$ , is defined by Mallinson et al.[8] given in Section 8.1.1. The value of  $\bar{\chi}$  can be used to ascertain whether an interaction is strong or weak; large values of  $\bar{\chi}$  correspond

to the strong interaction region, and small values of  $\bar{\chi}$  denote a weak interaction region.

The pressure distributions obtained from the present solution are compared with available experimental data [7] and Stollery & Bates Theory [61]. It can be seen that there are strong viscous interaction for all cases due to shock-wave/boundary layer interaction. The obtained results are similar to experimental data and theory.

In Figures 8.41 to 8.48, the obtained pressure distributions are compared by Bertram and Blackstock Theory [58], also.

The heat transfer rate distributions over the flat plate are compared with available experimental data and Eckert [57] and Stollery & Bates [61] laminar perfect gas theory in Figures 8.49 to 8.56. The present Stanton number distribution was obtained from integral post processing based on edge variables. The details of Stanton number post processing is given in Appendix B.

The obtained  $St\sqrt{Re_{x,e}}$  distributions are compared with Van Driest [60] theory in Figures 8.57 to 8.64. The integral and differential post processing based on edge variables are used to obtain present solutions. However, the freestream values are used in the Van Driest theory. Therefore, the obtained results do not compared well with the Van Driest theory [60]. Differential and integral post processing details of Stanton number are given in Appendix D.

The skin friction coefficient distributions are presented in Figures 8.65 to 8.72. The integral and differential post processing based on edge variables are used to obtain present solutions. The present results are compared with Van Driest [60] theory only because of lack of experimental data for the skin friction coefficient. The obtained results do not compare well with the Van Driest theory. Because, the leading edge shock effects are not considered by this theory and freestream values are used as edge values. Differential and integral post processing details of skin friction coefficient are given in Appendix C.

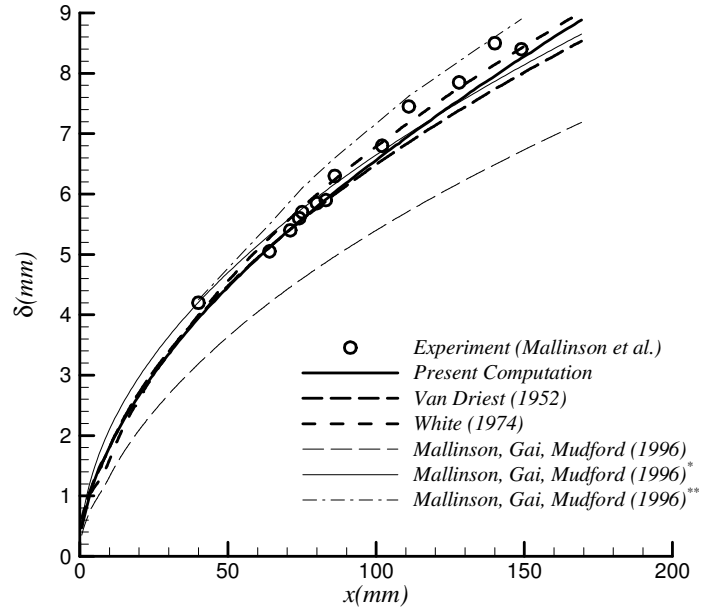


**Figure 8.9** Boundary layer thicknesses, Case B.

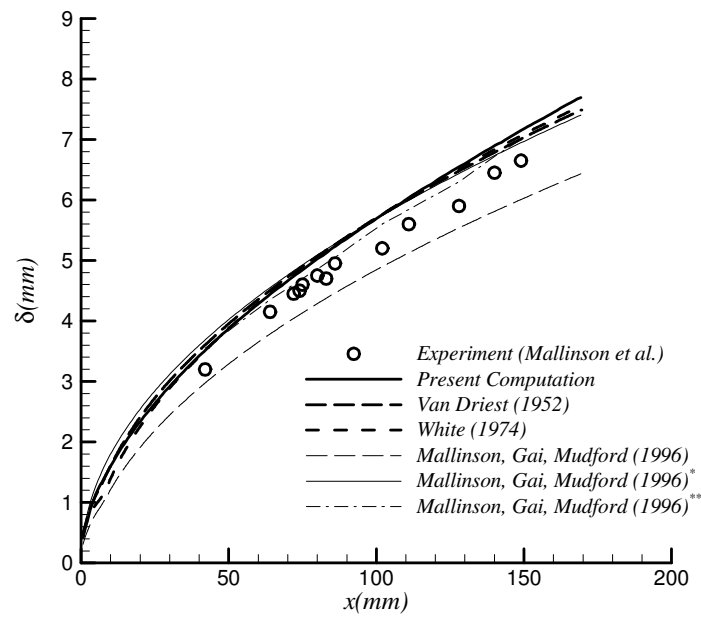


**Figure 8.10** Boundary layer thicknesses, Case D.

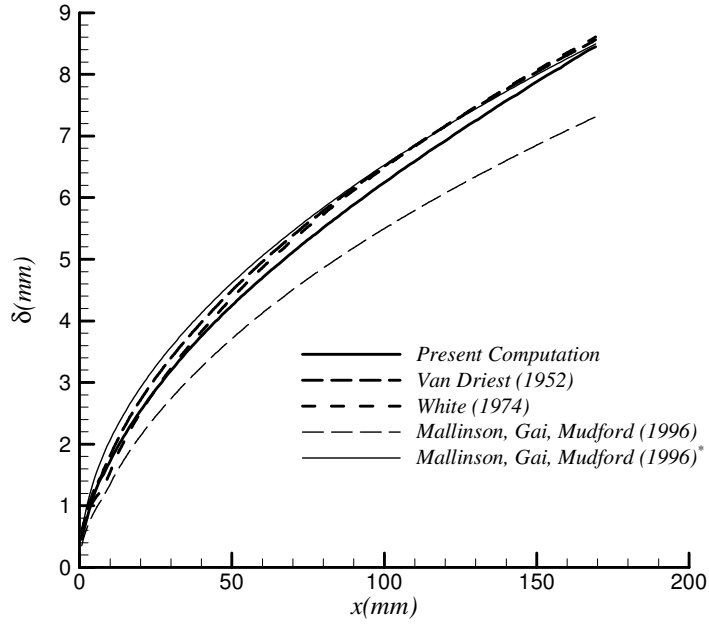


**Figure 8.11** Boundary layer thicknesses, Case Modified D.

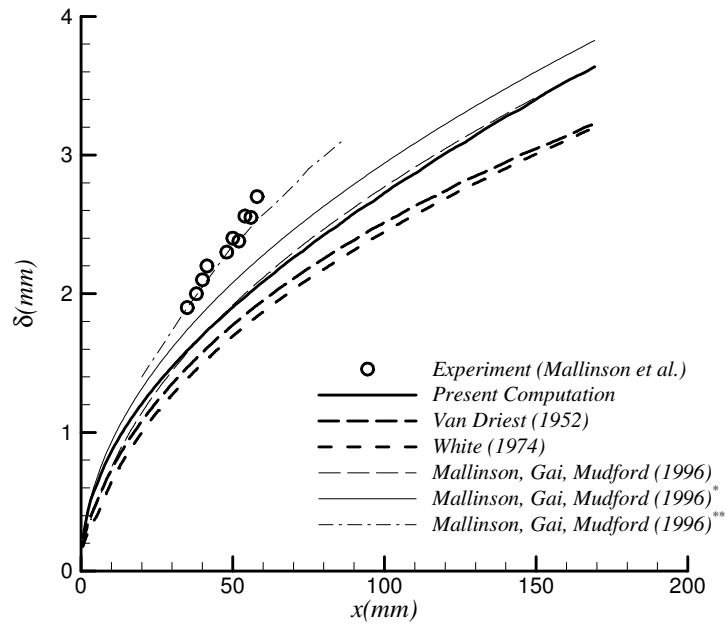


**Figure 8.12** Boundary layer thicknesses, Case G.

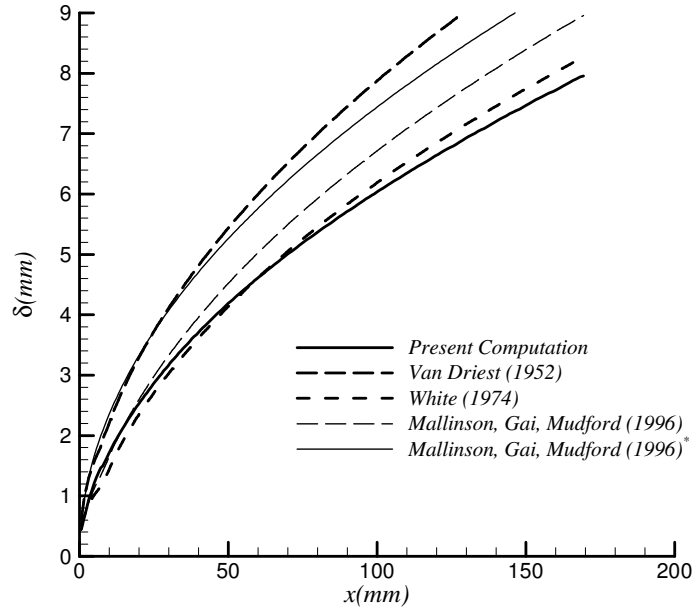


**Figure 8.13** Boundary layer thicknesses, Case Modified G.

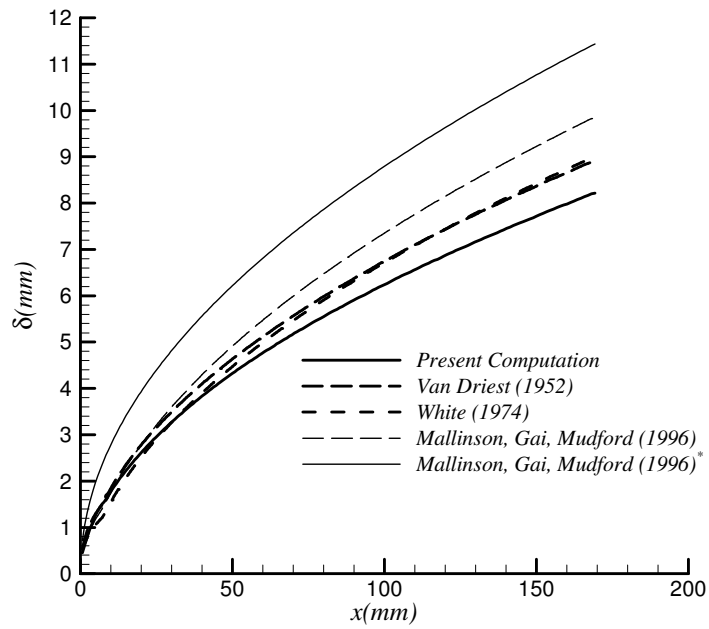


**Figure 8.14** Boundary layer thicknesses, Case X1.

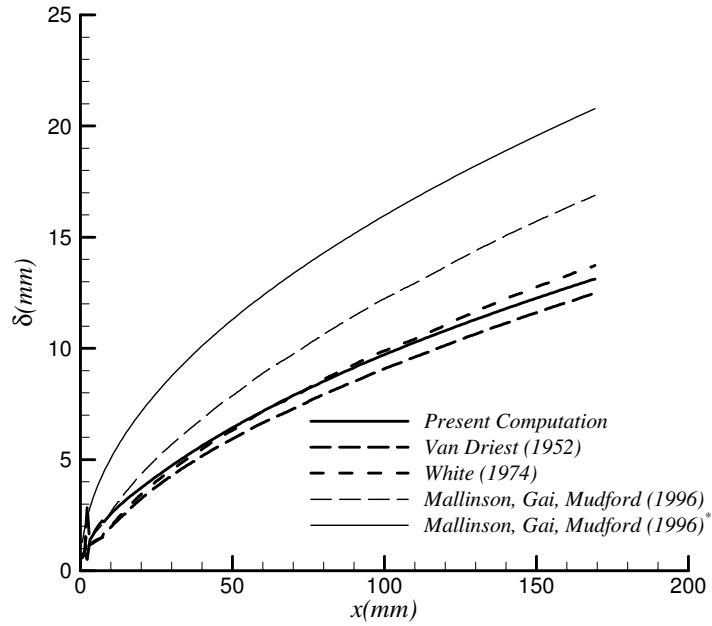


**Figure 8.15** Boundary layer thicknesses, Case X2.

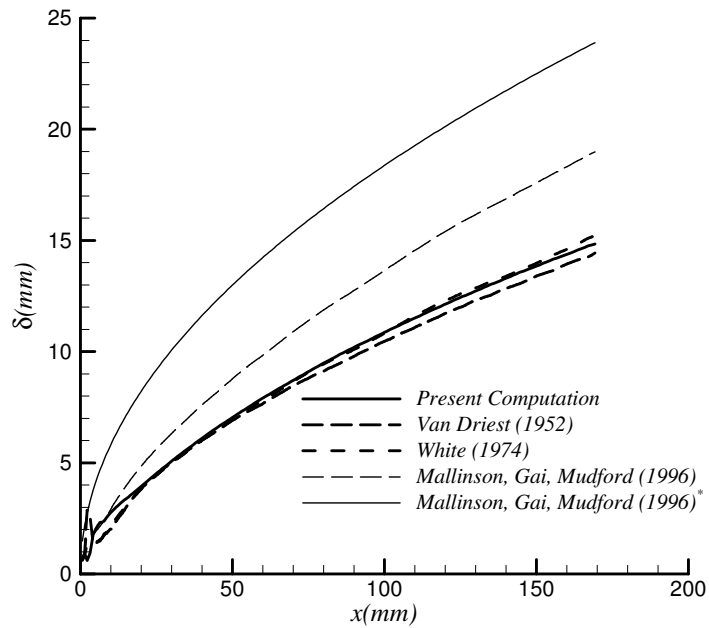


**Figure 8.16** Boundary layer thicknesses, Case X3.

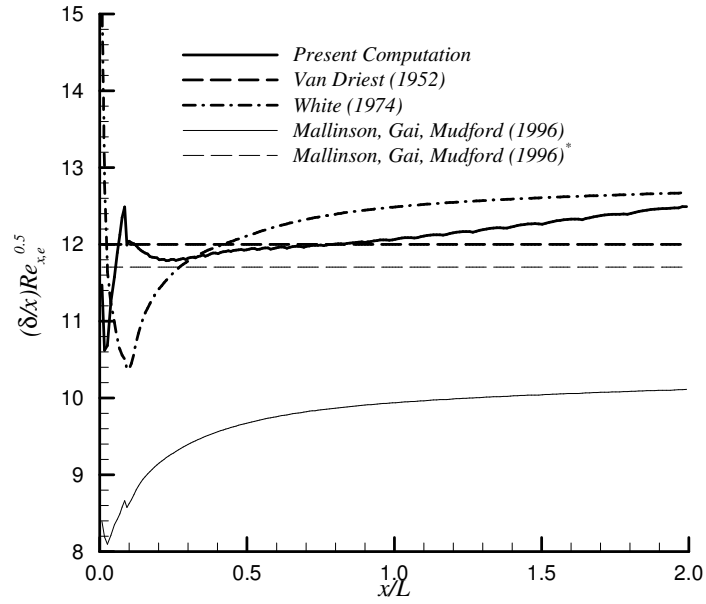


**Figure 8.17** Comparison of boundary layer thickness with theory, Case B.

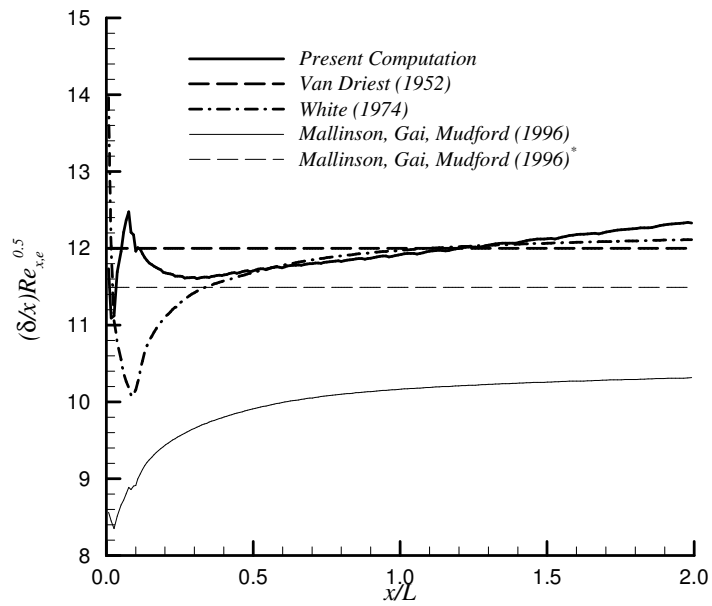


**Figure 8.18** Comparison of boundary layer thickness with theory, Case D.

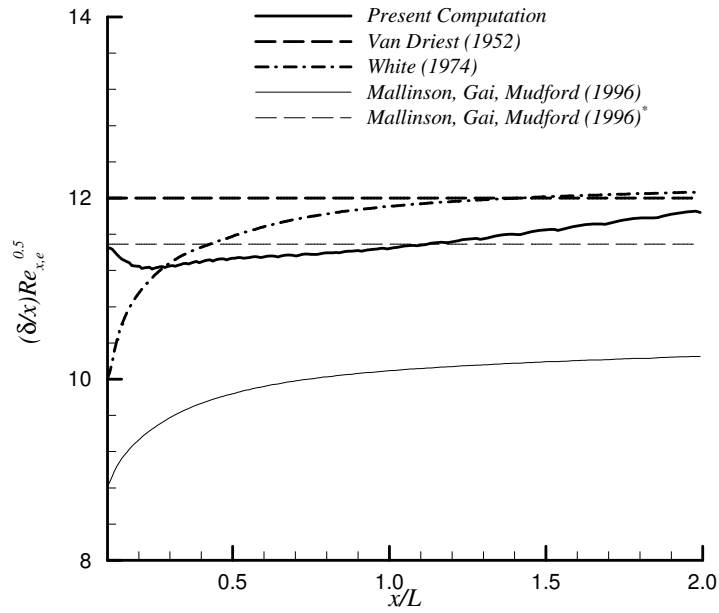


**Figure 8.19** Comparison of boundary layer thickness with theory, Case Modified D.

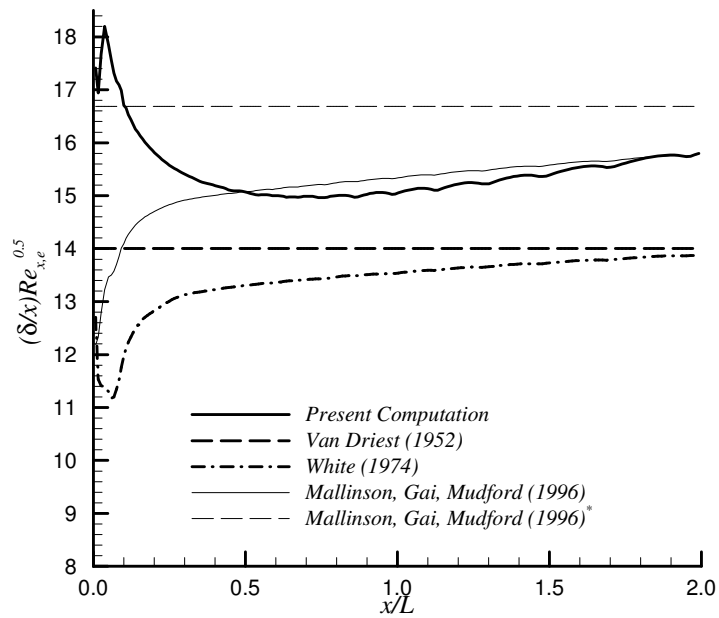


**Figure 8.20** Comparison of boundary layer thickness with theory, Case G.

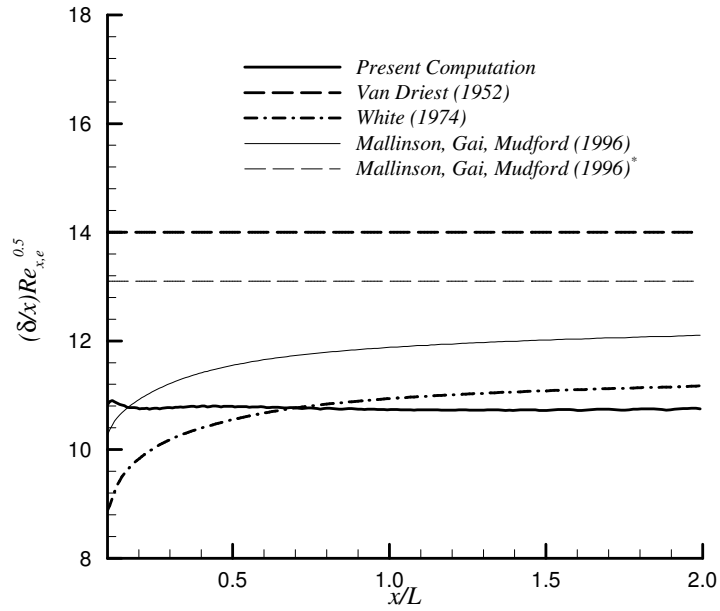


**Figure 8.21** Comparison of boundary layer thickness with theory, Case Modified G.

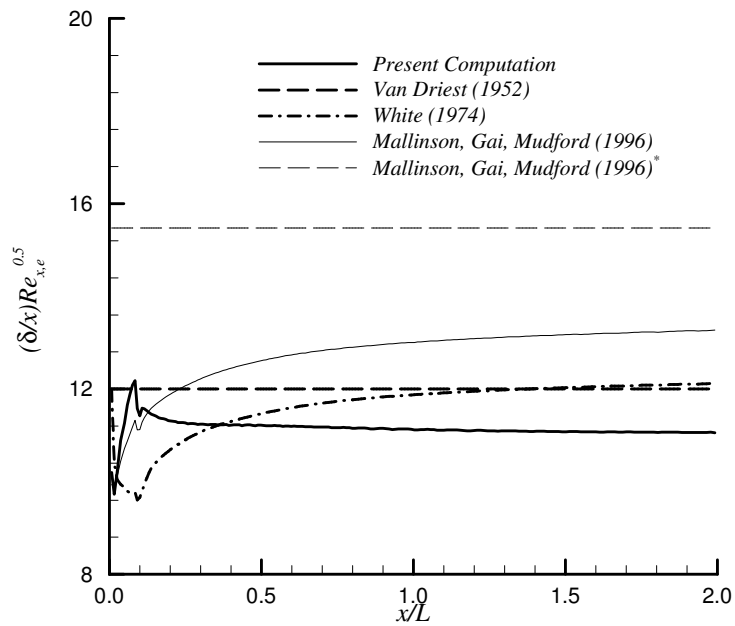


**Figure 8.22** Comparison of boundary layer thickness with theory, Case X1.

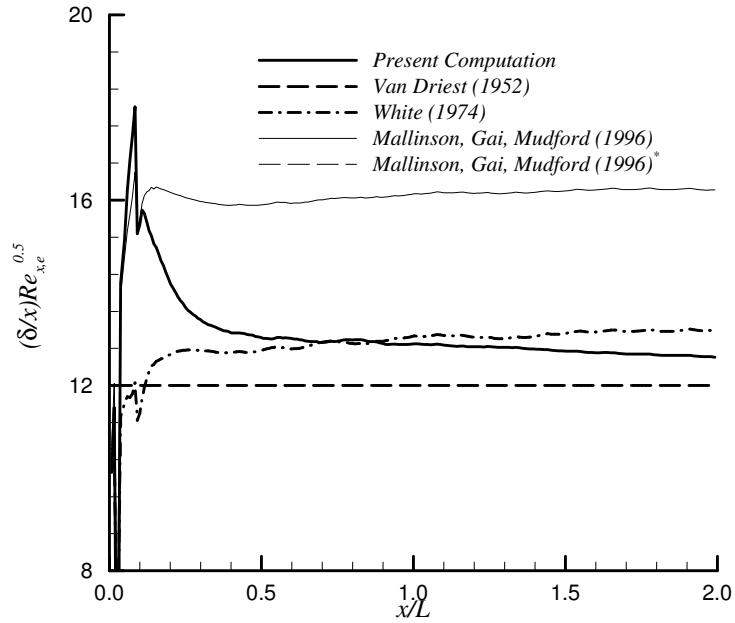


**Figure 8.23** Comparison of boundary layer thickness with theory, Case X2.

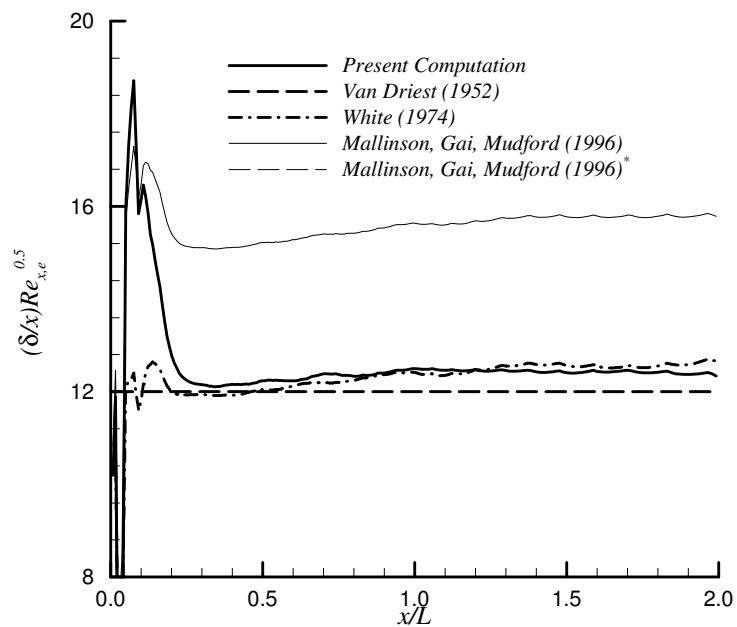


**Figure 8.24** Comparison of boundary layer thickness with theory, Case X3.

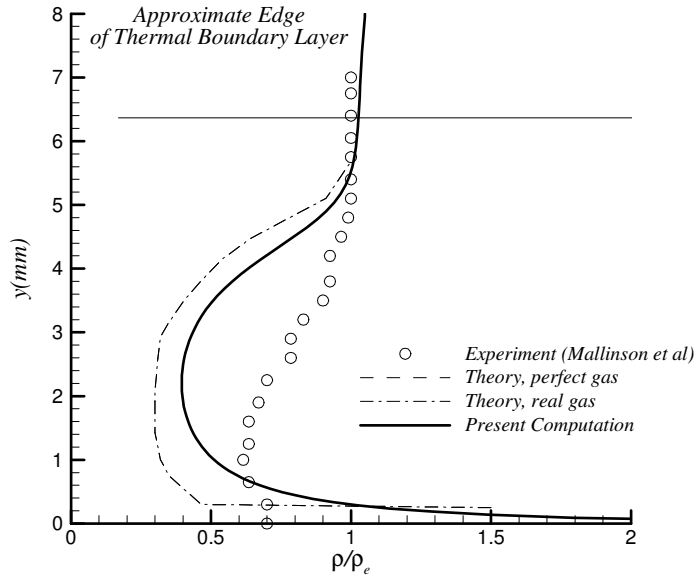


**Figure 8. 25** Density profile through the boundary layer, Case D. (Distance from the leading egde  $x=74$  mm)

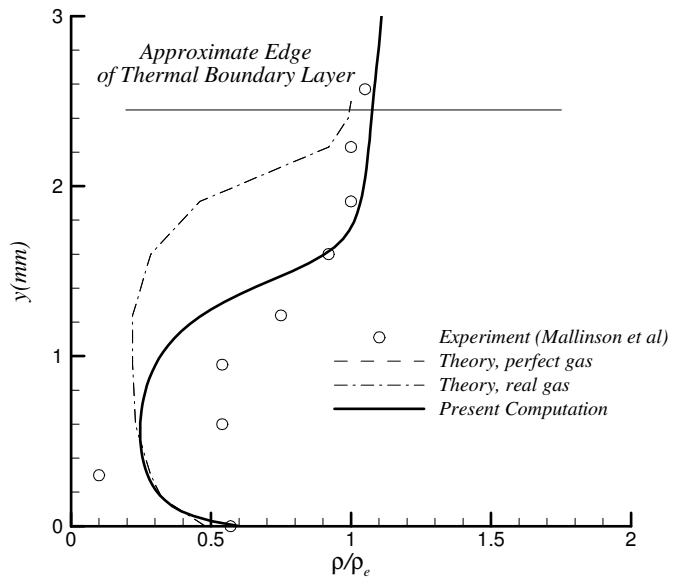


**Figure 8.26** Density profile through the boundary layer. Case G. (Distance from the leading egde  $x=33$  mm)

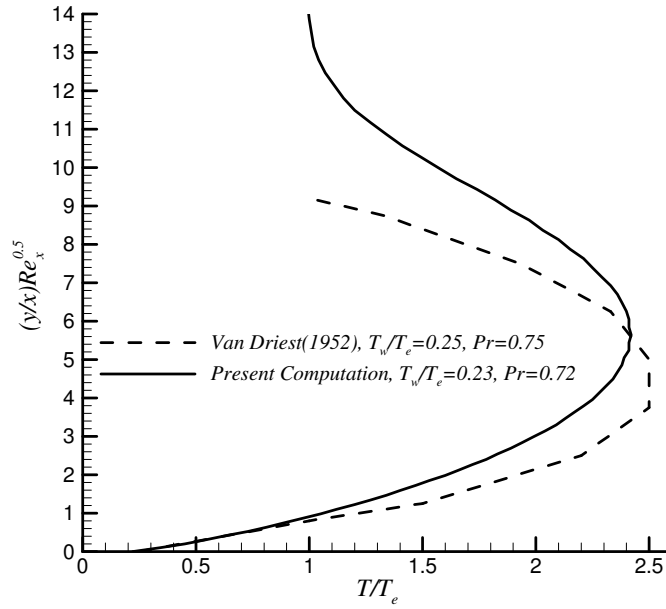


**Figure 8.27** Temperature profiles over a cold flat plate,  $M_e=7.04$ , Case B.

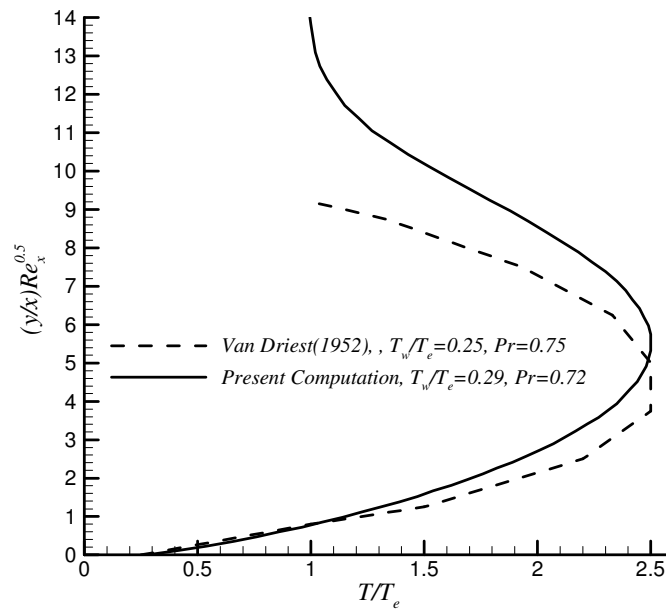


**Figure 8.28** Temperature profiles over a cold flat plate,  $M_e=7.1$ , Case D.

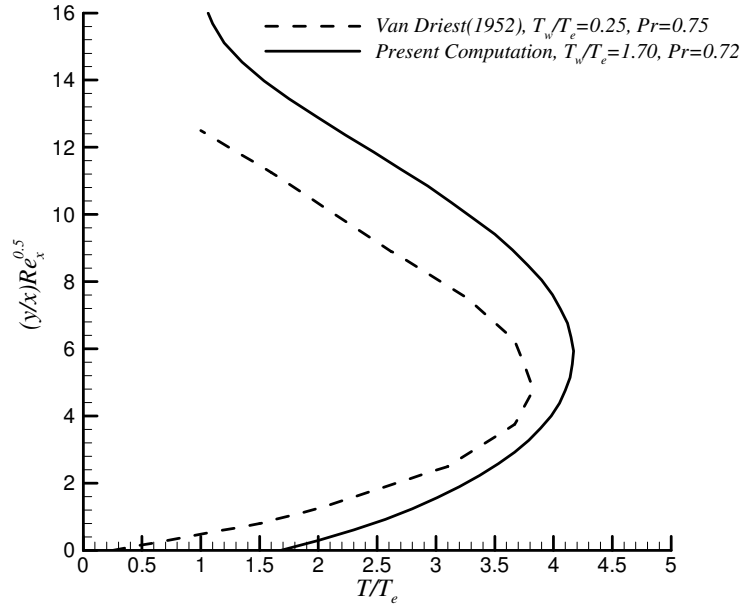


**Figure 8.29** Temperature profiles over a cold flat plate,  $M_e=8.8$ , Case G.

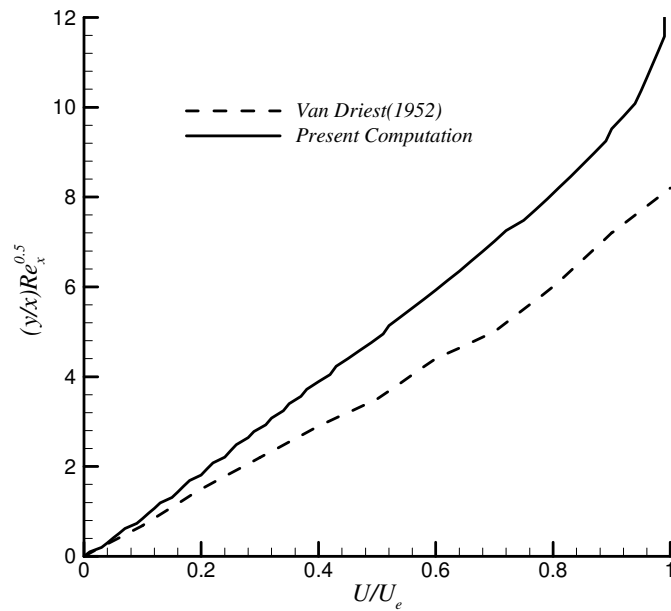


**Figure 8.30** Velocity profiles over a cold flat plate,  $M_e=7.04$ , Case B.

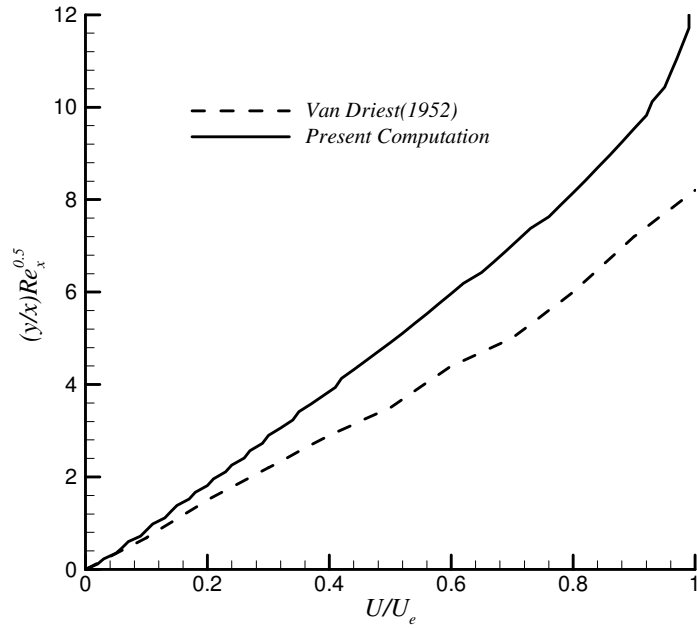


**Figure 8.31** Velocity profiles over a cold flat plate,  $M_e=7.1$ , Case D.

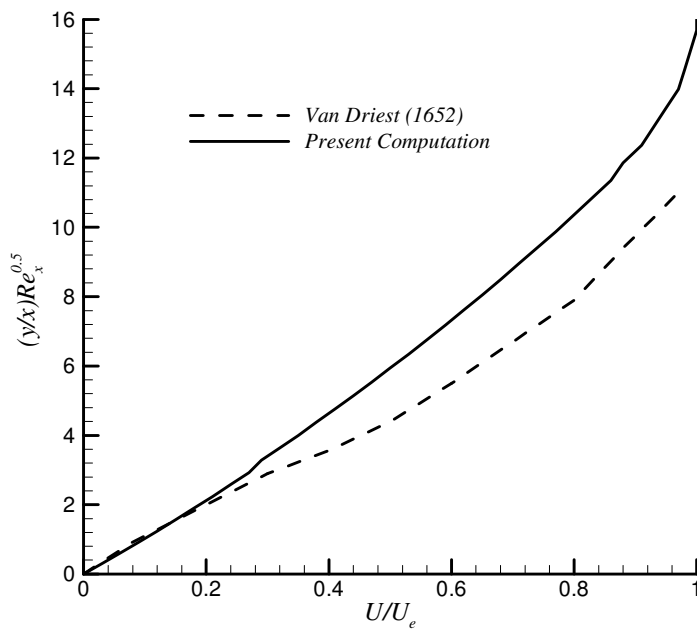


**Figure 8.32** Velocity profiles over a cold flat plate,  $M_e=8.8$ , Case G.

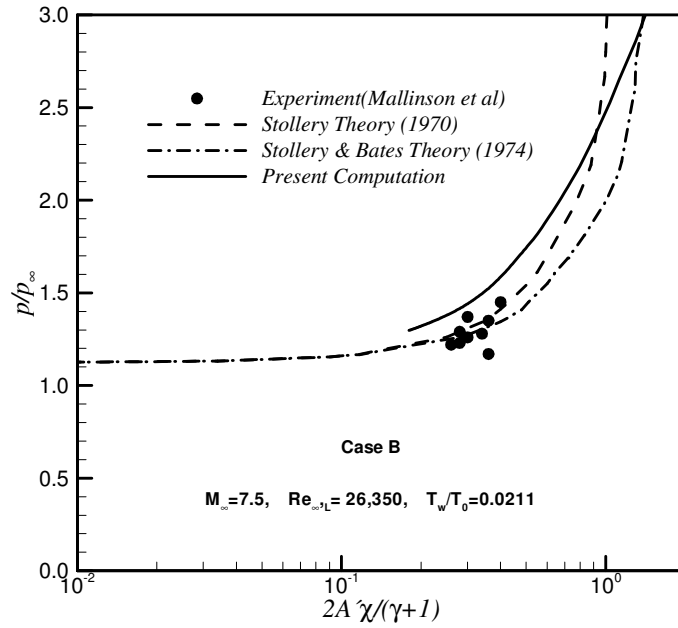


**Figure 8.33** Surface pressure distribution, Case B.

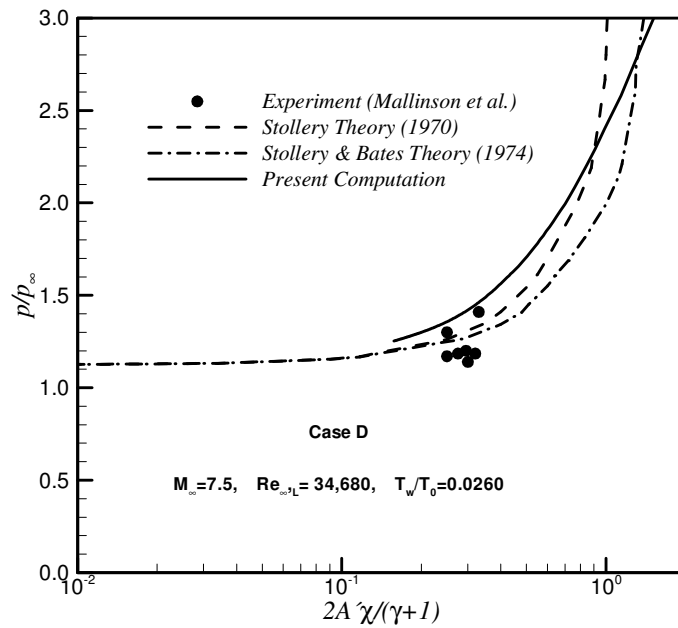


**Figure 8.34** Surface pressure distribution, Case D.

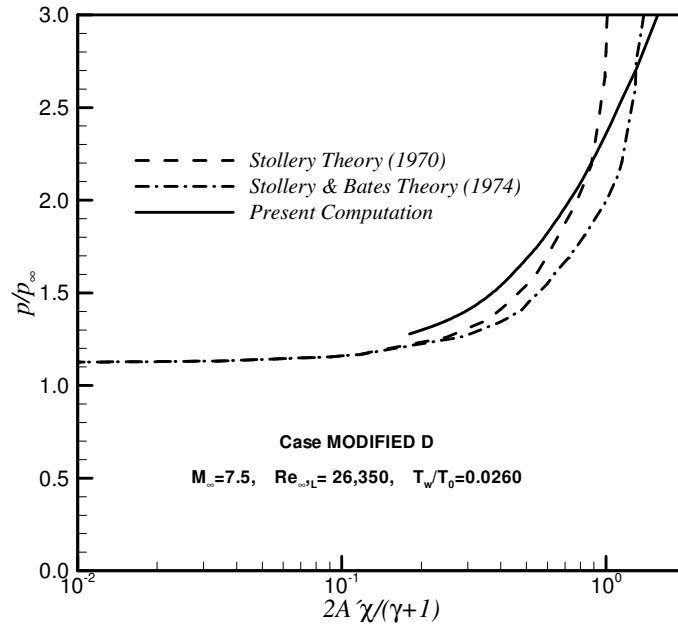


Figure 8.35 Surface pressure distribution, Case Modified D.

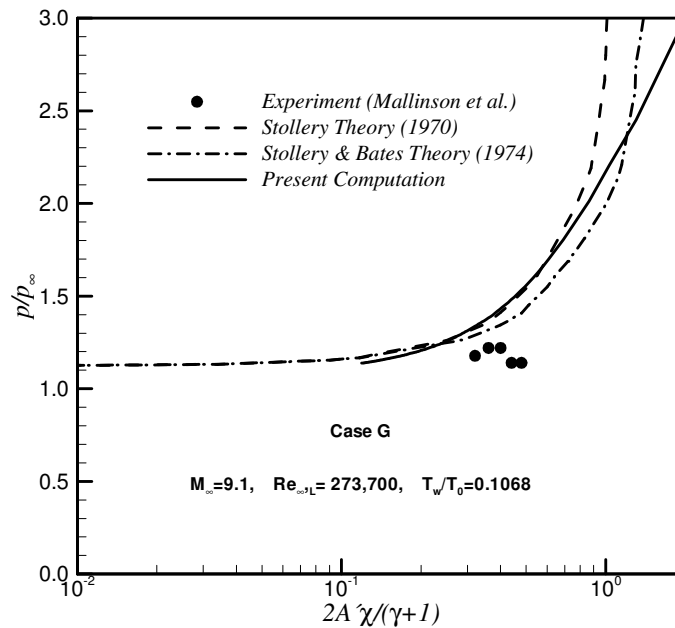
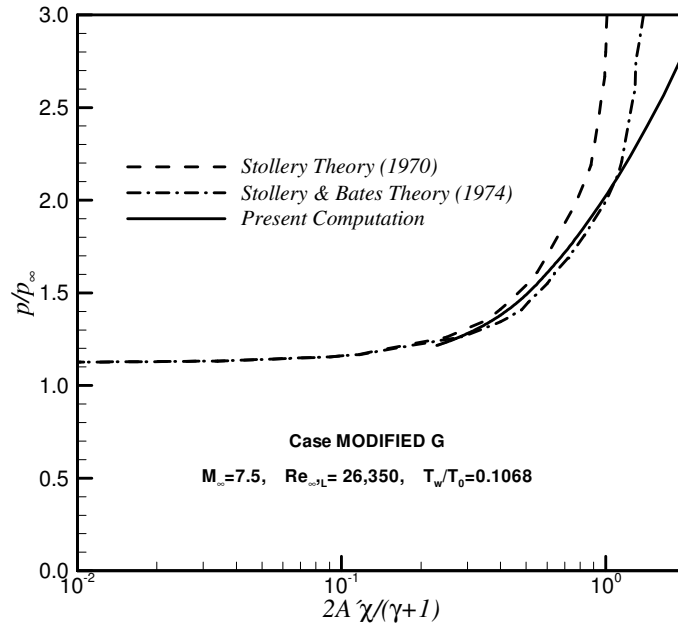
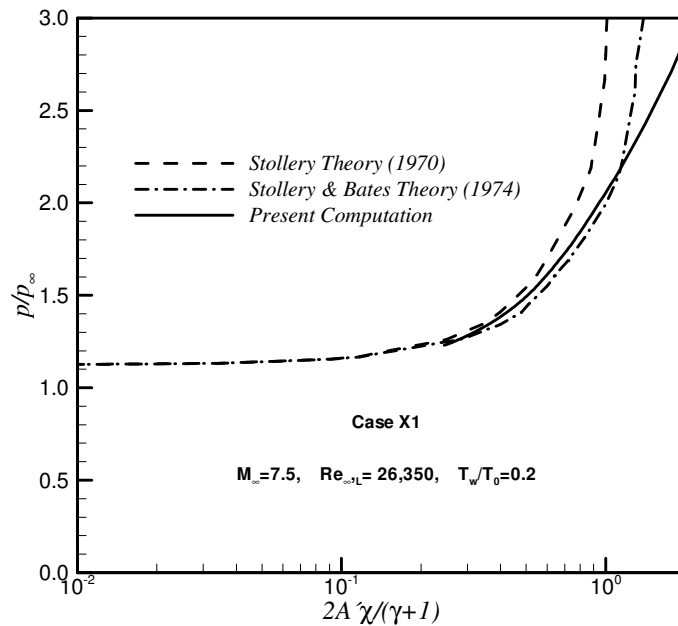


Figure 8.36 Surface pressure distribution, Case G.



**Figure 8.37** Surface pressure distribution, Case Modified G.



**Figure 8.38** Surface pressure distribution, Case X1.

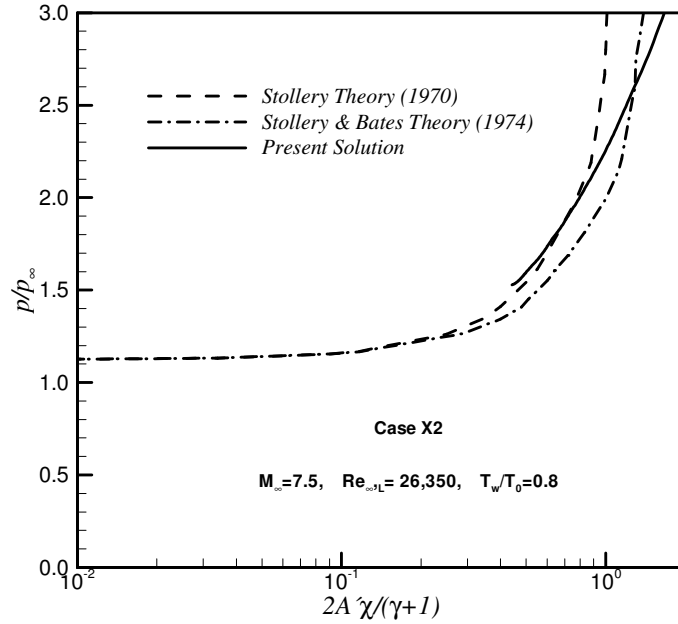


**Figure 8.39** Surface pressure distribution, Case X2.

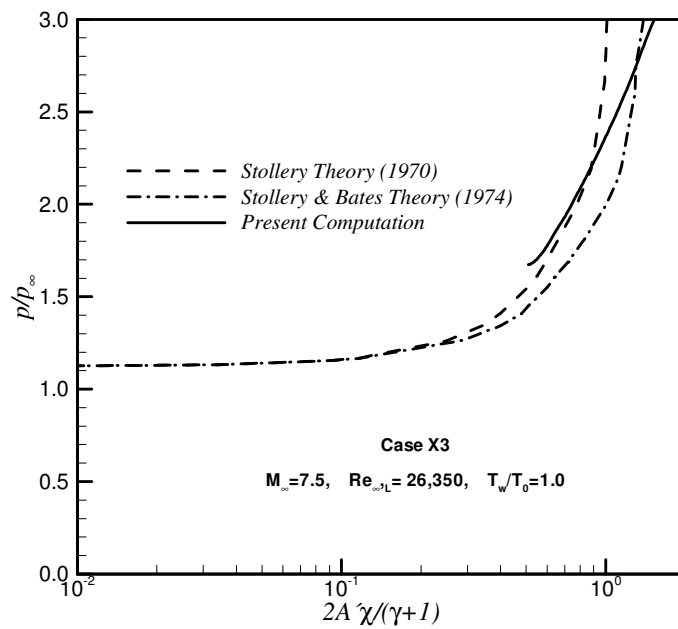


**Figure 8.40** Surface pressure distribution, Case X3.

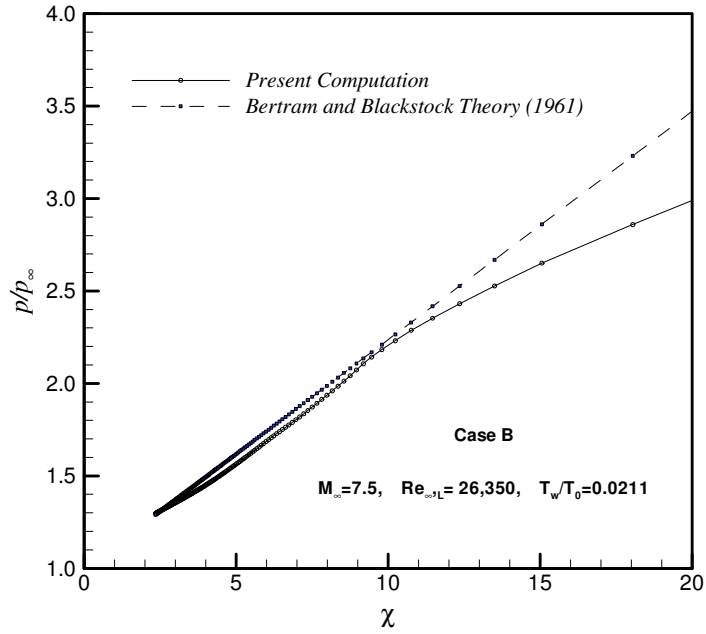


Figure 8.41 Surface pressure distribution, Case B.

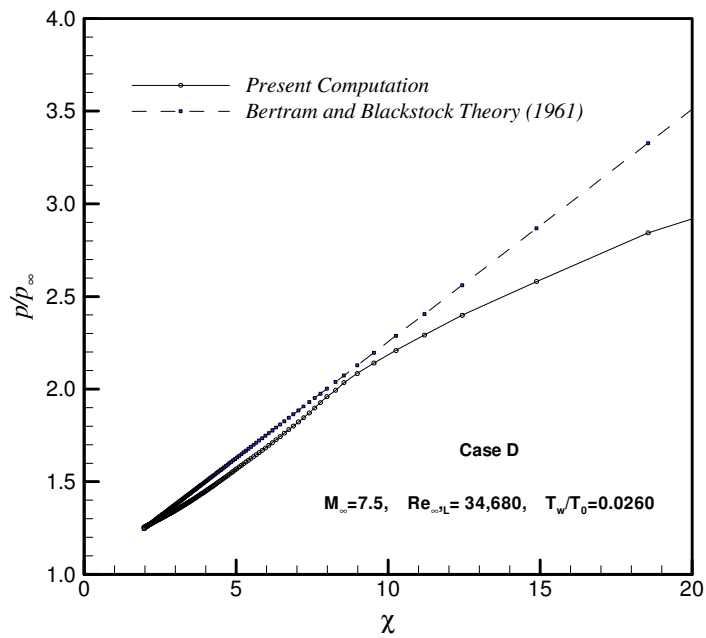


Figure 8.42 Surface pressure distribution, Case D.

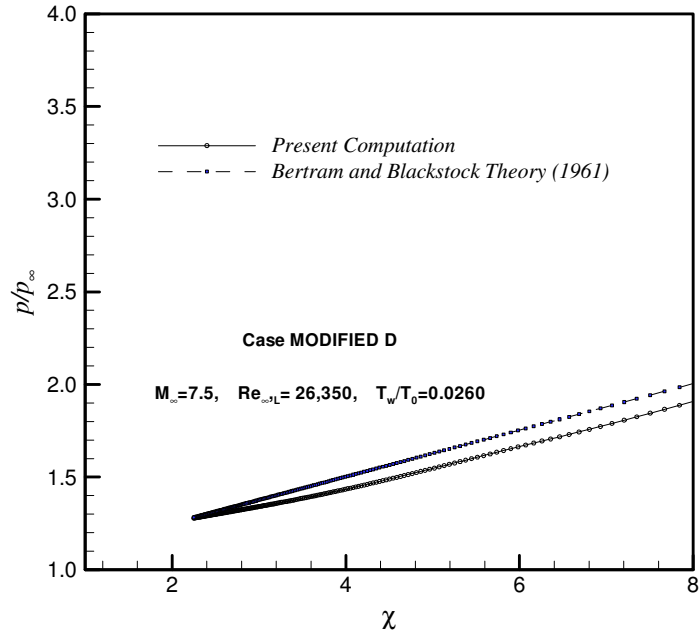


Figure 8.43 Surface pressure distribution, Case Modified D.

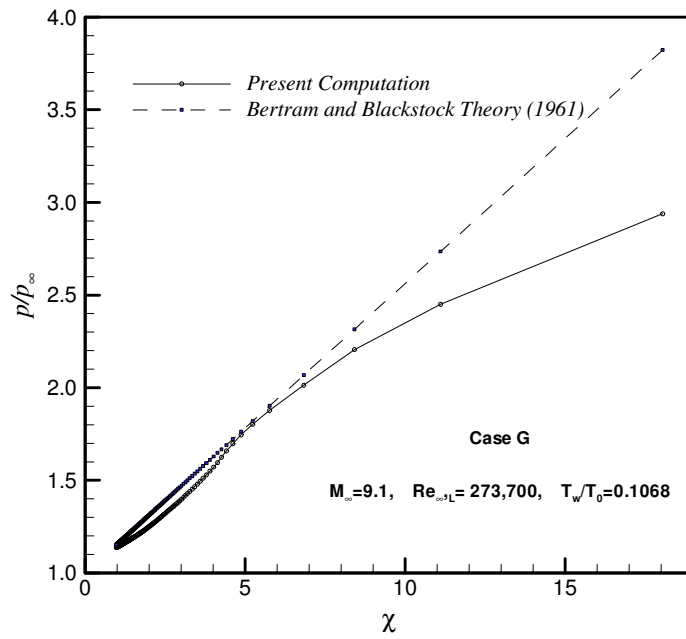


Figure 8.44 Surface pressure distribution, Case G.

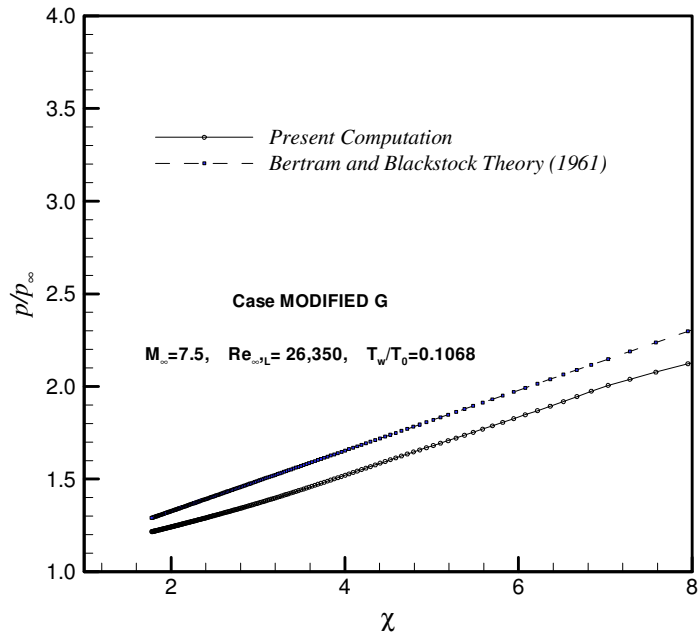


Figure 8.45 Surface pressure distribution, Case Modified G.

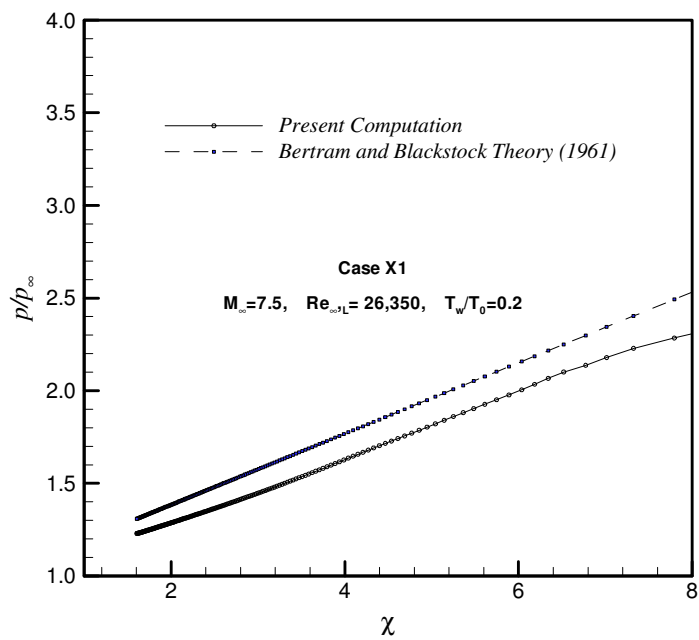


Figure 8.46 Surface pressure distribution, Case X1.

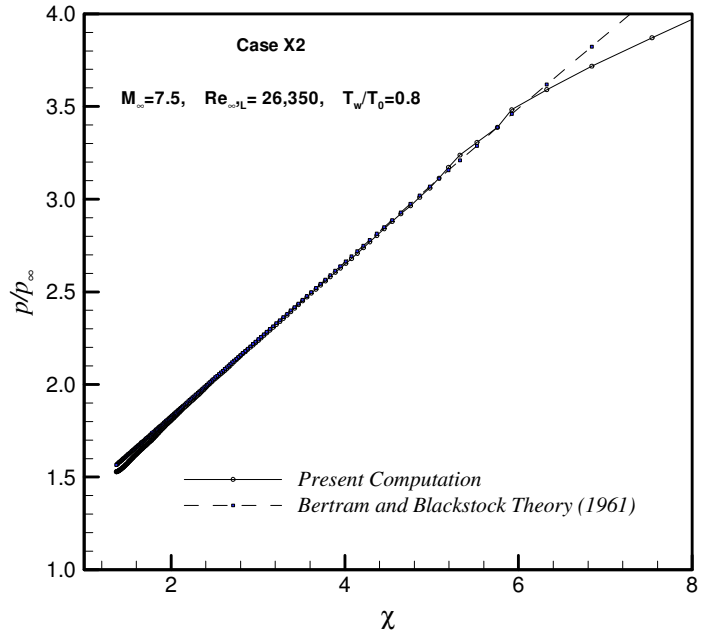


Figure 8.47 Surface pressure distribution, Case X2.

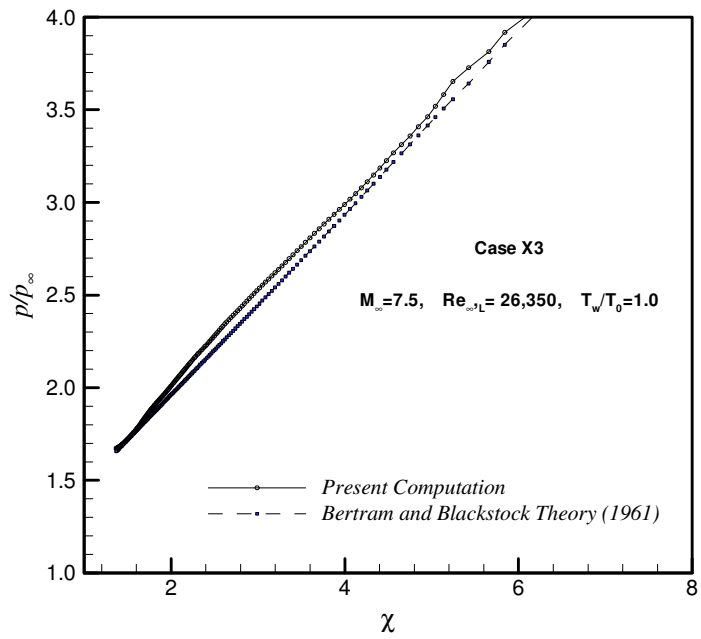
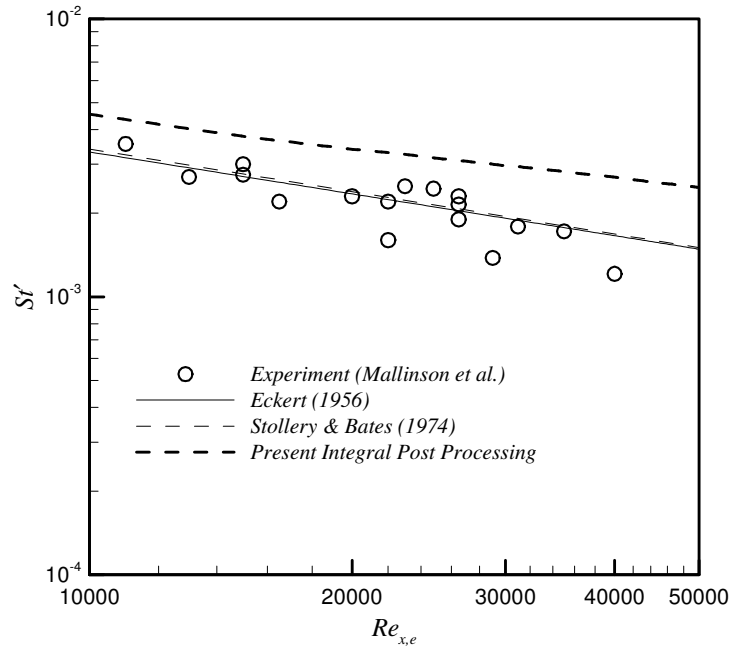
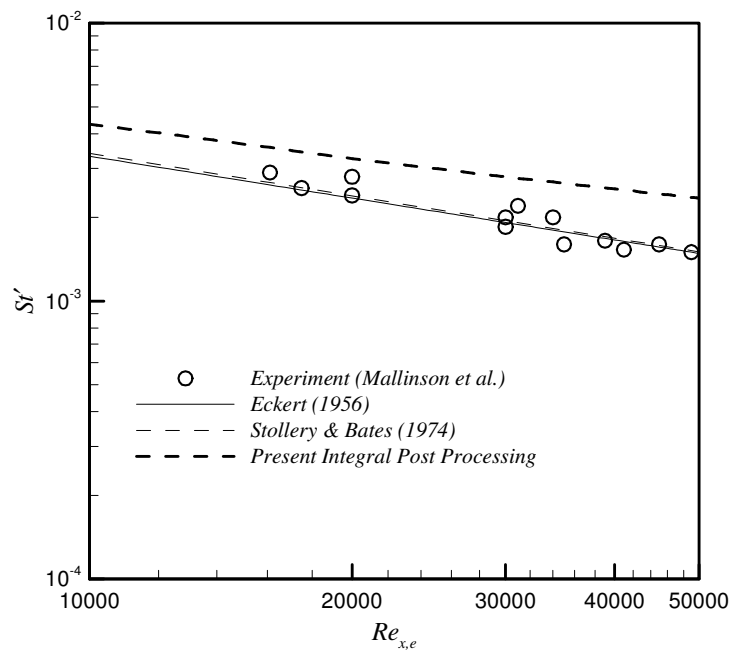


Figure 8.48 Surface pressure distribution, Case X3.



**Figure 8.49** Stanton number distribution, Case B.



**Figure 8.50** Stanton number distribution, Case D.

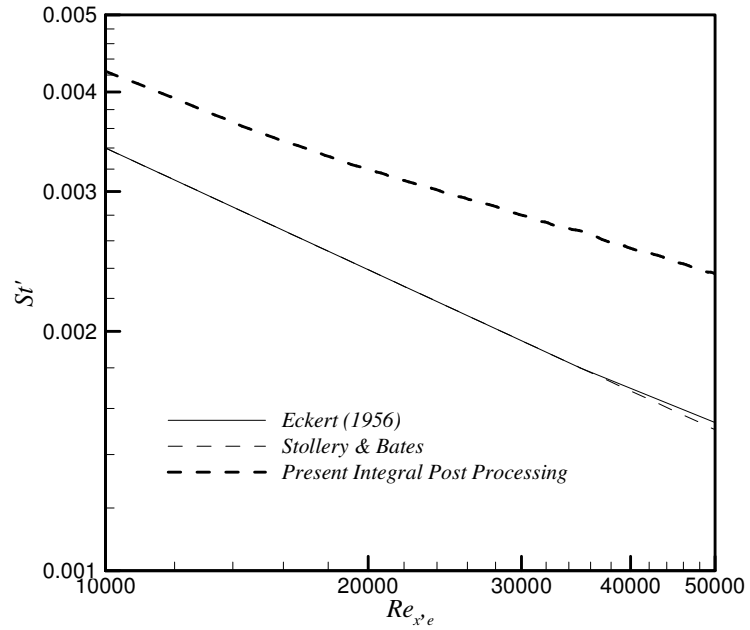


**Figure 8.51** Stanton number distribution, Case Modified D.

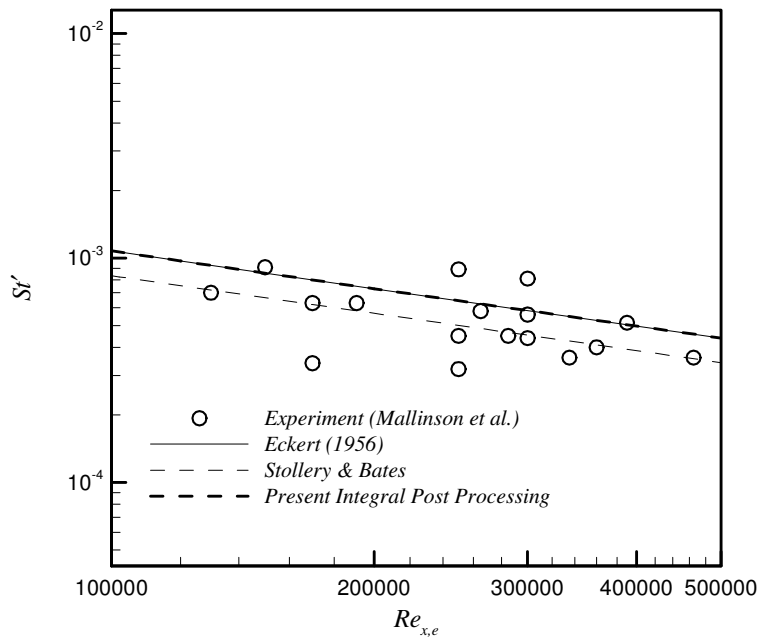


**Figure 8.52** Stanton number distribution, Case G.

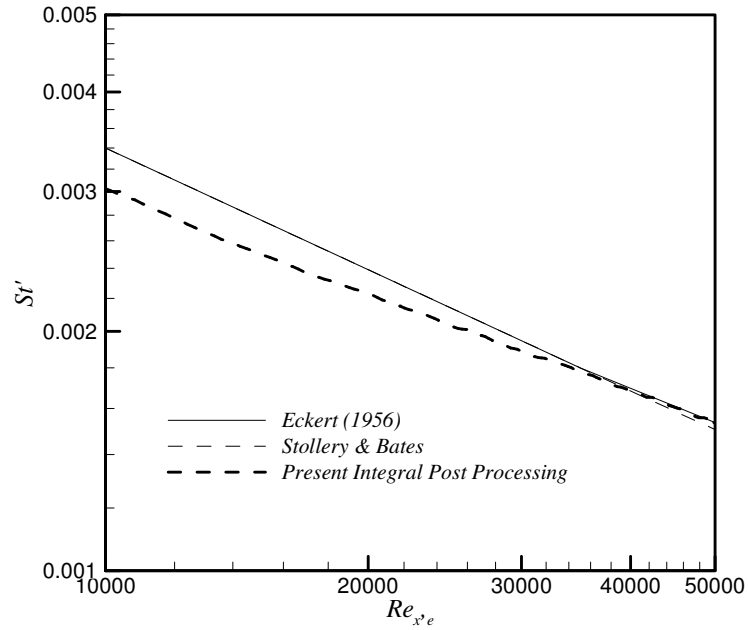


**Figure 8.53** Stanton number distribution, Case Modified G.

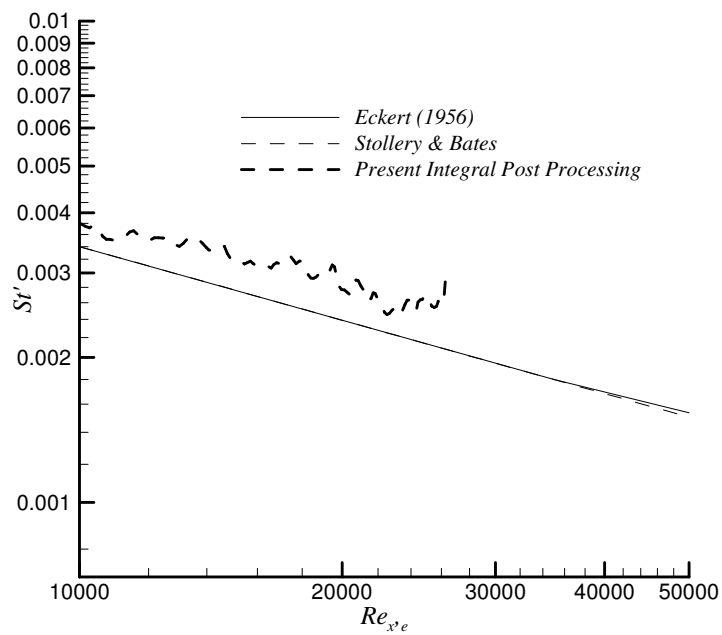


**Figure 8.54** Stanton number distribution, Case X1.

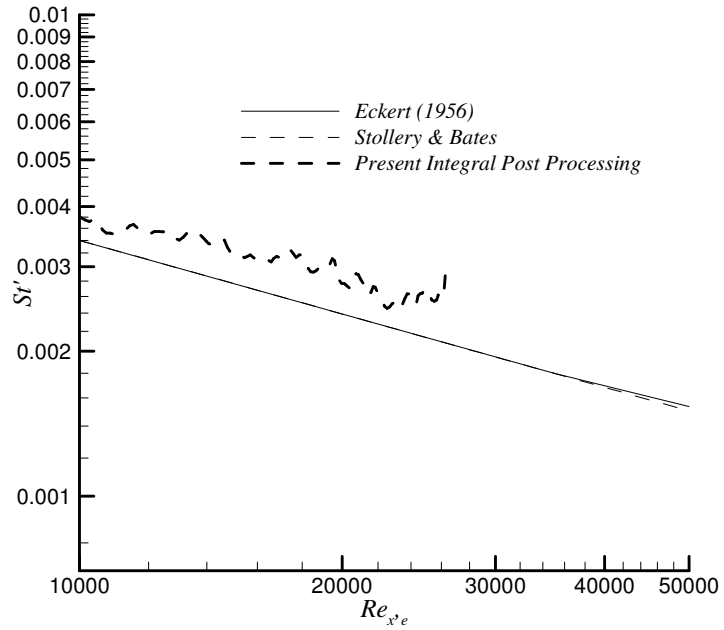


**Figure 8.55** Stanton number distribution, Case X2.

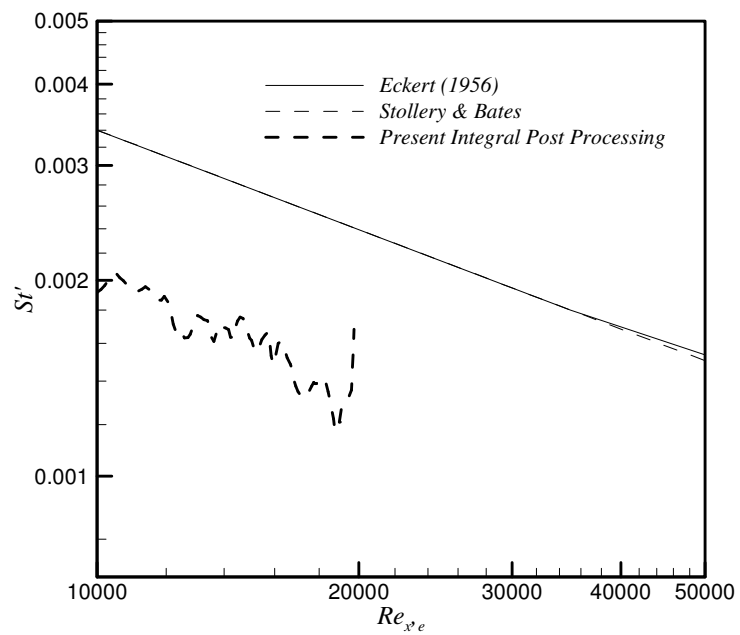


**Figure 8.56** Stanton number distribution, Case X3.

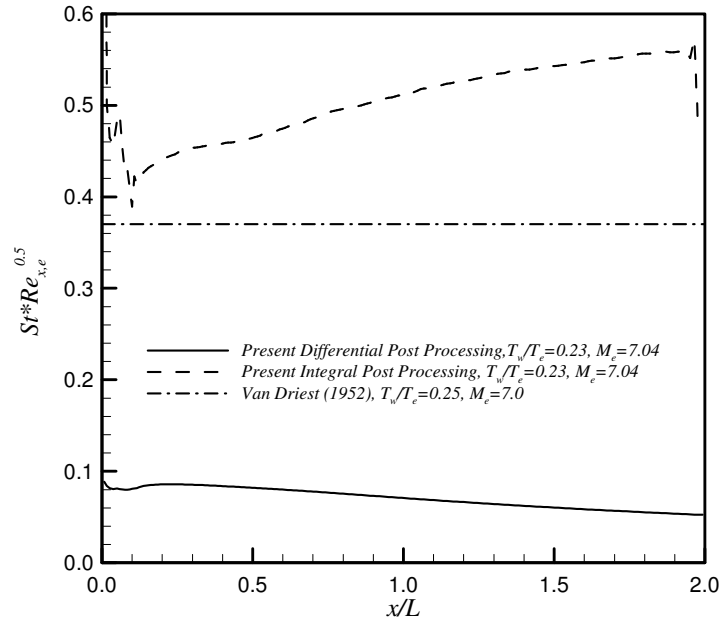


**Figure 8.57**  $St \sqrt{Re_{x,e}}$  distribution, Case B.

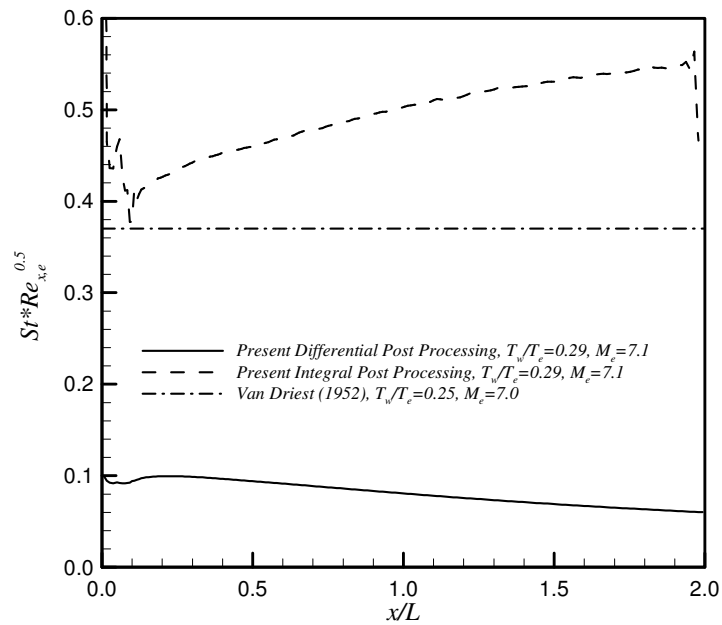


**Figure 8.58**  $St \sqrt{Re_{x,e}}$  distribution, Case D.

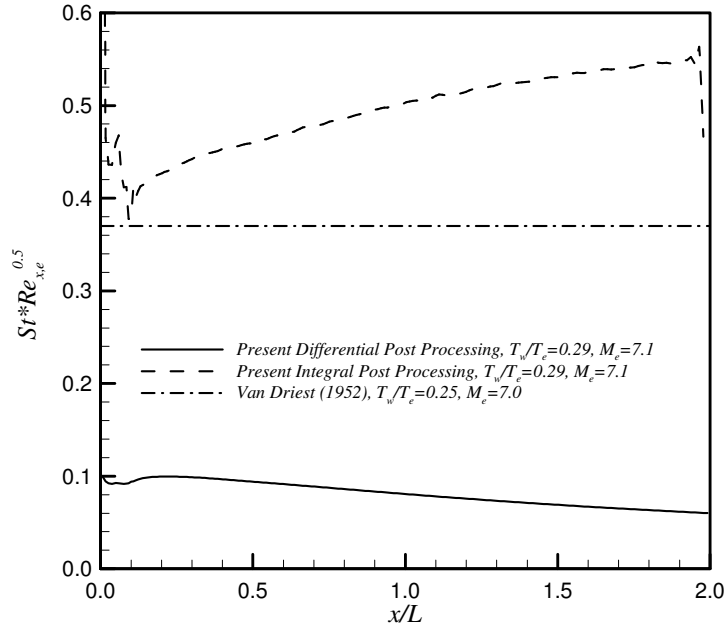


Figure 8.59  $St\sqrt{Re_{x,e}}$  distribution, Case Modified D.

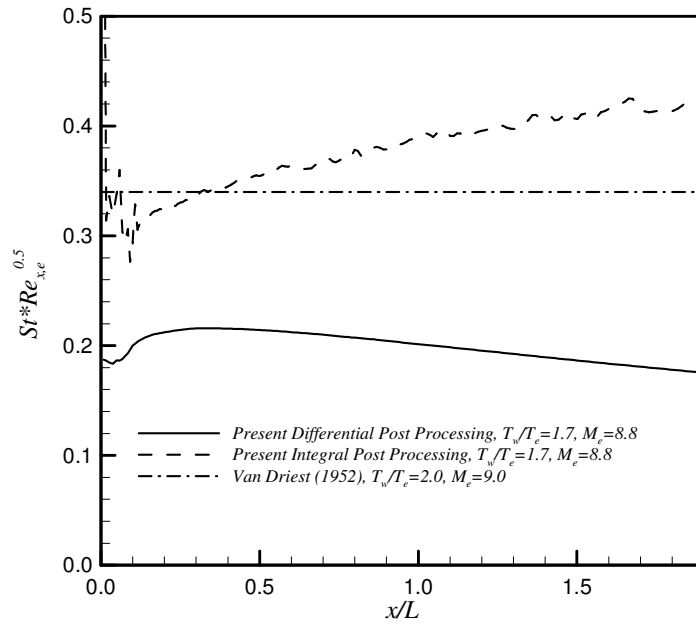
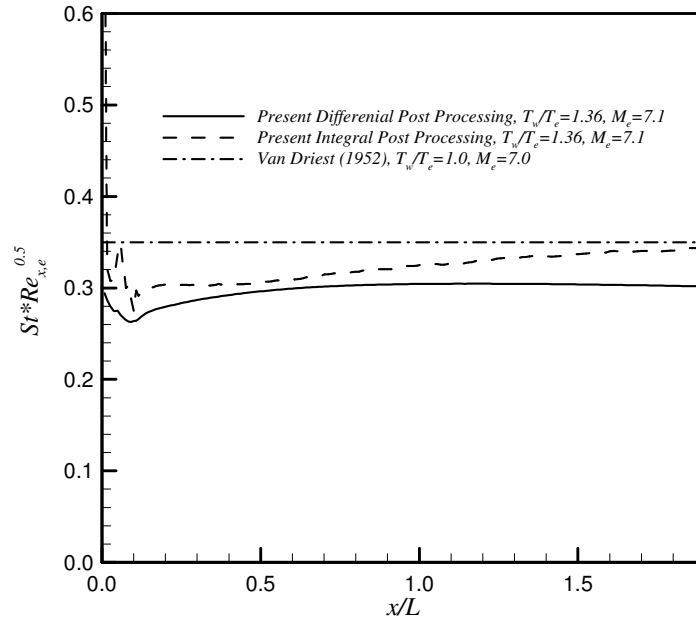
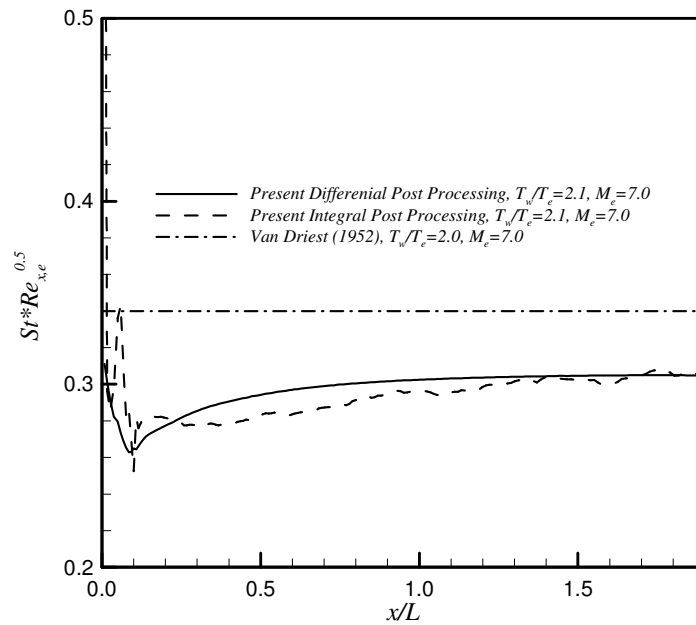


Figure 8.60  $St\sqrt{Re_{x,e}}$  distribution, Case G.



**Figure 8.61**  $St\sqrt{Re_{x,e}}$  distribution, Case Modified G.



**Figure 8.62**  $St\sqrt{Re_{x,e}}$  distribution, Case X1.

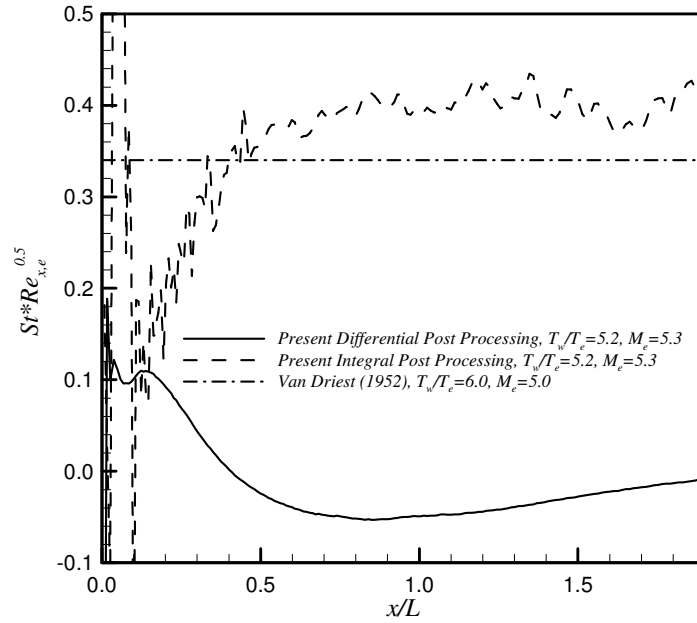


Figure 8.63  $St\sqrt{Re_{x,e}}$  distribution, Case X2.

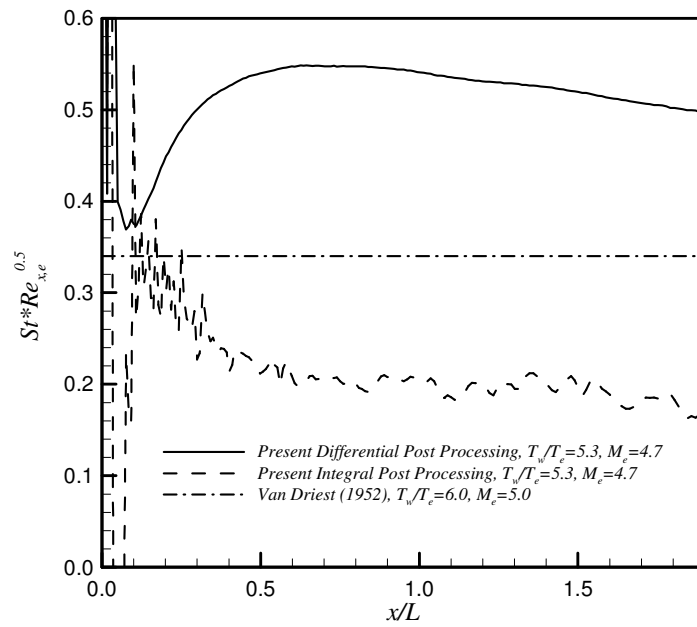
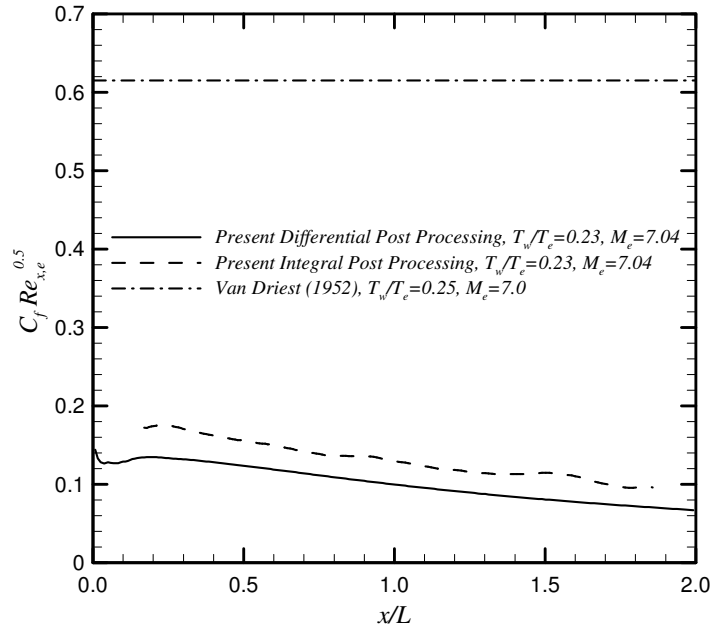
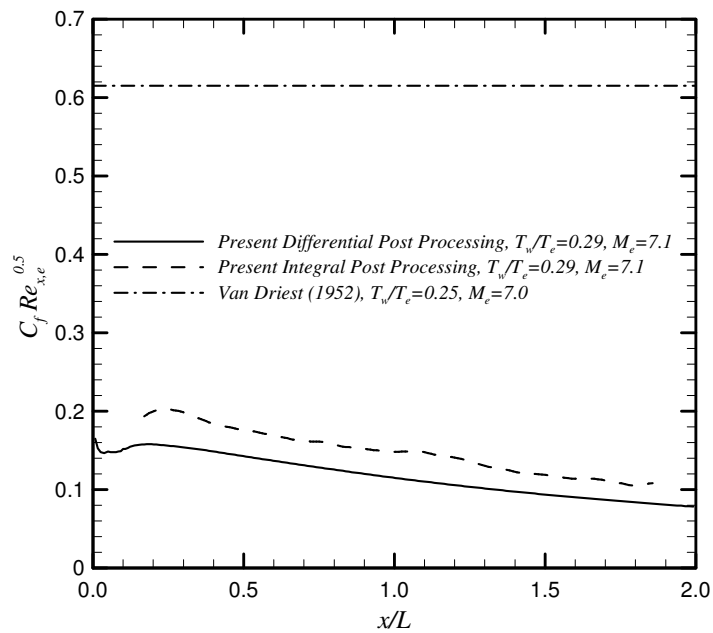


Figure 8.64  $St\sqrt{Re_{x,e}}$  distribution, Case X3.



**Figure 8.65** Skin friction coefficient distribution, Case B.



**Figure 8.66** Skin friction coefficient distribution, Case D.

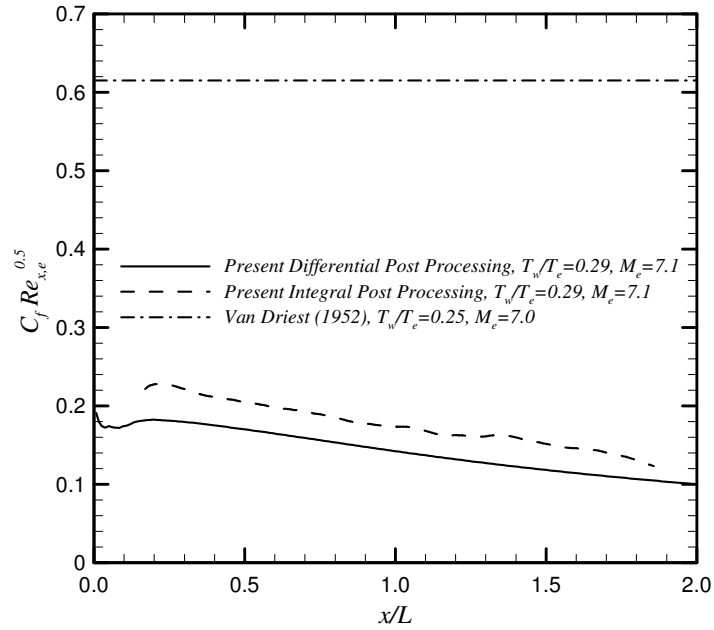


**Figure 8.67** Skin friction coefficient distribution, Case Modified D.

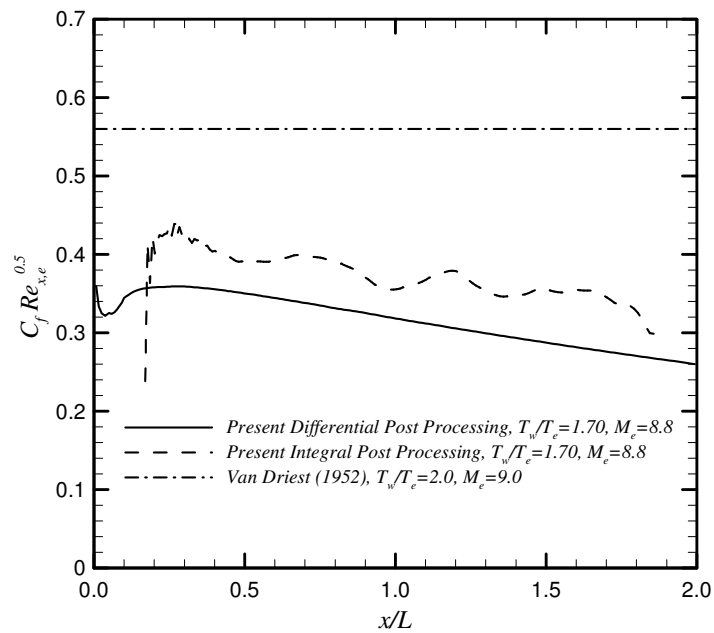


**Figure 8.68** Skin friction coefficient distribution, Case G.

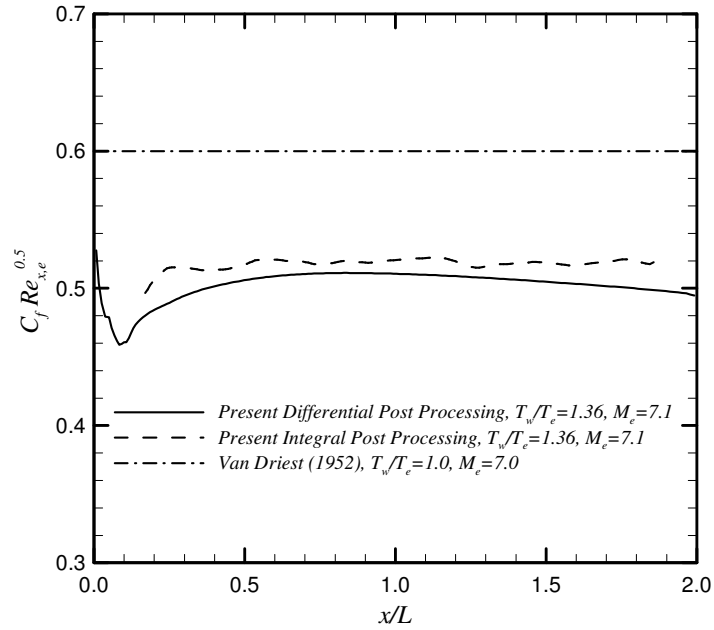


**Figure 8.69** Skin friction coefficient distribution, Case Modified G.

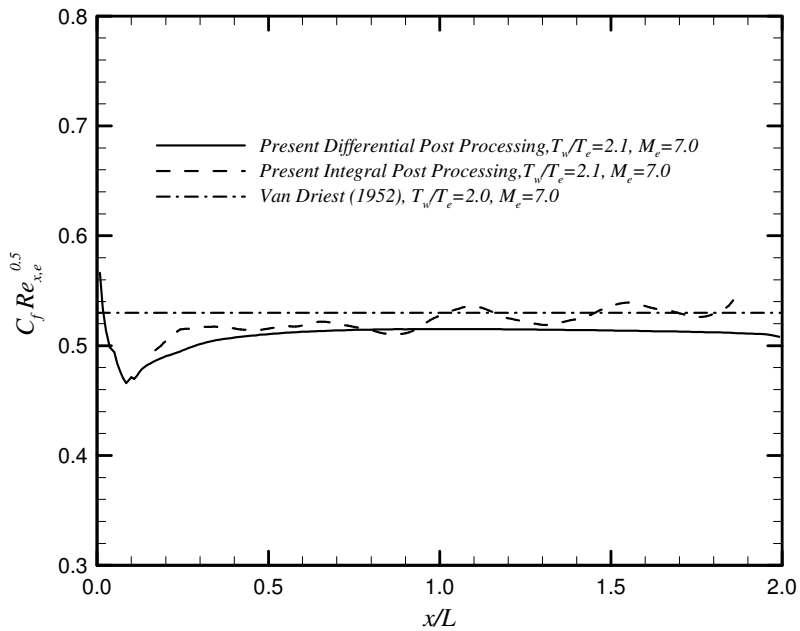


**Figure 8.70** Skin friction coefficient distribution, Case X1.

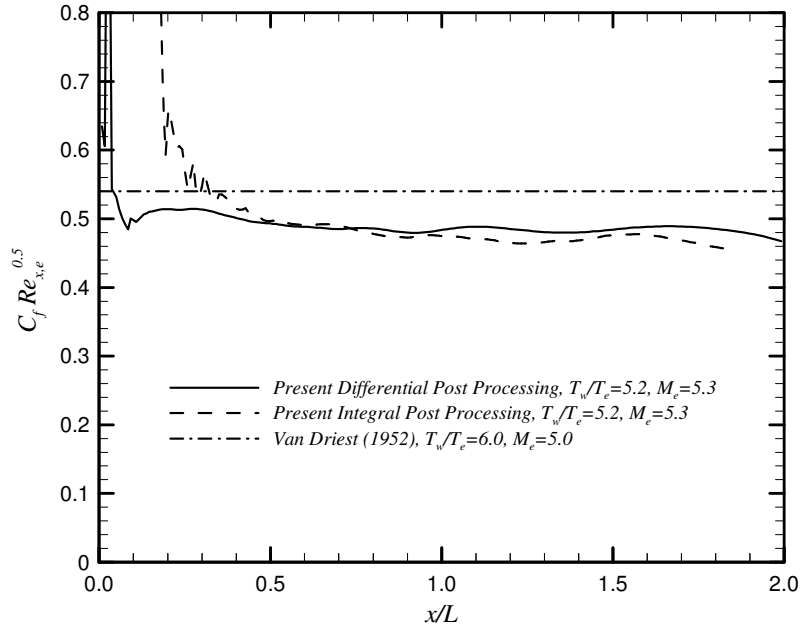


**Figure 8.71** Skin friction coefficient distribution, Case X2.

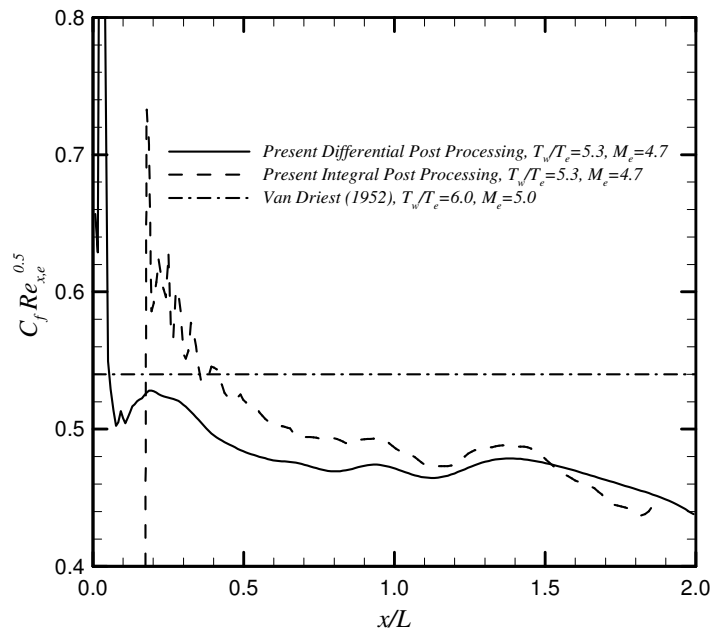


**Figure 8.72** Skin friction coefficient distribution, Case X3.

### 8.1.5. Results of the Effects of $T_w/T_0$ Study

Up to this point, eight different test cases are analyzed over flat plate in terms of flow variable, boundary layer variable, pressure distribution, heat transfer rate distribution and skin friction coefficient distribution.

During this study, one of the most critical flow properties is considered as  $T_w/T_0$  ratio. In this section, the effects of  $T_w/T_0$  on the heat transfer and pressure distributions and the boundary layer flow variables are presented. The Case B, Modified D, Modified G, X1, X2 and X3 are chosen according to the  $T_w/T_0$  values to compare the results. For these six test cases;  $M_\infty$  is 7.5 and  $Re_{\infty,L}$  is 26,350. Navier Stokes solutions are obtained for  $T_w/T_0$  ratios from 0.0211 to 1.0 for six test cases for fixed  $M_\infty$  and  $Re_{\infty,L}$  and same flat plate grid given in Figure 7.5. The Case X2 ( $T_w= 3,000$  °K and  $T_{aw}=3,335$  °K) and X3 ( $T_w= 3,000$  °K and  $T_{aw}=2,720$  °K) are close to adiabatic wall case and the heat transfer is weak for these cases.

The effect of  $T_w/T_0$  on convergence history is given in Figure 8.73. As seen from the figure that the convergence decreases with the increasing  $T_w/T_0$  ratio.

Figure 8.74 shows the effect of  $T_w/T_0$  on the number of grid points in the boundary layer.

The effect of  $T_w/T_0$  on the temperature profiles, velocity profiles and the heat transfer parameter ( $f_{qw}$ ) distribution at the mid-point of the flat plate,  $x/L=1.0$ , are shown in Figures 8.75 to 8.77. The results of the Cases G and X1 lie upon one another.

In Figures 8.78 to 8.80, the effect of  $T_w/T_0$  on temperature distributions ( $T_e/T_w$ ,  $T_{max}/T_w$  and  $T^*/T_w$ ) along the boundary layer are presented.

The effects of  $T_w/T_0$  on Mach contours are given in Figures 8.81 to 8.86 for six test cases.

The effects of  $T_w/T_0$  on streamlines are given in Figures 8.87 to 8.92 for the six cases. In a direction normal to surface, between the leading edge shock and the thermal boundary layer thickness, the flow properties are not constant due to a

slight expansion. This expansion is again a result of the boundary layer displacement thickness. At this region, the flow turns upwards as can, clearly, be seen from figures.

In Figures 8.93 and 8.94, the effects of  $T_w/T_0$  on the pressure distributions are shown. It is observed that with the increasing  $T_w/T_0$  ratio the pressure increases for fixed  $M_\infty$  and  $Re_\infty$ .

The effect of  $T_w/T_0$  ratio on the skin friction coefficient is presented in Figures 8.95 to 8.100. It is clear that skin friction increases with the increasing  $T_w/T_0$  ratio. The differential and integral post processing details are given in Appendix C.

The  $T_w/T_0$  ratio effect on the heat transfer rate is shown in Figures 8.101 to 104. Here the results are presented as obtained from both integral and differential post processing. Accuracy of the differential post processing depends on the prediction of the temperature gradient at the wall. Accuracy of the integral post processing depends on the prediction of the distribution of the heat transfer parameter,  $f_{qw}$ , which was described in section 8.1.1 and its variation in the stream wise direction. The results of the differential post processing show that the heat transfer increases by increasing  $T_w/T_0$  ratio for fixed  $M_\infty$  and  $Re_\infty$ . On the other hand the results of the integral post processing show that the heat transfer decreases by increasing  $T_w/T_0$  ratio. For lower  $T_w/T_0$  ratios there is more temperature difference between the wall and the freestream therefore there should be more heat transfer. From here we may conclude that integral post processing is more reliable.

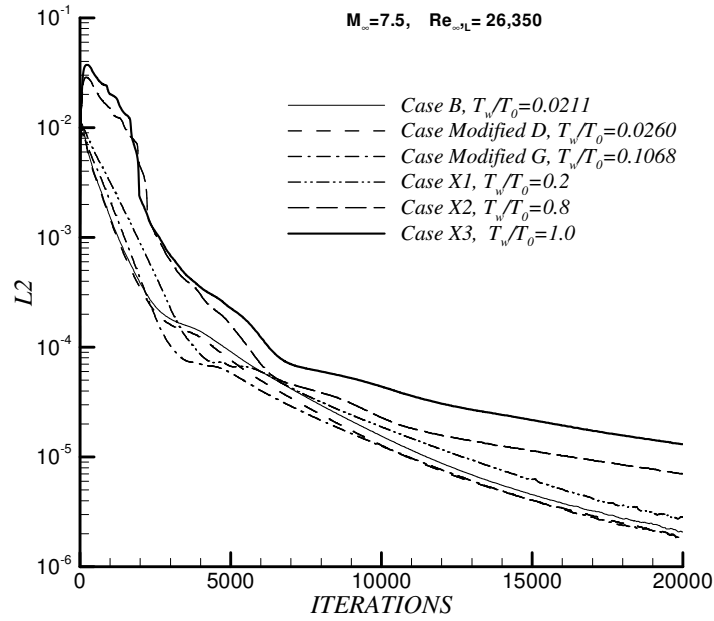


**Figure 8.73** Effect of  $T_w/T_0$  on convergence history.

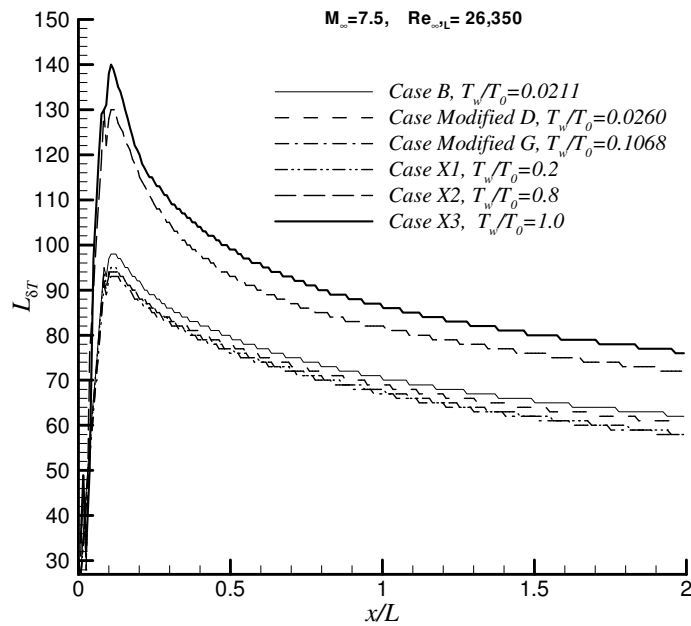


**Figure 8.74** Effect of  $T_w/T_0$  on number of grid points.

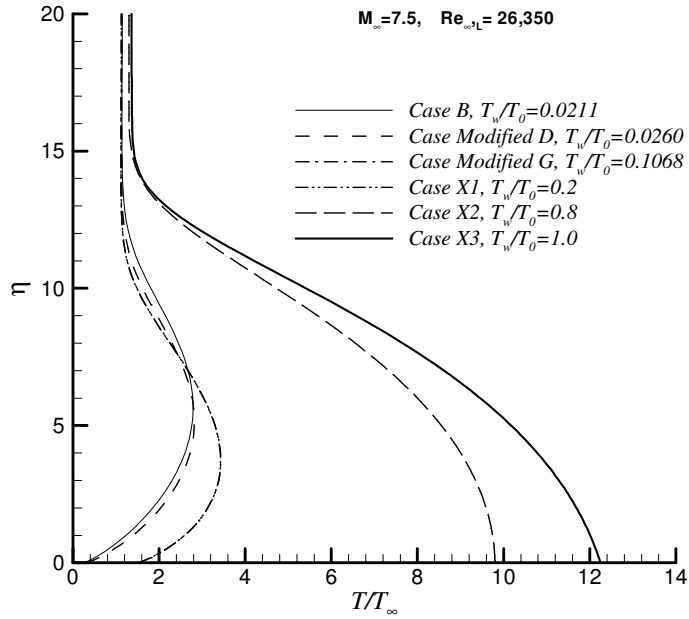


**Figure 8.75** Effect of  $T_w/T_0$  on temperature profiles at  $x/L=1.0$ .

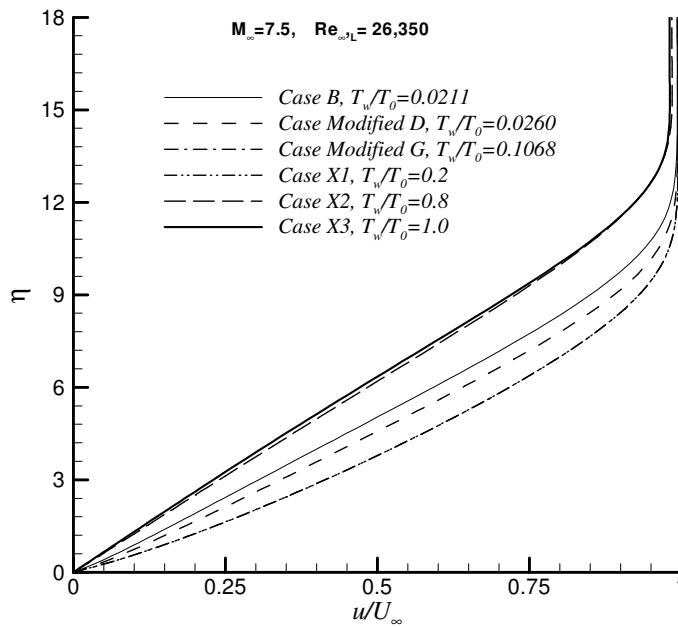


**Figure 8.76** Effect of  $T_w/T_0$  on velocity profiles at  $x/L=1.0$ .

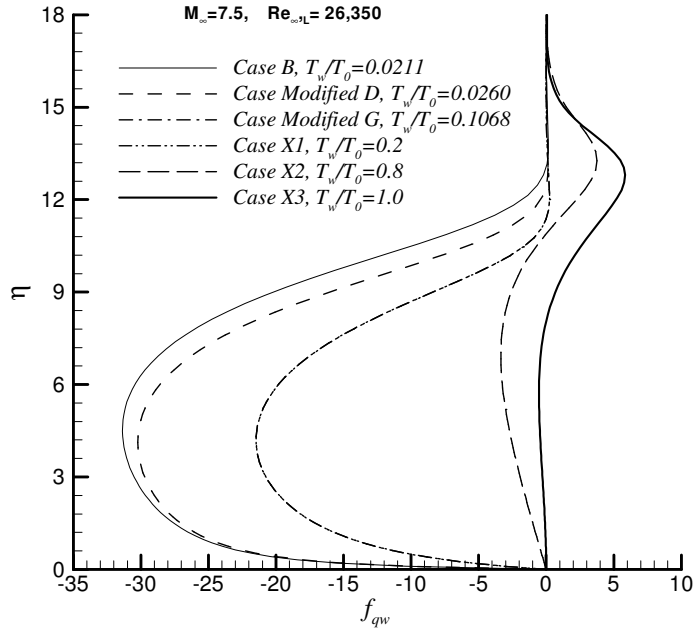


Figure 8.77 Effect of  $T_w/T_0$  on heat transfer parameter at  $x/L=1.0$ .

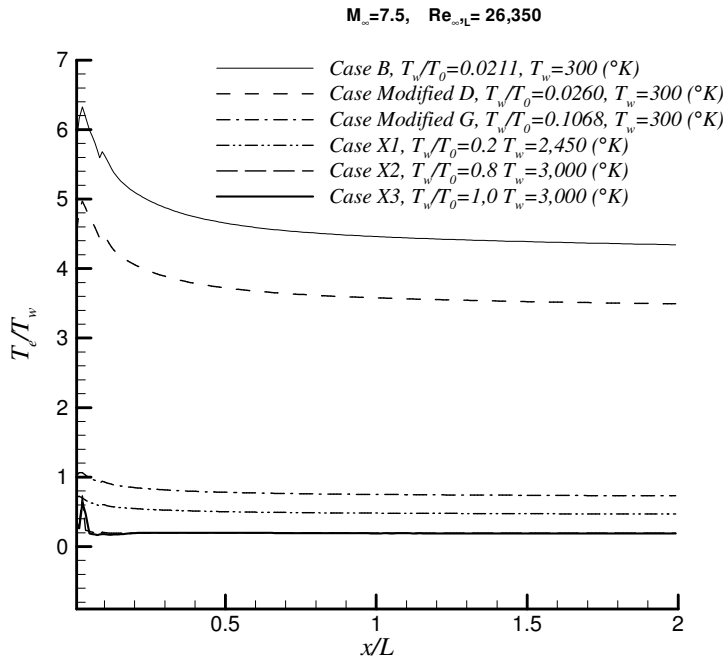
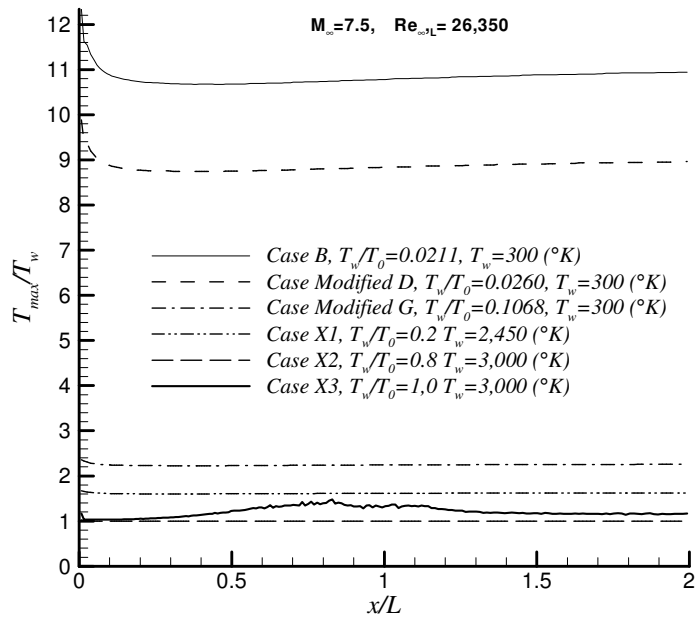
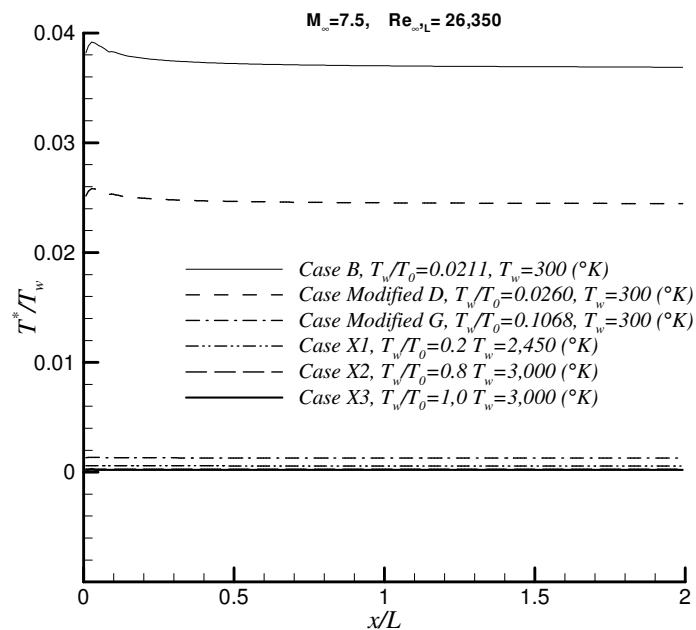


Figure 8.78 Effect of  $T_w/T_0$  on  $T_e$  distribution along the boundary layer.



**Figure 8.79** Effect of  $T_w/T_0$  on  $T_{\max}$  distribution along the boundary layer.



**Figure 8.80** Effect of  $T_w/T_0$  on  $T^*$  distribution along the boundary layer.

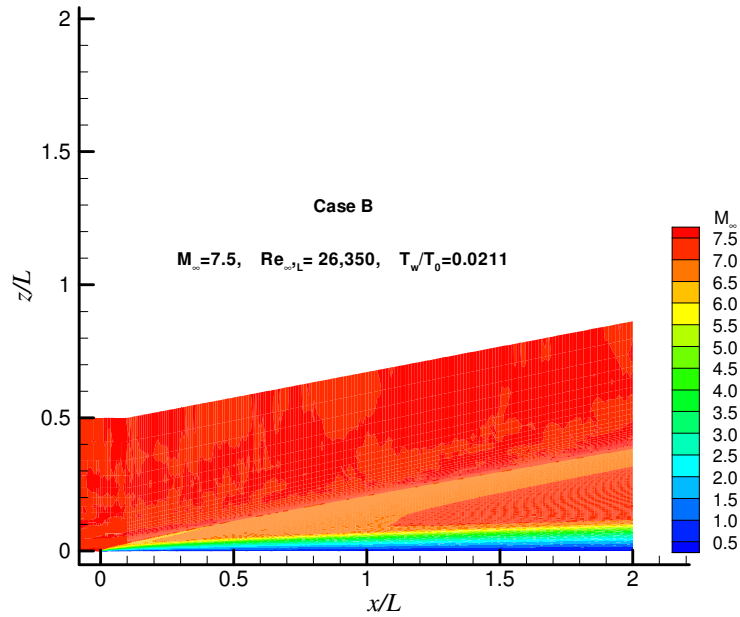


Figure 8.81 Mach contours, Case B.

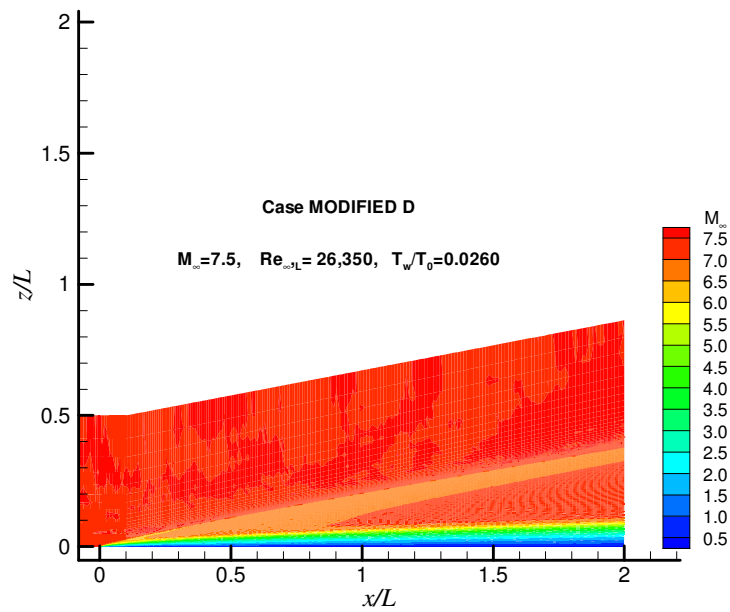


Figure 8.82 Mach contours, Case Modified D.

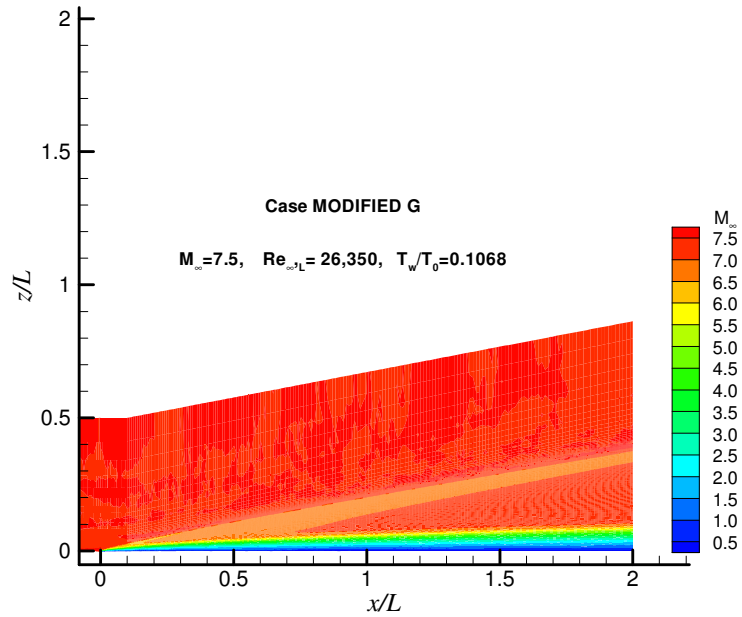


Figure 8.83 Mach contours, Case Modified G.

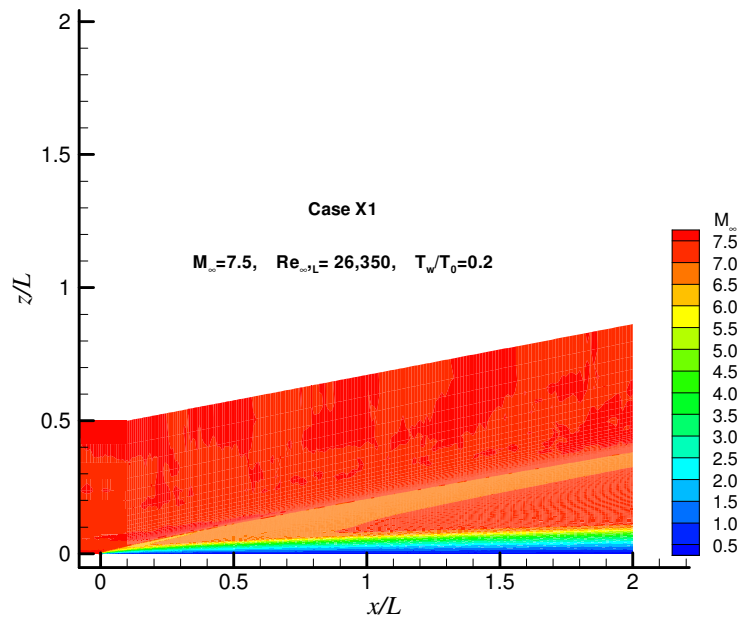


Figure 8.84 Mach contours, Case X1.

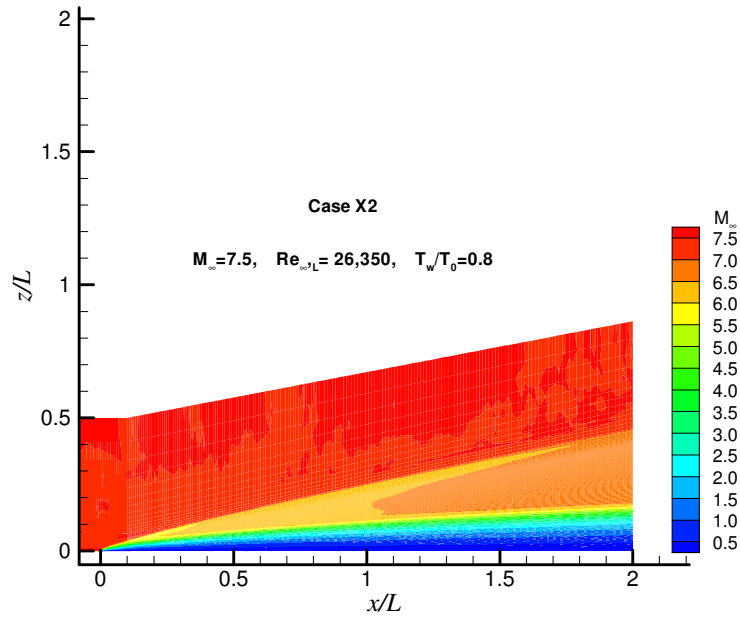


Figure 8.85 Mach contours, Case X2.

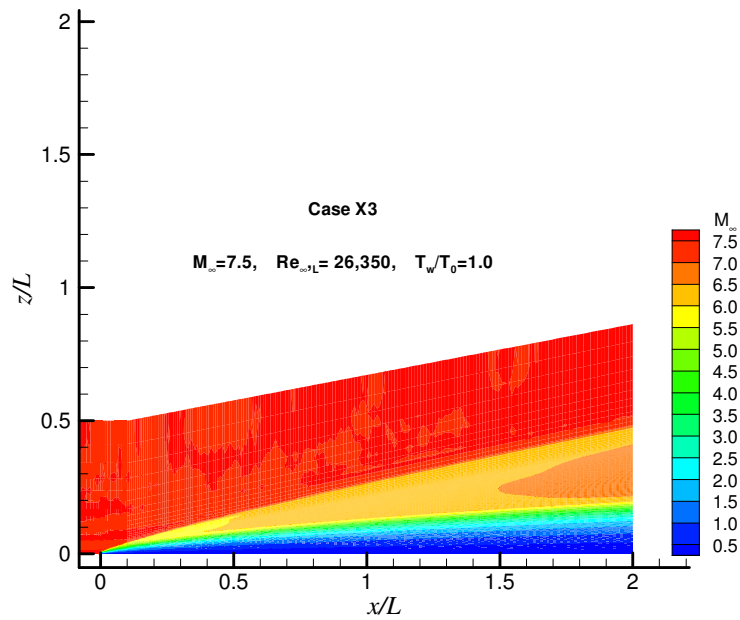
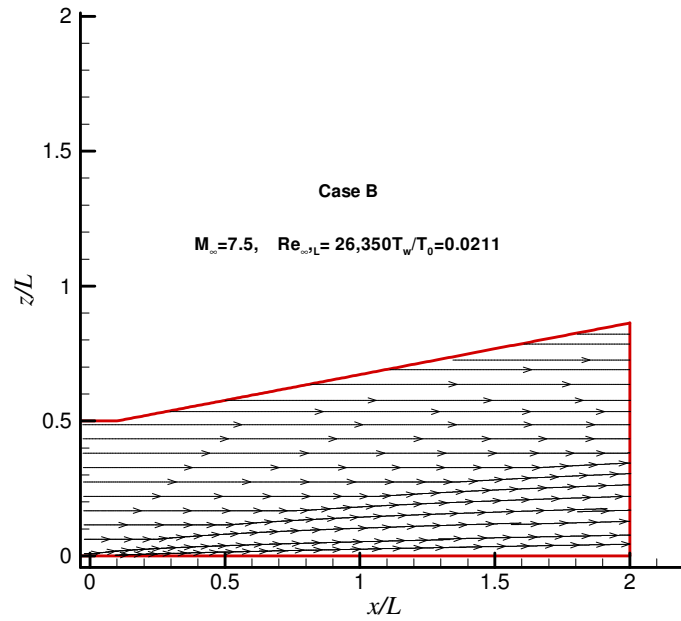
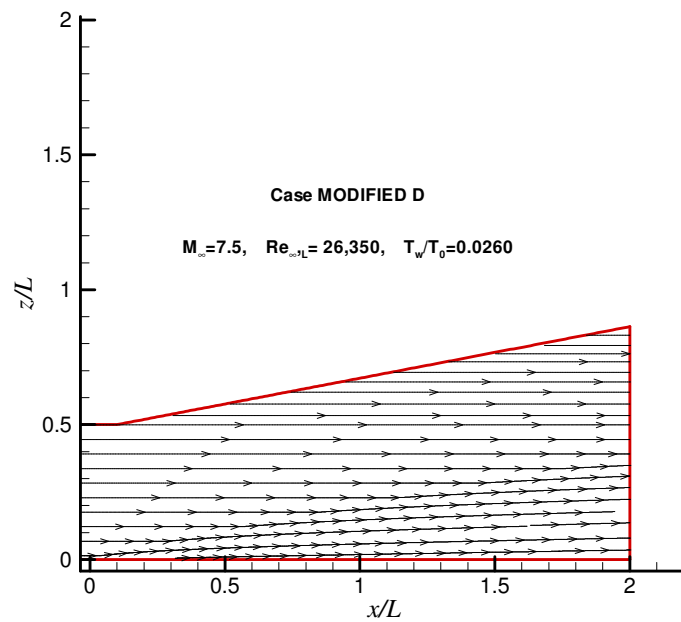


Figure 8.86 Mach contours, Case X3.



**Figure 8.87** Effect of  $T_w/T_0$  on streamlines, Case B.



**Figure 8.88** Effect of  $T_w/T_0$  on streamlines, Case Modified D.

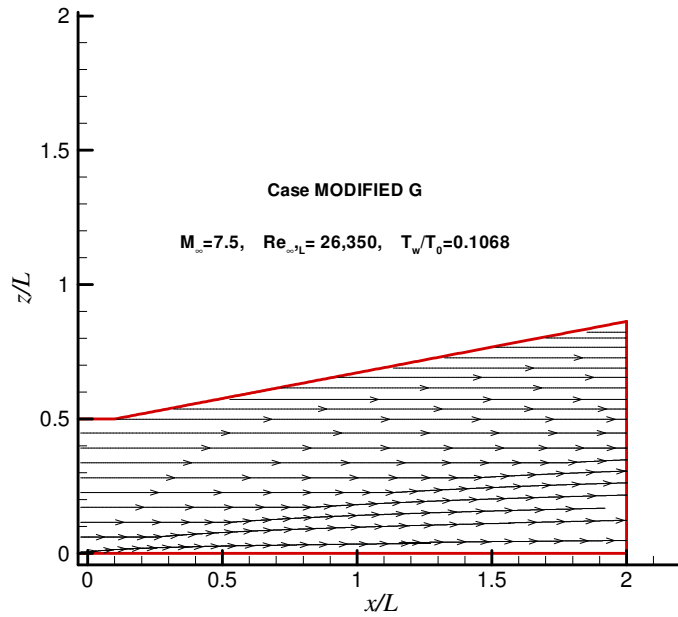


**Figure 8.89** Effect of  $T_w/T_0$  on streamlines, Case Modified G.

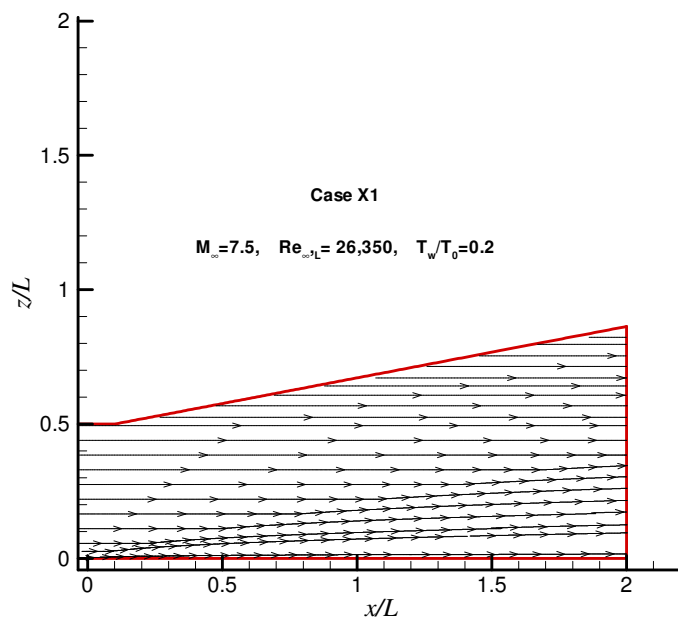


**Figure 8.90** Effect of  $T_w/T_0$  on streamlines, Case X1.

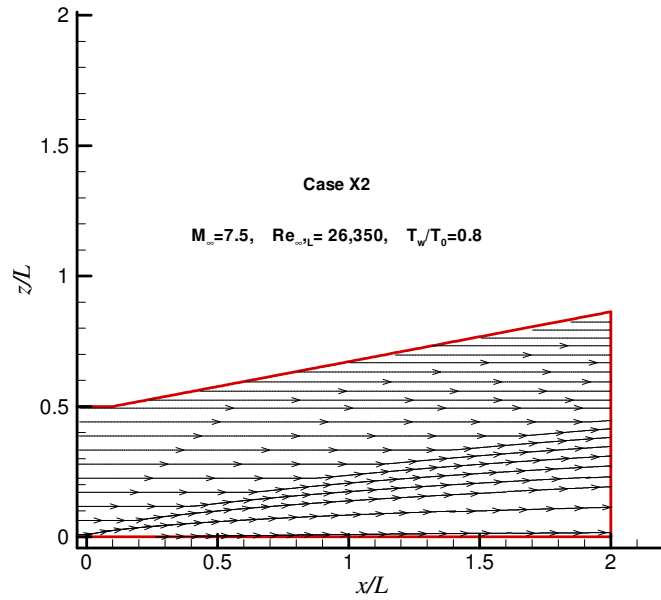


**Figure 8.91** Effect of  $T_w/T_0$  on streamlines, Case X2.

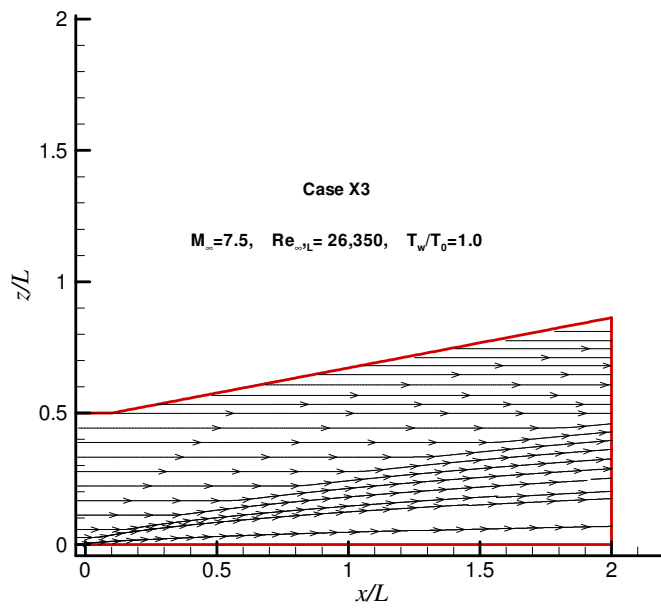


**Figure 8.92** Effect of  $T_w/T_0$  on streamlines, Case X3.

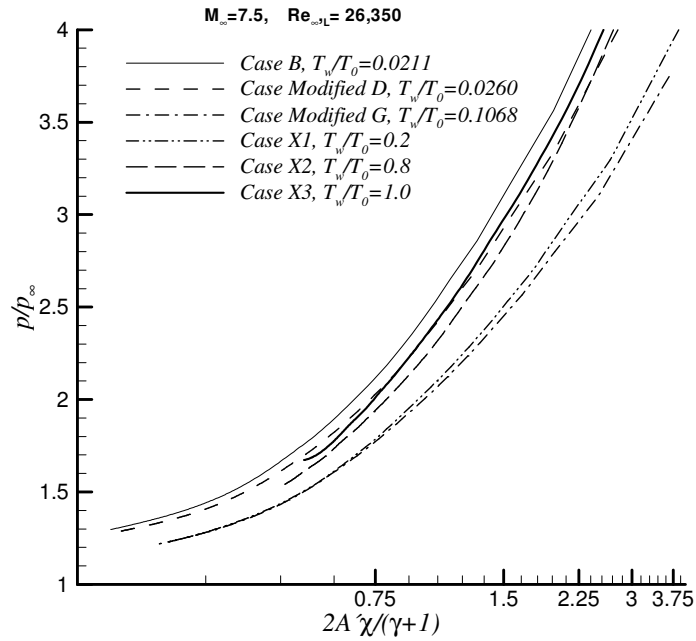


**Figure 8.93** Effect of  $T_w/T_0$  on pressure distribution.

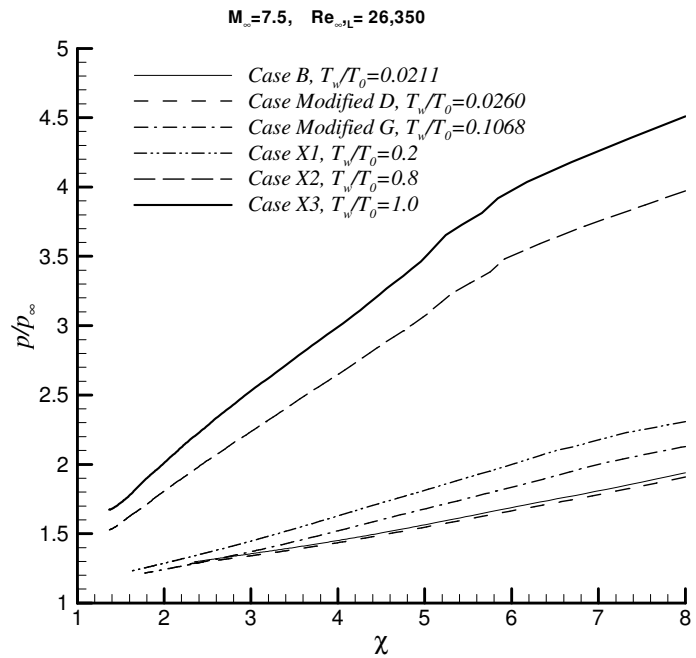


**Figure 8.94** Effect of  $T_w/T_0$  on pressure distribution.

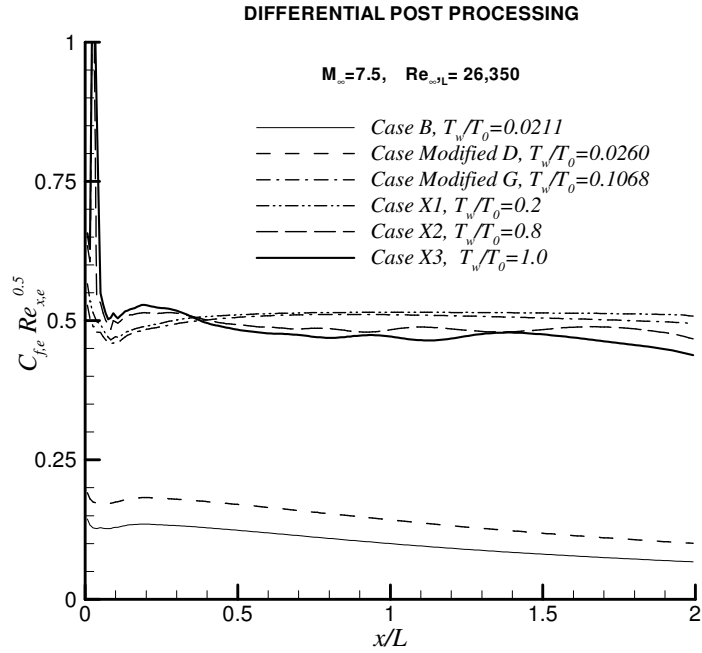


**Figure 8.95** Effect of  $T_w/T_0$  on skin friction,  $C_f$ , distribution.

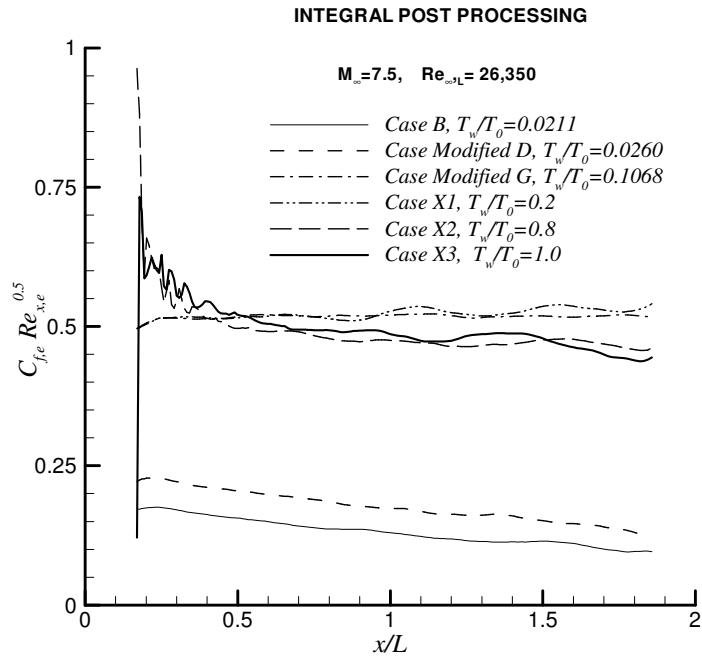


**Figure 8.96** Effect of  $T_w/T_0$  on skin friction,  $C_f$ , distribution.

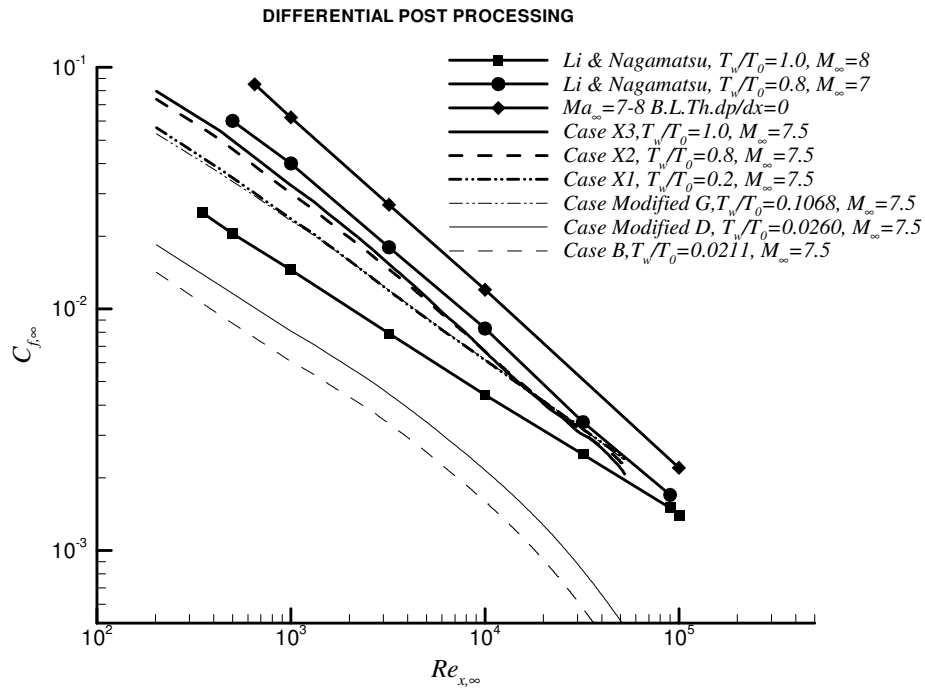


**Figure 8.97** Effect of  $T_w/T_0$  on skin friction coefficient.

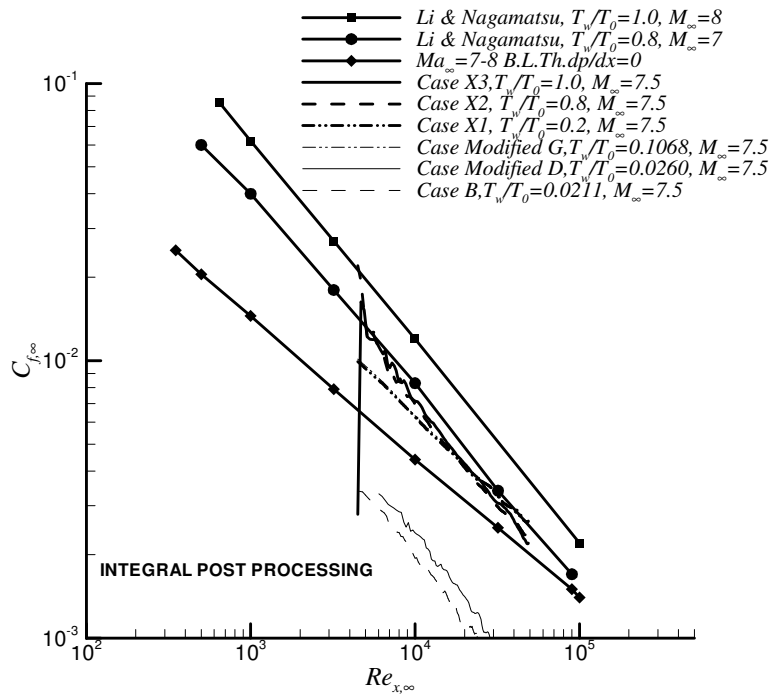


**Figure 8.98** Effect of  $T_w/T_0$  on skin friction coefficient.

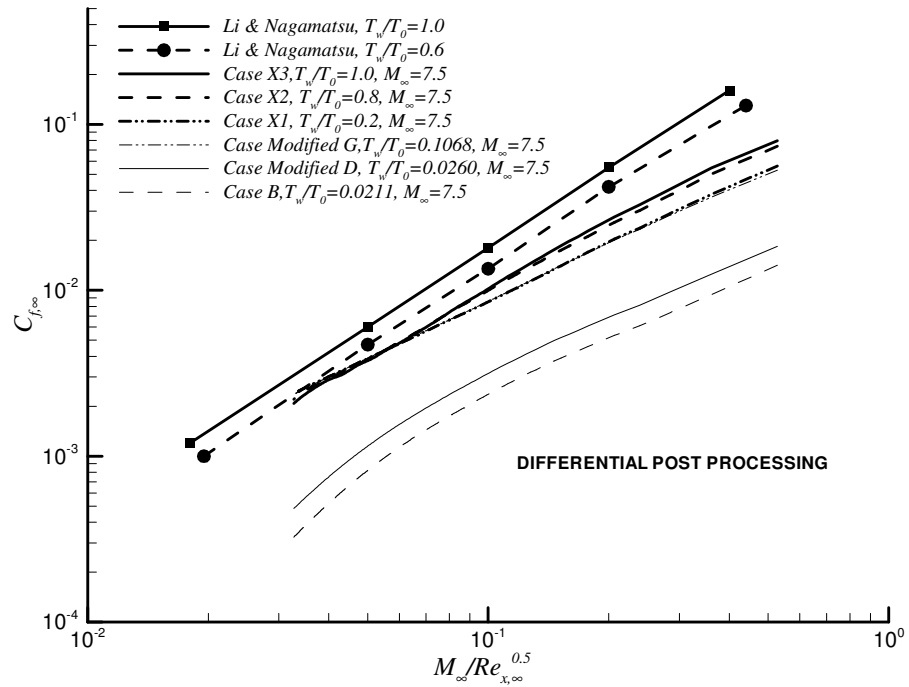


Figure 8.99 Effect of  $T_w/T_0$  on skin friction coefficient.

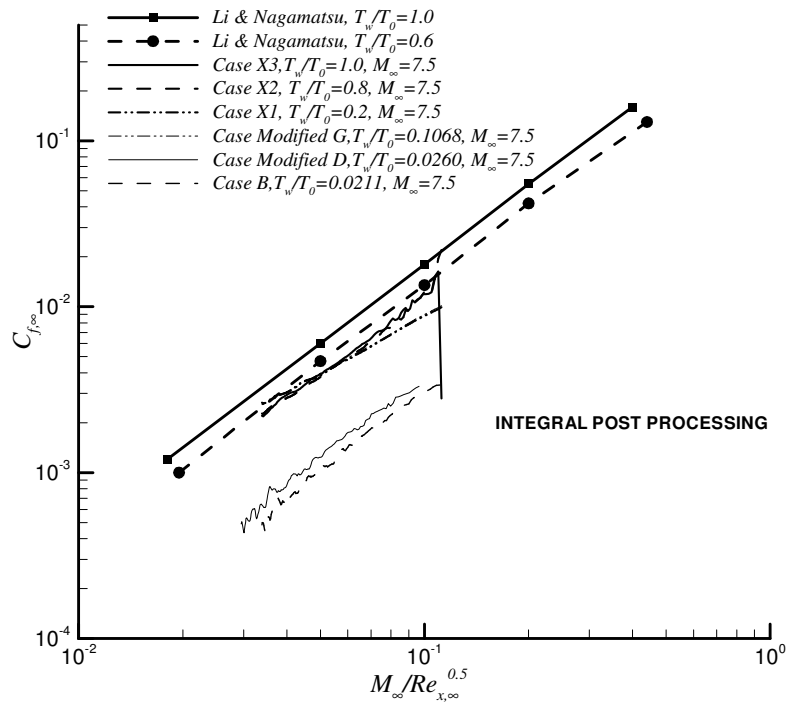
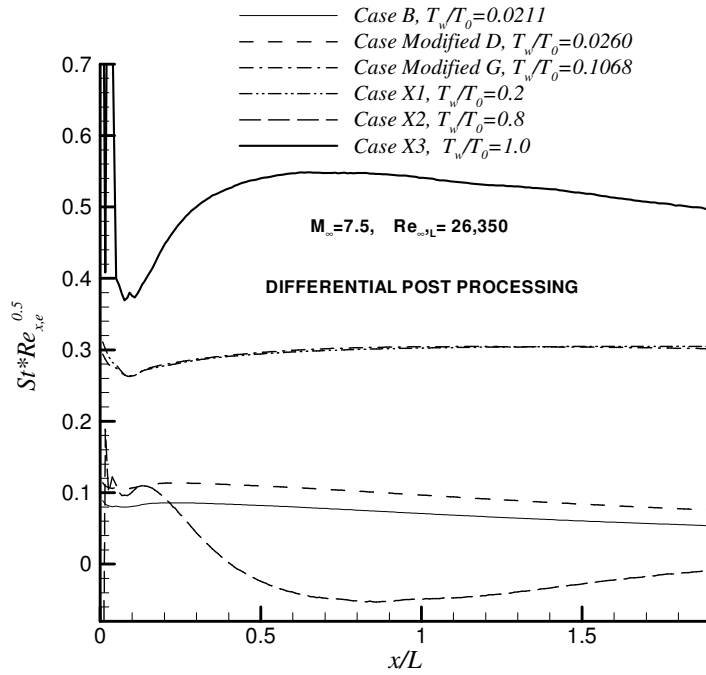
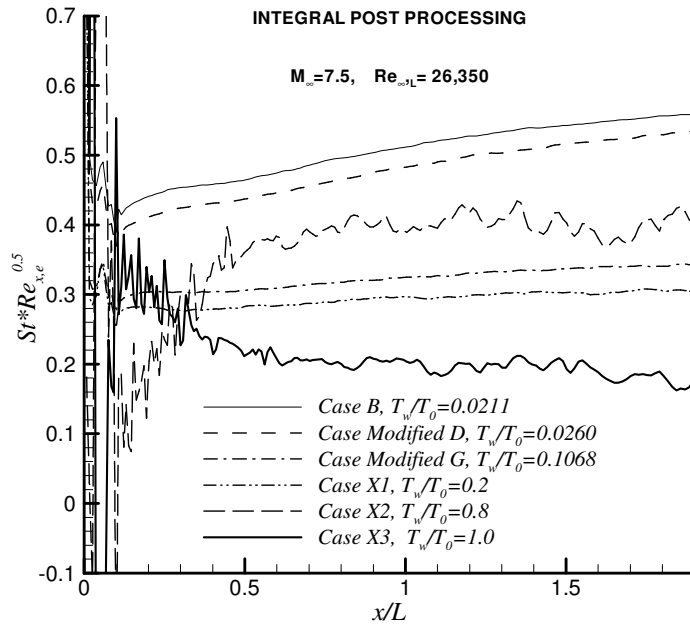


Figure 8.100 Effect of  $T_w/T_0$  on skin friction coefficient.



**Figure 8.101** Effect of  $T_w/T_0$  on heat transfer distribution.



**Figure 8.102** Effect of  $T_w/T_0$  on heat transfer distribution.

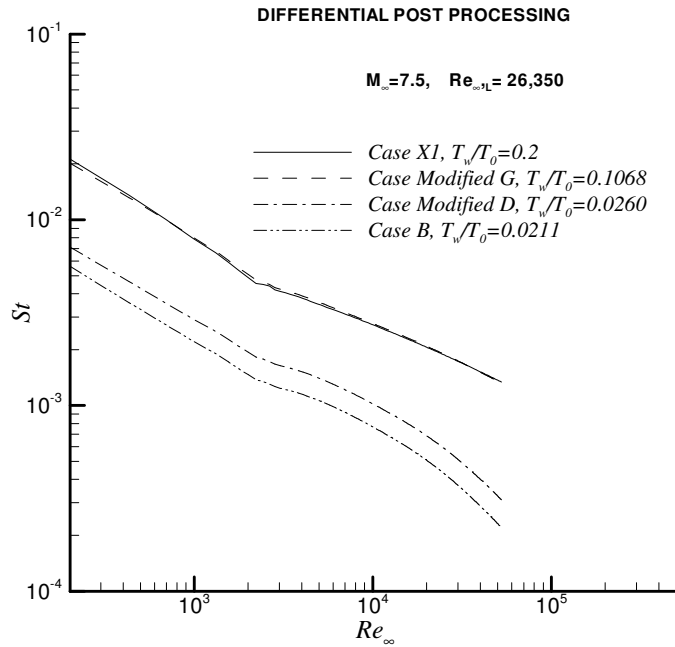


**Figure 8.103** Effect of  $T_w/T_0$  on heat transfer distribution.

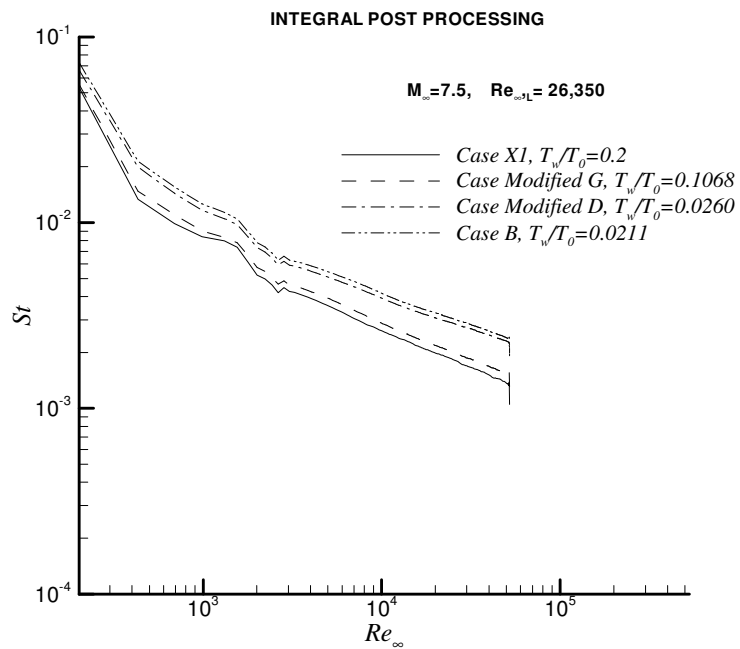


**Figure 8.104** Effect of  $T_w/T_0$  on heat transfer distribution.

## 8.2 HYPERSONIC COMPRESSION CORNER FLOWS

The obtained numerical results of laminar, hypersonic flows over seven different compression corners with  $\theta_w = 5^\circ, 10^\circ, 14^\circ, 15^\circ, 16^\circ, 18^\circ, 24^\circ$  will be presented and discussed in this section. During the analysis, eight different free-stream and wall conditions (flow conditions or test cases) are selected: three of those test cases corresponds to the experiments and numerical studies of Mallinson et al. [8] and these conditions are referred to as B, D, G by Mallinson et al [8]. The Case X1, X2 and X3, are chosen according to the  $T_w/T_0$  values to investigate the effect of the  $T_w/T_0$  on the flow variables, boundary layer variables etc. The Cases Modified D and Modified G are corresponded Case D and G of Mallinson et al. [8] with the differences of  $M_\infty$  and  $Re_\infty$ . For test cases Modified D, Modified G, X1, X2 and X3; the numerical solutions are performed over  $14^\circ, 18^\circ$  and  $24^\circ$  compression corners, only.

### 8.2.1. Post Processing and Theoretical Knowledge for Comparisons

The post processing on numerical solutions of compression corners are same with flat plate post processing for boundary layer flow variables and pressure distributions.

The heat transfer rate distributions over the compression corners are compared with the available experimental data [8] and Stollery & Bates [61] laminar perfect gas theory for the selected cases. The Stollery & Bates theory results presented here are taken from Ref. [8] and are plotted after being multiplied by the factor  $\{1 - h_{chem}/(h_r - h_w)\}$  in order to consider the effect of dissociated species in the free stream [8].

The Stanton number is defined as [8]:

$$St = \frac{q_w}{\rho_e U_e (h_r - h_w)} \quad (18)$$

After the numerical analysis, the heat transfer distribution is calculated from the integral energy equation [57];

$$St = \frac{q_w}{\rho_e U_e (h_r - h_w)} = \frac{\frac{d}{dx}(f(x))}{g(x)} \quad (19)$$

where  $f(x)$  is

$$f(x) = \left[ \int_0^\infty \bar{\rho} \bar{U} \left\{ \left( \frac{\gamma}{\gamma-1} \right) \left( \frac{\bar{p}}{\bar{\rho}} - \frac{\bar{p}_\infty}{\bar{\rho}_\infty} \right) + \frac{1}{2} (\bar{U}^2 - \bar{M}_\infty^2) \right\} dy \right]$$

$$q_w = \frac{d}{dx}(f(x)) = \frac{d}{dx} \left[ \int_0^\infty \bar{\rho} \bar{U} \left\{ \left( \frac{\gamma}{\gamma-1} \right) \left( \frac{\bar{p}}{\bar{\rho}} - \frac{\bar{p}_\infty}{\bar{\rho}_\infty} \right) + \frac{1}{2} (\bar{U}^2 - \bar{M}_\infty^2) \right\} dy \right] \quad (21)$$

where

$$g(x) = \bar{\rho}_e \bar{U}_e \left[ \frac{\gamma}{\gamma-1} \left( \frac{\bar{p}_\infty}{\bar{\rho}_\infty} - \frac{\bar{p}_w}{\bar{\rho}_w} \right) + 0.5 (M_\infty^2 + (\text{Pr}^{*1/2} - 1) \bar{U}_e^2) \right]$$

Details of the applied post processing are given in Appendix B, C and D.

## 8.2.2. Computational Details

The computations are carried out on Nautilus System at METU. Rorqual machine was used as a host and cases are given as job to various Nautilus Central Processing Units. (CPU)

Nautilus is an IBM Scalable POWER parallel 2 (SP2). SP2 system frame houses 8 wide nodes. The each wide node has 67 MHZ CPU with Power2 processors and 128 MB memory.

In the present study, 138,000 points (230\*3\*200) are used for the flat plate grid.

The computations are started from freestream conditions. A slow start of boundary conditions is implemented for 30 iterations from the starting point. The calculations are continued until a steady state solution is obtained. 15,000 iterations is considered to be sufficient for this.

For 15,000 iterations:

**Table 8.2** Computational Details of 14° Compression Corner Flows

Test Case	Real Time	CPU Time	Memory
Case B	13 h. 11 min	13h. 12 min	16 M
D	13 h. 12 min	13h. 13 min	16 M
Modified D	13 h. 24 min.	13 h. 23 min.	16 M
G	13 h. 32 min.	13 h. 30 min.	16 M
Modified G	13 h. 35 min.	13 h. 33 min.	16 M
X1	13 h. 19 min.	13 h. 18 min.	16 M
X2	13 h. 26 min.	13 h. 25 min.	16 M
X3	13 h. 24 min.	13 h. 21 min.	16 M

An Implicit smoothing constant ( $\epsilon_i$ ) of 1.0 and an explicit smoothing constant ( $\epsilon_e$ ) of 1.0 are used, respectively. The reservoir and freestream flow conditions of the test cases are shown in Table 6.1. Prandtl number is 0.72 for the laminar solution. The selected Courant numbers for different iteration intervals are given below:

$$1 < N < 5.000, \text{ CNBR} = 0.1$$

$$5.000 < N < 10.000, \text{ CNBR} = 0.5$$

$$10.000 < N < 15.000, \text{ CNBR} = 1.0$$

Air composition was assumed to be 21% oxygen and 79% nitrogen. The high level of atomic Oxygen which existed in the experimental case was ignored.

A decrease by at least three orders of magnitude in residual error is a criterion for convergence. A typical convergence and iteration history is shown in Figure 8.105 for  $\theta_w = 14^\circ$ , Case B as an example. The iterations are continued until the number of iterations reached 15,000.

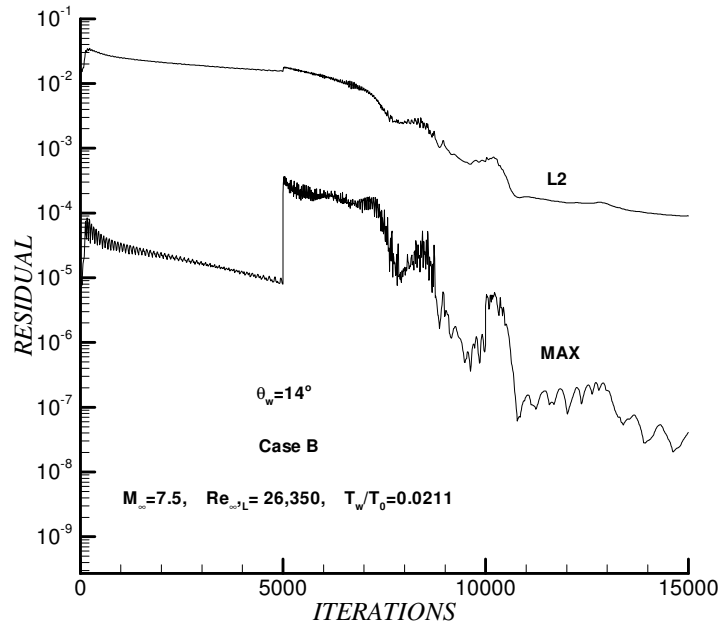


**Figure 8.105** Convergence and iteration history,  $\theta_w=14^\circ$ , Case B.

### 8.2.3. General Results

In this part of the chapter, the general results for  $\theta_w=14^\circ$  Case B, with flow parameters  $M_\infty=7.5$ ,  $Re_{\infty,L}=26,350$  and  $T_w/T_0=0.0211$ , are presented.

The Mach contours and streamline distributions for the selected case are shown in Figure 8.106. and Figure 8.107, respectively. It can be seen from Mach contours that there is strong interaction between boundary layer and leading edge shock around the corner region in accordance with oblique shock theory.

The shock wave from the corner interacts with the flat-plate boundary layer some distance upstream of the corner. For sufficiently strong shocks, the flow separates and a recirculating region is formed. As the flow reattaches, the boundary layer thickness is reduced and a reattachment shock is formed due to the coalescence of the compression waves. It was predicted that the flow is an attached flow.

In Figure 8.108, boundary layer thicknesses are shown for  $\theta_w=14^\circ$  Case B. In this figure, the leading edge shock due to the boundary layer displacement thickness effect is seen.  $\delta_T$ , is the thermal boundary layer thickness,  $\delta$ , is the boundary layer thickness,  $\delta^*$ , is the displacement thickness,  $\delta_{T,max}$ , is the location of maximum temperature inside the boundary layer, and  $\theta$  is the momentum thickness. In a direction normal to surface, between the leading edge shock and the boundary layer, the flow properties are not constant due to a slight expansion. Since, the flow variables are not constant between the edge of the boundary layer and the shock, determination of the boundary layer edge requires special care. Thermal boundary layer is thicker than the momentum boundary layer and edge variables ( $U_e$ ,  $T_e$ , etc.) are obtained at the thermal boundary layer edge.

The number of grid points in the boundary layer during the numerical solution is very important to get reliable results. In Figure 8.109, number of grid points distribution for  $\theta_w=14^\circ$  Case B is shown. For this case at the average, there are about 70 grid points in the boundary layer.

Typical velocity, temperature, Mach number and a heat transfer parameter ( $f_{qw}$ ), distributions inside the boundary layer are shown for  $\theta_w=14^\circ$  Case B in Figure 8.110 to 8.112 at the flat plate part of the compression corner,  $x/L=0.5$ , at the corner region,  $x/L=1.0$ , and at the mid-point of ramp surfaces,  $x/L=2.0$ , respectively. It can be seen that  $f_{qw}$  makes a small maximum before it goes to zero asymptotically at the edge of the thermal boundary layer. This small maximum is used as criteria to locate the edge of the thermal boundary layer, thus the edge conditions, in the present study.

The boundary layer edge variables; distributions of Reynolds number, Mach number, temperature, density, velocity and viscosity at the edge of the boundary layer at mid-point of the flat plate are shown in Figure 8.113 for Case  $\theta_w=14^\circ$  B. It can be seen clearly that the boundary layer variables do not converge a constant value due to slight expansion as mentioned above.

In Figure 8.114 shows the distribution of various temperatures along the boundary layer for  $\theta_w=14^\circ$  Case B. The formulas for  $T_{aw}$ ,  $T^*$  and  $T_0$  are given in Section 8.1.1.

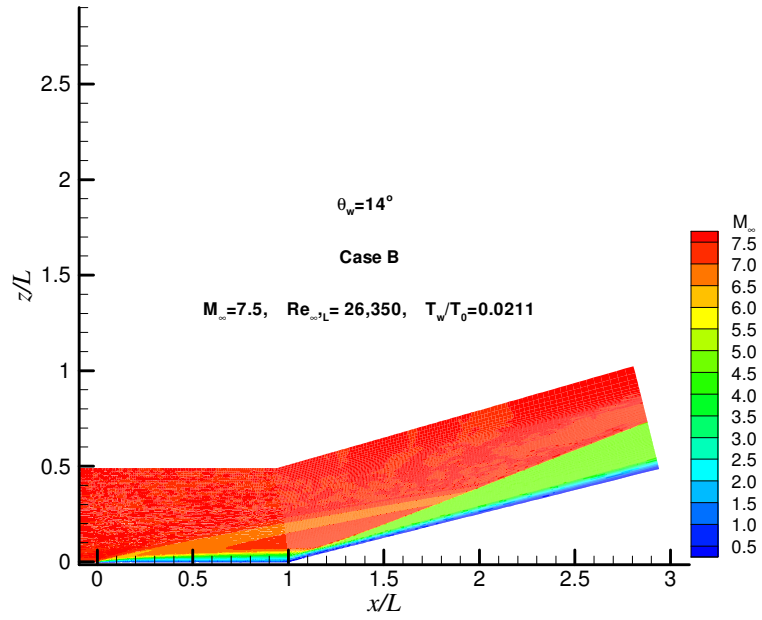


Figure 8.106 Mach contours,  $\theta_w = 14^\circ$ , Case B.

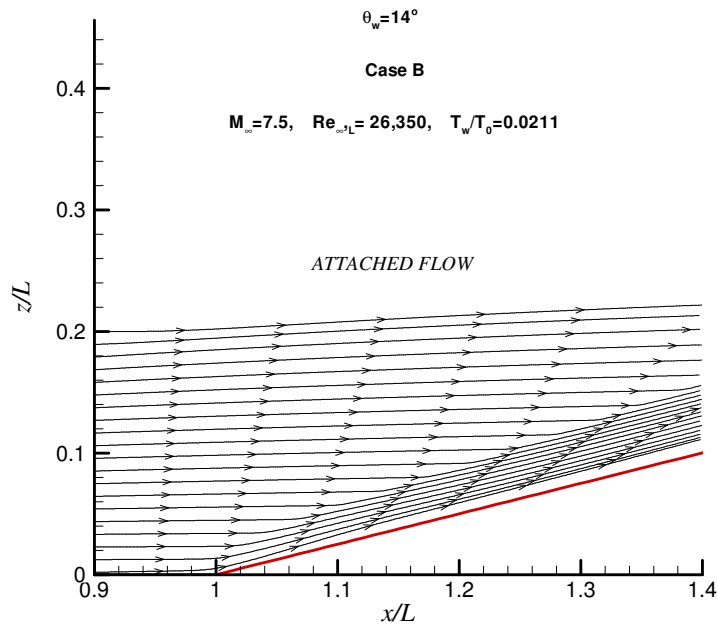


Figure 8.107 Streamlines distribution over corner region,  $\theta_w = 14^\circ$ , Case B.

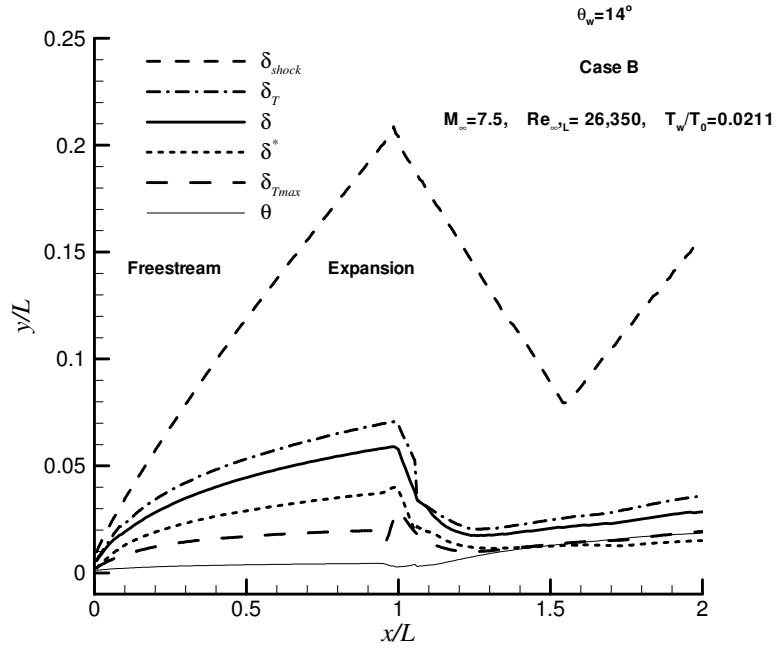


Figure 8.108 Boundary layer thicknesses,  $\theta_w = 14^\circ$ , Case B.

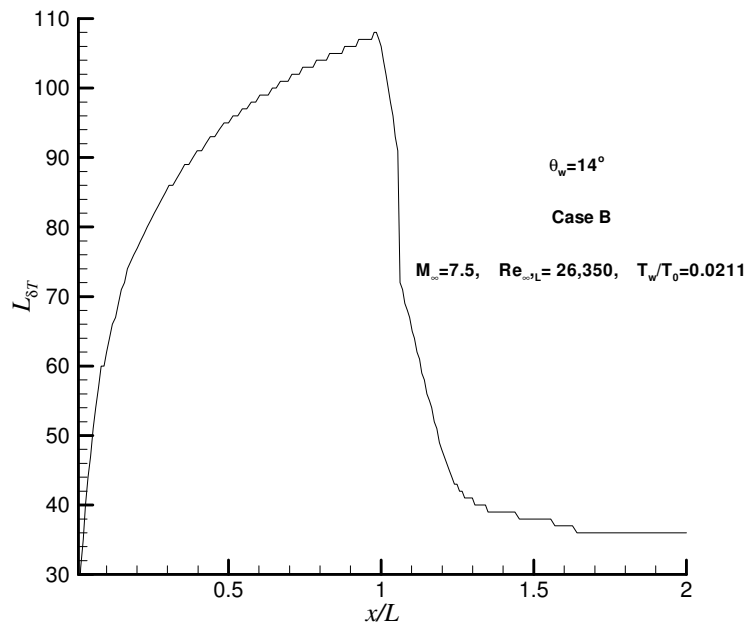
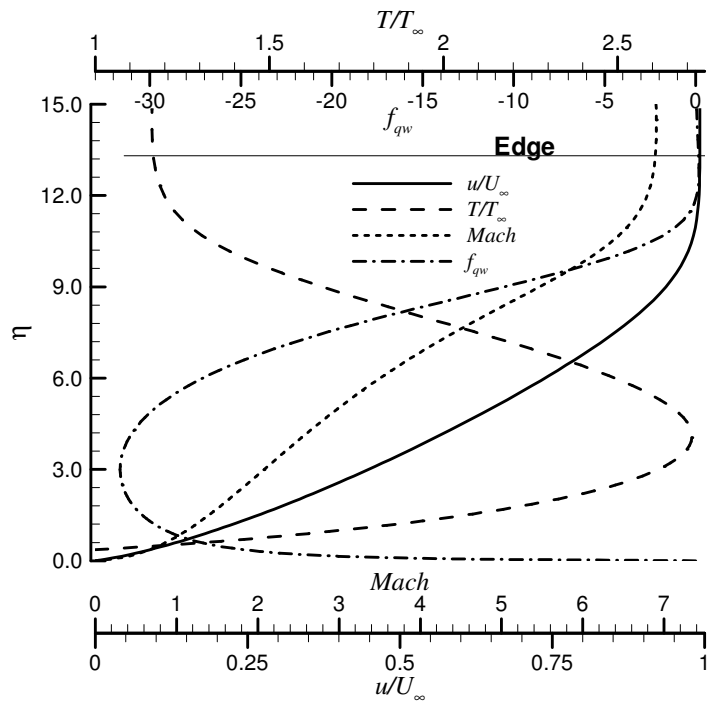


Figure 8.109 Number of grid points in the boundary layer,  $\theta_w = 14^\circ$ , Case B.



$M_\infty=7.5$

$Re_{\infty,L}=26,350$

$T_w/T_0=0.0211$

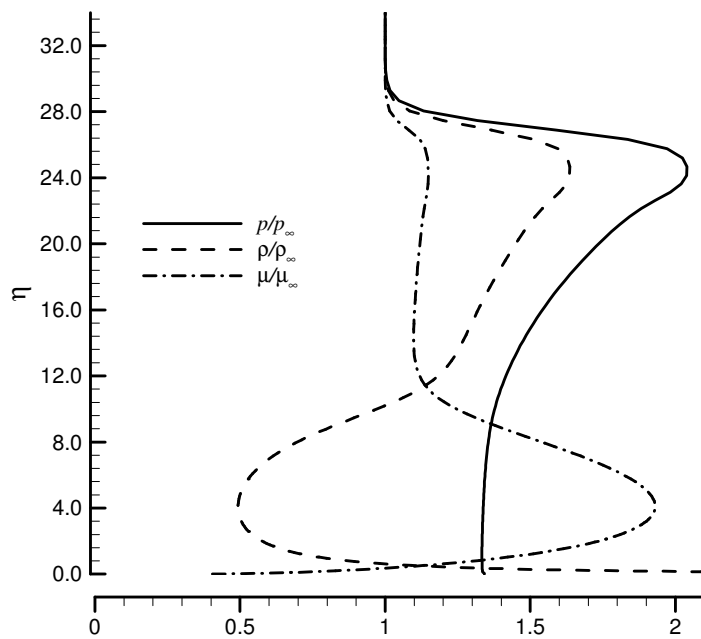


Figure 8.110 Boundary layer flow variables at  $x/L=0.5$ ,  $\theta_w=14^\circ$ , Case B.

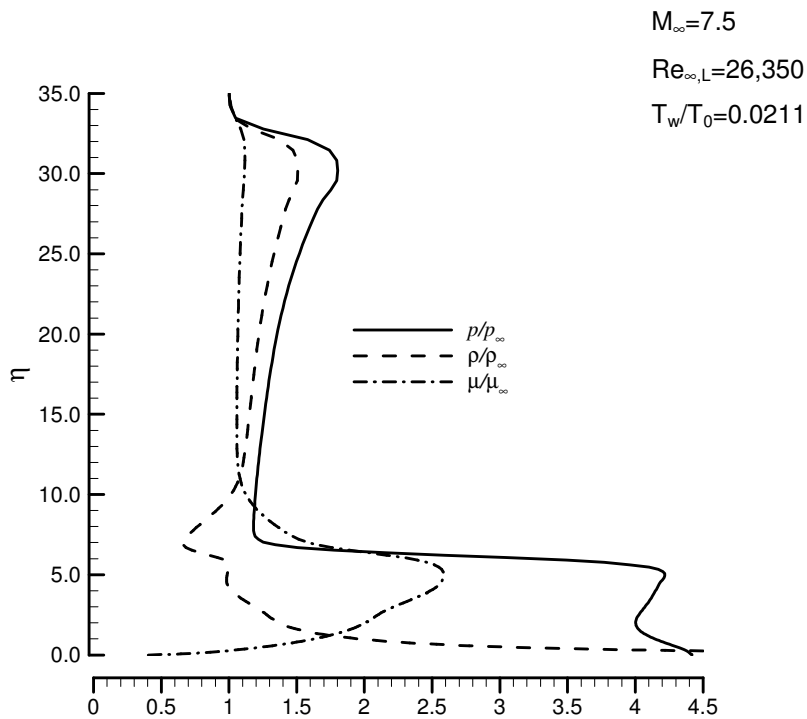
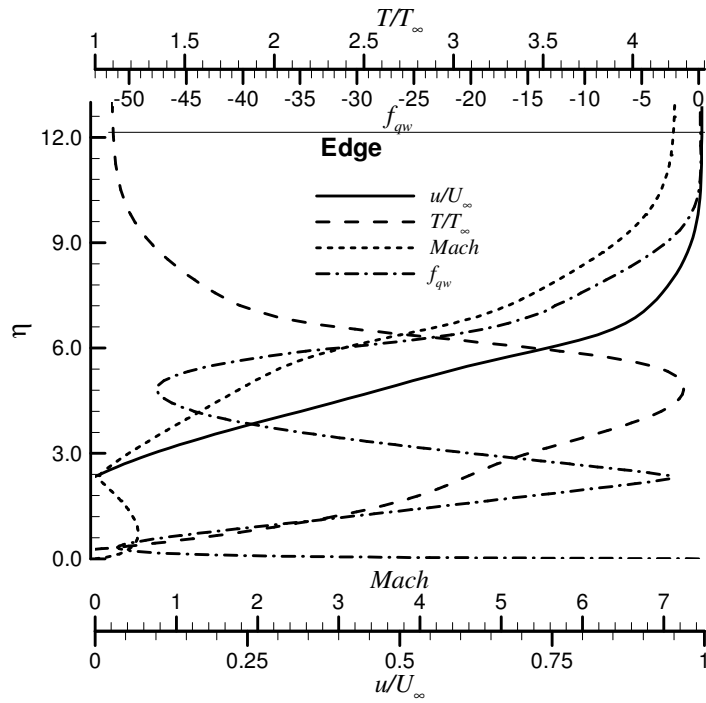
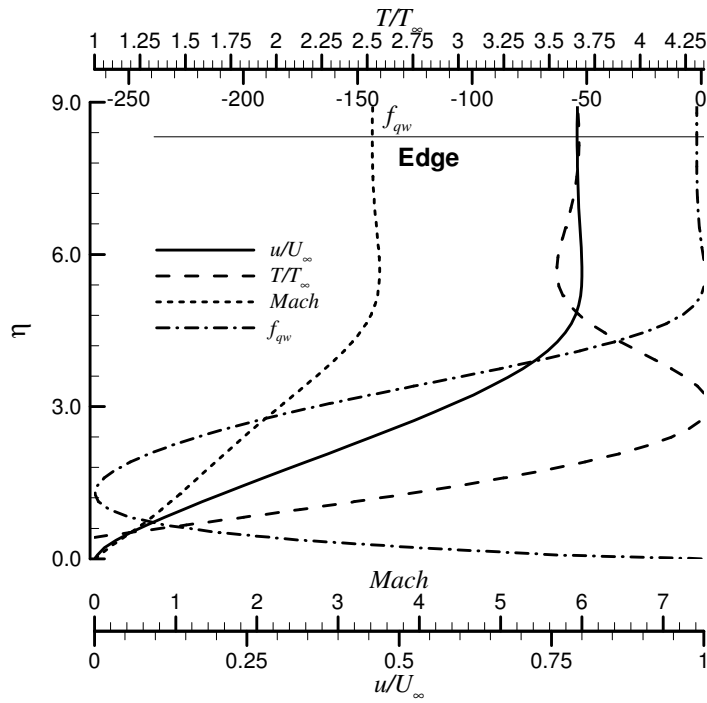


Figure 8.111 Boundary layer flow variables at  $x/L=1.0$ ,  $\theta_w=14^\circ$ , Case B.



$M_\infty=7.5$   
 $Re_{\infty,L}=26,350$   
 $T_w/T_0=0.0211$

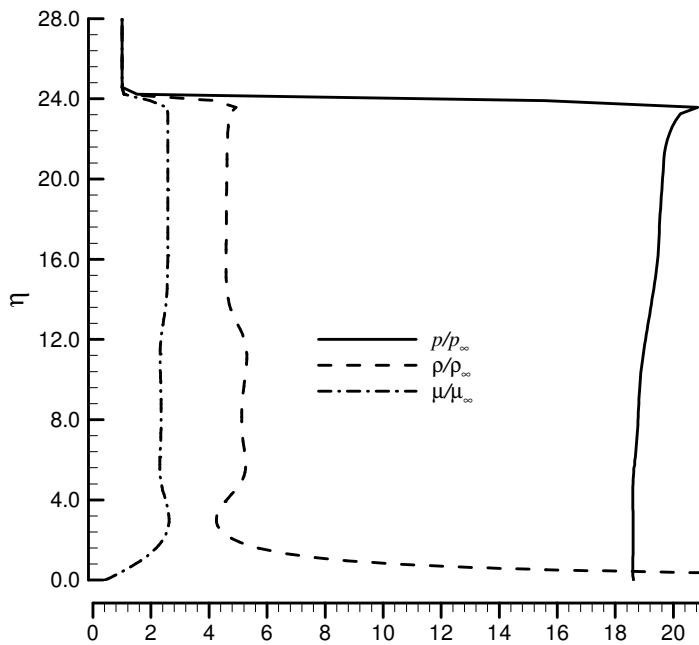


Figure 8.112 Boundary layer flow variables at  $x/L=2.0$ ,  $\theta_w=14^\circ$ , Case B.

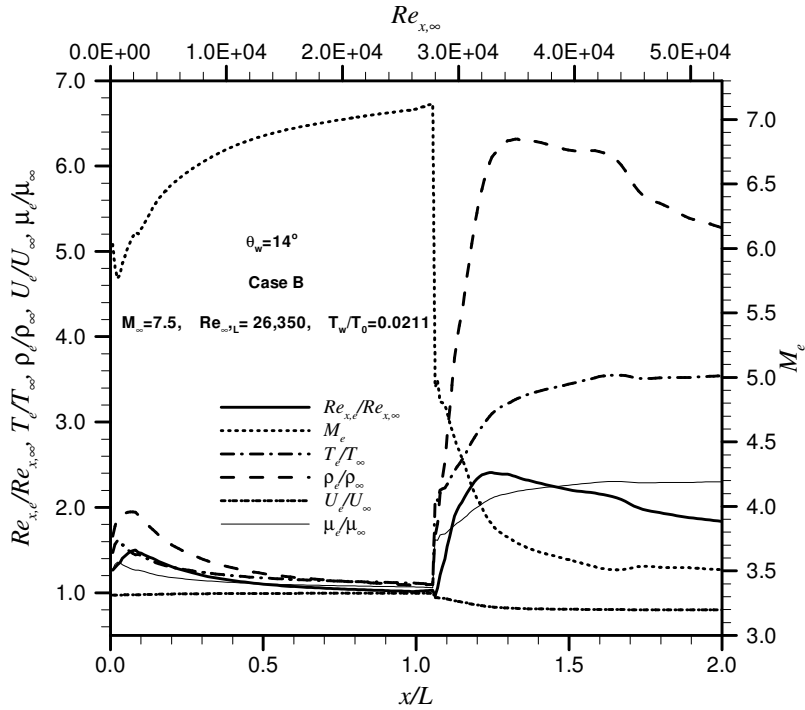


Figure 8.113 Boundary layer edge variables,  $\theta_w=14^\circ$ , Case B.

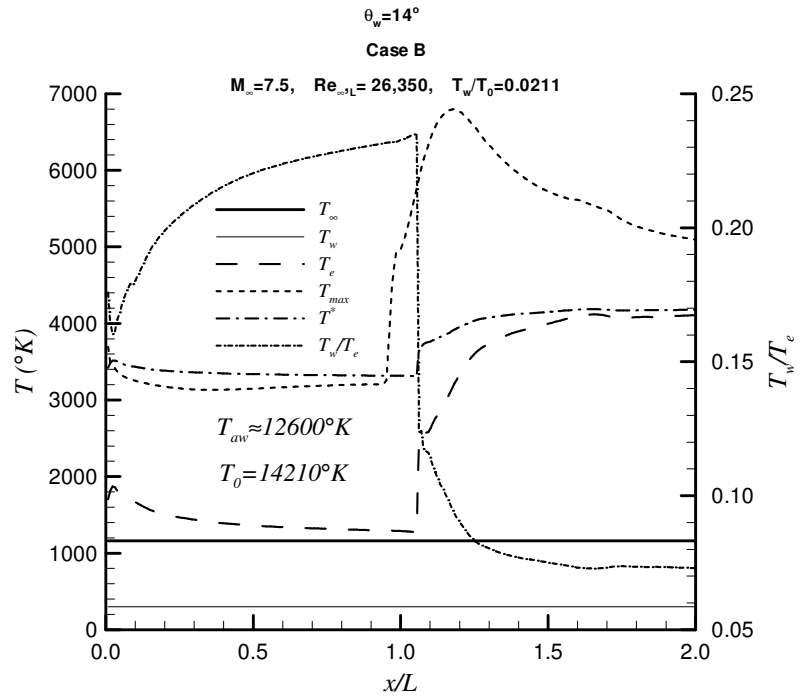


Figure 8.114 Temperature distributions along the boundary layer,  $\theta_w=14^\circ$ , Case B.

#### 8.2.4. Results of the Code Validation Study

In this section, the obtained numerical results are compared with available numerical, experimental and theoretical data.

Figures 8.115 to 8.150 show the pressure distributions over compression corners with seven corner angles  $\theta_w = 5^\circ - 24^\circ$  and for the eight cases. The obtained results are compared with available experimental data of Mallinson [8] et al, analytic solution (oblique shock theory) and Stollery & Bates [61] perfect gas theory. The analytical solution was found from the oblique shock relation for temperature ratio across the wave which is,

$$\frac{P_2}{P_1} = 1 + \frac{2\gamma}{\gamma+1} (M_1^2 \sin^2 \beta - 1)$$

The flow over  $10^\circ$  compression corner is a typical attached flow as can be seen from Figures 8.118 to 8.120. The pressure rises from the flat plate values at a small distance upstream of the corner. For  $15^\circ$  compression corner flow, Figures 8.129 to 8.131, the pressure distribution shows a small inflection near the corner, this is the result of the incipient separation. The separation and reattachment points of the flow for  $18^\circ$  and  $24^\circ$  compression corners are seen very clearly from the pressure distributions in Figures 8.135 to 8.150. Those flows have large separated regions. It is seen that the separation region and the maxima of the pressure increases as the corner angle is increased [57, 62, 63, 64]. There is strong viscous interaction for all cases due to shock-wave/boundary layer interaction.

The corner angle ( $\theta_w$ ) effect on pressure distributions is shown in Figures 8.151 to 8.153 for Cases B, D and G. It is clearly seen that the peak pressure values increase as the corner angles deflected from  $\theta_w = 5^\circ - 24^\circ$  for fixed  $M_\infty$  and  $Re_\infty$ . Also, the peak pressure values increases by  $M_\infty$  and  $Re_\infty$ .

In Figures 8.154 to 8.173, the heat transfer rate distributions over the seven compression corners are compared with the available experimental data [8] and Stollery & Bates [61] laminar perfect gas theory for three different test cases. The

present Stanton number distribution was obtained from integral post processing based on edge variables. The details of Stanton number post processing is given in Appendix D.

The general shape of the heat transfer is captured up to corner regions, along the flat plate. After the reattachment point of the flow the obtained results are underestimated according to the experiment and theory. A similar discrepancy was reported by Amaratunga et al. [65] with the two-dimensional flow.

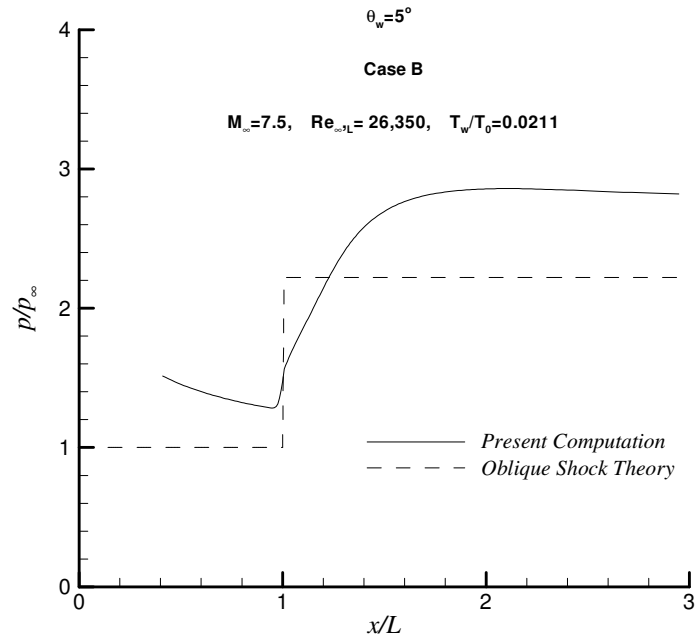


Figure 8.115 Surface pressure distribution,  $\theta_w = 5^\circ$ , Case B.

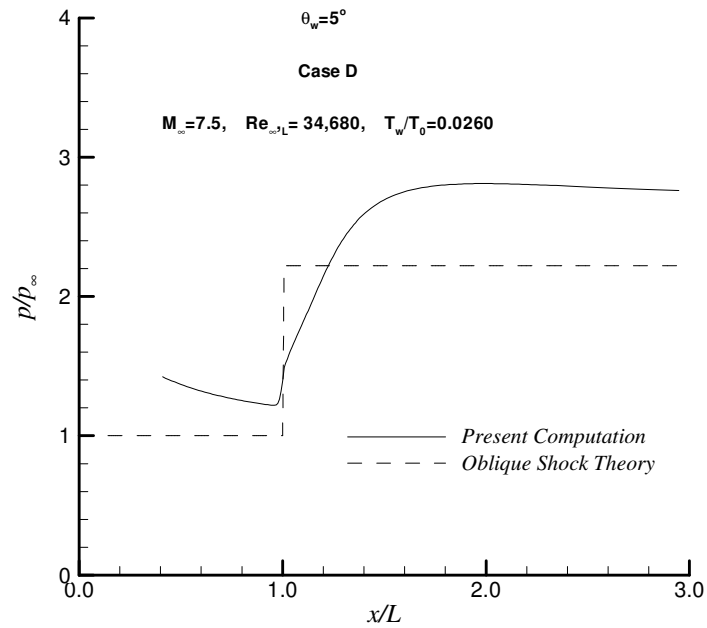


Figure 8.116 Surface pressure distribution,  $\theta_w = 5^\circ$ , Case D.

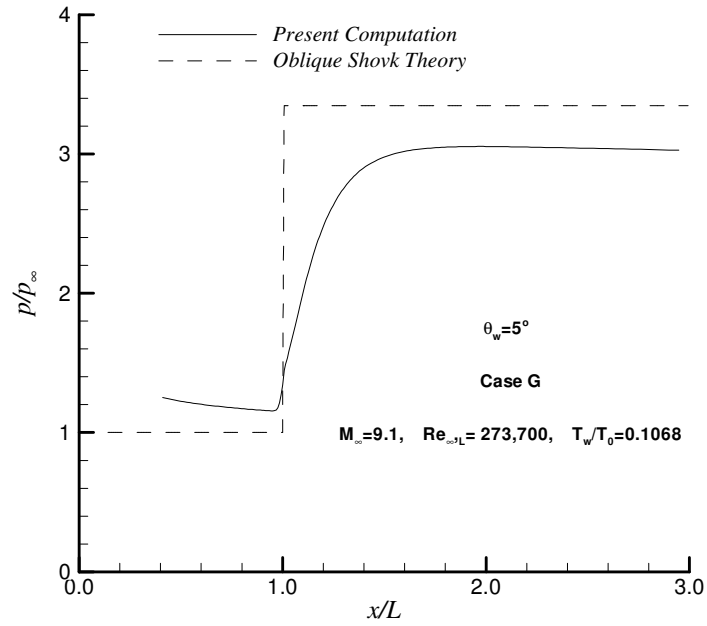


Figure 8.117 Surface pressure distribution,  $\theta_w = 5^\circ$ , Case G.

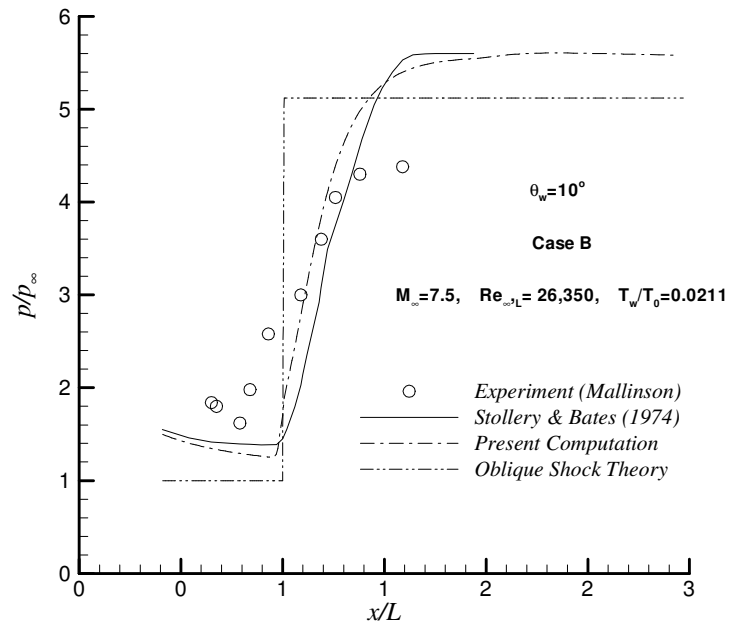


Figure 8.118 Surface pressure distribution,  $\theta_w = 10^\circ$ , Case B.

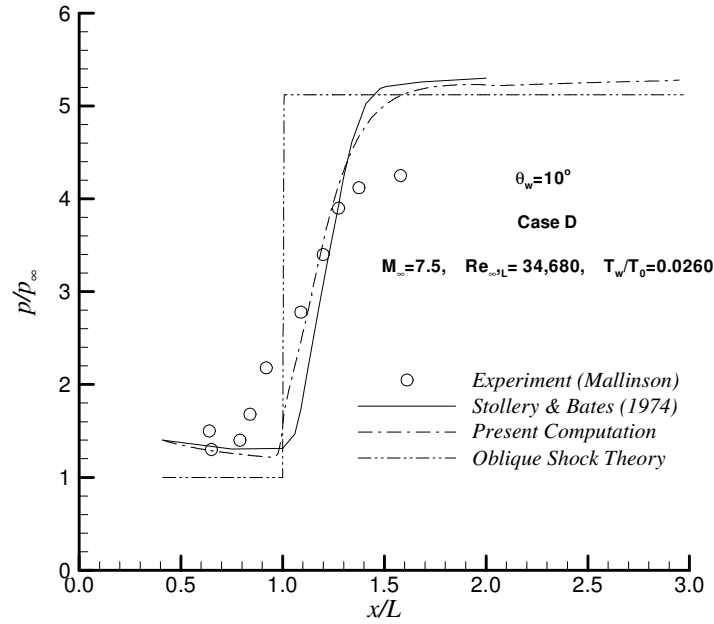


Figure 8.119 Surface pressure distribution,  $\theta_w = 10^\circ$ , Case D.

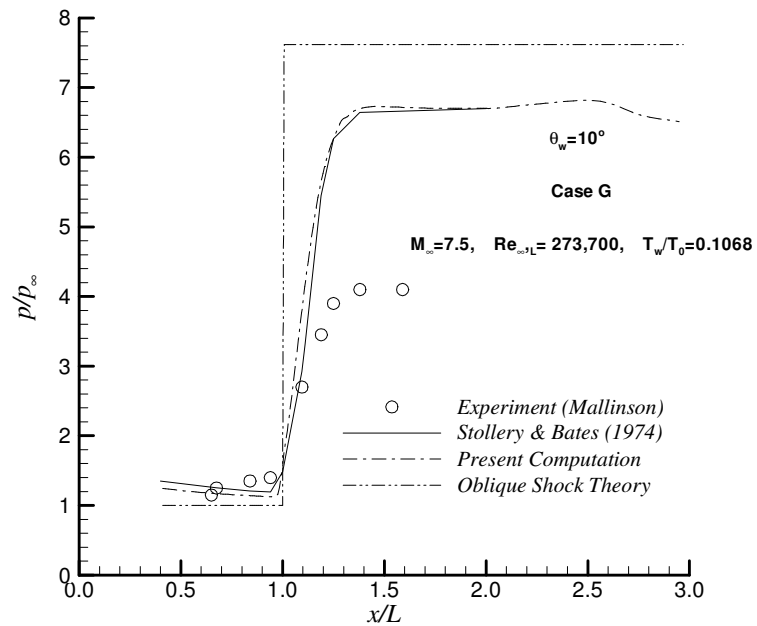
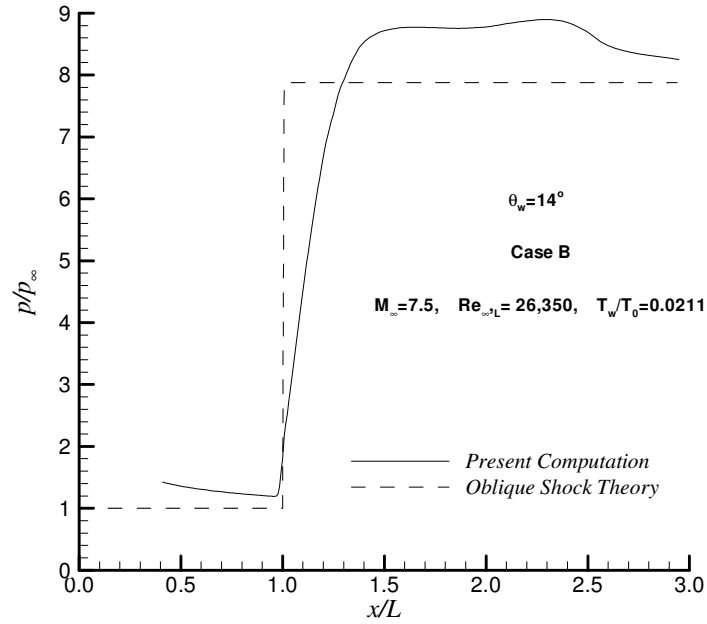
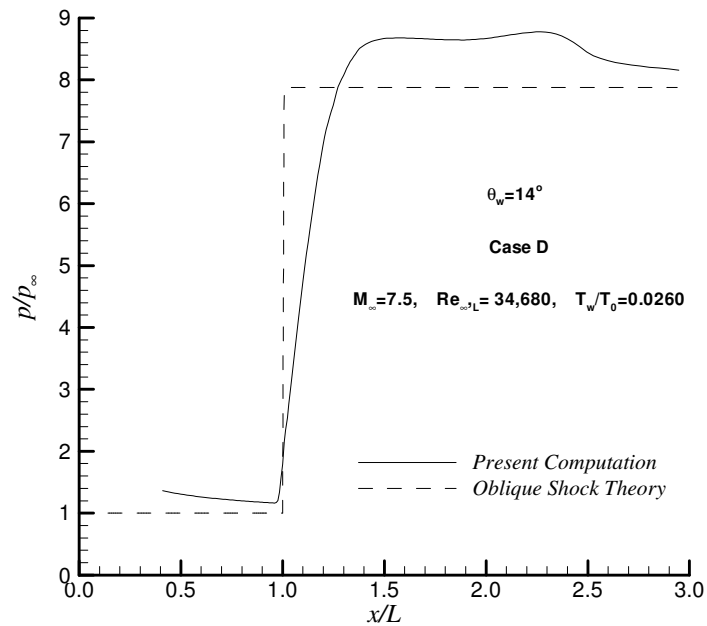


Figure 8.120 Surface pressure distribution,  $\theta_w = 10^\circ$ , Case G.



**Figure 8.121** Surface pressure distribution,  $\theta_w=14^\circ$ , Case B.



**Figure 8.122** Surface pressure distribution,  $\theta_w=14^\circ$ , Case D.

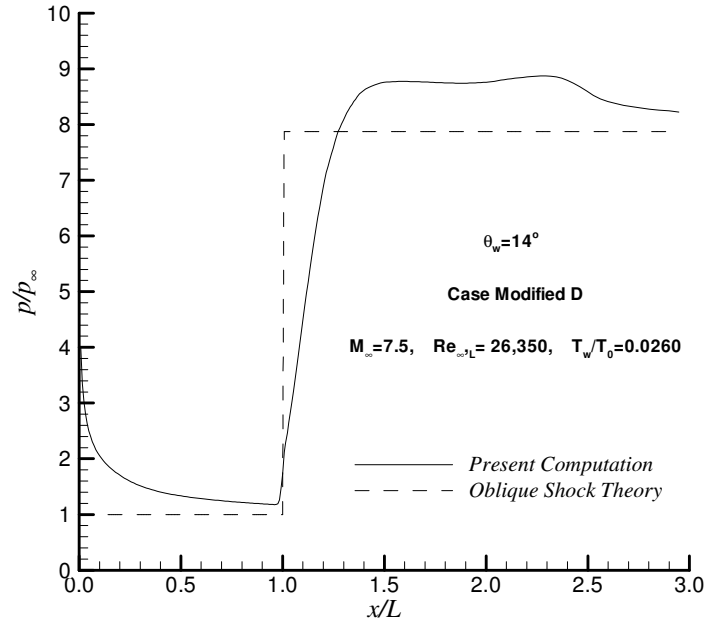


**Figure 8.123** Surface pressure distribution,  $\theta_w = 14^\circ$ , Case Modified D.

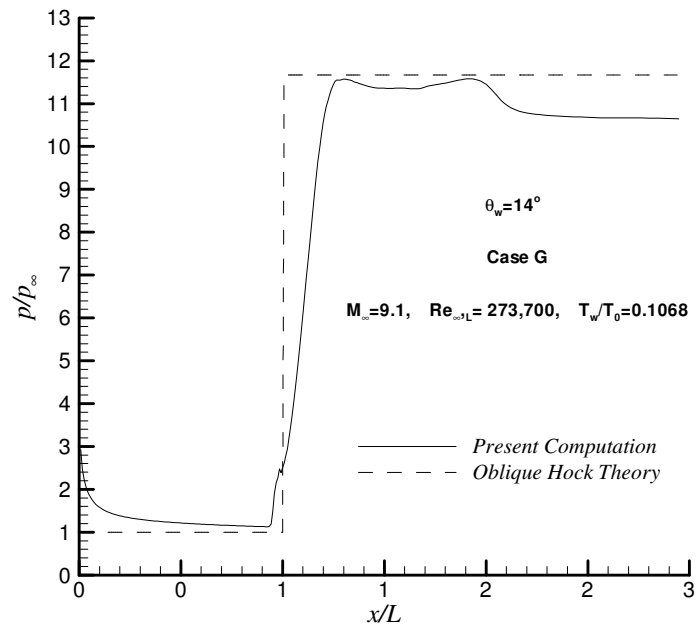


**Figure 8.124** Surface pressure distribution,  $\theta_w = 14^\circ$ , Case G.

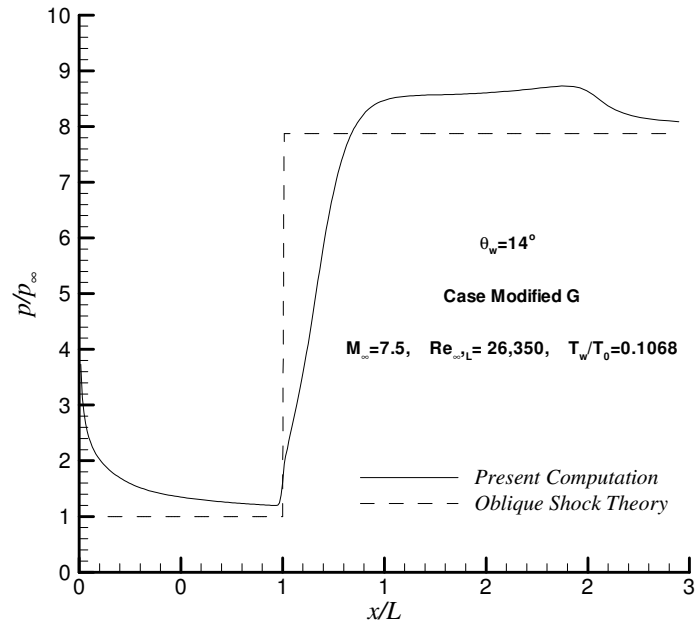


Figure 8.125 Surface pressure distribution,  $\theta_w=14^\circ$ , Case Modified G.

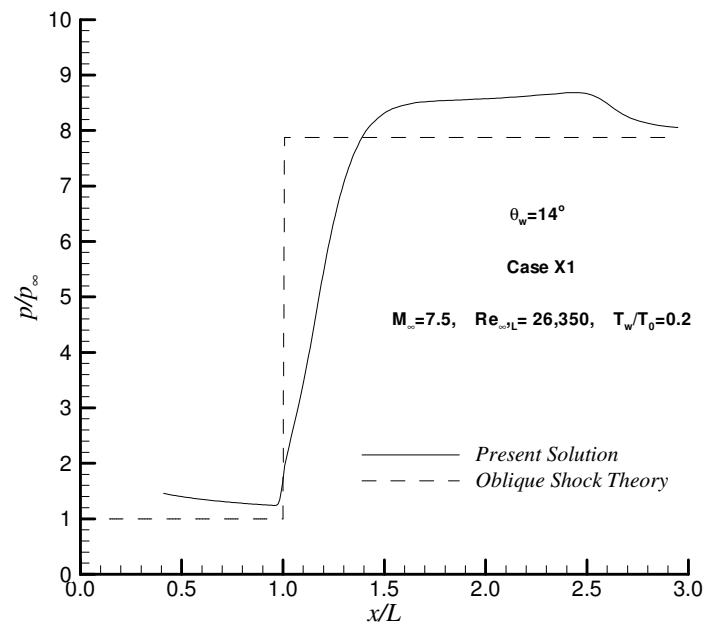


Figure 8.126 Surface pressure distribution,  $\theta_w=14^\circ$ , Case X1.

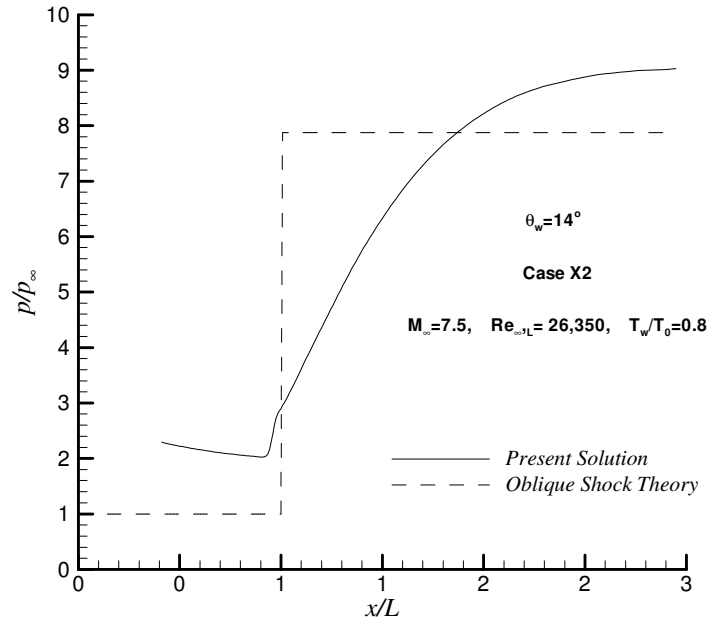


Figure 8.127 Surface pressure distribution,  $\theta_w = 14^\circ$ , Case X2.

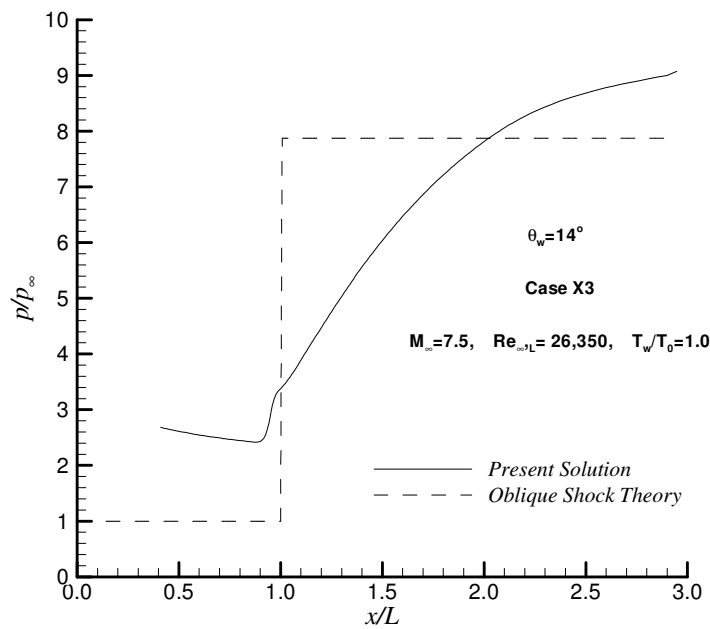


Figure 8.128 Surface pressure distribution,  $\theta_w = 14^\circ$ , Case X3.

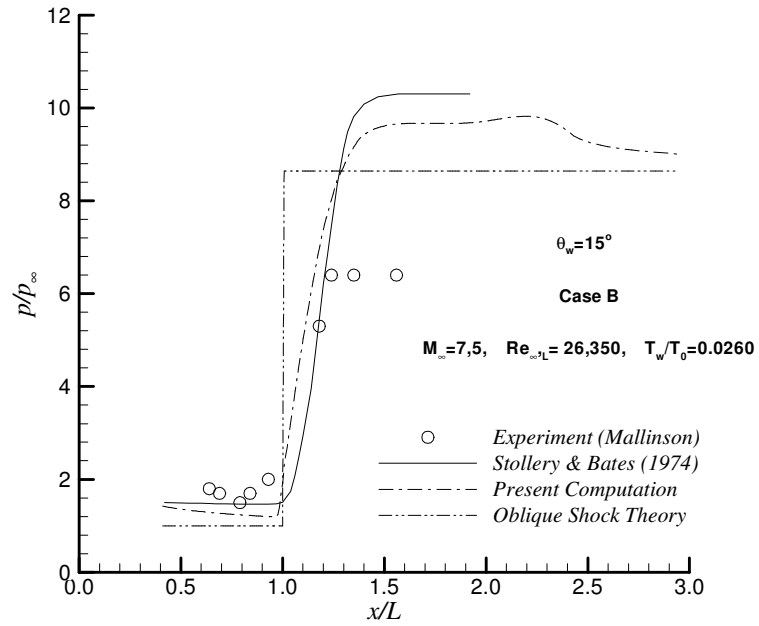


Figure 8.129 Surface pressure distribution,  $\theta_w=15^\circ$ , Case B.

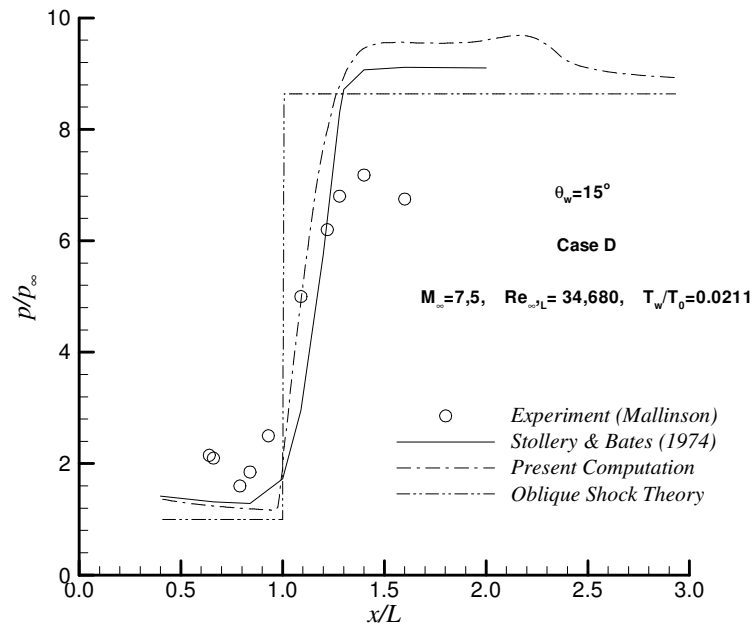
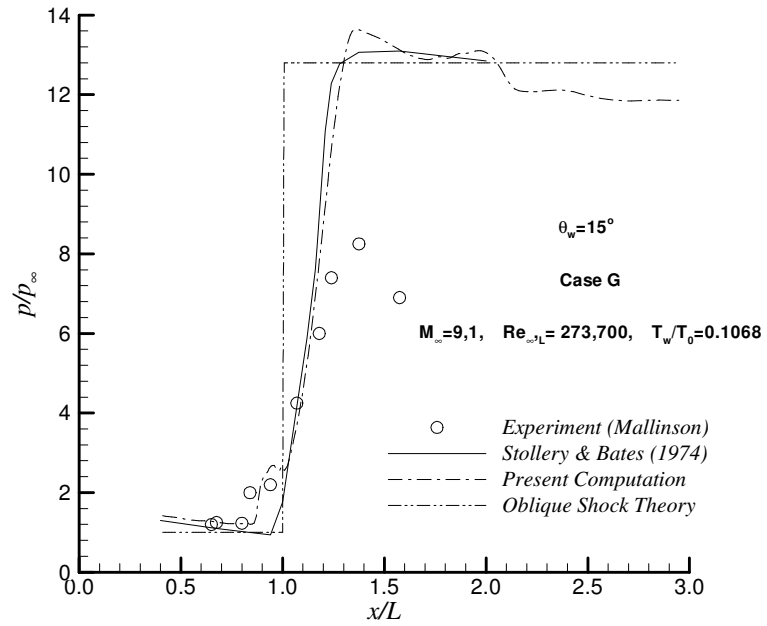
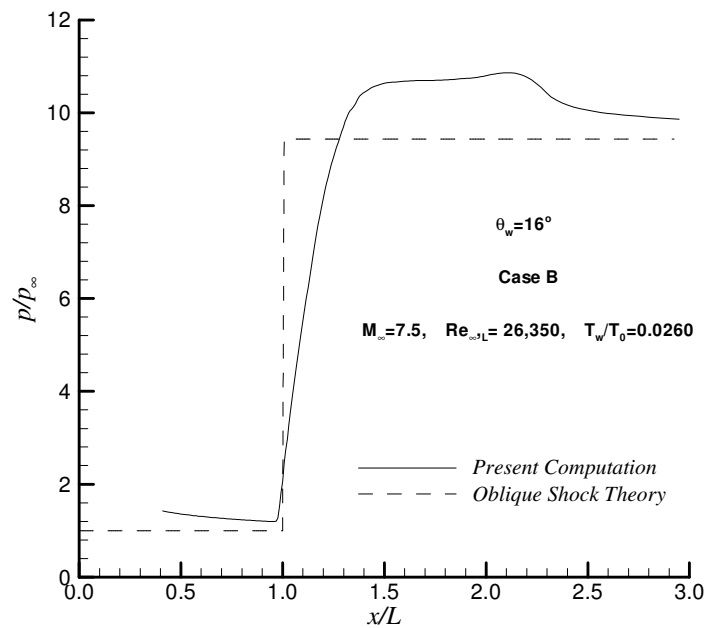


Figure 8.130 Surface pressure distribution,  $\theta_w=15^\circ$ , Case D.



**Figure 8.131** Surface pressure distribution,  $\theta_w = 15^\circ$ , Case G.



**Figure 8.132** Surface pressure distribution,  $\theta_w = 16^\circ$ , Case B.

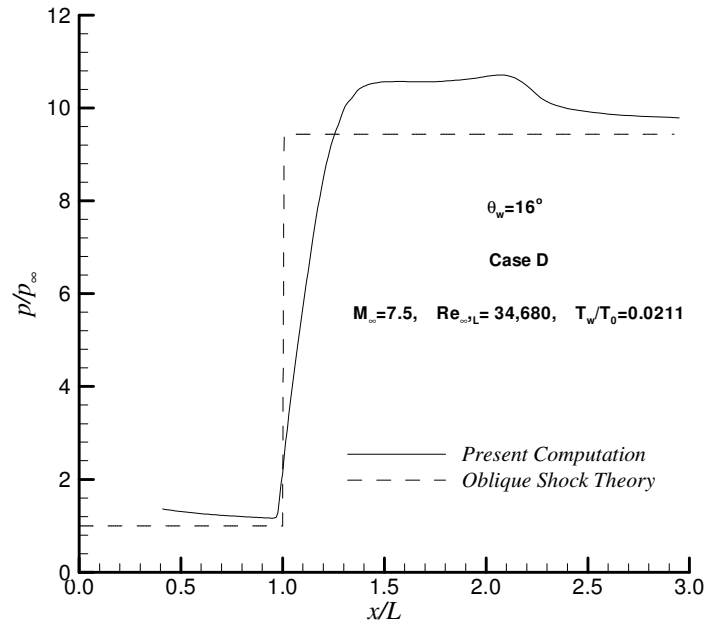


Figure 8.133 Surface pressure distribution,  $\theta_w=16^\circ$ , Case D.

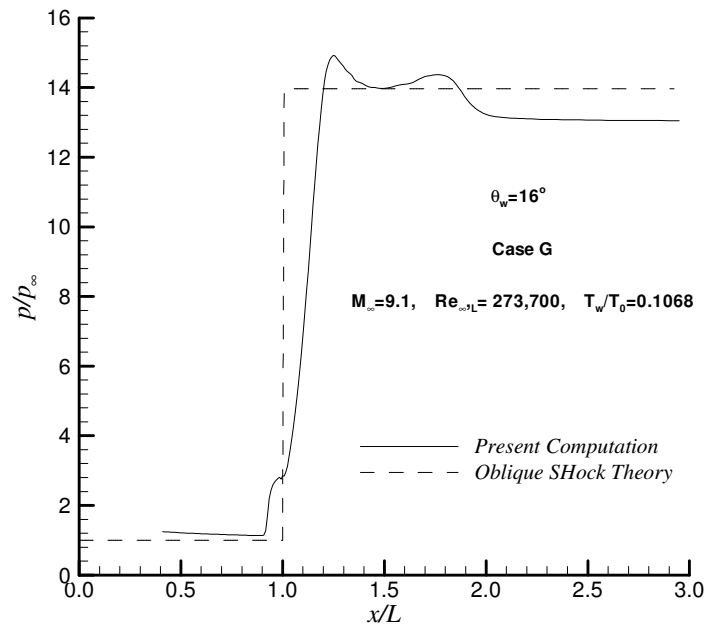


Figure 8.134 Surface pressure distribution,  $\theta_w=16^\circ$ , Case G.

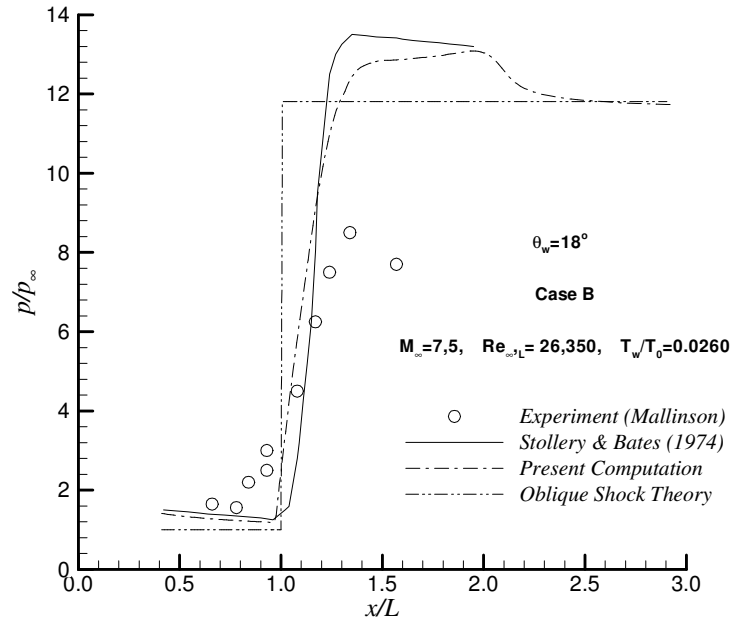


Figure 8.135 Surface pressure distribution,  $\theta_w = 18^\circ$ , Case B.

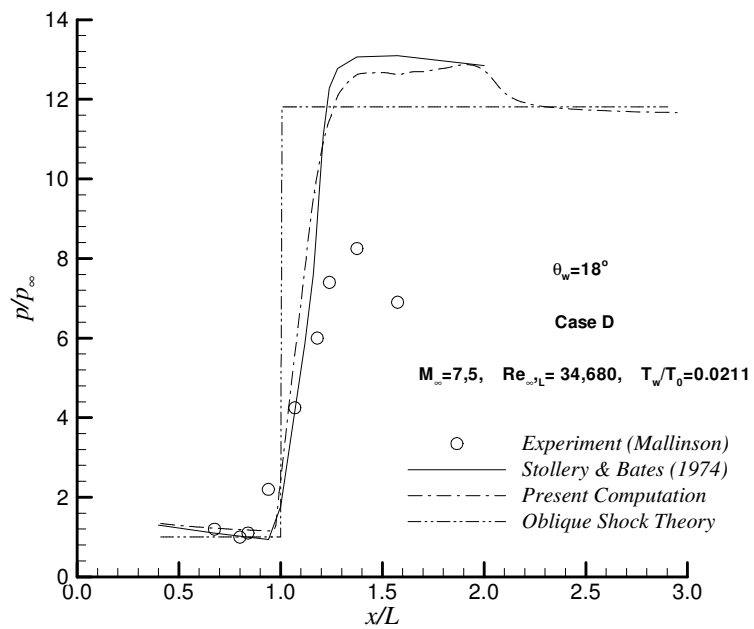
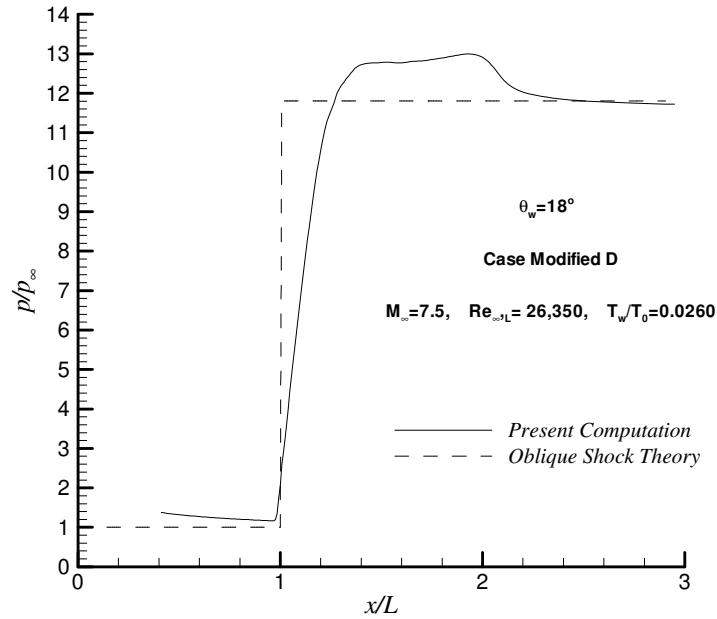
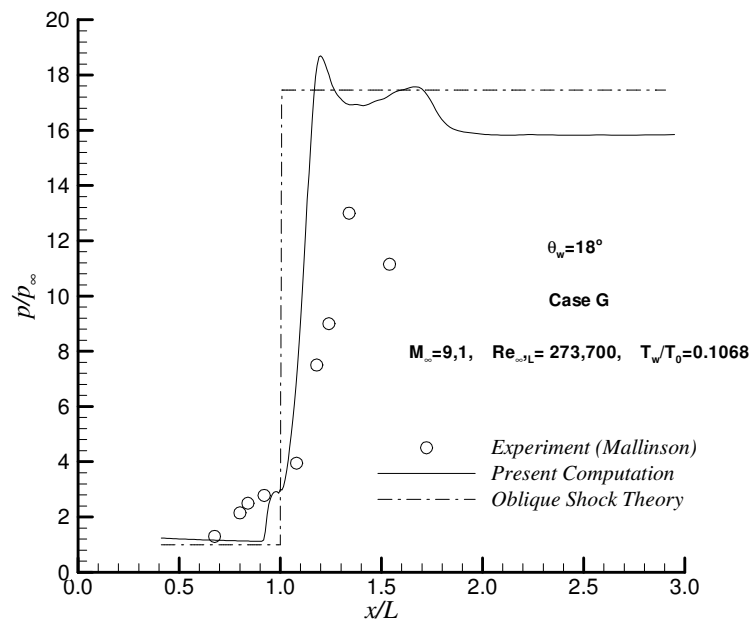


Figure 8.136 Surface pressure distribution,  $\theta_w = 18^\circ$ , Case D.



**Figure 8.137** Surface pressure distribution,  $\theta_w = 18^\circ$ , Case Modified D.



**Figure 8.138** Surface pressure distribution,  $\theta_w = 18^\circ$ , Case G.

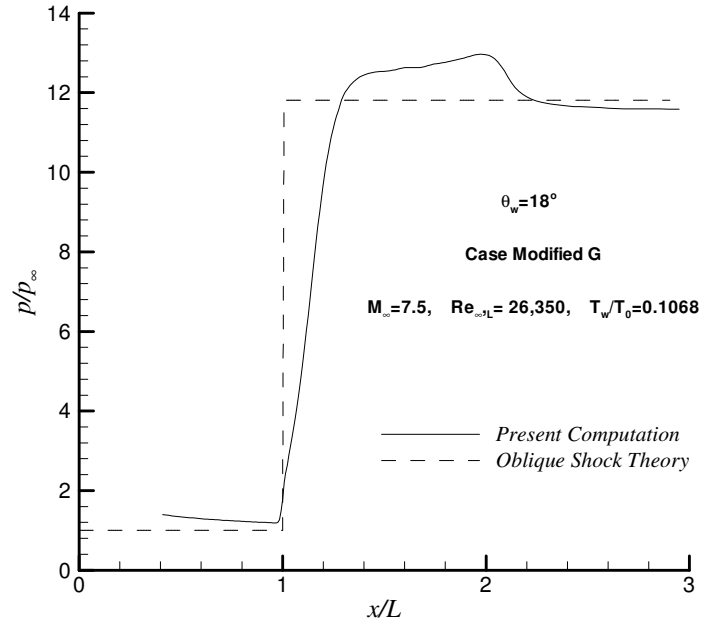


**Figure 8.139** Surface pressure distribution,  $\theta_w = 18^\circ$ , Case Modified G.

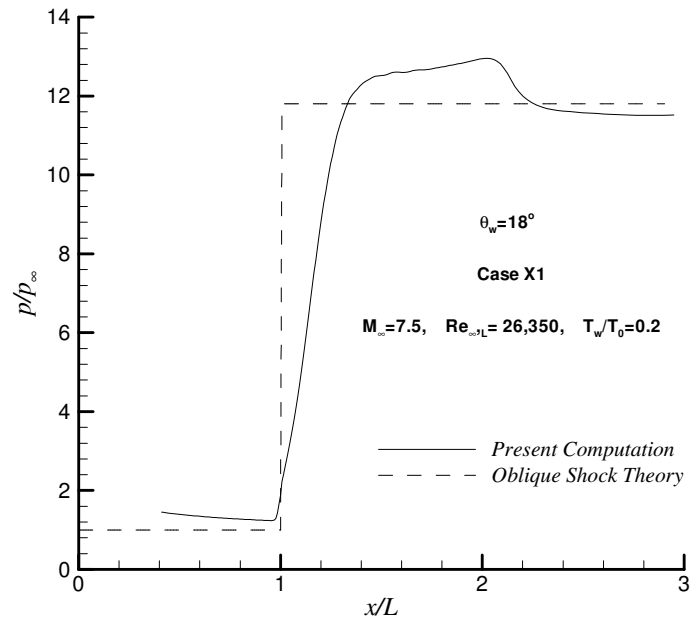


**Figure 8.140** Surface pressure distribution,  $\theta_w = 18^\circ$ , Case X1.

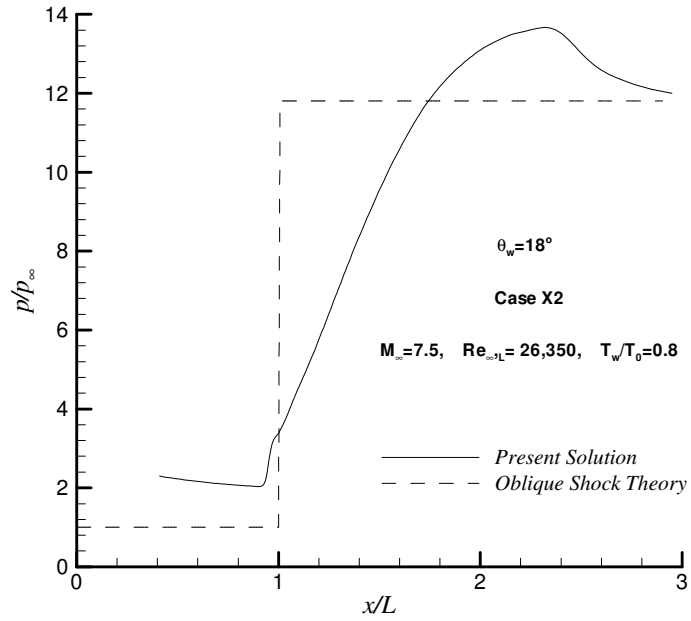


Figure 8.141 Surface pressure distribution,  $\theta_w=18^\circ$ , Case X2.

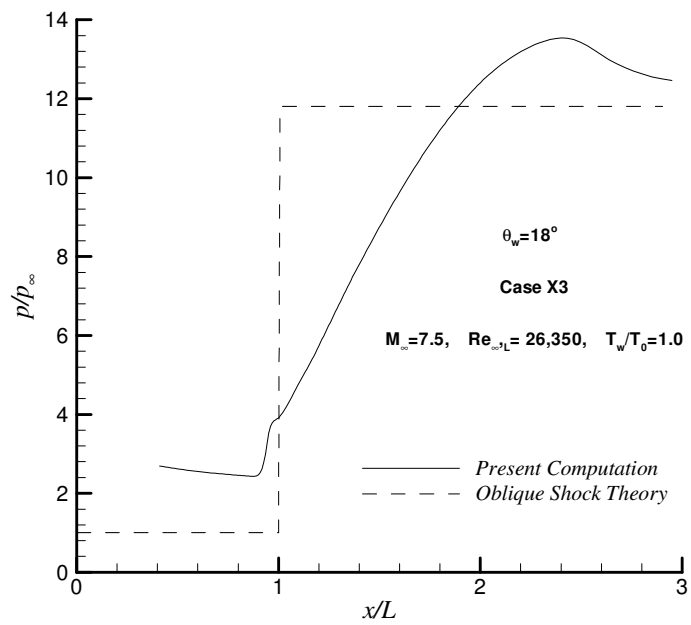


Figure 8.142 Surface pressure distribution,  $\theta_w=18^\circ$ , Case X3.

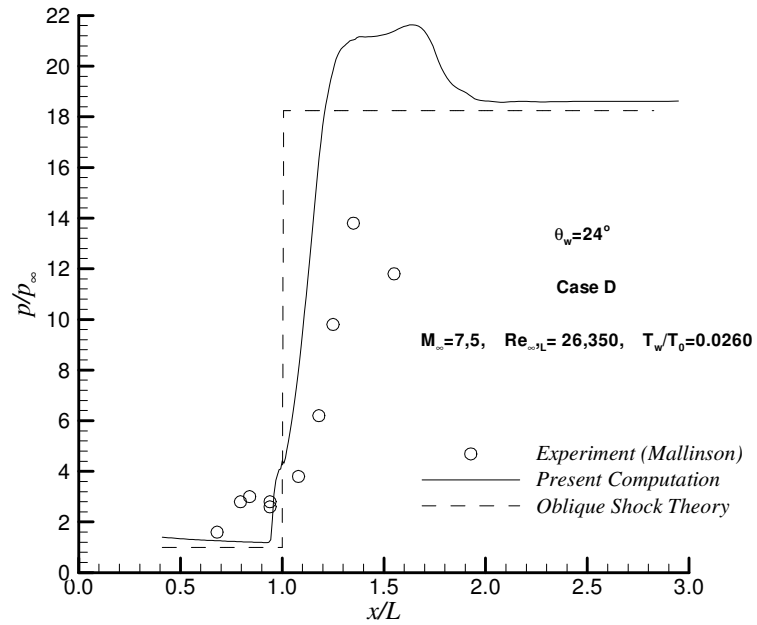


Figure 8.143 Surface pressure distribution,  $\theta_w = 24^\circ$ , Case B.

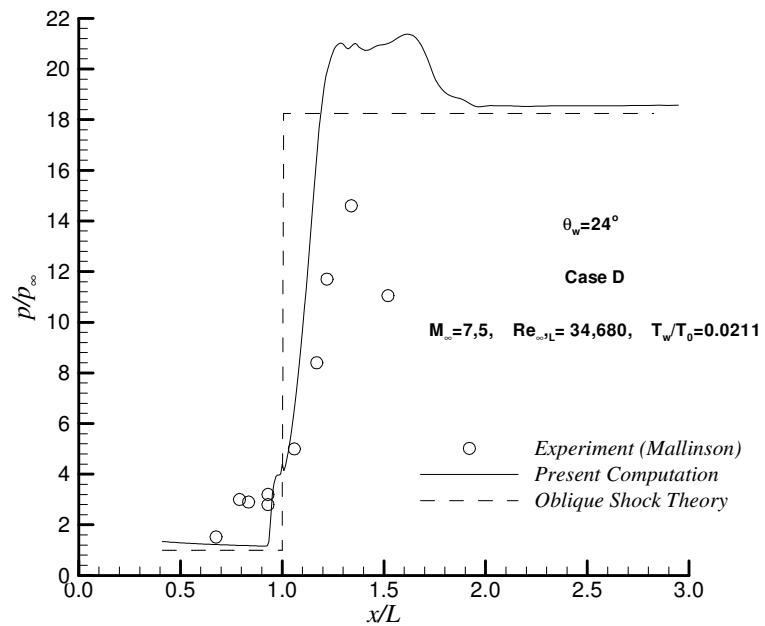
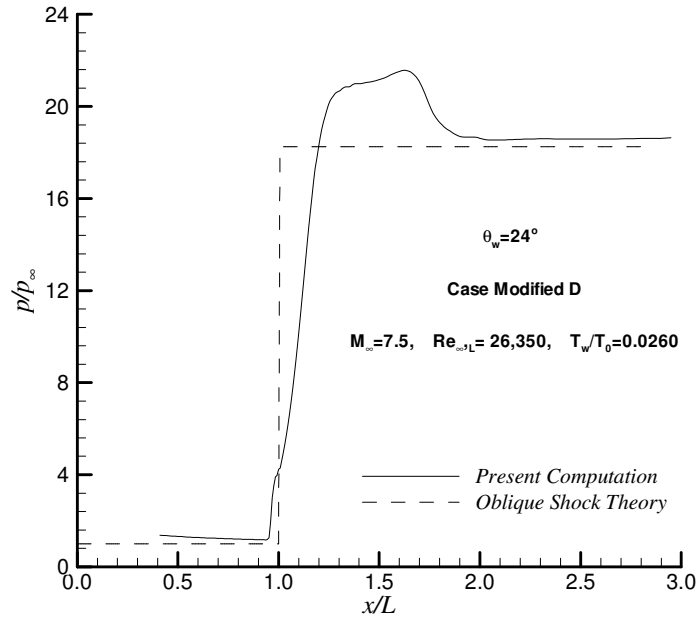
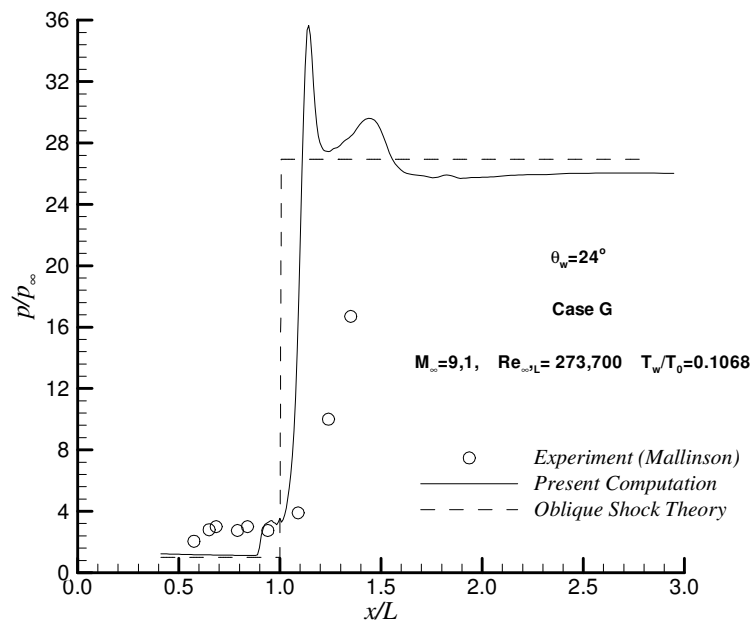


Figure 8.144 Surface pressure distribution,  $\theta_w = 24^\circ$ , Case D.



**Figure 8.145** Surface pressure distribution,  $\theta_w = 24^\circ$ , Case Modified D.



**Figure 8.146** Surface pressure distribution,  $\theta_w = 24^\circ$ , Case G.

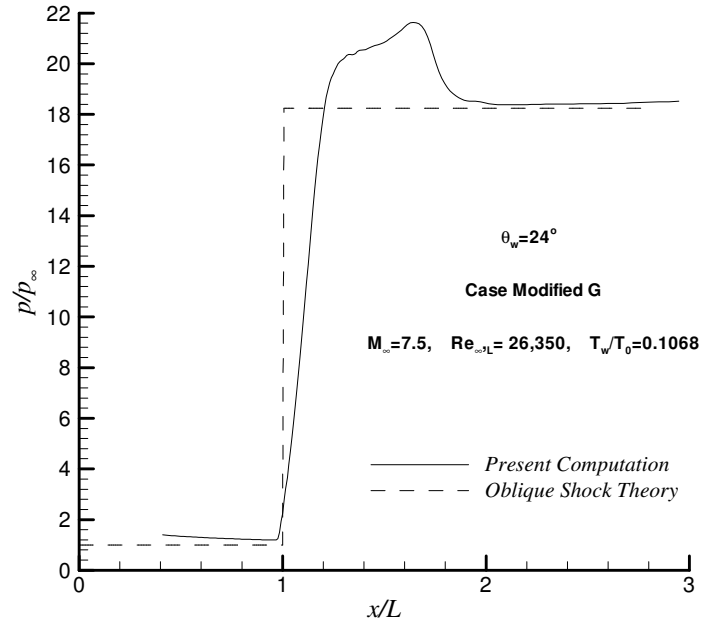


**Figure 8.147** Surface pressure distribution,  $\theta_w=24^\circ$ , Case Modified G.

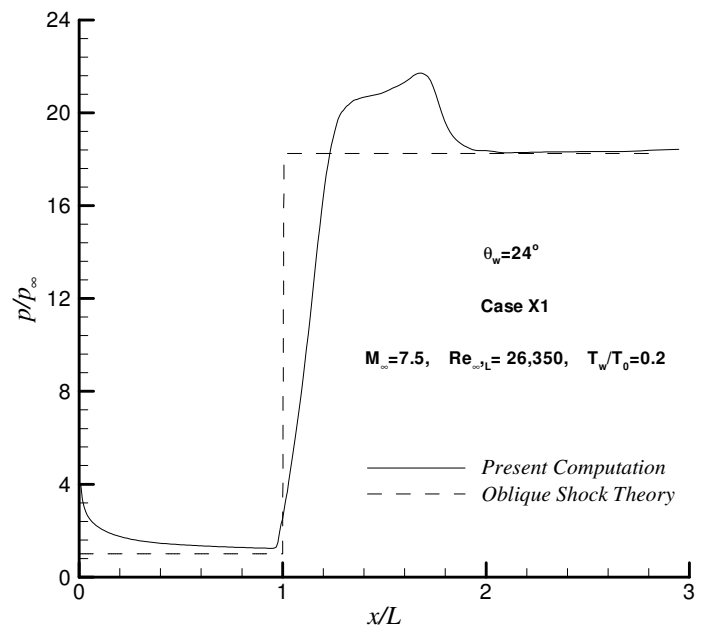


**Figure 8.148** Surface pressure distribution,  $\theta_w=24^\circ$ , Case X1.

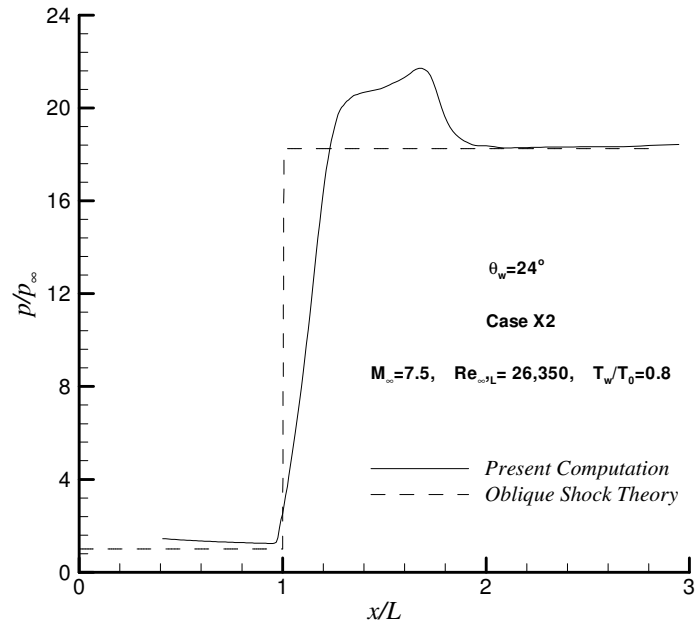


Figure 8.149 Surface pressure distribution,  $\theta_w=24^\circ$ , Case X2.

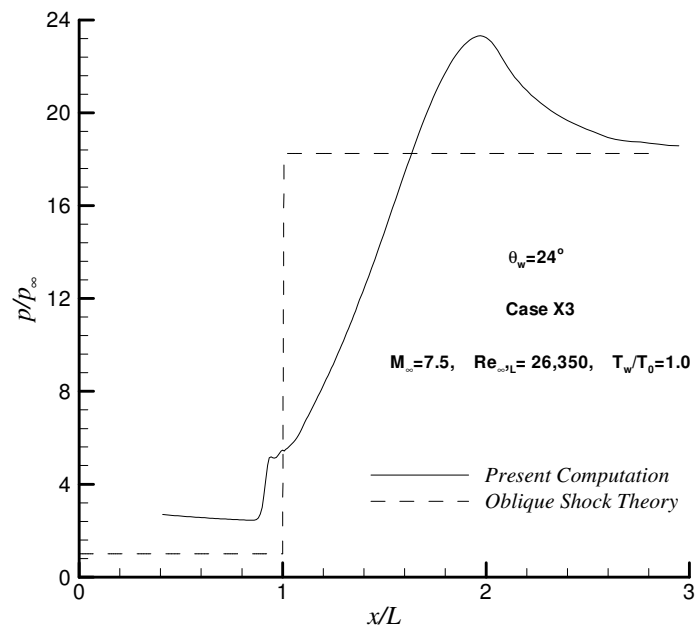


Figure 8.150 Surface pressure distribution,  $\theta_w=24^\circ$ , Case X3.

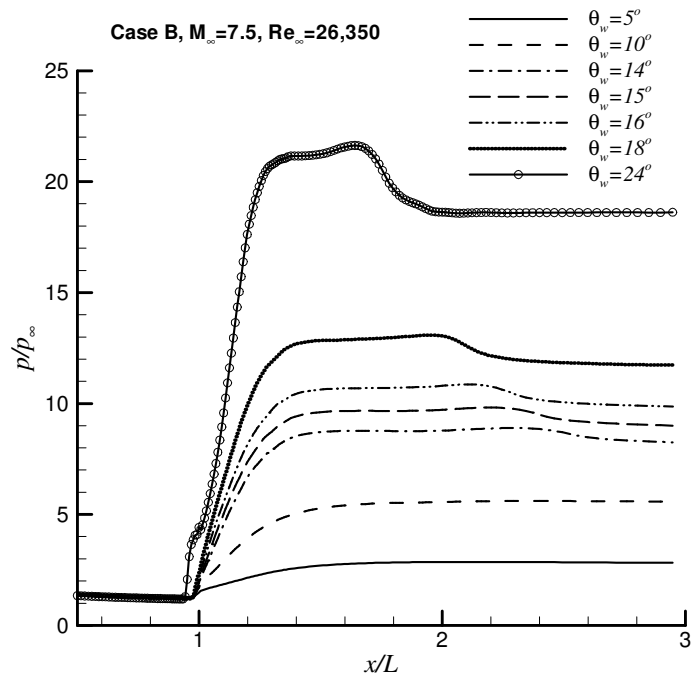


Figure 8.151 Effect of corner angle ( $\theta_w$ ) on surface pressures, Case B.

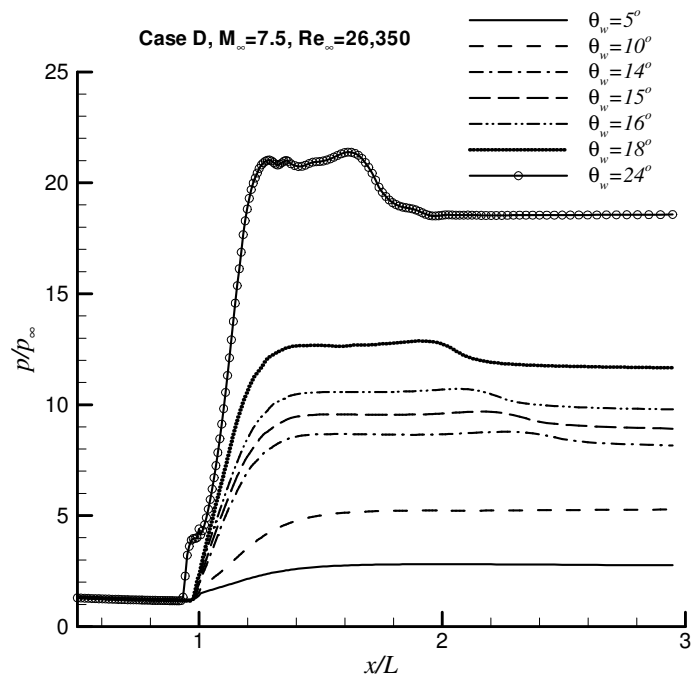


Figure 8.152 Effect of corner angle ( $\theta_w$ ) on surface pressures, Case D.

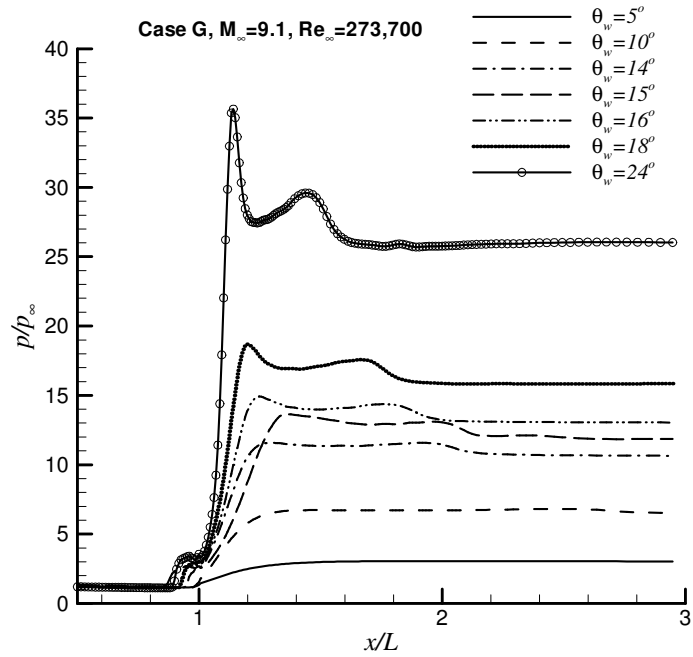


Figure 8.153 Effect of corner angle ( $\theta_w$ ) on surface pressures, Case G.

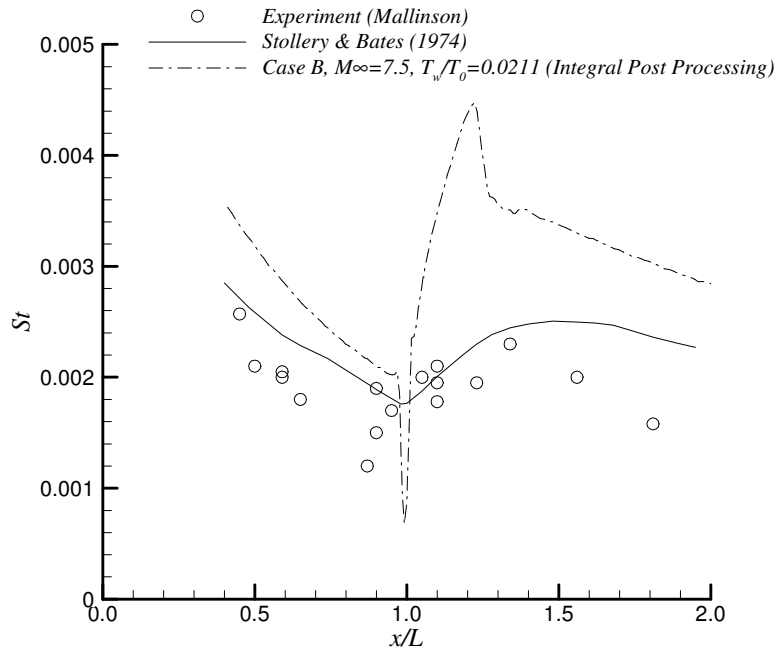
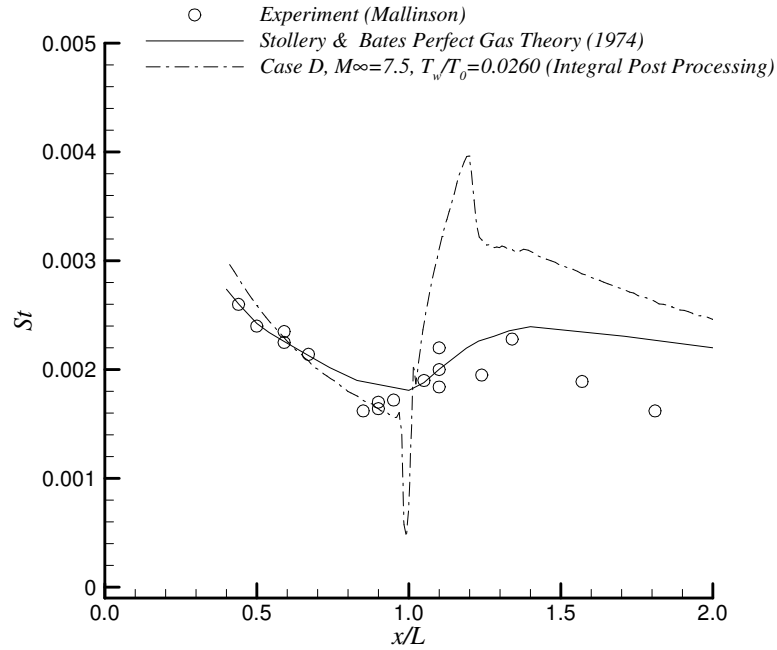
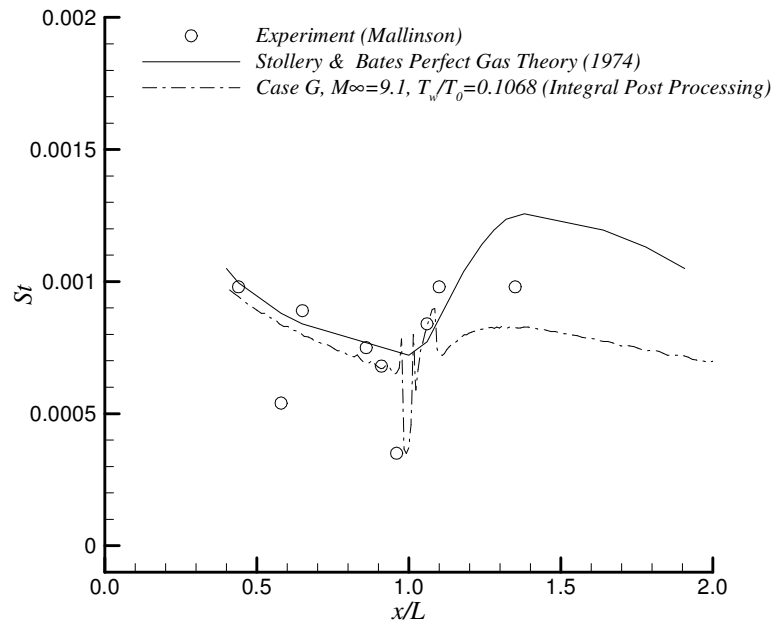


Figure 8.154 Stanton number distribution,  $\theta_w=5^\circ$ , Case B.



**Figure 8.155** Stanton number distribution,  $\theta_w=5^\circ$ , Case D.



**Figure 8.156** Stanton number distribution,  $\theta_w=5^\circ$ , Case G.

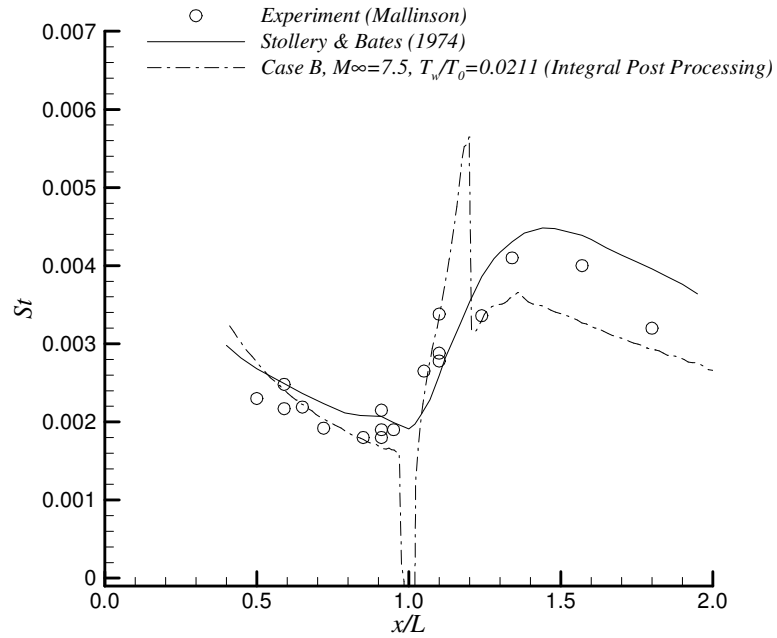


Figure 8.157 Stanton number distribution,  $\theta_w=10^\circ$ , Case B.

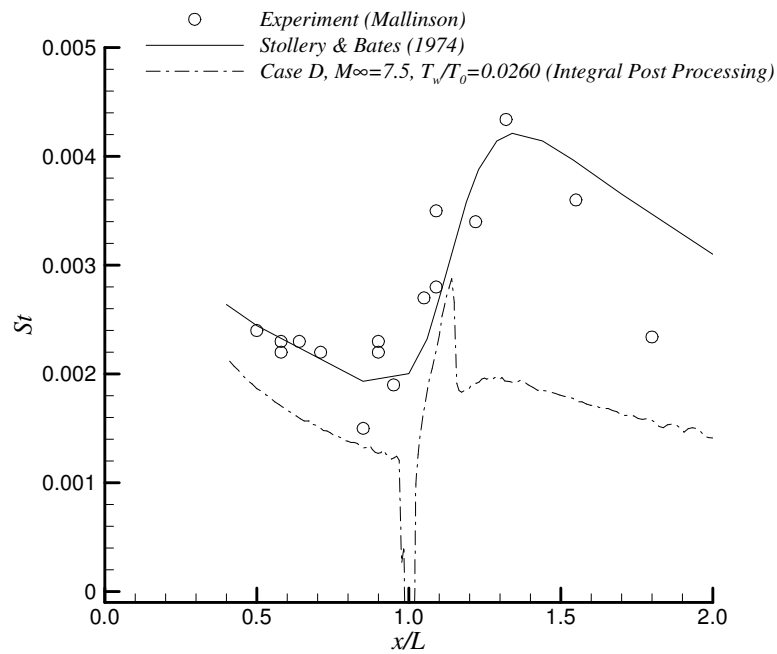
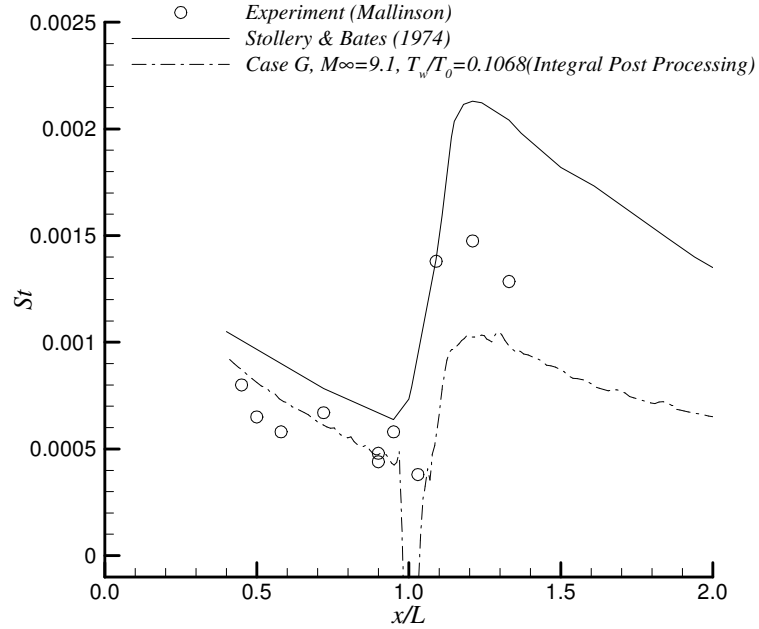
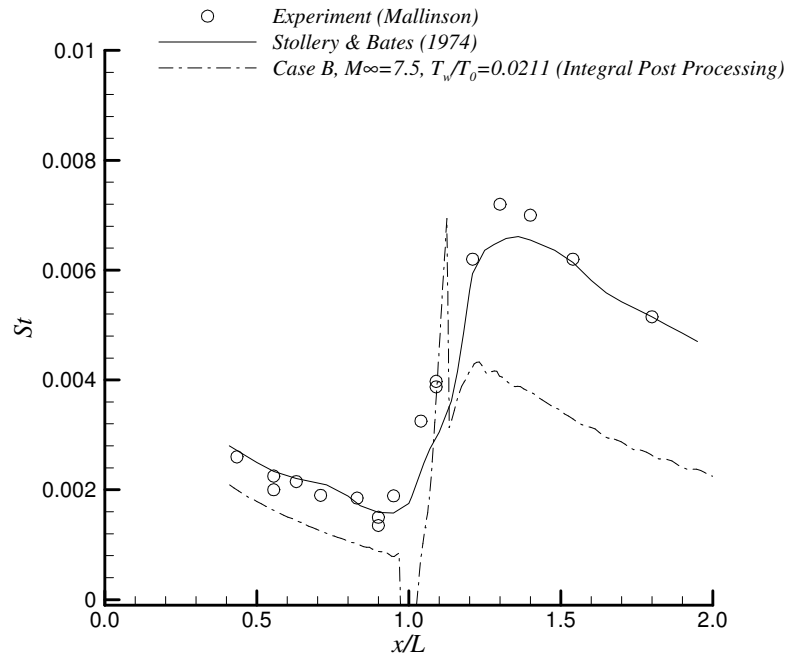


Figure 8.158 Stanton number distribution,  $\theta_w=10^\circ$ , Case D.



**Figure 8.159** Stanton number distribution,  $\theta_w=10^\circ$ , Case G.



**Figure 8.160** Stanton number distribution,  $\theta_w=14^\circ$ , Case B.

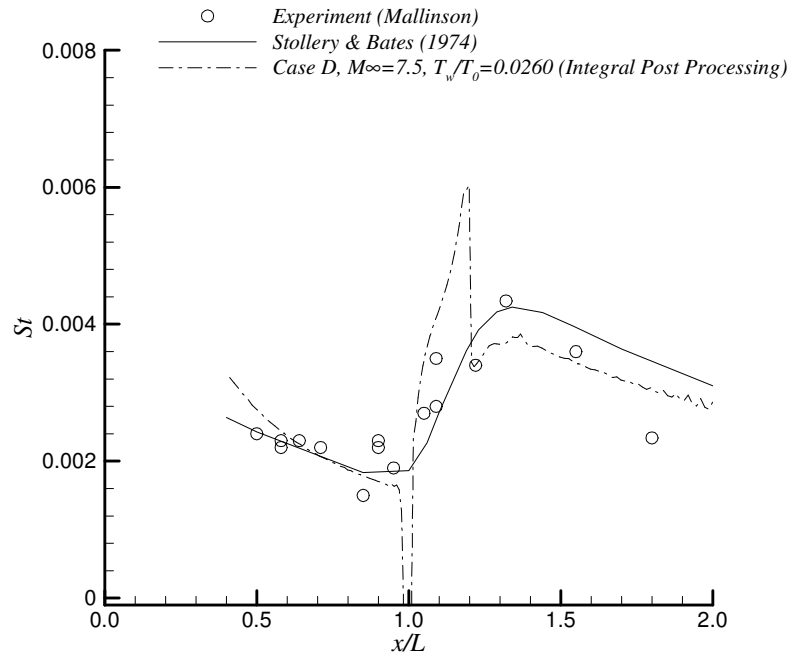


Figure 8.161 Stanton number distribution,  $\theta_w=14^\circ$ , Case D.

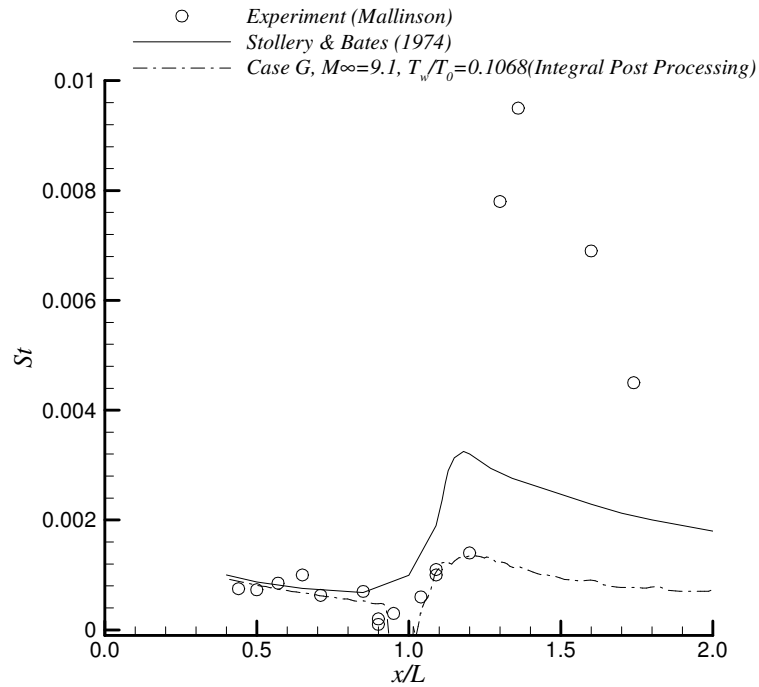
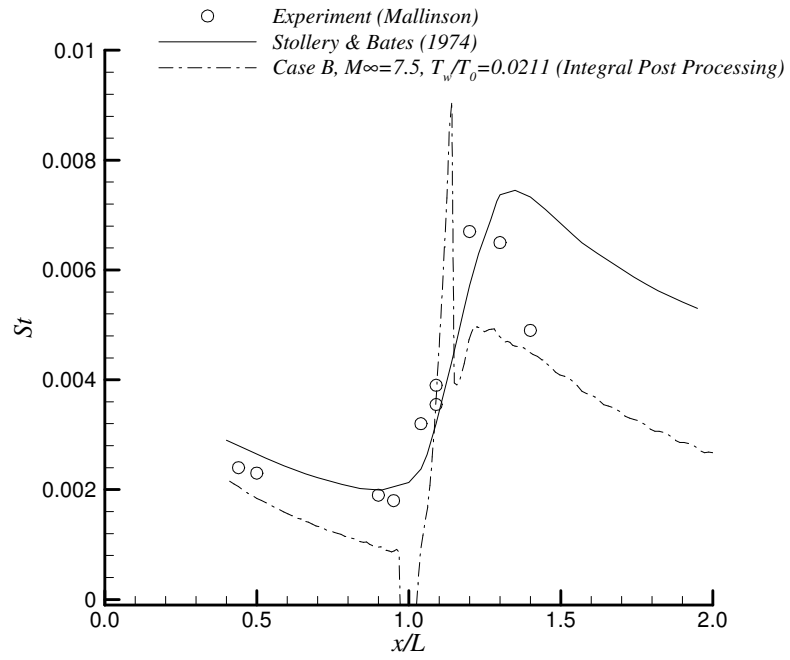
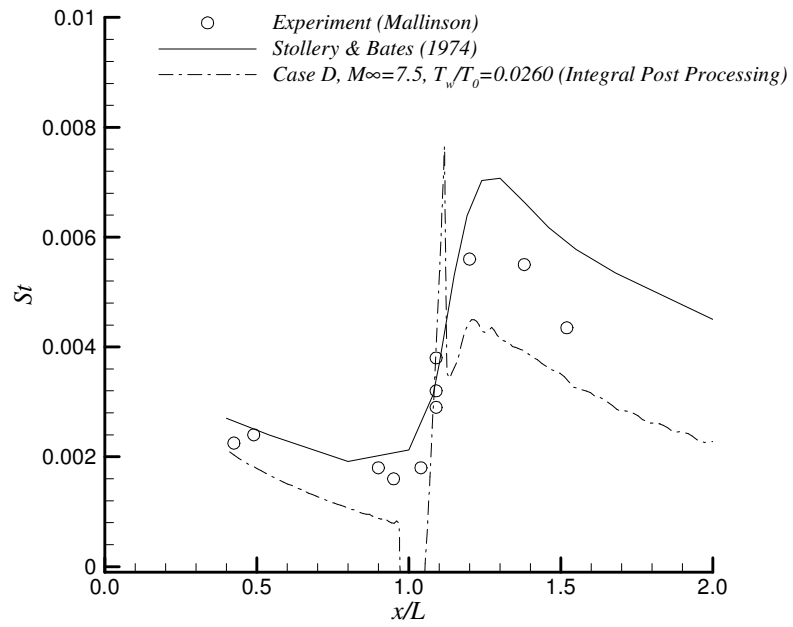


Figure 8.162 Stanton number distribution,  $\theta_w=14^\circ$ , Case G.



**Figure 8.163** Stanton number distribution,  $\theta_w=15^\circ$ , Case B.



**Figure 8.164** Stanton number distribution,  $\theta_w=15^\circ$ , Case D.

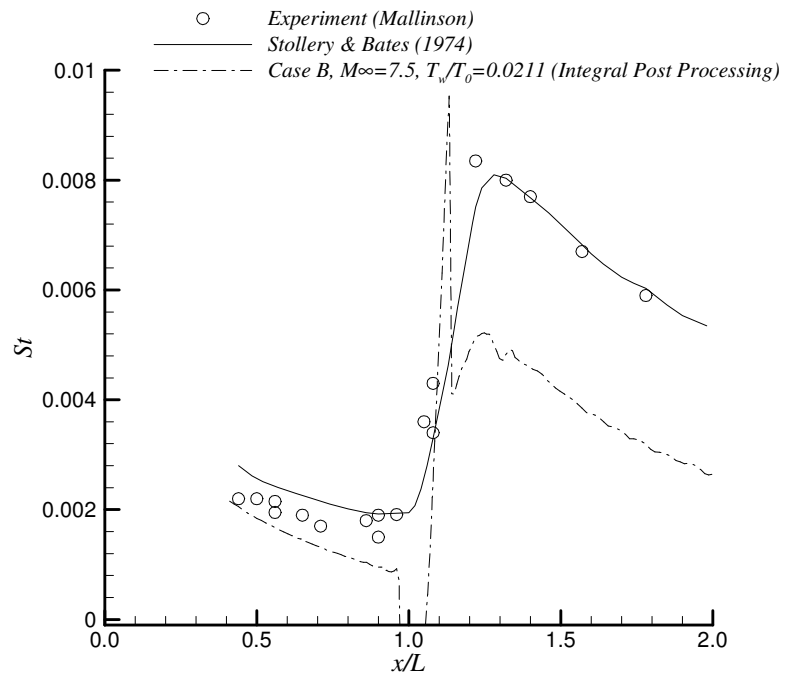


Figure 8.165 Stanton number distribution,  $\theta_w=16^\circ$ , Case B.

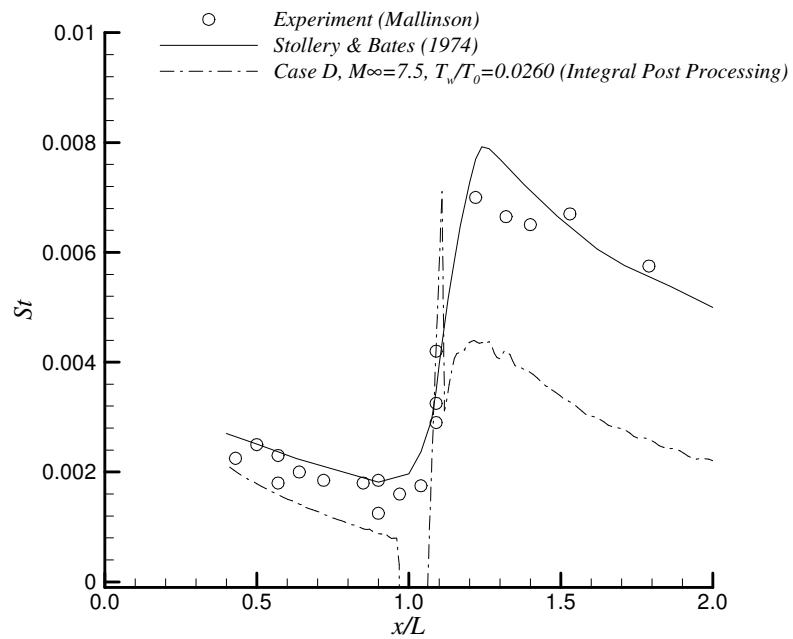
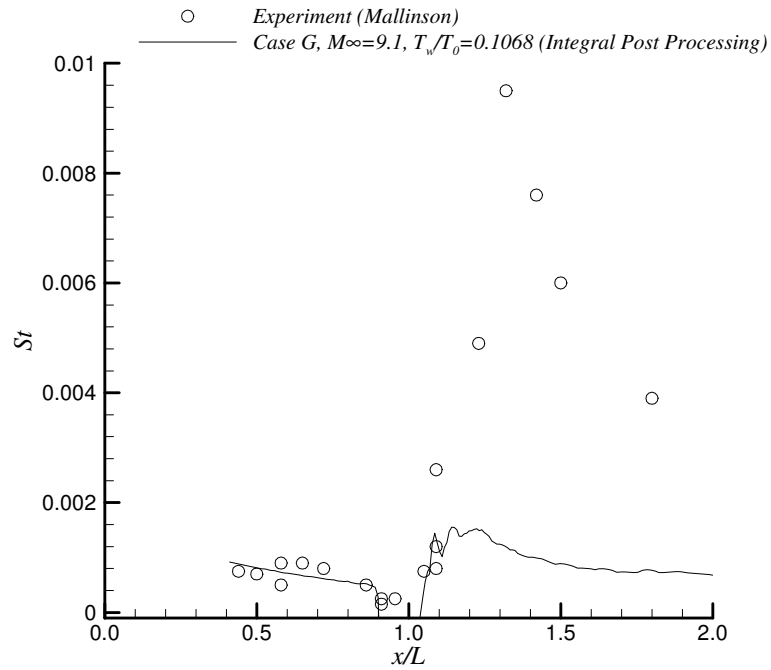
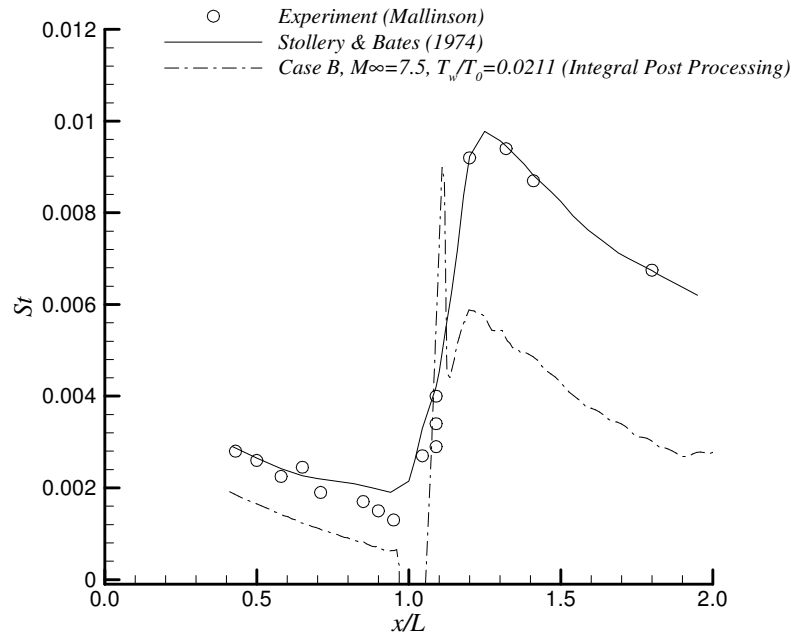


Figure 8.166 Stanton number distribution,  $\theta_w=16^\circ$ , Case D.



**Figure 8.167** Stanton number distribution,  $\theta_w=16^\circ$ , Case G.



**Figure 8.168** Stanton number distribution,  $\theta_w=18^\circ$ , Case B.

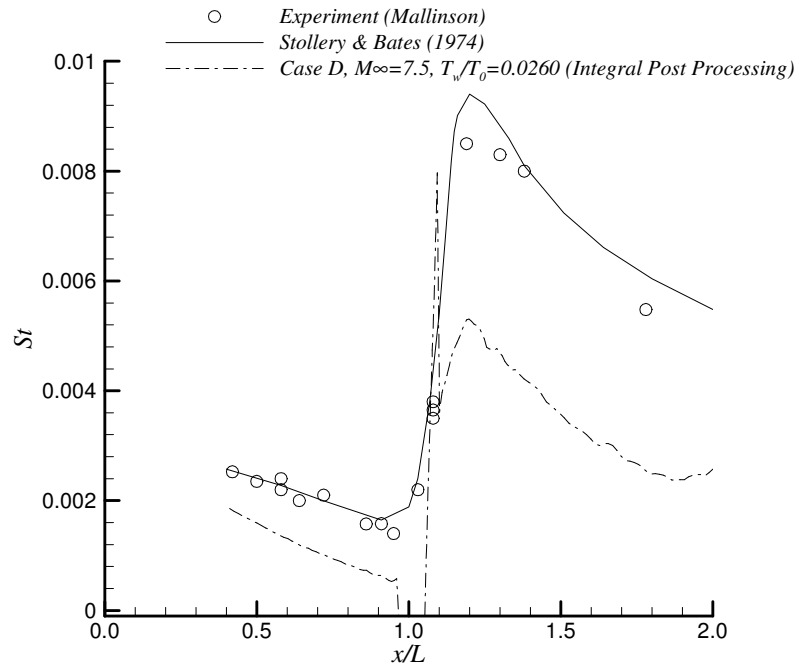


Figure 8.169 Stanton number distribution,  $\theta_w=18^\circ$ , Case D.

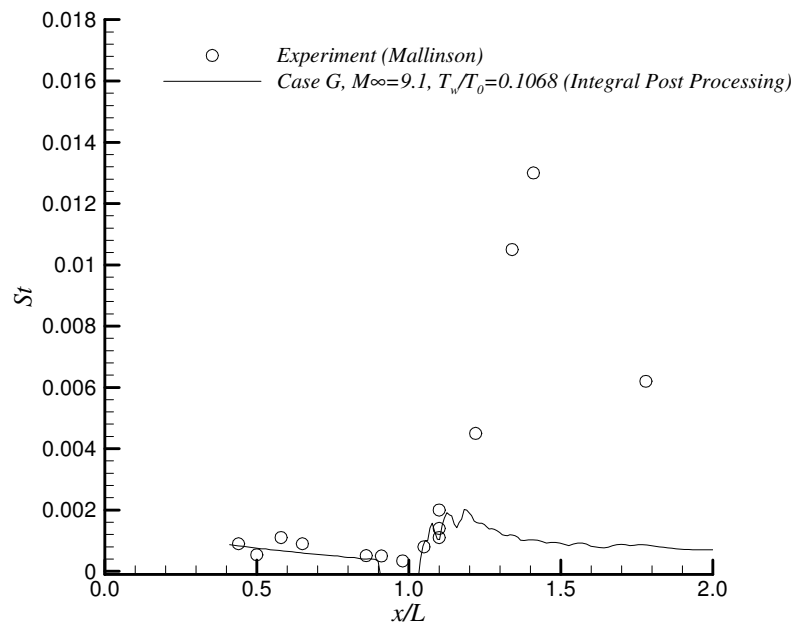
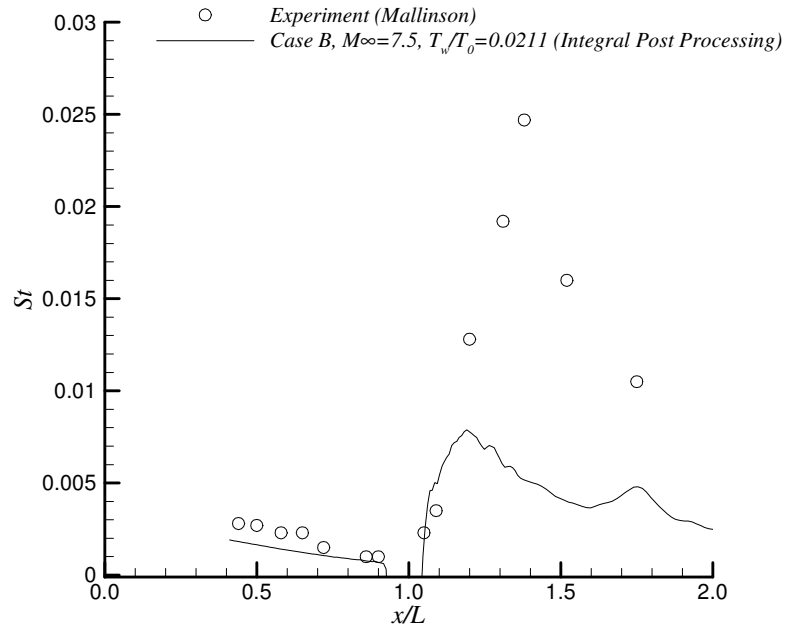
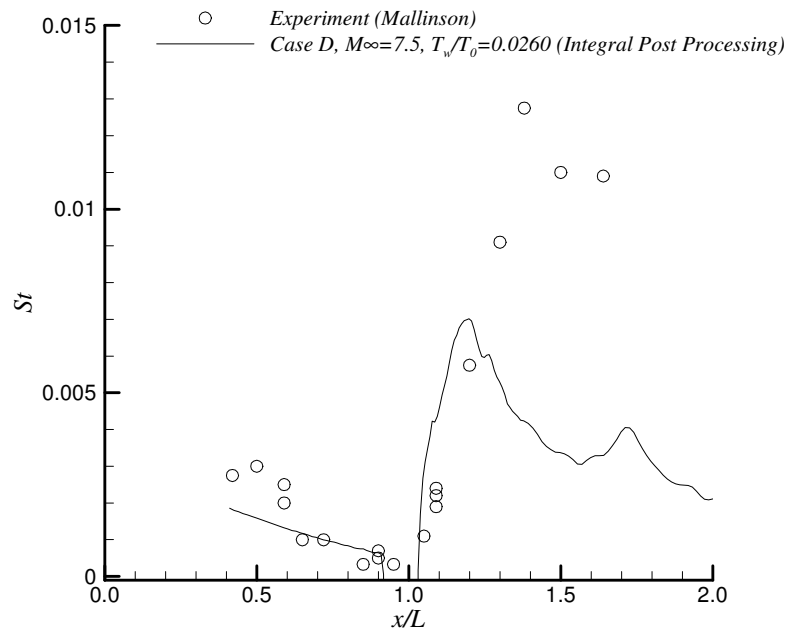


Figure 8.170 Stanton number distribution,  $\theta_w=18^\circ$ , Case G.



**Figure 8.171** Stanton number distribution,  $\theta_w=24^\circ$ , Case B.



**Figure 8.172** Stanton number distribution,  $\theta_w=24^\circ$ , Case D.

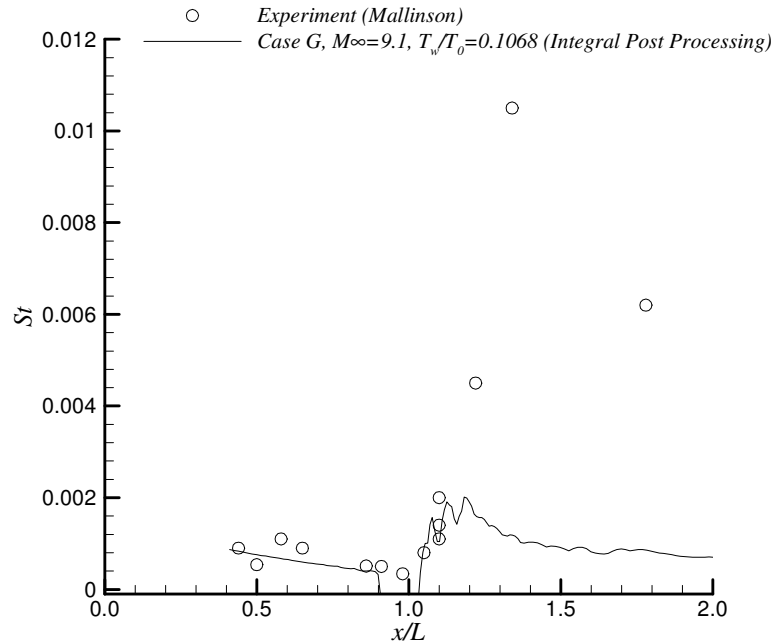


**Figure 8.173** Stanton number distribution,  $\theta_w=24^\circ$ , Case G.

### 8.2.5. Results of the Effects of $T_w/T_0$ Study

Up to this point, eight different test cases were analyzed over seven compression corners in terms of flow variable, boundary layer variable, pressure distribution, heat transfer rate distribution.

During this study, one of the most critical flow properties is considered as  $T_w/T_0$  ratio. In this section, the effects of  $T_w/T_0$  on the heat transfer and pressure distributions and the boundary layer flow variables are presented. The Case B, Modified D, Modified G, X1, X2 and X3 are chosen according to the  $T_w/T_0$  values to compare the results. For these six test cases;  $M_\infty$  is 7.5 and  $Re_{\infty,L}$  is 26,350. Navier Stokes solutions are obtained for  $T_w/T_0$  ratios from 0.0211 to 1.0 for six test cases for fixed  $M_\infty$  and  $Re_{\infty,L}$  and same compression corner grids given in Figure 7.6 to 7.12. The Case X2 ( $T_w= 3,000$  °K and  $T_{aw}=3,335$  °K) and X3 ( $T_w= 3,000$  °K and  $T_{aw}=2,720$  °K) are close to adiabatic wall case and the heat transfer is weak for these cases. The results are presented for  $\theta_w=14^\circ$ ,  $18^\circ$  and  $24^\circ$ .

The effect of  $T_w/T_0$  on convergence history is given in Figure 8.174. As seen from the figure that the convergence increases with the increasing  $T_w/T_0$  ratio.

Figure 8.175 shows the effect of  $T_w/T_0$  on the number of grid points in the boundary layer.

The effects of  $T_w/T_0$  on the Mach contours are given for six test cases in Figures 8.176 to 8.181 for  $\theta_w=14^\circ$ , in Figures 8.182 to 8.187 for  $\theta_w=18^\circ$  and in Figures 8.188 to 8.193 for  $\theta_w=24^\circ$ . It can be seen from mach contours that there is strong interaction between boundary layer and leading edge shock along the flat plate in accordance with oblique shock theory. Between the separation and reattachment shocks, expansion waves are generated where the boundary layer is turning back towards to the surface. At the point of reattachment, the boundary layer has become relatively thin, the pressure is high, and consequently this becomes a region of high local aerodynamic heating.

The effects of  $T_w/T_0$  on the streamlines are given for the six test cases in Figures 8.194 to 8.199 for  $\theta_w=14^\circ$ , in Figures 8.200 to 8.205 for  $\theta_w=18^\circ$  and in Figures 8.206 to 8.211 for  $\theta_w=24^\circ$ . The flow over  $14^\circ$  and  $18^\circ$  compression corners is attached for Cases B, Modified D, Modified G and X1 for. However, it is separated for Case X2 and X3. The flow over  $24^\circ$  compression corner is separated for all six test cases. It is concluded that the flow has tendency to separate as  $T_w/T_0$  ratio increases. It is also predicted that the flow has a tendency to separate as the corner angle increases and as a consequence separation region becomes larger. Here it should be mentioned that for Case X3 ( $T_w/T_0=1.0$ ), wall temperature is equal to the stagnation temperature of the freestream, and because of the no slip boundary condition, flow velocity at the wall is zero. This makes the wall to act as a stagnation region. In Figures 8.212 to 8.217 the effects of  $T_w/T_0$  on the pressure contours for  $\theta_w=14^\circ$ ,  $18^\circ$  and  $24^\circ$  and for Cases X2 and X3 are presented. In Figures 8.218 to 8.223 the effects of  $T_w/T_0$  on the temperature contours are shown for  $\theta_w=14^\circ$ ,  $18^\circ$  and  $24^\circ$  and for Cases X2 and X3. It can be seen from those figures that there is no abnormality and they reflect behaviors which agree with the streamlines distributions of Cases X2 and X3.  $T_w/T_0$  value is 0.0186 for Cases X2 and X3.

In Figures 8.224 to 8.226 the effects of  $T_w/T_0$  on the pressure distributions are shown for  $\theta_w=14^\circ$ ,  $18^\circ$  and  $24^\circ$ . It can be said that  $T_w/T_0$  ratio has a minor influence on the pressure distribution for fixed  $M_\infty$  and  $Re_\infty$ .

The  $T_w/T_0$  ratio effect on the heat transfer rate is shown in Figures 8.227 to 8.232. It is clear that, heat transfer decrease with the increasing  $T_w/T_0$  ratio for fixed  $M_\infty$  and  $Re_\infty$ . Here the results are presented as obtained from both integral and differential post processing. Accuracy of the differential post processing depends on the prediction of the temperature gradient at the wall. Accuracy of the integral post processing depends on the prediction of the distribution of the heat transfer parameter,  $f_{q,w}$ , which was described in section 8.1.1 and its variation in the stream wise direction. The results of the differential post processing show that the heat transfer increases by increasing  $T_w/T_0$  ratio for fixed  $M_\infty$  and  $Re_\infty$ . On the other hand the results of the integral post processing show that the heat transfer decreases by increasing  $T_w/T_0$  ratio. For lower  $T_w/T_0$  ratios there is more temperature difference between the wall and the freestream therefore there should be more heat transfer. From here we may conclude that integral post processing is more reliable. However, integral post processing causes a jump in the negative direction just at the corner which is not seen on the differential post processing results. Most likely, this jump is coming from the sudden slope change of the surface and not physical. Integral post processing needs to be modified for the corner regions or in its present form the results at the immediate vicinity of the corner should be disregarded.

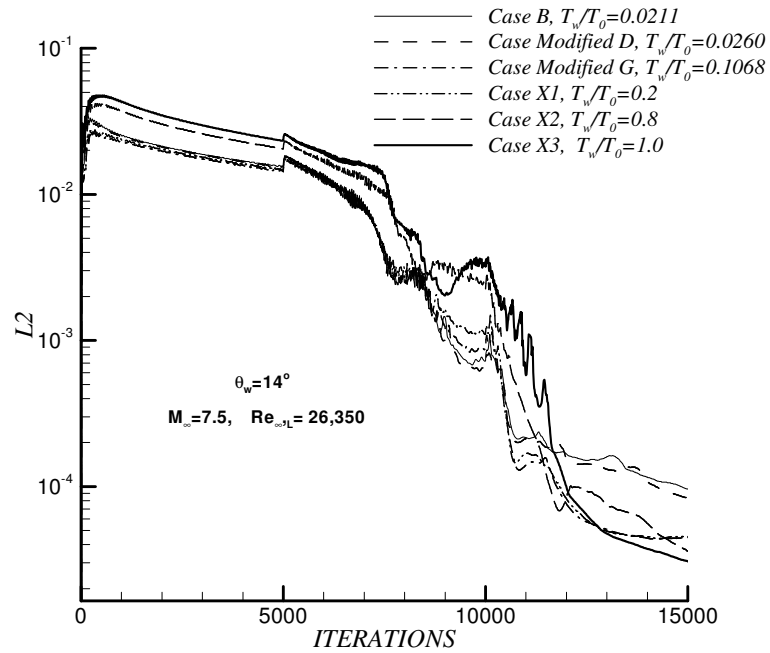


Figure 8.174 Effect of  $T_w/T_0$  on convergence histories,  $\theta_w=14^\circ$

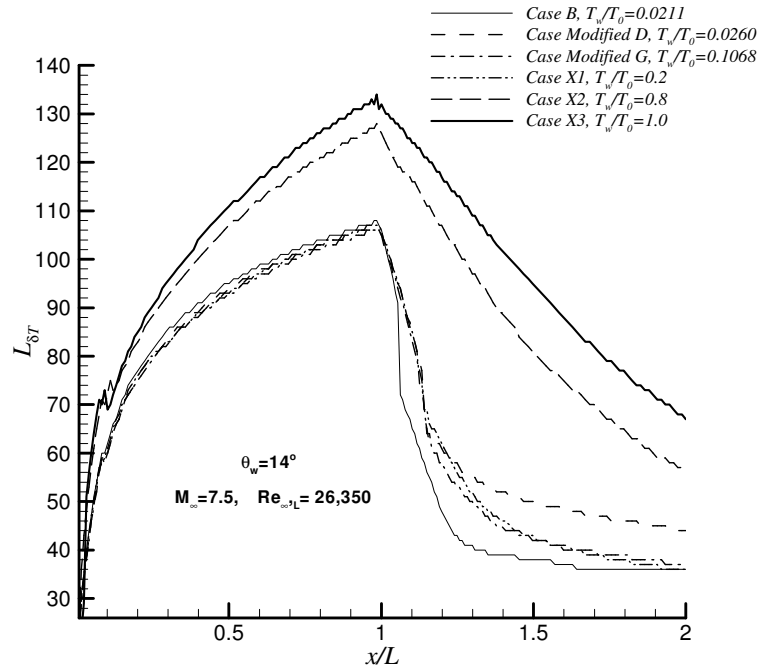


Figure 8.175 Effect of  $T_w/T_0$  on number of grid points in boundary layer,  $\theta_w=14^\circ$

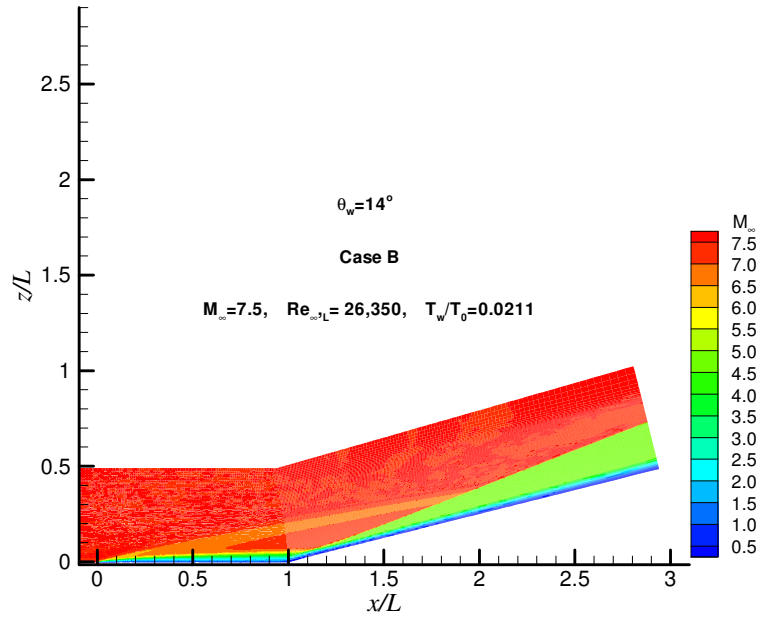


Figure 8.176 Mach contours,  $\theta_w = 14^\circ$ , Case B.

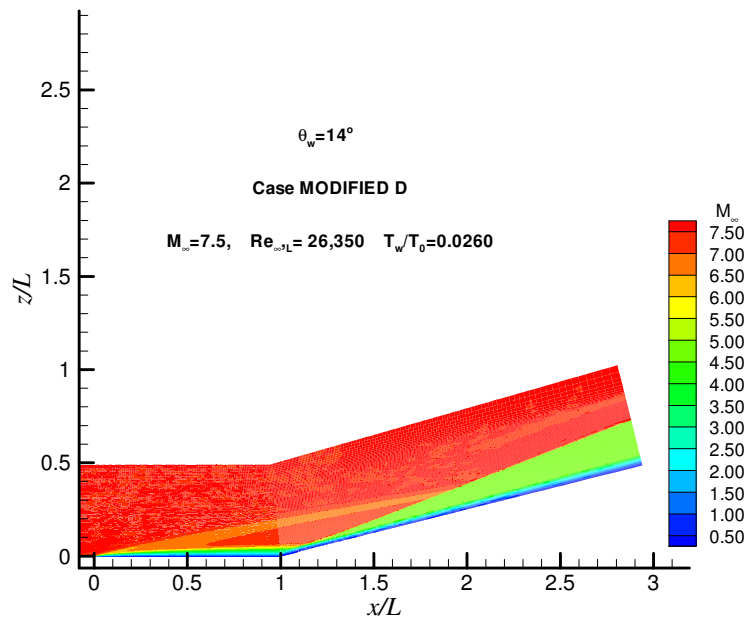
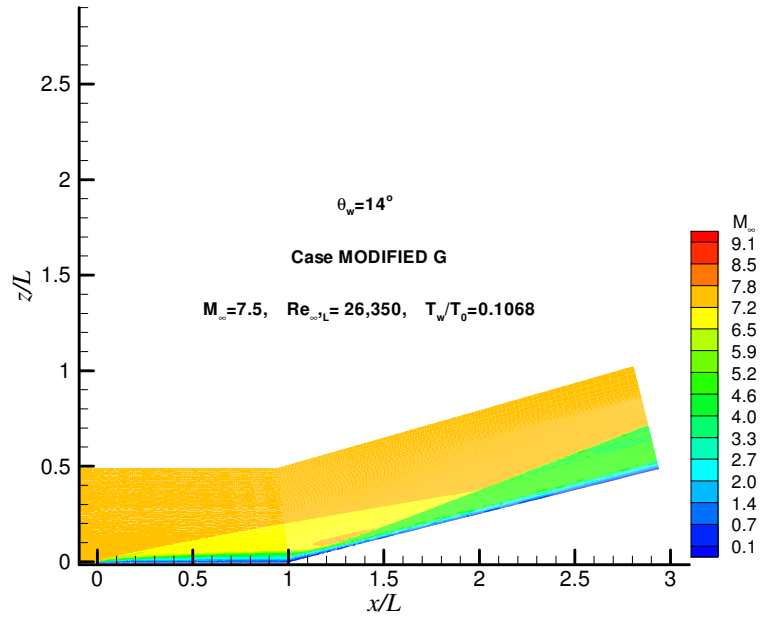
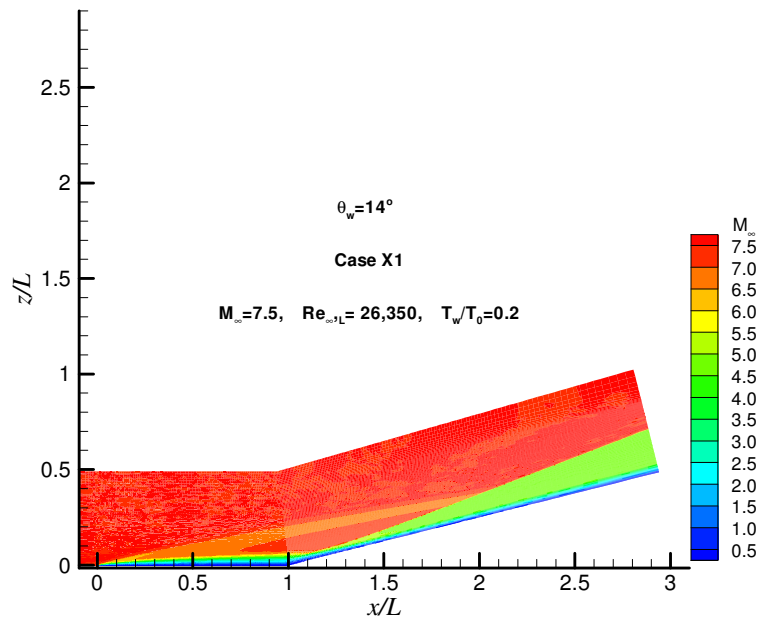


Figure 8.177 Mach contours,  $\theta_w = 14^\circ$ , Case Modified D.



**Figure 8.178** Mach contours,  $\theta_w = 14^\circ$ , Case Modified G.



**Figure 8.179** Mach contours,  $\theta_w = 14^\circ$ , Case X1.

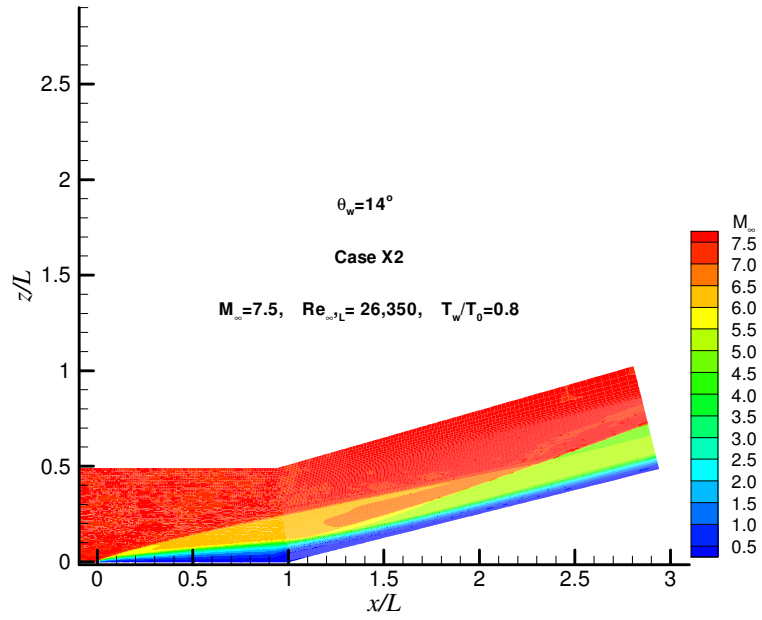


**Figure 8.180** Mach contours,  $\theta_w = 14^\circ$ , Case X2.

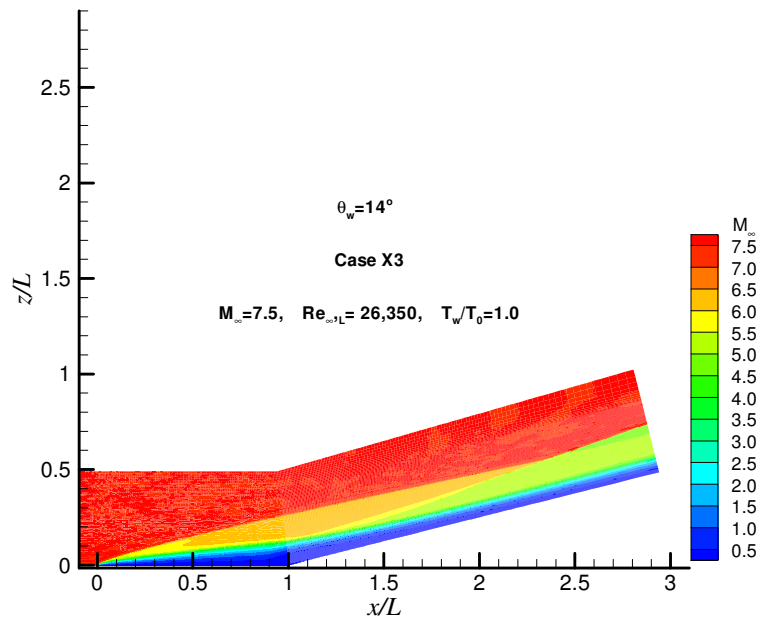


**Figure 8.181** Mach contours,  $\theta_w = 14^\circ$ , Case X3.

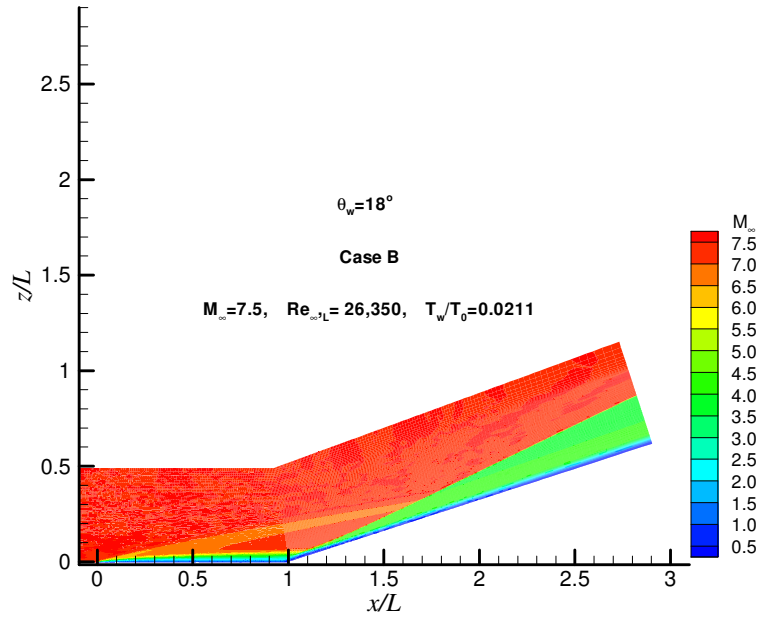


**Figure 8.182** Mach contours,  $\theta_w=18^\circ$ , Case B.

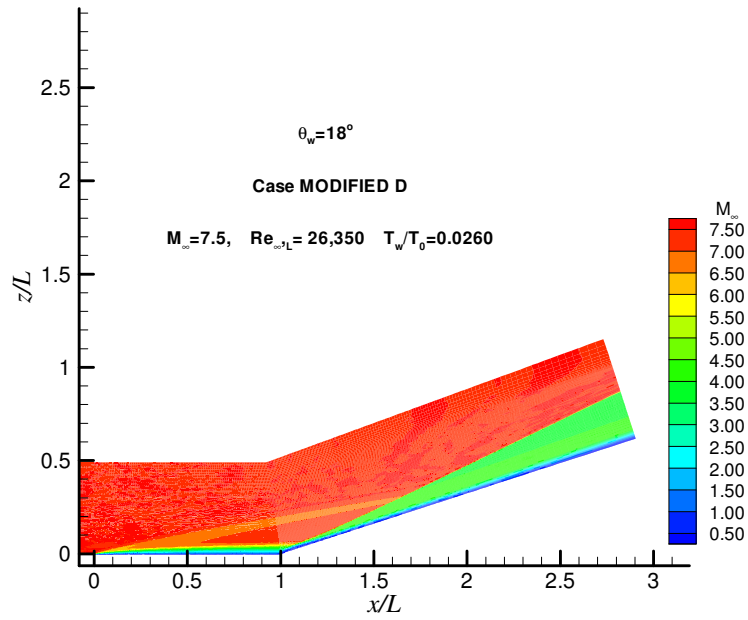


**Figure 8.183** Mach contours,  $\theta_w=18^\circ$ , Case Modified D.

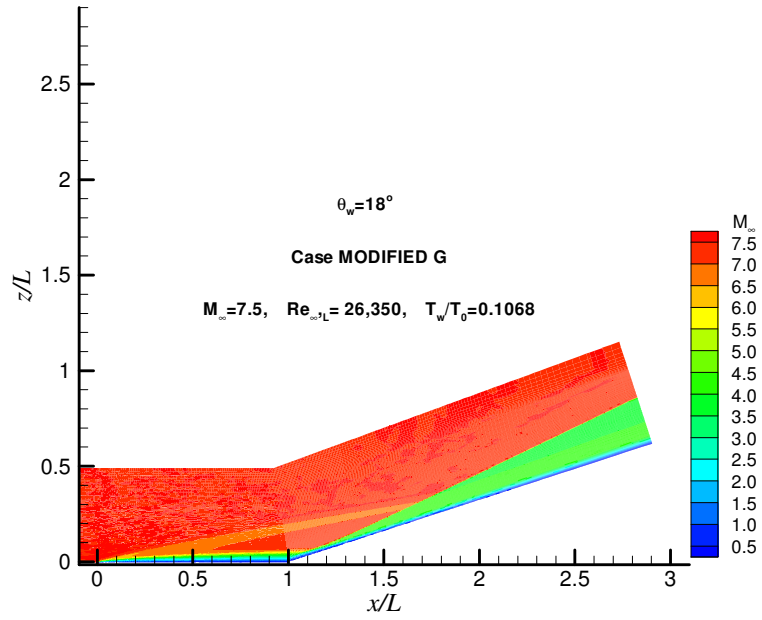


**Figure 8.184** Mach contours,  $\theta_w = 18^\circ$ , Case Modified G.

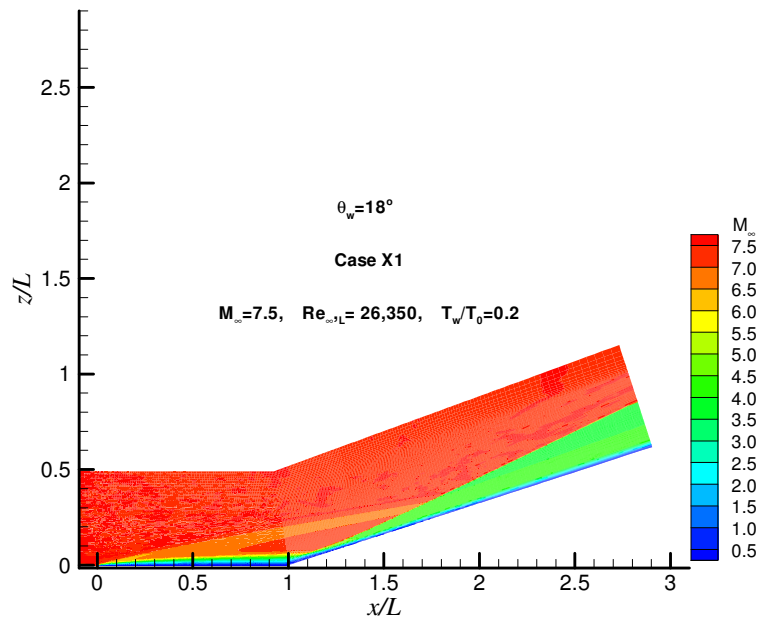


**Figure 8.185** Mach contours,  $\theta_w = 18^\circ$ , Case X1.

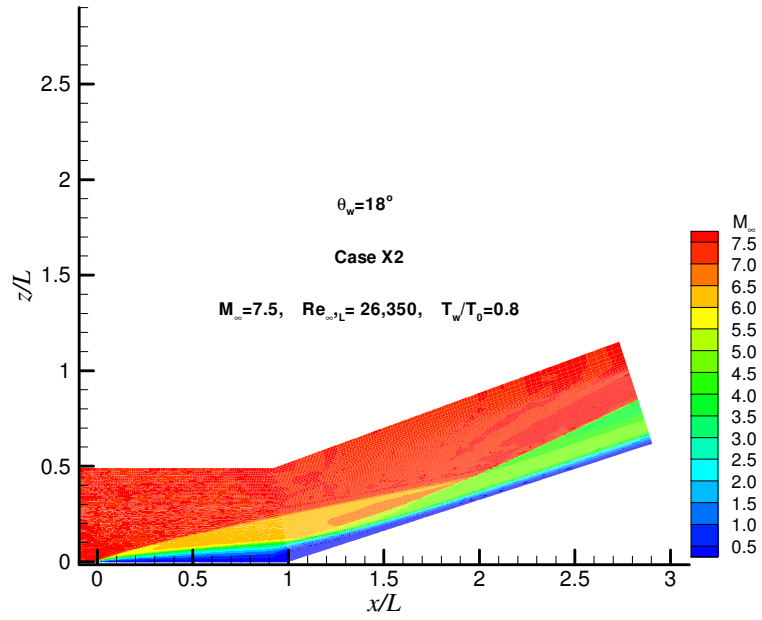


**Figure 8.186** Mach contours,  $\theta_w = 18^\circ$ , Case X2

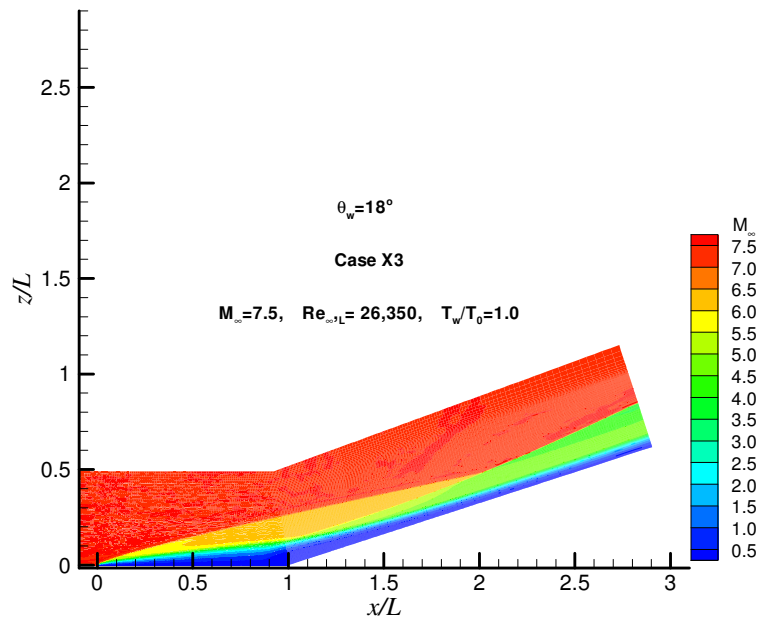


**Figure 8.187** Mach contours,  $\theta_w = 18^\circ$ , Case X3.

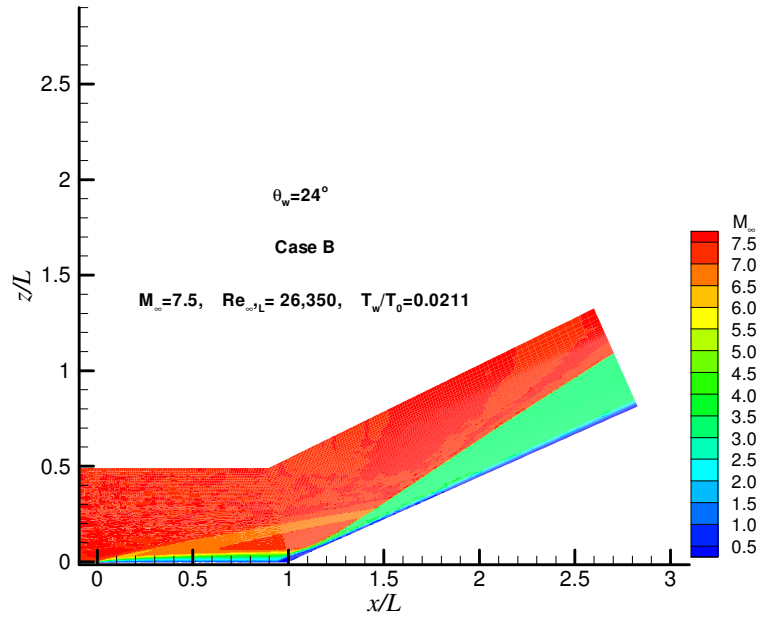


Figure 8.188 Mach contours,  $\theta_w = 24^\circ$ , Case B.

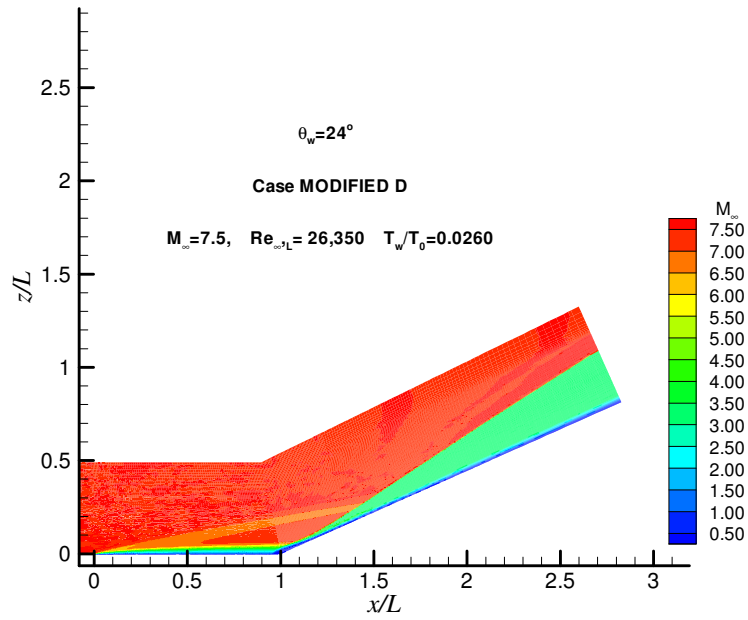
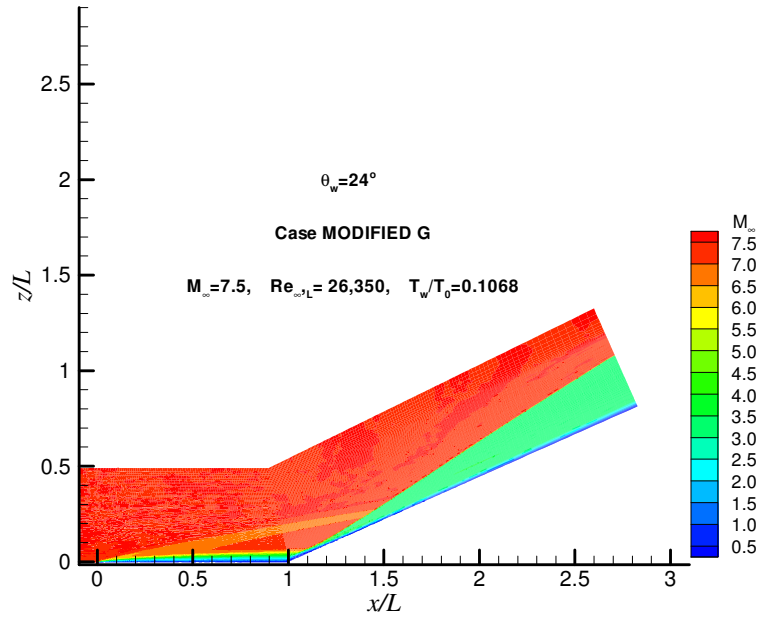
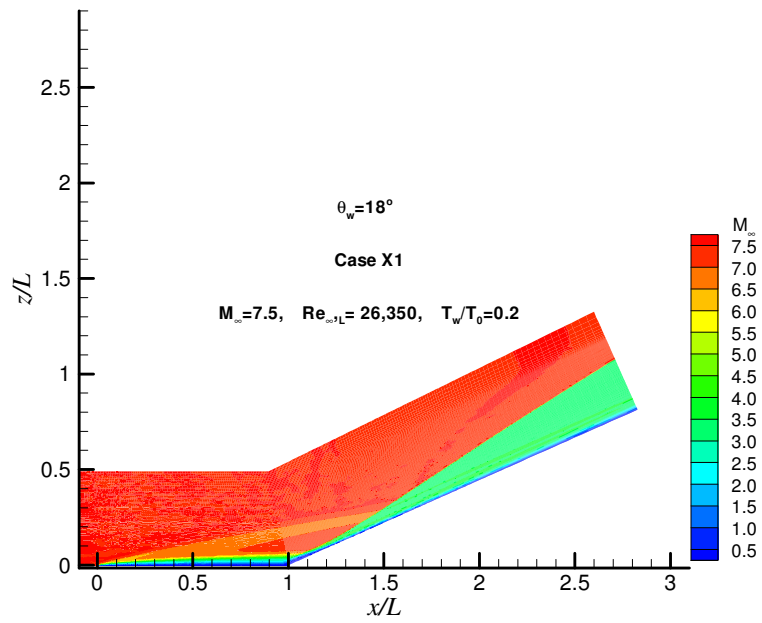


Figure 8.189 Mach contours,  $\theta_w = 24^\circ$ , Case Modified D.



**Figure 8.190** Mach contours,  $\theta_w = 24^\circ$ , Case Modified G.



**Figure 8.191** Mach contours,  $\theta_w = 24^\circ$ , Case X1.

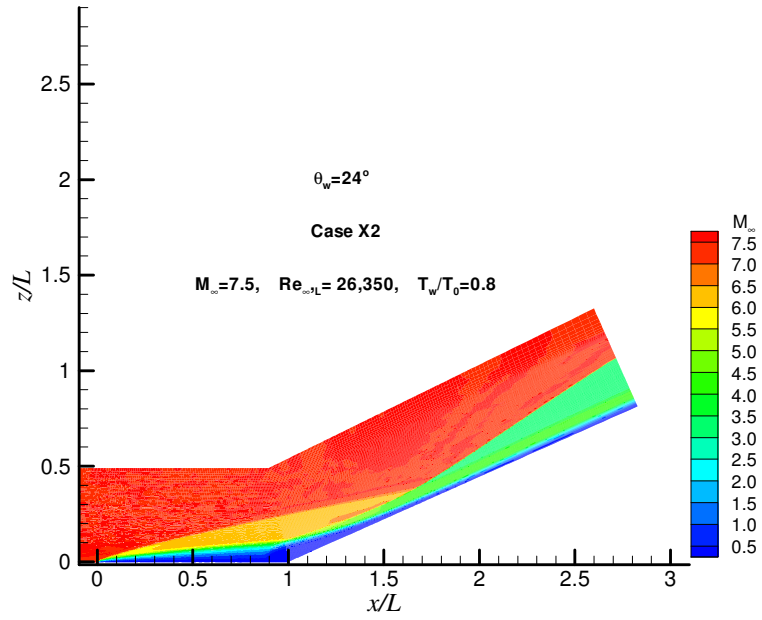


**Figure 8.192** Mach contours,  $\theta_w = 24^\circ$ , Case X2.

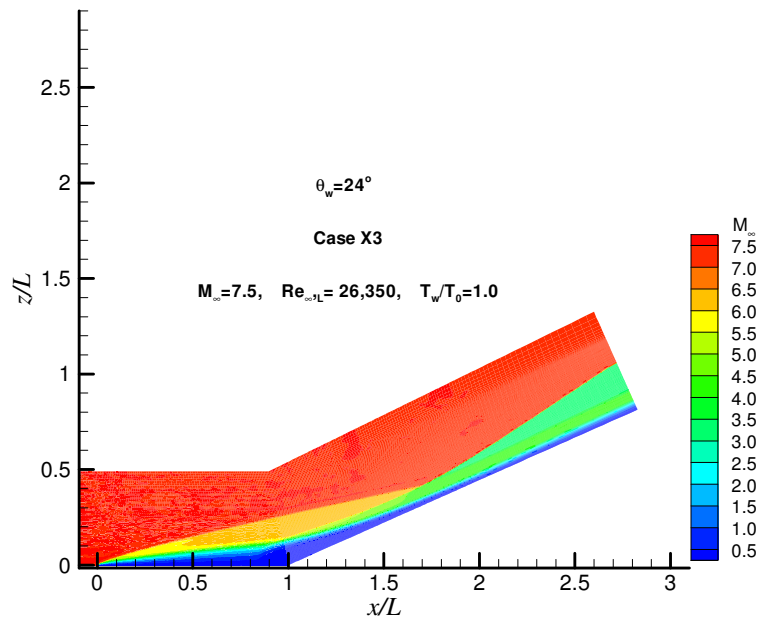


**Figure 8.193** Mach contours,  $\theta_w = 24^\circ$ , Case X3.

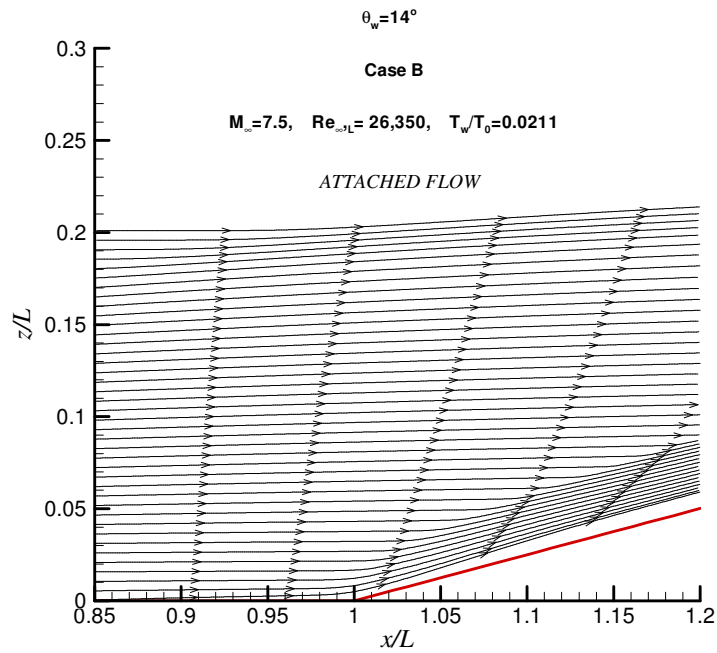


**Figure 8.194** Effect of  $T_w/T_0$  on streamlines,  $\theta_w = 14^\circ$ , Case B.

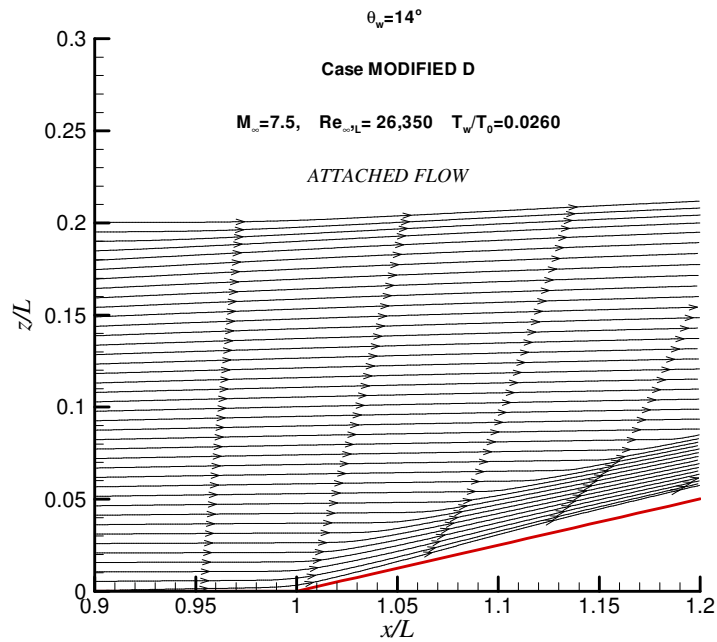


**Figure 8.195** Effect of  $T_w/T_0$  on streamlines,  $\theta_w = 14^\circ$ , Case Modified D.

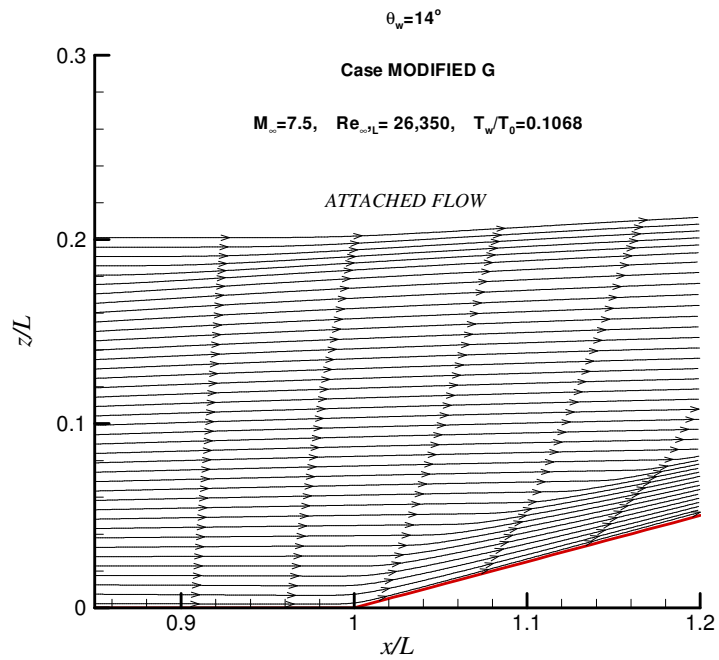


**Figure 8.196** Effect of  $T_w/T_0$  on streamlines,  $\theta_w = 14^\circ$ , Case Modified G.

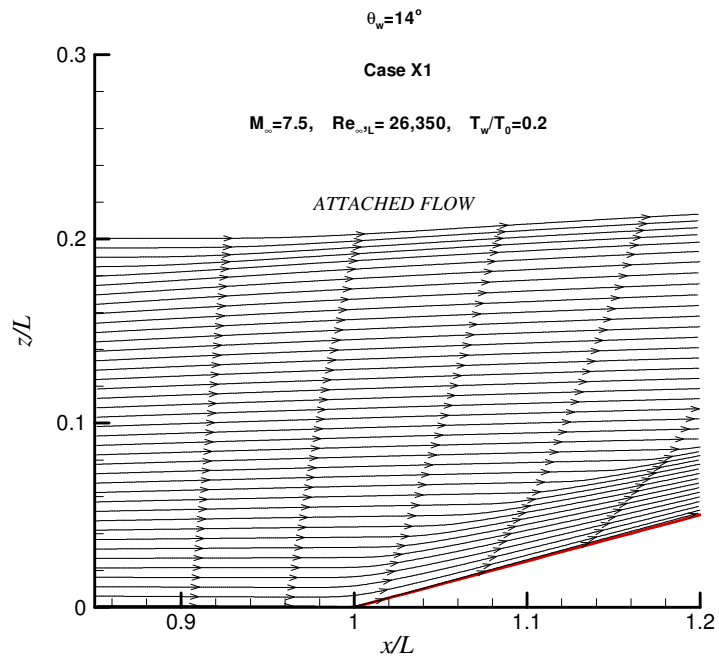


**Figure 8.197** Effect of  $T_w/T_0$  on streamlines,  $\theta_w = 14^\circ$ , Case X1.

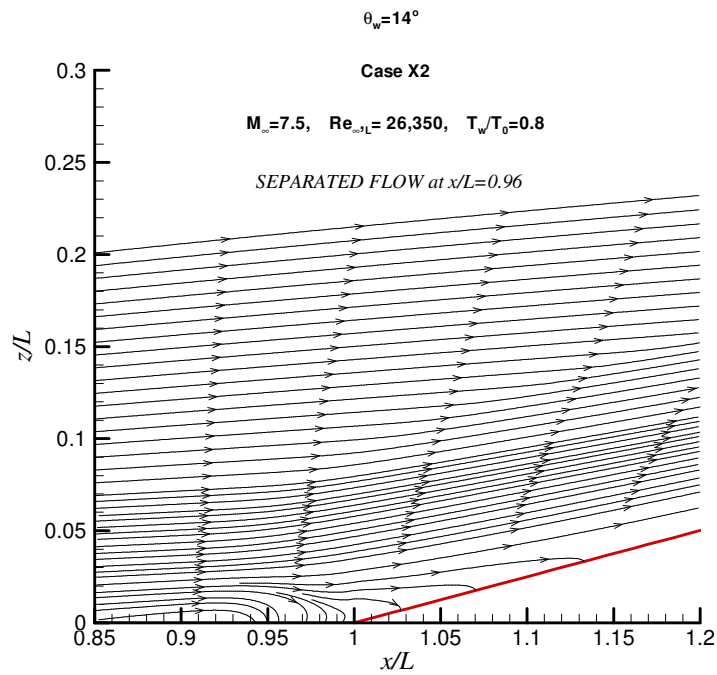


**Figure 8.198** Effect of  $T_w/T_0$  on streamlines,  $\theta_w = 14^\circ$ , Case X2.

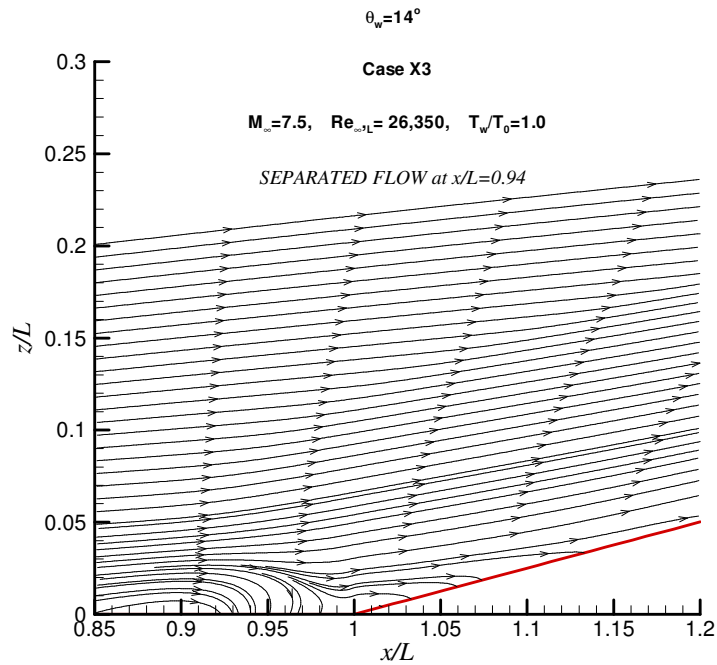


**Figure 8.199** Effect of  $T_w/T_0$  on streamlines,  $\theta_w = 14^\circ$ , Case X3.

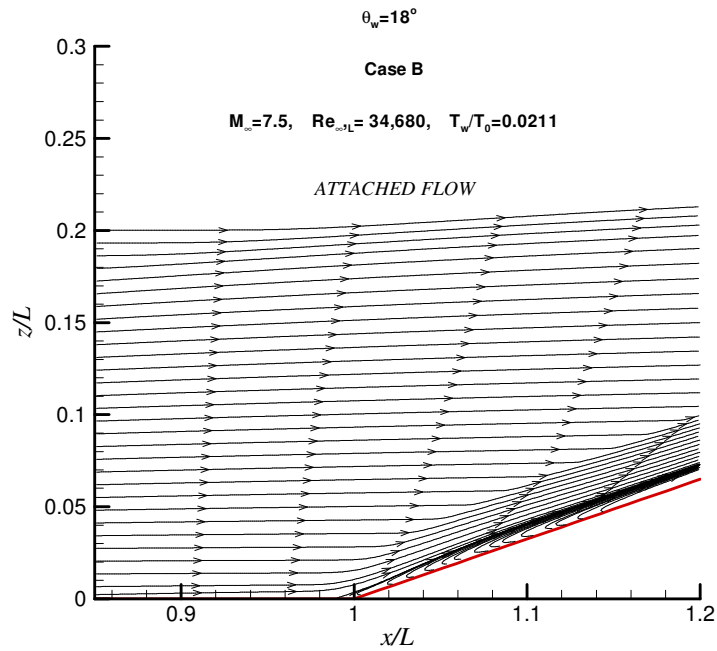


**Figure 8.200** Effect of  $T_w/T_0$  on streamlines,  $\theta_w = 18^\circ$ , Case B.

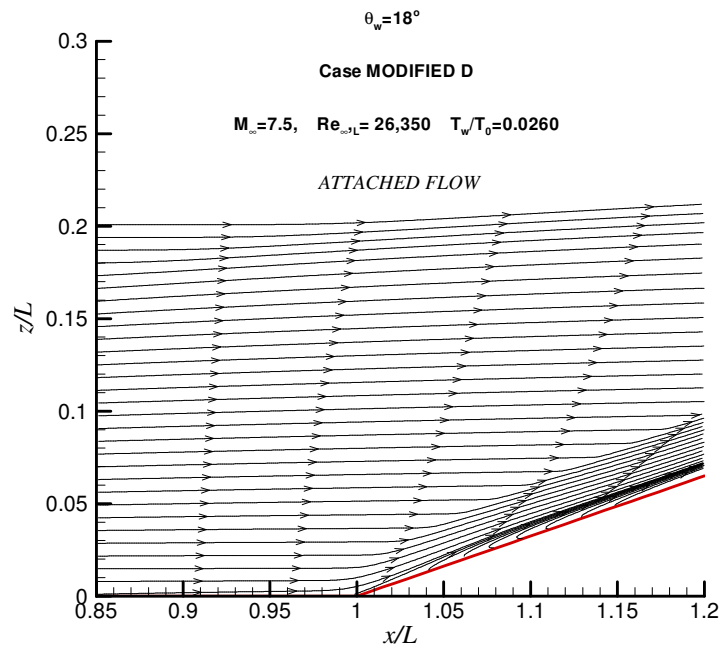


**Figure 8.201** Effect of  $T_w/T_0$  on streamlines,  $\theta_w = 18^\circ$ , Case Modified D.

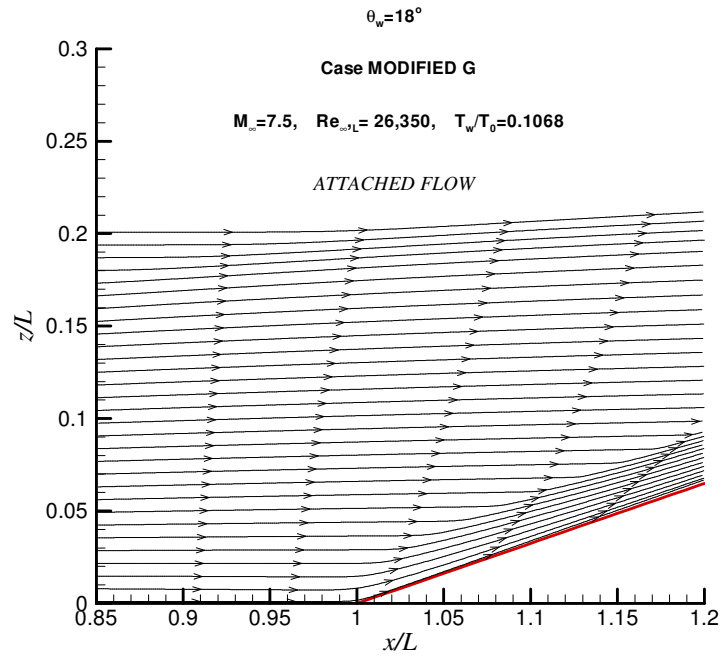


**Figure 8.202** Effect of  $T_w/T_0$  on streamlines,  $\theta_w = 18^\circ$ , Case Modified G.

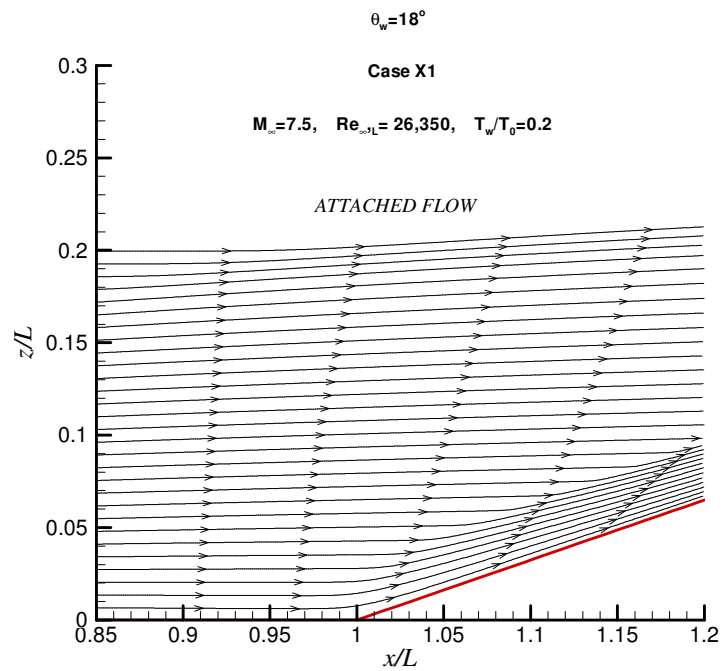


**Figure 8.203** Effect of  $T_w/T_0$  on streamlines,  $\theta_w = 18^\circ$ , Case X1.

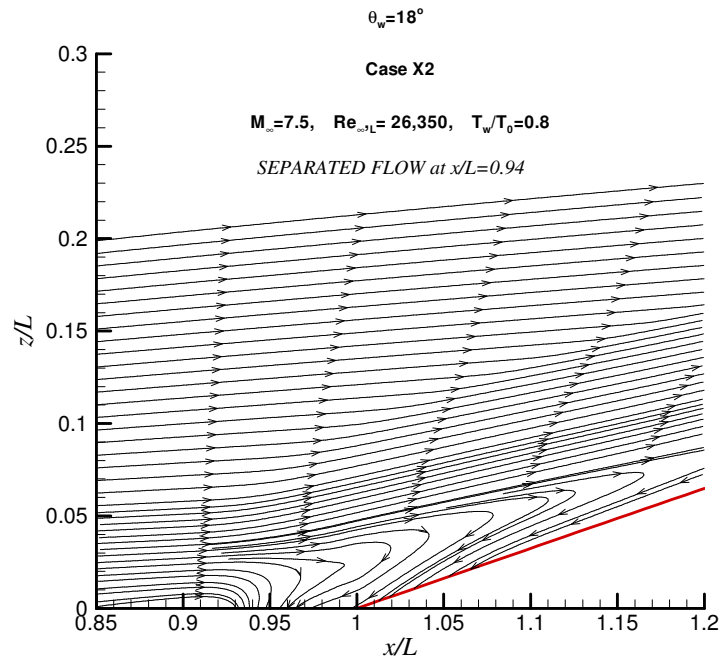


**Figure 8.204** Effect of  $T_w/T_0$  on streamlines,  $\theta_w = 18^\circ$ , Case X2.

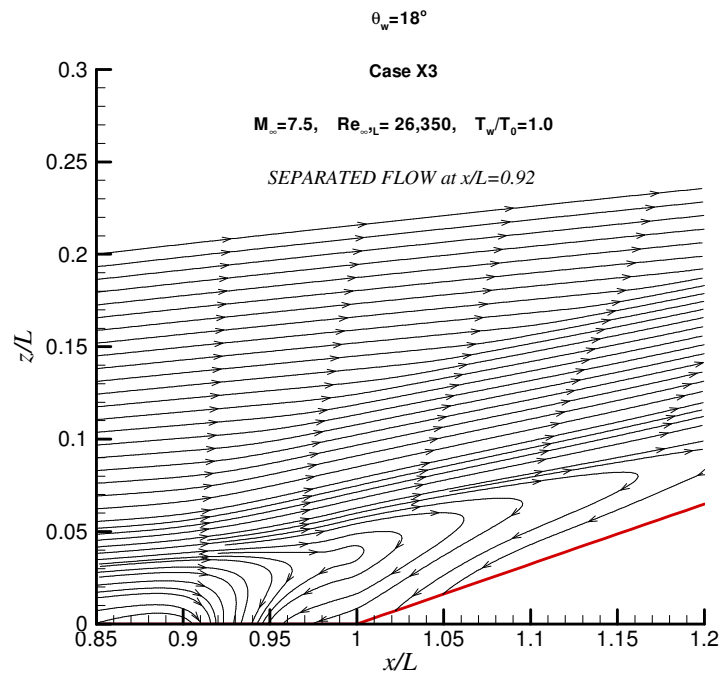


**Figure 8.205** Effect of  $T_w/T_0$  on streamlines,  $\theta_w = 18^\circ$ , Case X3.

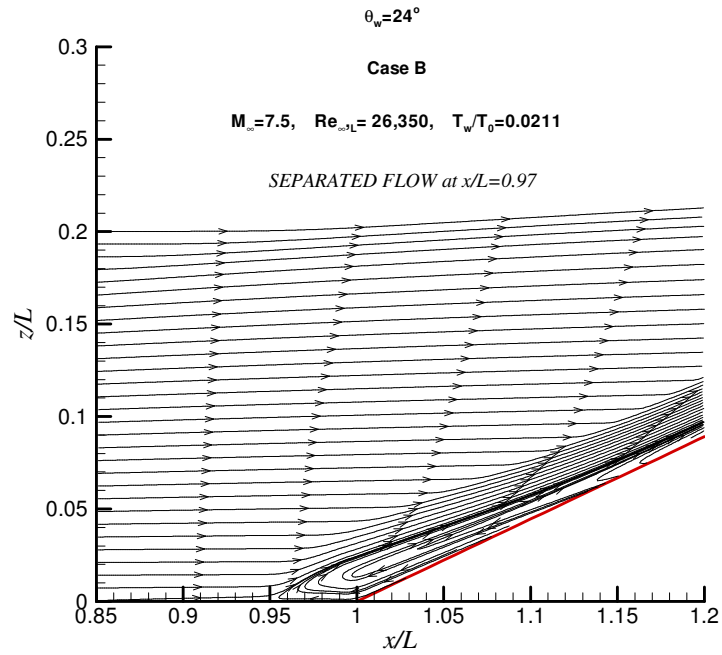


**Figure 8.206** Effect of  $T_w/T_0$  on streamlines,  $\theta_w = 24^\circ$ , Case B.

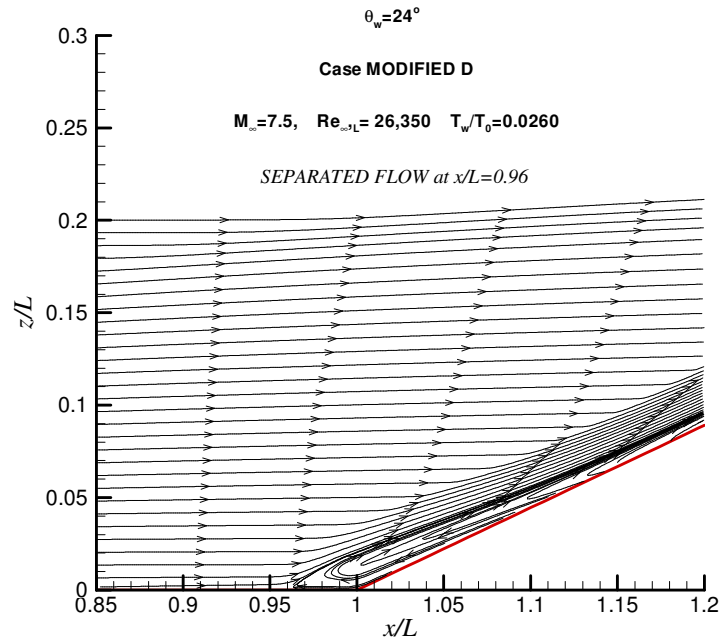


**Figure 8.207** Effect of  $T_w/T_0$  on streamlines,  $\theta_w = 24^\circ$ , Case Modified D.

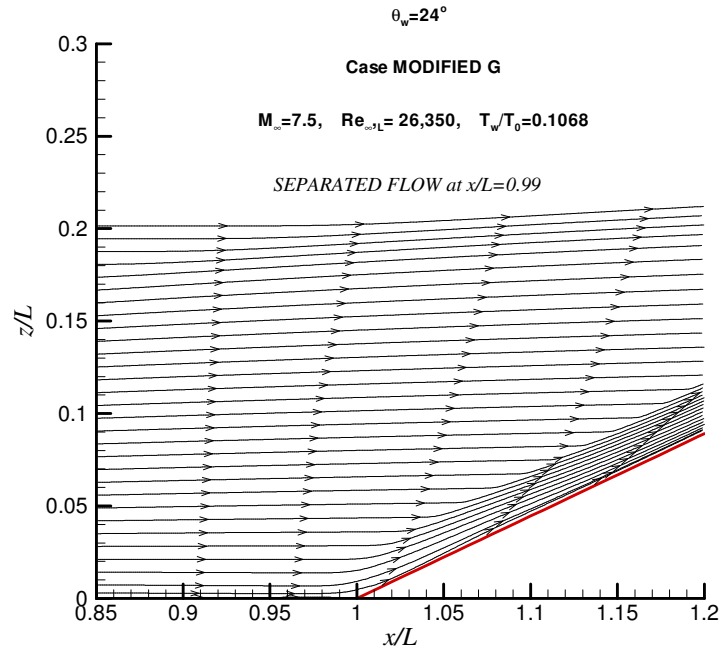


**Figure 8.208** Effect of  $T_w/T_0$  on streamlines,  $\theta_w=24^\circ$ , Case Modified G.

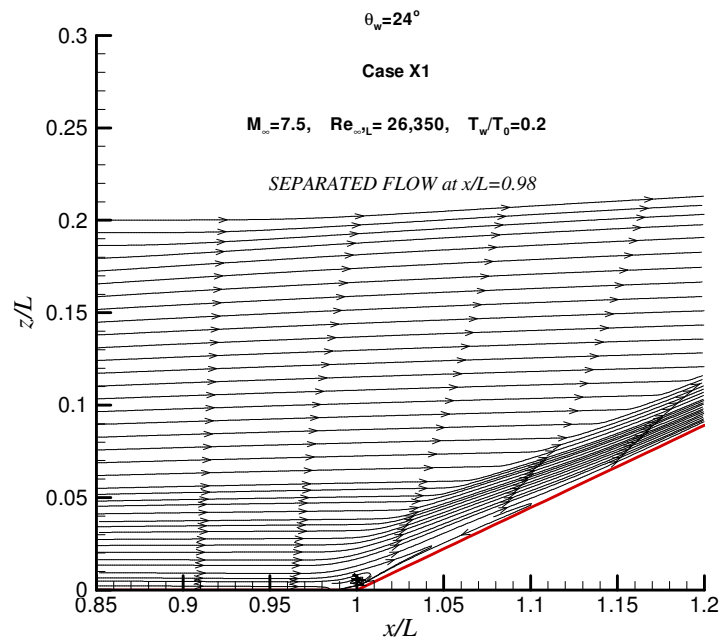


**Figure 8.209** Effect of  $T_w/T_0$  on streamlines,  $\theta_w=24^\circ$ , Case X1.

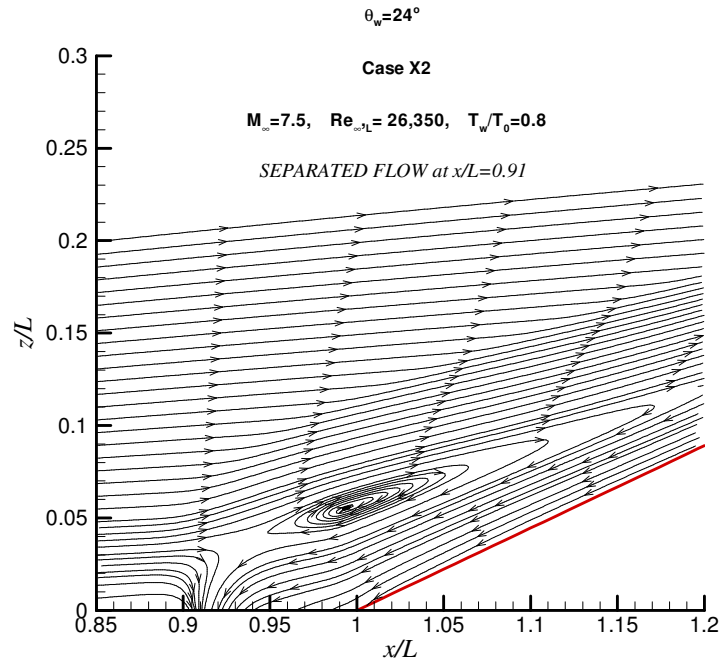


**Figure 8.210** Effect of  $T_w/T_0$  on streamlines,  $\theta_w=24^\circ$ , Case X2.

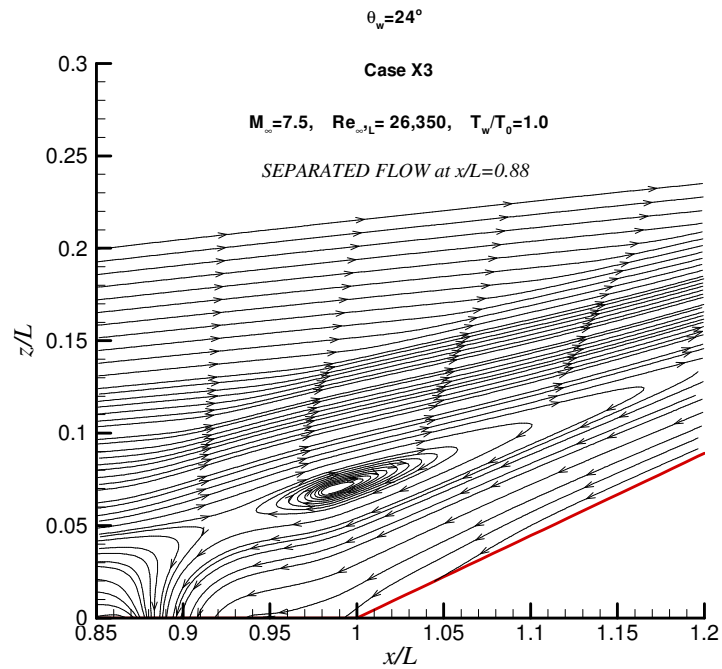


**Figure 8.211** Effect of  $T_w/T_0$  on streamlines,  $\theta_w=24^\circ$ , Case X3.

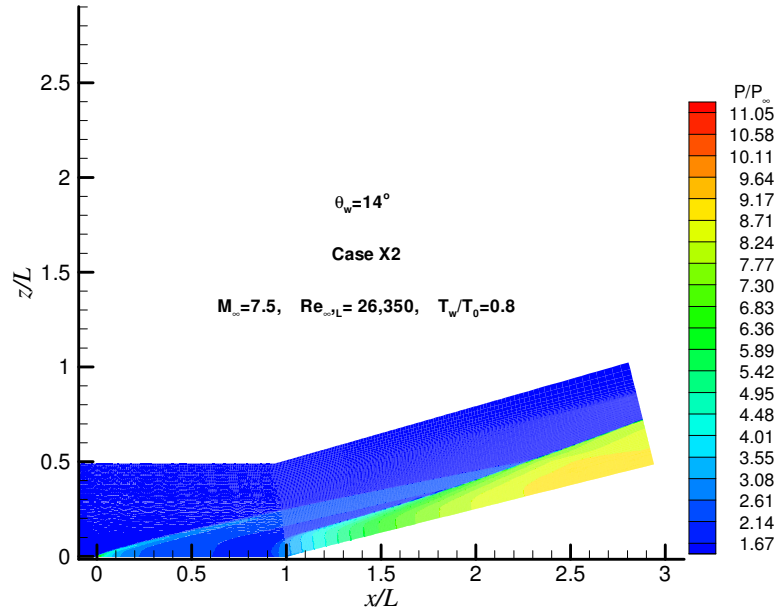


Figure 8.212 Effect of  $T_w/T_0$  on pressures contours,  $\theta_w=14^\circ$  Case X2.

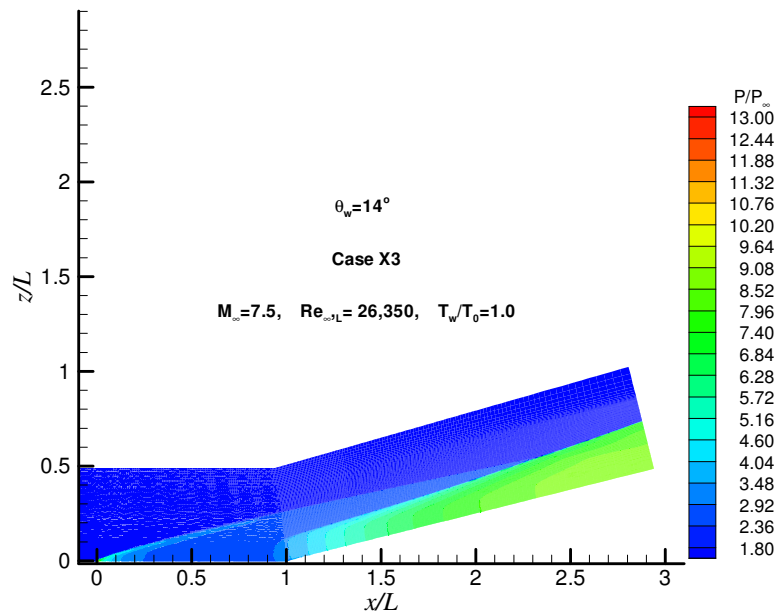
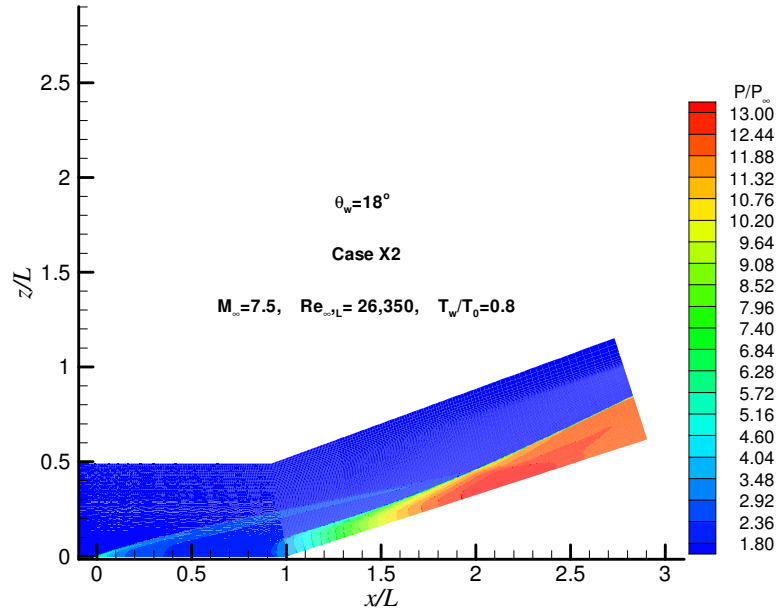
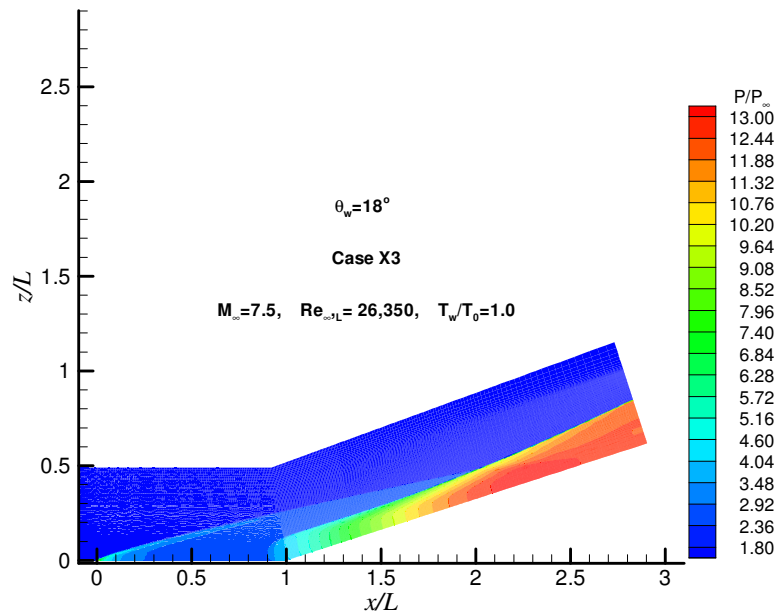


Figure 8. 213 Effect of  $T_w/T_0$  on pressures contours,  $\theta_w=14^\circ$  Case X3.



**Figure 8.214** Effect of  $T_w/T_0$  on pressures contours,  $\theta_w = 18^\circ$  Case X2.



**Figure 8.215** Effect of  $T_w/T_0$  on pressures contours,  $\theta_w = 18^\circ$  Case X3.

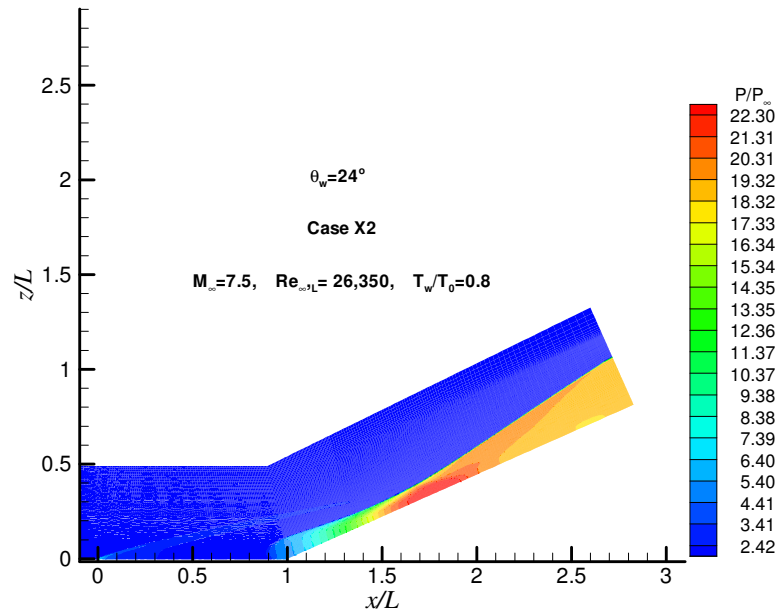


**Figure 8. 216** Effect of  $T_w/T_0$  on pressures contours,  $\theta_w = 24^\circ$  Case X2.

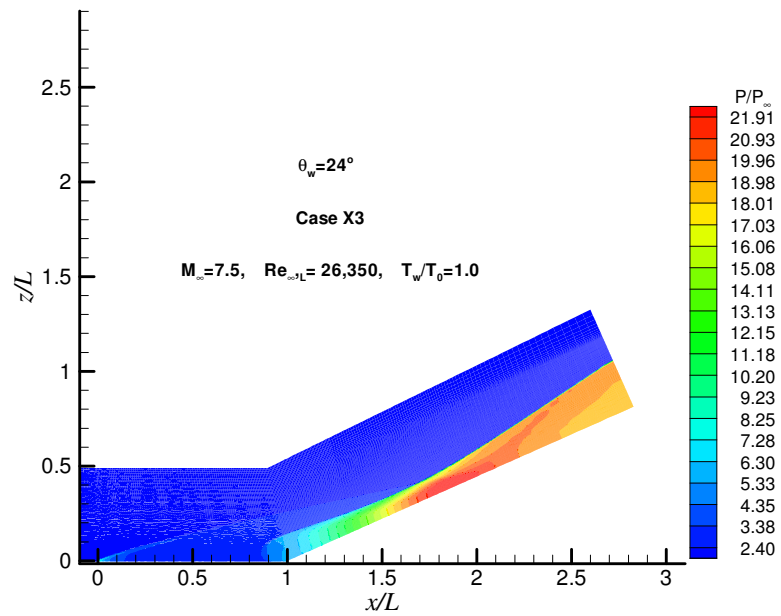


**Figure 8. 217** Effect of  $T_w/T_0$  on pressures contours,  $\theta_w = 24^\circ$  Case X3.

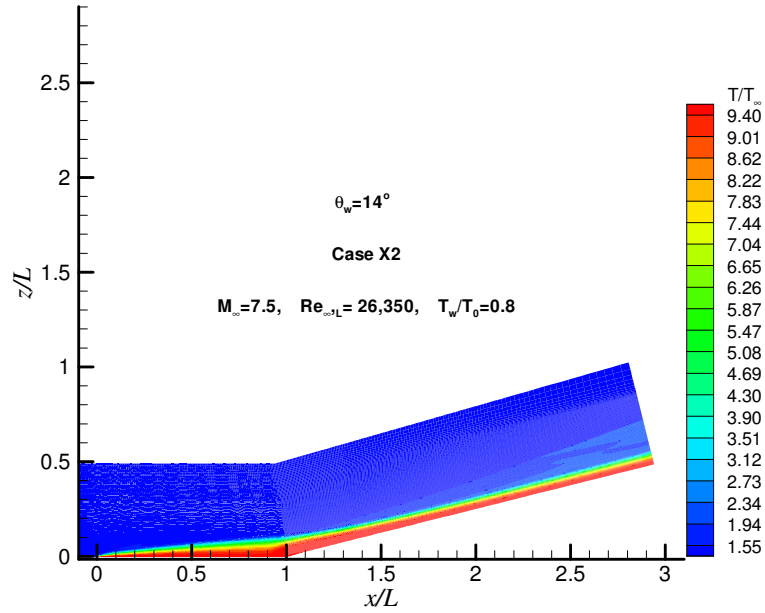


**Figure 8. 218** Effect of  $T_w/T_0$  on temperature contours,  $\theta_w=14^\circ$  Case X2.

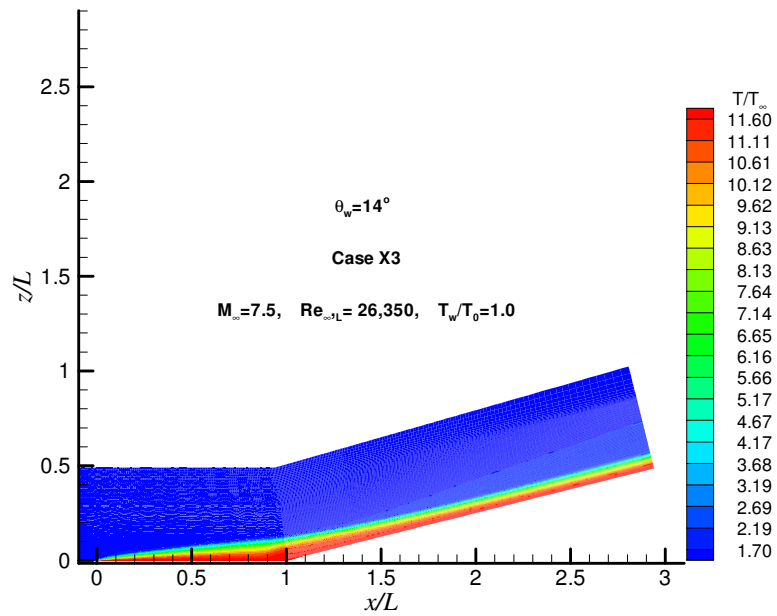


**Figure 8. 219** Effect of  $T_w/T_0$  on temperature contours,  $\theta_w=14^\circ$  Case X3.

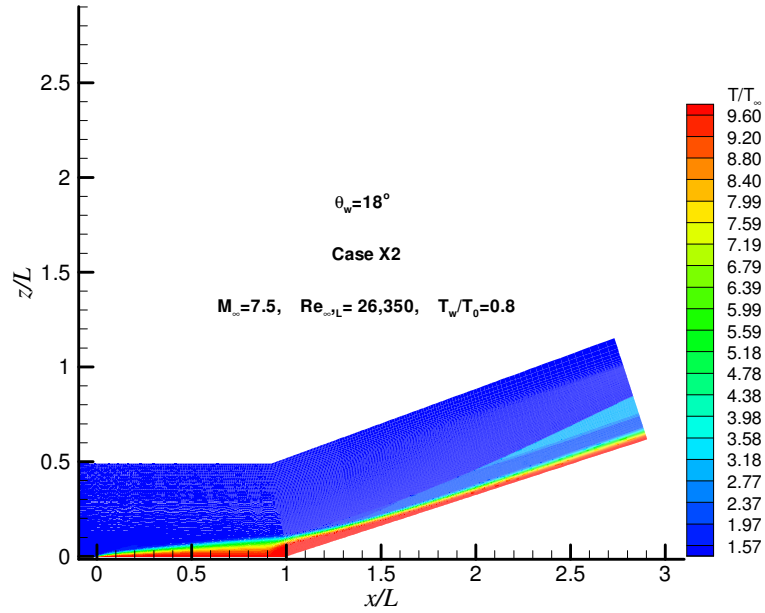


Figure 8. 220 Effect of  $T_w/T_0$  on temperature contours,  $\theta_w=18^\circ$  Case X2.

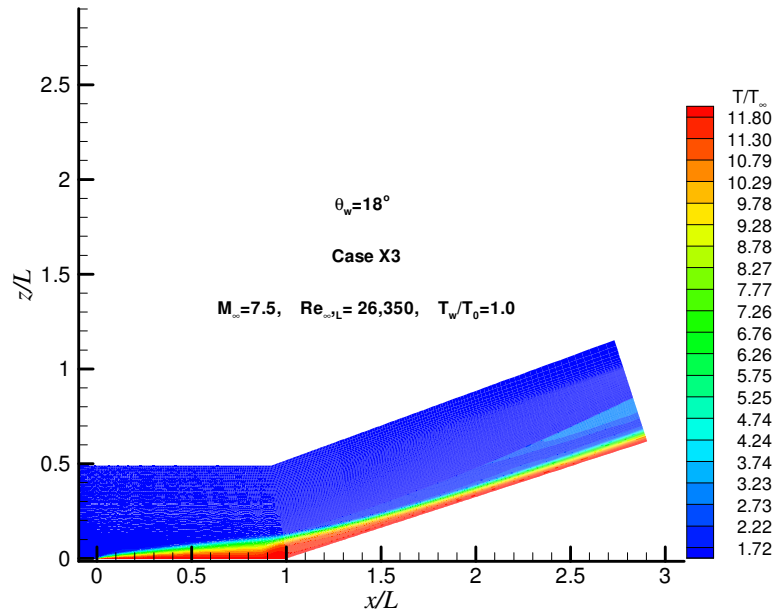
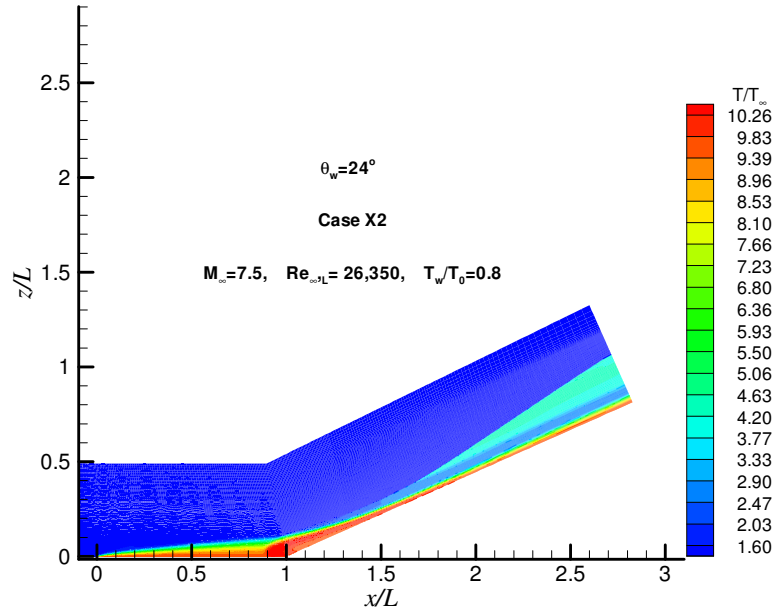
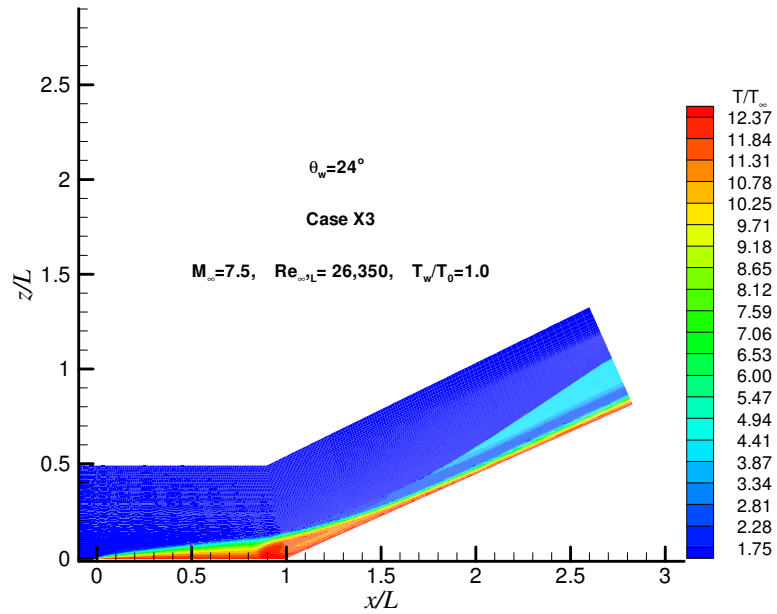


Figure 8. 221 Effect of  $T_w/T_0$  on temperature contours,  $\theta_w=18^\circ$  Case X3.



**Figure 8. 222** Effect of  $T_w/T_0$  on temperature contours,  $\theta_w = 24^\circ$  Case X2.



**Figure 8. 223** Effect of  $T_w/T_0$  on temperature contours,  $\theta_w = 24^\circ$  Case X3.

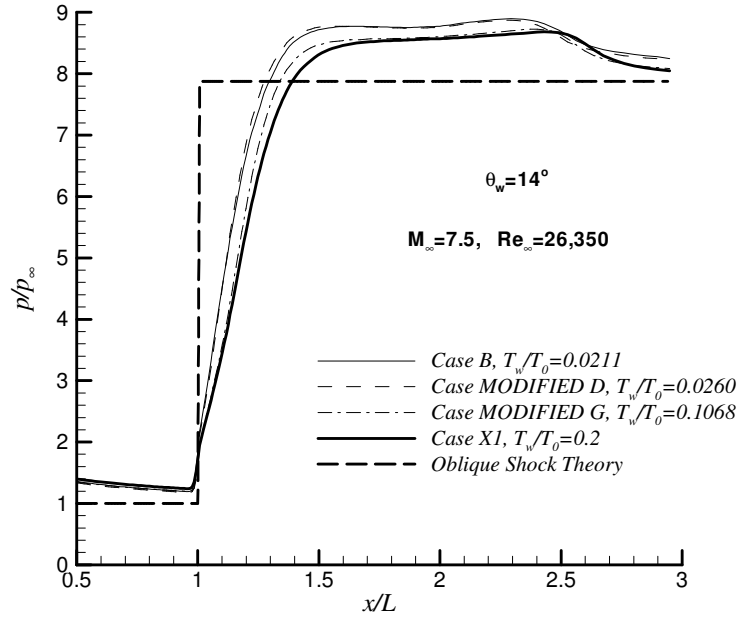


Figure 8.224 Effect of  $T_w/T_0$  on surface pressures,  $\theta_w = 14^\circ$

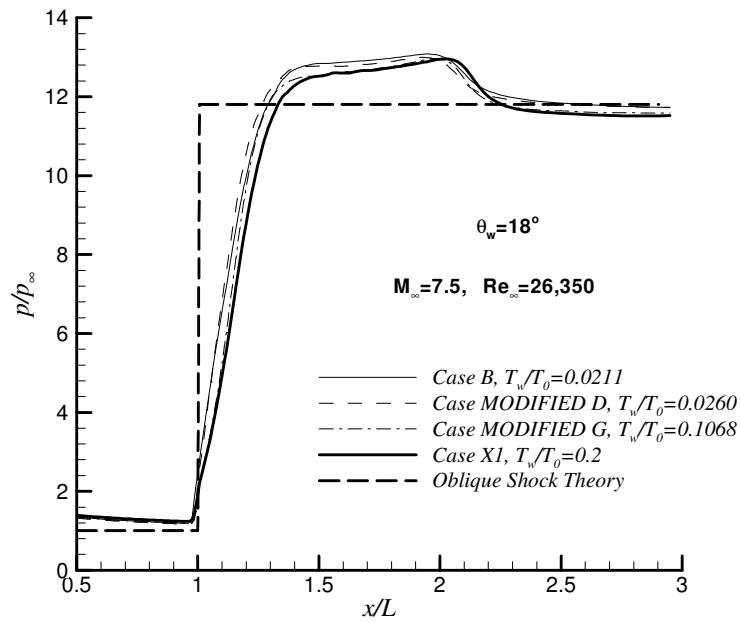
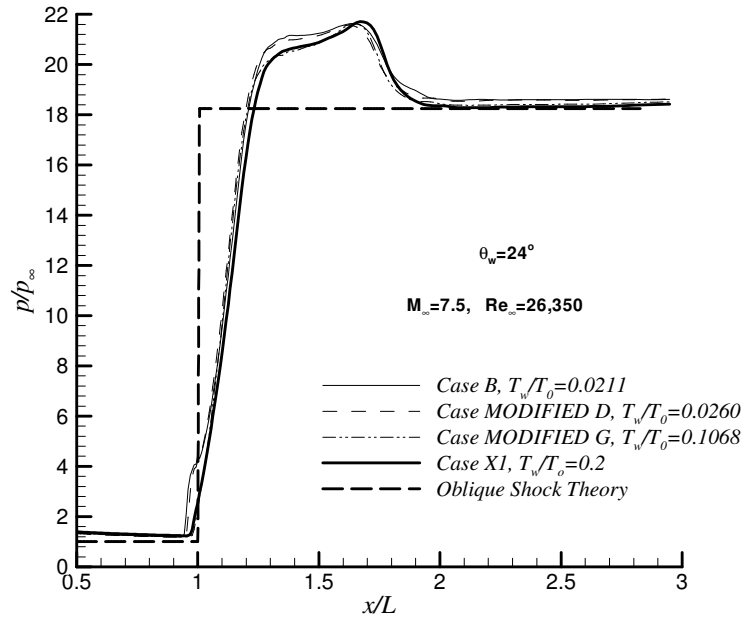
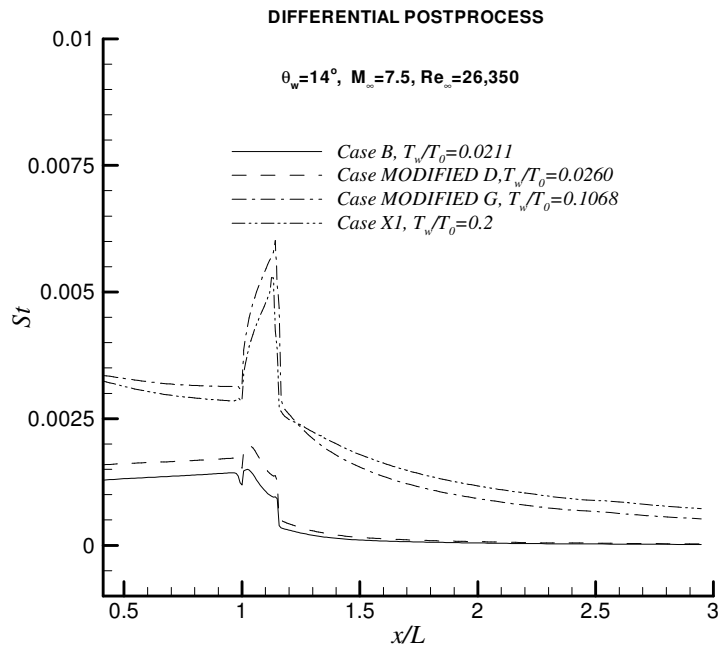


Figure 8.225 Effect of  $T_w/T_0$  on surface pressures,  $\theta_w = 18^\circ$



**Figure 8.226** Effect of  $T_w/T_0$  on surface pressures,  $\theta_w = 24^\circ$



**Figure 8.227** Effect of  $T_w/T_0$  on heat transfer,  $\theta_w = 14^\circ$

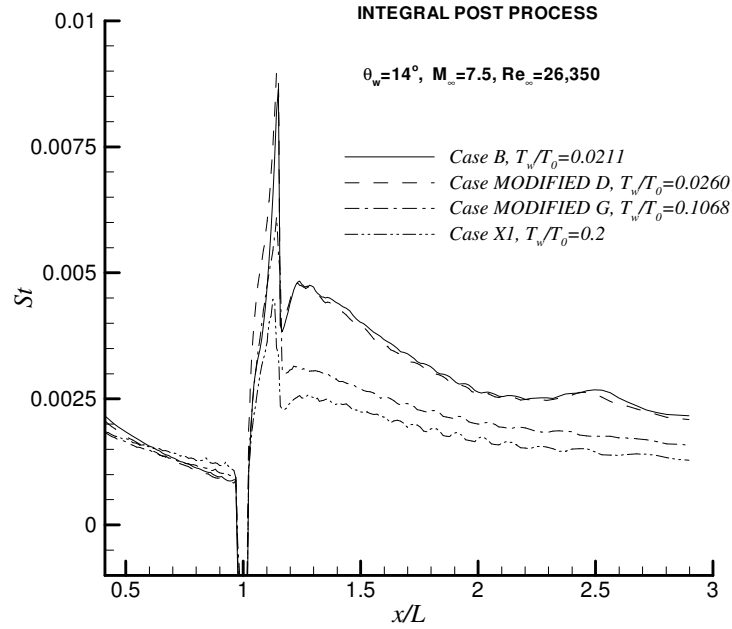


**Figure 8.228** Effect of  $T_w/T_0$  on heat transfer,  $\theta_w = 14^\circ$ .

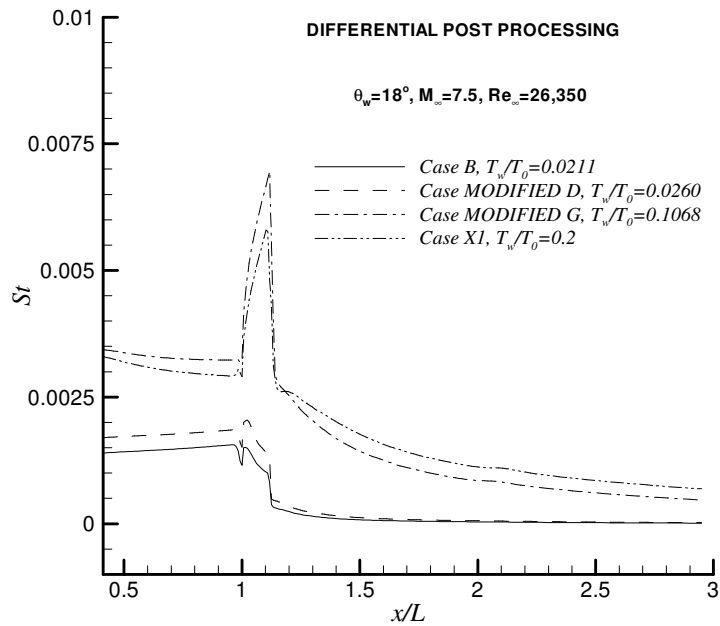


**Figure 8.229** Effect of  $T_w/T_0$  on heat transfer,  $\theta_w = 18^\circ$ .

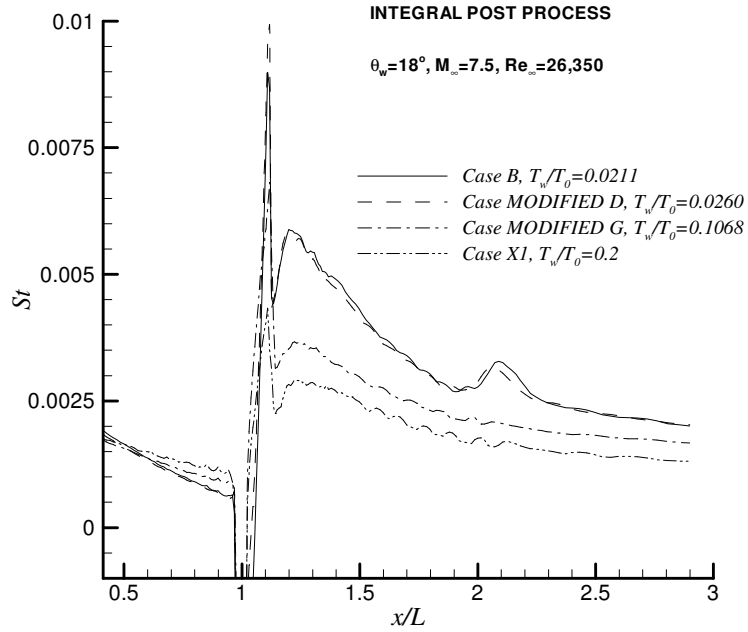


**Figure 8.230** Effect of  $T_w/T_0$  on heat transfer,  $\theta_w=18^\circ$ .

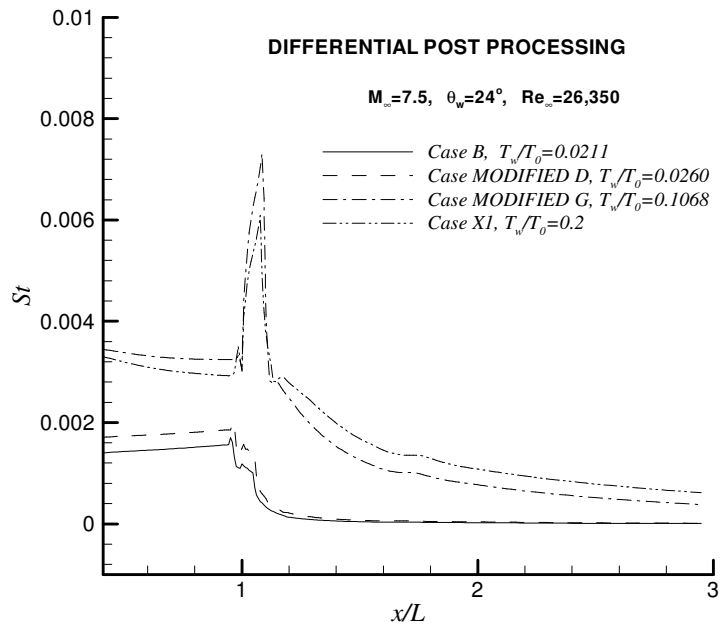


**Figure 8.231** Effect of  $T_w/T_0$  on heat transfer,  $\theta_w=24^\circ$ .

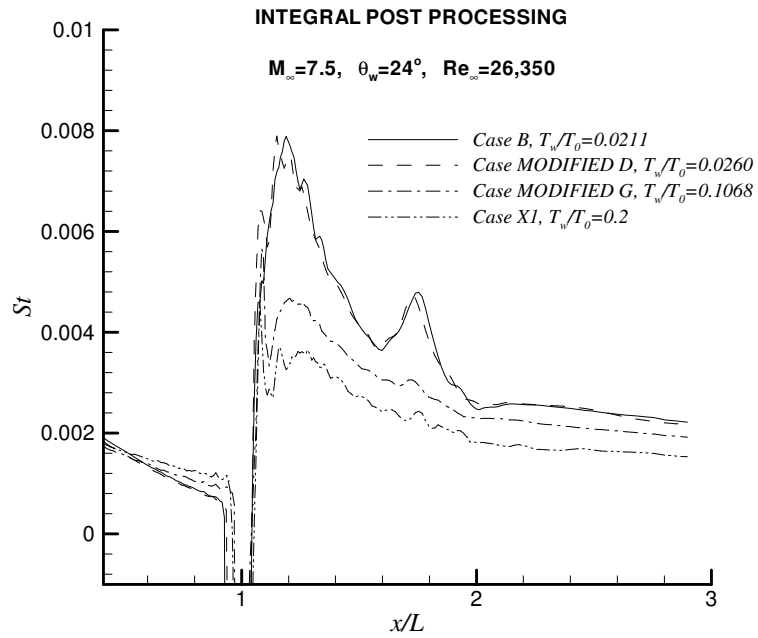


**Figure 8.232** Effect of  $T_w/T_0$  on heat transfer,  $\theta_w=24^\circ$ .

## CHAPTER 9

### CONCLUSION

In this thesis; numerical solutions of hypersonic, high temperature, perfect gas flows over various geometries are performed by solving three dimensional, thin layer, compressible, Navier-Stokes equations.

Two different basic geometries are considered. The first geometry was a flat plate at zero angle of incidence with the flow direction. The second geometry was a compression corner with seven different corner angles,  $\theta_w = 5^\circ, 10^\circ, 14^\circ, 15^\circ, 16^\circ, 18^\circ, 24^\circ$ .

It was assumed that the real gas effects are not significant for the cases solved. The test geometries and the flow conditions of some of the test cases are selected to correspond to the experimental work of Mallinson et al. [7, 8] for comparison purposes. The flow characteristics of the Mallinson et al. [7, 8] study, can be considered as two dimensional and laminar. During the present analysis, eight different free-stream and wall conditions (flow conditions or test cases) are selected: Three of those flow conditions correspond to the experiments and numerical studies of Mallinson et al. [8] and these test conditions are referred to as B, D and G by Mallinson et al. The flow conditions X1, X2 and X3, are chosen according to the  $T_w/T_0$  values to investigate the effect of the  $T_w/T_0$  on the flow characteristics, boundary layer variables etc. The flow conditions Modified D and Modified G are corresponded Case D and G of Mallinson et al. [8] with the differences of  $M_\infty$  and  $Re_\infty$ .

The shock/shock wave, shock wave/boundary layer interactions are studied. Surface heat transfer rates, local skin friction coefficients are obtained. The

effects of wall-to stagnation temperature ratio ( $T_w/T_0$ ) on the flow and boundary layer characteristics are obtained. The effects of corner angle ( $\theta_w$ ) on the main features of the flow field are studied. Results are compared with the available experimental, theoretical and/or numerical results.

The convergence and iteration histories of the solutions over both geometries and for all the flow conditions show that the convergence rates are satisfactory. It was observed that L2 norm of the residual dropped at least three orders of magnitude for all the cases solved.

For hypersonic flow over a flat plate, in a direction normal to surface, between the leading edge shock and the edge of the thermal boundary layer, the flow properties are not constant due to a slight expansion. The leading edge shock is caused by the growth of the boundary layer displacement thickness. The flow just past the leading edge shock deflects away from the surface. On the other hand, the flow just at the edge of the thermal boundary layer is almost parallel to the surface. Since, the flow variables are not constant between the edge of the boundary layer and the shock, determination of the boundary layer edge requires special care. Thermal boundary layer was thicker than the momentum boundary layer and the boundary layer edge variables ( $U_e$ ,  $T_e$ , etc.) are obtained at the thermal boundary layer edge. The heat transfer parameter ( $f_{qw}$ ) makes a small maximum before it goes to zero asymptotically at the edge of the thermal boundary layer. This small maximum was used as criteria to locate the edge of the thermal boundary layer, thus the edge conditions, in the present study.

For the flow over a flat plate, the pressure distributions obtained from the present solutions are compared with the available experimental data [8] and Stollery & Bates Theory [61]. It can be seen that there are strong viscous interactions for all the cases due to the growth of the boundary layer around the leading edge. The obtained results are similar to experimental data and theory.

The obtained pressure distributions over compression corners with seven corner angles from  $\theta_w = 5^\circ - 24^\circ$  and for the eight flow conditions are compared with available experimental data of Mallinson [8] et al, Stollery & Bates [61] perfect

gas theory and analytic solution (oblique shock theory). It is seen that the separation region and the maxima of the pressure increases as the corner angle is increased.

During this study, one of the most critical flow properties was considered as wall to stagnation temperature ratio,  $T_w/T_0$ . The effects of  $T_w/T_0$  on the heat transfer and pressure distributions and the boundary layer flow variables are presented for the flat plate and compression corners. The flow conditions B, Modified D, Modified G, X1, X2 and X3 are chosen according to the  $T_w/T_0$  values to compare the results. For these six flow conditions;  $M_\infty$  was 7.5 and  $Re_{\infty,L}$  was 26,350.  $T_w/T_0$  ratios varied from 0.0211 to 1.0.

The flow conditions X2 ( $T_w/T_0 = 0.8$ ) and X3 ( $T_w/T_0 = 1.0$ ) are particularly more difficult cases to converge.

For the flow over the compression corners, it is concluded that the flow has tendency to separate as  $T_w/T_0$  ratio increases. It is also predicted that the flow has a tendency to separate as the corner angle increases and as a consequence separation region becomes larger.

For the flow over the flat plate, it is observed that with the increasing  $T_w/T_0$  ratio the pressure increases for fixed  $M_\infty$  and  $Re_\infty$ . For compression corners, it can be said that  $T_w/T_0$  ratio has a minor influence on the pressure distribution for fixed  $M_\infty$  and  $Re_\infty$ .

For the flow over a flat plate, it was shown that with the increasing  $T_w/T_0$  ratio the skin friction increases for fixed  $M_\infty$  and  $Re_\infty$ .

For both geometries, the results of the differential post processing show that the heat transfer increases by increasing  $T_w/T_0$  ratio for fixed  $M_\infty$  and  $Re_\infty$ . On the other hand the results of the integral post processing show that the heat transfer decreases by increasing  $T_w/T_0$  ratio. For lower  $T_w/T_0$  ratios there is more temperature difference between the wall and the freestream, therefore there should be more heat transfer. From here we may conclude that the integral post processing is more reliable.

It is observed that, the corner angle ( $\theta_w$ ) has a strong impact on separation and pressure distribution. The separation length and surface pressure increase with increasing  $\theta_w$  for fixed  $M_\infty$  and  $Re_\infty$ .

In this study, temperature values inside the boundary layer are up to 3,000 K and continuum flow assumption is valid, for that reason perfect gas solutions are performed and real gas effects are not considered throughout the solutions.

At high speeds and temperatures, the molecular collisions are such that chemical reactions occur. The flowing gas medium then behaves as a reacting and diffusing mixture, and the flow properties must be described by non-equilibrium chemical thermodynamics. Real-gas effects are important in hypersonic flows both in terms of their influence on aerodynamic performance and their effect on aerothermodynamic heating. The most problems associated with lifting vehicles, the dominant real gas effects are associated with the dissociation of oxygen and nitrogen. Real-gas complexities include thermal and chemical time scales, multiple gas species, and coupled fluid/chemical processes.

In the present work for the hypersonic flows over compression corners, real-gas effects are not taken into account. As a suggestion for future work, real-gas phenomena can be included into the code. As a result of this addition, the heat transfer and skin friction predictions may be improved.

## REFERENCES

1. Bertin, J. J., Cummings, R. M., "Fifty years of hypersonics: where we've been, where we're going", *Progress in Aerospace Sciences* 39 (2003) 511–536, 2003.
2. Anderson, J. D. Jr., "Hypersonic and High Temperature Gas Dynamics", McGrawHill, 1989.
3. AGARD AR-319, "Hypersonic Experimental and Computational Capability, Improvement and Validation", May 1996.
4. Thomas, J. L., Dwoyer, D. L., Kumar, A., "Computational Fluid Dynamics for Hypersonic Airbreathing Aircraft. In: Desideri JA, Glowinski, R., Periaux, J, editors. *Hypersonic Flows for reentry problems*, Vol. I. Berlin: Springer, 1991.
5. Holden, M. S., "Boundary Layer Displacement and Leading Edge Bluntness Effects on Attached and Separated Laminar Boundary Layers in a Compression Corner", Part: II Experimental Study. *AIAA J.*, 1971, 9(1). 84-93.
6. Hankey, W. L. and Holden, M. S., "Two-Dimensional Shock Wave/Boundary Layer Interactions in High Speed Flows", *AGARDograph No. 203*, Part II, 1975.
7. Mallinson, S.G., Gai, S.L., Mudford, N.R., "The Boundary Layer on a Flat Plate in Hypervelocity Flow", *The Aeronautical Journal of the Royal Aeronautical Society*, April 1996.
8. Mallinson, S. G., Gai, S. L., Mudford, N. R., "The Interaction of a shock wave with a Laminar Boundary Layer at a Compression Corner in High-Enthalpy Flows Including Real Gas Effects", *Journal of Fluid Mechanics*, Vol. 342, pp. 1-35, 1997.

9. Simeonides, G. and Haase, W., "Experimental And Computational Investigations Of Hypersonic Flow About Compression Ramps", J. Fluid Mech., Vol. 283, pp. 17-42, 1992.
10. Schulte, D., Henckels, A., and Neubacher, R., "Manipulation of Shock/Boundary Layer Interactions in Hypersonic Inlets", Journal of Propulsion and Power, Vol. 17, NO. 3, May-June 2001.
11. Hozumi, K., Yamamoto, Y, and Fujii, K., "Investigation of Hypersonic Compression Ramp Heating at High Angles of Attack", Journal of Spacecraft and Rockets, Vol. 38, No. 4, July-August 2001.
12. Chanetz, B., Benay, R., Bousquet, J. M., Bur, R., Pot, T., Grasso, F., Moss, J., "Experimental and Numerical Study of the Laminar Separation in Hypersonic Flow", Aerospace Science and Technology, No. 3, 205-218,1998.
13. Rudy, D. H., Thomas, J. L., Kumar, A., Gnoffo, P. A., and Chakravarthy, S. R., "Computation Of Laminar Hypersonic Compression Corner Flows", AIAA J., Vol. 29, No. 7, pp. 1108-1113, 1991.
14. Brenner, G., Gerhold, T., Hanneman, K., and Rues, D., "Numerical Simulation of Shock/Shock and Shock Wave/Boundary Layer Interactions in Hypersonic Flows", Computers Fluids Vol. 22, No. 4/5, pp. 427-439, 1993.
15. Grasso, F. and Marini, M., "Analysis of Hypersonic Shock Wave/Boundary Layer Interaction Phenomena", Computers & Fluids, Vol. 25, No. 6, pp. 561-581, 1996.
16. D'Ambrosio, D., "Numerical Prediction of Laminar Shock/Shock Interactions in Hypersonic Flow", Journal of Spacecraft and Rockets, Vol. 40, No. 2, March-April 2003.
17. Navarro-Martinez, S., Tutty, O. R., "Numerical Simulation of Görtler Vortices in Hypersonic Compression Ramp", Preprint submitted to Elsevier Science, June 2004.
18. Dogrusoz, Ş., "Numerical Solution Of Hypersonic Compression Corner Flows", MSc. Study, METU, September 1999.

19. Carter, J. E., "Numerical Solution For Supersonic Laminar Flow Over A Two Dimensional Compression Corner", Lecture Notes in Physics ,Vol. 19, pp. 69-78, 1973.
20. Hung, C. M., MacCormack, R. W., "Numerical Solution For Supersonic And Hypersonic Turbulent Compression Corner Flows", AIAA J., Vol. 15, No. 3, pp. 410-416, 1977.
21. Lawrence, S. L., Tannehill, J. C., and Chaussee, D. S., "An Upwind Algorithm For The Parabolized Navier Stokes Equations", AIAA Paper 86-1117, 1986.
22. Ray, R., Erdos, J. and Pulsonetti, M. V., "Hypersonic Laminar Strong Interaction Theory and Experiment Revisited Using A Navier Stokes Code", AIAA Paper 87-1191, 1987.
23. Hollanders, H., Marmignon, C., "Navier Stokes High-Speed Flow Calculations By An Implicit Non-centered Method", AIAA Paper 89-0282, 1989.
24. Rudy, D. H., Kumar, A., Gnoffo, P. A., and Chakravarthy, S. R., "A Validation Study of Four Navier Stokes Codes for High-Speed Flows", AIAA Paper 89-1838, 1989.
25. Thajera, R. R., Prabhu, R. K., Morgan, K., Peraire, J., Peiro, J., and Soltani, S., "Applications of An Adaptive Unstructured Solution Algorithm To The Analysis Of High Speed Flows", AIAA Paper 90-0395, 1990.
26. Simeonides, G., "Hypersonic Shock-wave/Boundary-Layer Interactions Over Compression Corners", Ph. D. Thesis, von Karman Institute/University of Bristol, 1992.
27. Grasso, F. and Leone, G., "Chemistry Effects In Shock-wave/Boundary-Layer Interaction Problems", IUTAM Symposium On Aerothermochemistry of Spacecraft and Associated Hypersonic Flows, Marseille, France, 1992.
28. Leyland, P., "In Shock-wave/Boundary-Layer Interaction at Hypersonic Speeds By An Implicit Navier Stokes Solver", AIAA Paper 93-2938, 1993.
29. Lewis, J. E., Kunota, T. and Lees, L., "Experimental Investigation Of Supersonic Laminar, Two-Dimensional Boundary-Layer Separation In A

- Compression Corner With And Without Cooling”, AIAA J., Vol. 6, No. 1, pp. 7-14, 1968.
30. Erençil, M. E. and Dolling, D. S., “Unsteady Wave Structure Near Separation In A Mach 5 Compression Ramp Interaction”, AIAA J., Vol. 29, No. 5, pp. 728-735, 1991.
  31. Galassi, L., Scaggs, N., “Experimental and Computational Comparisons of Mach 6 High Reynolds Number Heat Transfer and Skin Friction”, AGARD-CP-514, Theoretical and Experimental Methods in Hypersonic Flows, 1993.
  32. Paciorri, R., Dieudonne, W., Degrez, G., Charbonnier and Deconinck, H., “Exploring The Validity Of The Spalart -Allmaras Turbulence Model For Hypersonic Flows”, Journal Of Spacecraft And Rockets, Vol. 35, No. 2, pp. 121-126, 1998.
  33. Aziz, Ş., “Numerical Solution of Hypersonic Boundary Layer and Compression Corner Flows (Extensive Research Results of PhD study)”, September 2005. Available from the author ([sdogrusoz@ssm.gov.tr](mailto:sdogrusoz@ssm.gov.tr)) and M. S. Kavsaoglu ([kavsaoglu@itu.edu.tr](mailto:kavsaoglu@itu.edu.tr)).
  34. Bertin, J. J., “Hypersonic Aerothermodynamics”, AIAA Education Series, 1994.
  35. Delery, J. M., “Shock Interference Phenomena in Hypersonic Flows”, notes from the Third Joint Europe/U.S. Short Course in Hypersonics, Aachen, Germany, October 1990.
  36. Markarian, C. F., “Heat Transfer in Shock Wave/Boundary Layer Interaction Regions”, Naval weapons Center NWC TP4485, November 1968.
  37. Hoffmann, K. A., “Computational Fluid Dynamics For Engineers”, Publication of Engineering Education System, Austin, Texas 78713.
  38. Laçin, F., “Navier-Stokes Analysis of Flow Aspect Ratio Rectangular Wings in Compressible Flow Fields”, METU, Dept. of Aeronautical Engineering, M. Sc. Thesis, September 1995.
  39. Sutherland, W., “The Viscosity of Gases and Molecular Force”, Philos. Mag., Ser.5, 1893.

40. Svehla, R. A., "Estimated Viscosities and Thermal Conductivities of Gases at High Temperatures", NASA TR R-132, 1962.
41. Obayashi, S., Matsushima, K., Fujii, K. and Kuwahara, K. "Improvements in Efficiency and Reliability for Navier-Stokes Computations Using the LU-ADI Factorization Algorithm", AIAA Paper 86-0338, Jan. 1986.
42. Obayashi, S. and Kuwahara, K., "LU Factorization of an Implicit Scheme for the Compressible Navier-Stokes Equations", AIAA Paper 84-1670, Snowmass, Colorado, June, 1984
43. Steger, J. L. and Warming, R. F., "Flux Vector Splitting of the Inviscid Gasdynamic Equations with Application to Finite Difference Method", Journal of Computational Physics, Vol. 40, pp, 263-293, 1981.
44. MacCormack, W., "A Numerical Method for Solving the Equations of Compressible Viscous Flow", AIAA Journal, Vol. 20, No. 9, Sept., pp.1275-1281, 1982.
45. Kaynak, Ü., Yılmaz, Ş., Çete, R., "Accuracy Improvements for Transonic Wing Flows Using a Nonequilibrium Algebraic Turbulence Model", AIAA Paper 98-5573, World Aviation Conference, Anaheim, CA. Sept., 1998.
46. Obayashi, S., Guruswamy, G. and Goorgian, P., "Application of a Streamwise Upwind Algorithm for Unsteady Transonic Computations Over Oscillating Wings", AIAA-90-3103, August 1990, Portland, OR.
47. Obayashi, S. and Fuji, K., "Computation of Three Dimensional Viscous Flows with the LU factored scheme", AIAA-85-1510, Cincinnati, OH.
48. Pulliam, T. H. and Chaussee, D. S., "A Diagonal Form of an Implicit Approximate Factorization Algorithm", Journal of Computational Physics, Vol. 39, No. 2, 1981, pp. 347-363
49. Hirsch, C., "Numerical Computation of Internal and External Flows", A Wiley - Interscience Publication, 1990
50. Tarhan, E., "An Approach to Numerical Simulation of Three-Dimensional Flow With Spray Combustion", METU, Dept. of Aeronautical Engineering, M.Sc. Thesis, June 1996.

51. Stalker, R. J., "Development of a Hypervelocity Wind Tunnel", *Aeronaut J.*, 1972, 76, pp 374-384.
52. Hirschfelder, J. O., Curtis, C. F., and Bird, R. B., "Molecular Theory of Gases and Liquids", Wiley & Sons New York, 1967.
53. Hansen, C. F., "Approximations for the Thermodynamic and Transport Properties of High-Temperature Air" NASA Tech Rept R-50, 1959.
54. Mallinson, S. G., "Shock Wave-Boundary Layer Interaction at a Compression Corner in Hypervelocity Flow", PhD Thesis, University College (UNSW), 1994.
55. Şen, S. T., "Numerical Solution Of Various Test Cases By Using A Thin Layer Navier-Stokes Code", M.Sc. Thesis, METU, Dept. of Aeronautical Engineering, September 1994.
56. White, F. M., "Viscous Fluid Flow", McGraw-Hill, 1974.
57. Eckert, E. R. G., *Journal of Aeronautical Science*, Vol. 22, pp. 585-587.
58. Bertram, M. H. and Blackstock, T. A., NASA Technical Note D-798, 1961
59. Lees, L. and Probstein, R. F., Princeton University Aeronautical Engineering Lab. Report, 1952
60. Van Driest, E. R., "Investigation of Laminar Boundary Layer in Compressible Fluids Using the Crocco Method", NACA TN 2597, January 1952.
61. Stollery J. L., and Bates L., *J. Fluid Mechanics*, Vol. 63, part 1, pp. 145-156, 1974.
62. Hankey, W.L., Holden, M.S., "Two-Dimensional Shock wave Boundary Layer Interactions in High speed Flows", AGARDograph No.203, Part II, 1975.
63. Hayakawa, K., Squire L.C., "The Effect of the Upstream Boundary Layer state on the shock interaction at a compression corner, *J. Fluid Mech.*, 1982, 122, 369-394.

64. Dogrusoz, S. Kavsoglu, M.S., Kaynak U., "Numerical Solution of Hypersonic Compression Corner Flows", 10th AIAA/NAL/NASDA/ISAS, International Space Planes and Hypersonic Systems and Technologies Conference April 24-27, 2001 Kyoto, JAPAN, AIAA 01-1750.
  
65. Amaratunga, S., Tutty, O.R. ad Roberts, G.T., "Computations of laminar, high enthalpy air flow over a compression ramp, Proceeding of the 3rd European Symposium on Aerothermodynamics for Space Vehicles (ESA, 1998), 213-220.

## APPENDIX A

### GENERALIZED COORDINATE TRANSFORMATION AND NONDIMENSIONALIZATION

The equation of motion are transformed from the physical space  $(x, y, z)$  to the computational space  $(\xi, \eta, \zeta)$  by the following relations [55]:

$$\tau = t \quad (\text{A.1})$$

$$\xi = \xi(x, y, z) \quad (\text{A.2})$$

$$\eta = \eta(x, y, z) \quad (\text{A.3})$$

$$\zeta = \zeta(x, y, z) \quad (\text{A.4})$$

Writing the following differential equations:

$$dt = d\tau \quad (\text{A.5})$$

$$dx = x_\tau d\tau + x_\xi d\xi + x_\eta d\eta + x_\zeta d\zeta \quad (\text{A.6})$$

$$dy = y_\tau d\tau + y_\xi d\xi + y_\eta d\eta + y_\zeta d\zeta \quad (\text{A.7})$$

$$dz = z_\tau d\tau + z_\xi d\xi + z_\eta d\eta + z_\zeta d\zeta \quad (\text{A.8})$$

where  $x_\tau$  represents partial derivative of  $x$  with respect to  $\tau$  (i.e.  $\frac{\partial x}{\partial \tau}$ )

Equations (A.9) through (A.12) can be written in a matrix form as [55];

$$\begin{bmatrix} dt \\ dx \\ dy \\ dz \end{bmatrix} = \begin{bmatrix} 1 & 0 & 0 & 0 \\ x_\tau & x_\xi & x_\eta & x_\zeta \\ y_\tau & y_\xi & y_\eta & y_\zeta \\ z_\tau & z_\xi & z_\eta & z_\zeta \end{bmatrix} \begin{bmatrix} d\tau \\ d\xi \\ d\eta \\ d\zeta \end{bmatrix} \quad (\text{A.9})$$

Reversing the role of the independent variables;

$$d\tau = dt \quad (\text{A.10})$$

$$d\xi = \xi_t dt + \xi_x dx + \xi_y dy + \xi_z dz \quad (\text{A.11})$$

$$d\eta = \eta_t dt + \eta_x dx + \eta_y dy + \eta_z dz \quad (\text{A.12})$$

$$d\zeta = \zeta_t dt + \zeta_x dx + \zeta_y dy + \zeta_z dz \quad (\text{A.13})$$

Equations (A.14) through (A.17) can be written in a matrix form as;

$$\begin{bmatrix} d\tau \\ d\xi \\ d\eta \\ d\zeta \end{bmatrix} = \begin{bmatrix} 1 & 0 & 0 & 0 \\ \xi_t & \xi_x & \xi_y & \xi_z \\ \eta_t & \eta_x & \eta_y & \eta_z \\ \zeta_t & \zeta_x & \zeta_y & \zeta_z \end{bmatrix} \begin{bmatrix} dt \\ dx \\ dy \\ dz \end{bmatrix} \quad (\text{A.14})$$

Comparing equations (A.13) and (A.18)

$$\begin{bmatrix} 1 & 0 & 0 & 0 \\ \xi_t & \xi_x & \xi_y & \xi_z \\ \eta_t & \eta_x & \eta_y & \eta_z \\ \zeta_t & \zeta_x & \zeta_y & \zeta_z \end{bmatrix} = \begin{bmatrix} 1 & 0 & 0 & 0 \\ x_\tau & x_\xi & x_\eta & x_\zeta \\ y_\tau & y_\xi & y_\eta & y_\zeta \\ z_\tau & z_\xi & z_\eta & z_\zeta \end{bmatrix}^{-1} \quad (\text{A.15})$$

Therefore the metrics can be form,

$$\xi_x = J(y_\eta z_\zeta - y_\zeta z_\eta), \quad \xi_y = J(z_\eta x_\zeta - z_\zeta x_\eta), \quad \xi_z = J(x_\eta y_\zeta - x_\zeta y_\eta) \quad (\text{A.16.1, 2, 3})$$

$$\eta_x = J(z_\xi y_\zeta - z_\zeta y_\xi), \quad \eta_y = J(x_\xi z_\zeta - x_\zeta z_\xi), \quad \eta_z = J(y_\xi x_\zeta - x_\xi y_\zeta) \quad (\text{A.16.4, 5, 6})$$

$$\zeta_x = J(y_\xi z_\eta - y_\eta z_\xi), \quad \zeta_y = J(x_\eta z_\xi - x_\xi z_\eta), \quad \zeta_z = J(x_\xi y_\eta - x_\eta y_\xi) \quad (\text{A.16.7, 8, 9})$$

$$\xi_t = -J[x_\tau (y_\eta z_\zeta - y_\zeta z_\eta) + y_\tau (x_\xi z_\eta - x_\eta z_\xi) + z_\tau (x_\eta y_\zeta - x_\zeta y_\eta)] \quad (\text{A.17.1})$$

$$\eta_t = -J \left[ x_\tau (y_\zeta z_\xi - y_\xi z_\zeta) + y_\tau (x_\xi z_\zeta - x_\zeta z_\xi) + z_\tau (x_\zeta y_\xi - x_\xi y_\zeta) \right] \quad (\text{A.17.2})$$

$$\zeta_t = -J \left[ x_\tau (y_\xi z_\eta - y_\eta z_\xi) + y_\tau (x_\eta z_\xi - x_\xi z_\eta) + z_\tau (x_\xi y_\eta - x_\eta y_\xi) \right] \quad (\text{A.17.3})$$

where J is the Jacobian of transformation defined by

$$J = \frac{\partial(\xi, \eta, \zeta)}{\partial(x, y, z)} = \frac{1}{x_\xi(z_\zeta y_\eta - z_\eta y_\zeta) - x_\eta(y_\xi z_\zeta - y_\zeta z_\xi) + x_\zeta(y_\xi z_\eta - y_\eta z_\xi)} \quad (\text{A.18})$$

The Navier Stokes equations may be nondimensionalized using freestream conditions and reference values.

$$\begin{aligned} t &= \frac{tU_\infty}{L}, & x &= \frac{x}{L}, & y &= \frac{y}{L}, & z &= \frac{z}{L}, \\ u &= \frac{u}{U_\infty}, & v &= \frac{v}{U_\infty}, & w &= \frac{w}{U_\infty}, & \rho &= \frac{\rho}{\rho_\infty U_\infty^2}, \\ \mu &= \frac{\mu}{\mu_\infty}, & \rho &= \frac{\rho}{\rho_\infty}, & T &= \frac{T}{T_\infty}, & e_t &= \frac{e_t}{U_\infty^2} \end{aligned}$$

In the present code  $a_\infty$  was used instead of  $U_\infty$ .

The nondimensional parameters are defined as;

$$\text{Reynolds number: } \text{Re}_\infty = \frac{\rho_\infty U_\infty L}{\mu_\infty}$$

$$\text{Prandtl number : } \text{Pr} = \frac{\mu C_p}{k}$$

The chain rule of partial differentiation provides the following expression for the Cartesian derivatives:

$$\frac{\partial}{\partial t} = \frac{\partial}{\partial \tau} + \xi_t \frac{\partial}{\partial \xi} + \eta_t \frac{\partial}{\partial \eta} + \zeta_t \frac{\partial}{\partial \zeta} \quad (\text{A.19})$$

$$\frac{\partial}{\partial x} = \xi_x \frac{\partial}{\partial \xi} + \eta_x \frac{\partial}{\partial \eta} + \zeta_x \frac{\partial}{\partial \zeta} \quad (\text{A.20})$$

$$\frac{\partial}{\partial y} = \xi_y \frac{\partial}{\partial \xi} + \eta_y \frac{\partial}{\partial \eta} + \zeta_y \frac{\partial}{\partial \zeta} \quad (\text{A.21})$$

$$\frac{\partial}{\partial z} = \xi_z \frac{\partial}{\partial \xi} + \eta_z \frac{\partial}{\partial \eta} + \zeta_z \frac{\partial}{\partial \zeta} \quad (\text{A.22})$$

After rearranging terms, the nondimensional form of the Navier Stokes equations in the computational space is given by;

$$\frac{\partial \bar{Q}}{\partial \tau} + \frac{\partial \bar{E}}{\partial \xi} + \frac{\partial \bar{F}}{\partial \eta} + \frac{\partial \bar{G}}{\partial \zeta} = \frac{\partial \bar{E}_v}{\partial \xi} + \frac{\partial \bar{F}_v}{\partial \eta} + \frac{\partial \bar{G}_v}{\partial \zeta} \quad (\text{A.23})$$

where

$$\bar{Q} = \frac{Q}{J} \quad (\text{A.24})$$

$$\bar{E} = \frac{1}{J} (\xi_t Q + \xi_x E + \xi_y F + \xi_z G) \quad (\text{A.25})$$

$$\bar{F} = \frac{1}{J} (\eta_t Q + \eta_x E + \eta_y F + \eta_z G) \quad (\text{A.26})$$

$$\bar{G} = \frac{1}{J} (\zeta_t Q + \zeta_x E + \zeta_y F + \zeta_z G) \quad (\text{A.27})$$

$$\bar{E}_v = \frac{1}{J} (\xi_x E_v + \xi_y F_v + \xi_z G_v) \quad (\text{A.28})$$

$$\bar{F}_v = \frac{1}{J} (\eta_x E_v + \eta_y F_v + \eta_z G_v) \quad (\text{A.29})$$

$$\bar{G}_v = \frac{1}{J} (\zeta_x E_v + \zeta_y F_v + \zeta_z G_v) \quad (\text{A.30})$$

## APPENDIX B

### BOUNDARY LAYER POST PROCESSING

After completion of a Navier-Stokes solution, the results are post processed to obtain boundary layer characteristics. Details of the formulations are given below.

#### B.1 GENERAL

##### Calculation of the Freestream Conditions

During post processing,  $\gamma$  is taken as 1.4. Pr at infinity is 0.72

The non-dimensional pressure at infinity is defined as

$$p_{\infty} = \frac{p_{\infty}}{\rho_{\infty} a_{\infty}^2} = \frac{\rho_{\infty} R T_{\infty}}{\rho_{\infty} \gamma R T_{\infty}} = \frac{1}{\gamma} \quad (\text{B.1})$$

The value of the non-dimensional density at the infinity is

$$\rho_{\infty} = \frac{\rho_{\infty}}{\rho_{\infty}} = 1 \quad (\text{B.2})$$

The value of the non-dimensional speed of sound at the infinity is

$$a_{\infty} = \frac{a_{\infty}}{a_{\infty}} = 1 \quad (\text{B.3})$$

The value of the non-dimensional viscosity at the infinity is

$$\mu_{\infty} = \frac{\mu_{\infty}}{\mu_{\infty}} = 1 \quad (\text{B.4})$$

The Reynolds number at the infinity is defined as

$$\text{Re}_{\infty} = \frac{\rho_{\infty} \mu_{\infty} U_{\infty}}{L} \quad (\text{B.5})$$

### Calculation of the Local Reynolds Number

The local Reynolds number is defined as

$$\text{Re}_x = \frac{\rho_{\infty} U_{\infty} x}{\mu_{\infty}} = \text{Re}_L \frac{x}{L} \quad (\text{B.6})$$

For curved surfaces  $s$  is used instead of  $x$ :

$$\text{Re}_s = \frac{\rho_{\infty} U_{\infty} s}{\mu_{\infty}} = \text{Re}_L \frac{s}{L} \quad (\text{B.7})$$

### Primary Variables:

$Q$  ( $Q_1, Q_2, Q_3, Q_4, Q_5$ ) is the solution vector where

$$Q_1: \rho / \rho_{\infty}, \quad Q_2: \frac{\rho u}{\rho_{\infty} a_{\infty}}, \quad Q_3: \frac{\rho v}{\rho_{\infty} a_{\infty}}, \quad Q_4: \frac{\rho w}{\rho_{\infty} a_{\infty}}, \quad Q_5: \frac{\rho e_t}{\rho_{\infty} a_{\infty}^2}$$

$$\rho / \rho_{\infty} = Q_1$$

$$u / a_{\infty} = (\rho u / \rho_{\infty} a_{\infty}) / (\rho / \rho_{\infty}) = Q_2 / Q_1 \quad (\text{B.8})$$

$$v / a_{\infty} = (\rho v / \rho_{\infty} a_{\infty}) / (\rho / \rho_{\infty}) = Q_3 / Q_1 \quad (\text{B.9})$$

$$w / a_{\infty} = (\rho w / \rho_{\infty} a_{\infty}) / (\rho / \rho_{\infty}) = Q_4 / Q_1 \quad (\text{B.10})$$

$$\rho e_t / \rho_{\infty} a_{\infty}^2 = Q_5 \quad (\text{B.11})$$

$$V_{TOT} / a_{\infty} = \sqrt{\left(\frac{u}{a_{\infty}}\right)^2 + \left(\frac{v}{a_{\infty}}\right)^2 + \left(\frac{w}{a_{\infty}}\right)^2} \quad (\text{B.12})$$

## B.2 CALCULATION OF PRESSURE

The energy equation is

Total Energy = Internal Energy + Kinetic Energy + Potential Energy (ignored)

$$e_t = C_v T + \frac{1}{2} V_{TOT}^2 = \frac{R}{\gamma - 1} \frac{p}{\rho R} + \frac{1}{2} V_{TOT}^2 \quad (\text{B.13})$$

$$p = (\gamma - 1) \left[ \rho e_t - \frac{1}{2} \rho V_{TOT}^2 \right]$$

$$\frac{p}{\rho_{\infty} a_{\infty}^2} = (\gamma - 1) \left[ \frac{\rho}{\rho_{\infty}} \frac{e_t}{a_{\infty}^2} - \frac{1}{2} \frac{\rho}{\rho_{\infty}} \frac{V_{TOT}^2}{a_{\infty}^2} \right] \quad (\text{B.14})$$

## B.3 CALCULATION OF THE VELOCITIES NON DIMENSIONAL BY $U_{\infty}$

x component of the velocity is

$$\frac{u}{U_{\infty}} = \frac{u}{a_{\infty}} \frac{a_{\infty}}{U_{\infty}} = \frac{u}{a_{\infty}} \frac{1}{M_{\infty}} \quad (\text{B.15})$$

y component of the velocity is

$$\frac{v}{U_{\infty}} = \frac{v}{a_{\infty}} \frac{a_{\infty}}{U_{\infty}} = \frac{v}{a_{\infty}} \frac{1}{M_{\infty}} \quad (\text{B.16})$$

z component of the velocity is

$$\frac{w}{U_{\infty}} = \frac{w}{a_{\infty}} \frac{a_{\infty}}{U_{\infty}} = \frac{w}{a_{\infty}} \frac{1}{M_{\infty}} \quad (\text{B.17})$$

Total velocity is

$$\frac{V_{TOT}}{U_{\infty}} = \frac{V_{TOT}}{a_{\infty}} \frac{a_{\infty}}{U_{\infty}} = \frac{V_{TOT}}{a_{\infty}} \frac{1}{M_{\infty}} \quad (\text{B.18})$$

#### B.4 CALCULATION OF $p/p_\infty$ , $C_p$ , $T/T_\infty$ , Local Speed of Sound,

Temperature ratio is

$$\frac{T}{T_\infty} = \frac{\frac{p}{\rho R}}{\frac{p_\infty}{\rho_\infty R}} = \frac{\rho_\infty}{\rho} \frac{\frac{p}{\rho_\infty a_\infty^2}}{\frac{p_\infty}{\rho_\infty a_\infty^2}} = \frac{1}{\rho} \frac{\rho_\infty a_\infty^2}{\frac{p_\infty}{\rho_\infty \gamma}} \quad (\text{B.19})$$

Pressure ratio is

$$\frac{p}{p_\infty} = \frac{\frac{p}{\rho_\infty a_\infty^2}}{\frac{p_\infty}{\rho_\infty a_\infty^2}} \quad (\text{B.20})$$

Pressure coefficient,  $C_p$ , is

$$C_p = \frac{p - p_\infty}{\frac{1}{2} \rho_\infty U_\infty^2} = \frac{\frac{p}{\rho_\infty a_\infty^2} - \frac{p_\infty}{\rho_\infty a_\infty^2}}{\frac{1}{2} \frac{\rho_\infty U_\infty^2}{\rho_\infty a_\infty^2}} = \frac{\frac{p}{\rho_\infty a_\infty^2} - \frac{p_\infty}{\rho_\infty a_\infty^2}}{\frac{1}{2} M_\infty^2} \quad (\text{B.21})$$

Local speed of sound non-dimensionalized with  $a_\infty$

$$\frac{a}{a_\infty} = \frac{\sqrt{\gamma \frac{p}{\rho}}}{a_\infty} = \sqrt{\gamma \frac{\rho_\infty}{\rho} \frac{p}{\rho_\infty a_\infty^2}} \quad (\text{B.22})$$

Local Mach Number:

$$M = \frac{V_{TOT}}{a} = \frac{V_{TOT} / a_\infty}{a / a_\infty} \quad (\text{B.23})$$

## B.5 CALCULATION OF THE DISTANCE NORMAL TO SURFACE: $n$

From vector analysis the area of the surface element formed by vectors  $\vec{B}$  and  $\vec{C}$  is:

$$Area = |\vec{B} \times \vec{C}| = |(b_y c_z - b_z c_y)\vec{i} + (b_z c_x - b_x c_z)\vec{j} + (b_x c_y - b_y c_x)\vec{k}|$$

The volume formed by vectors  $\vec{A}$ ,  $\vec{B}$  and  $\vec{C}$  is:

$$Volume = \vec{A} \cdot (\vec{B} \times \vec{C}) = a_x (b_y c_z - b_z c_y) + a_y (b_z c_x - b_x c_z) + a_z (b_x c_y - b_y c_x)$$

The height of this volume is:

$$h = Volume / Area$$

The normal distance from the point (J,K,L) to the surface (L=1) is:

Form the  $\vec{A}$ ,  $\vec{B}$  and  $\vec{C}$  vectors as follows (Fig. B.1):

$\vec{B}$  vector: on the surface from (J-1,K,1) to (J+1,K,1)

$\vec{C}$  vector: on the surface from (J,K-1,1) to (J,K+1,1)

$\vec{A}$  vector: from surface to the point: from (J,K,1) to (J,K,L)

Find the area formed by  $\vec{B}$  and  $\vec{C}$  vectors and the volume formed by the  $\vec{A}$ ,  $\vec{B}$  and  $\vec{C}$  vectors. Then,

$$N = n = VOLUME/AREA$$

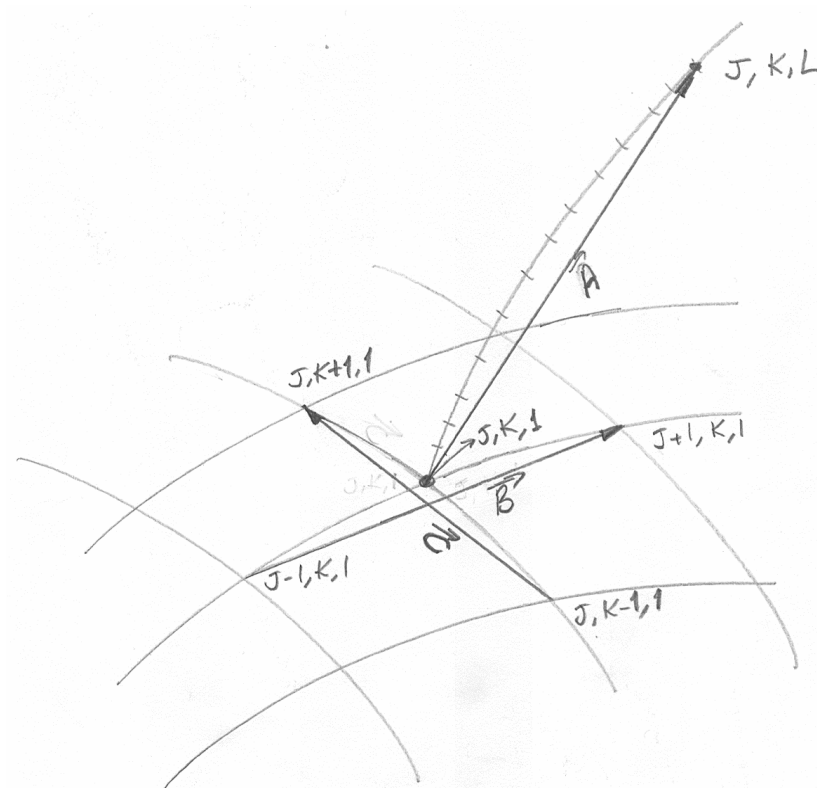


**Figure B.1** Estimation of distance normal to the surface.

**B.6 CALCULATION OF THE NONDIMENSIONAL COORDINATE  
NORMAL TO SURFACE:  $\eta$**

$$\eta = \frac{1}{\sqrt{2}} \frac{y}{x} \sqrt{Re_s} \quad (\text{B.24})$$

or for curved surfaces:

$$\eta = \frac{1}{\sqrt{2}} \frac{y}{s} \sqrt{Re_s} \quad (\text{B.25})$$

## B.7 DETERMINATION OF THE SHOCK LOCATION

The shock location is the normal distance from the surface to the point where

$$\frac{M}{M_\infty} = 0.99 \quad (\text{B.26})$$

## B.8 DETERMINATION OF THE MAXIMUM TEMPERATURE LOCATION

The maximum temperature location,  $\delta_{T,\max}$  is the normal distance from the surface to the point where

$$\frac{\partial T}{\partial n} = 0 \quad (\text{B.27})$$

## B.9 DETERMINATION OF THE EDGE OF THERMAL BOUNDARY LAYER

The edge of the thermal boundary layer,  $\delta_{T,\max}$ , is at the normal distance from the surface to the point where

$$\frac{\partial f_{qw}}{\partial n} = 0 \quad (\text{B.28})$$

$f_{qw}$  is defined as

$$f_{qw} = \left[ \int_0^\infty \bar{\rho} \bar{U} \left\{ \left( \frac{\gamma}{\gamma-1} \right) \left( \frac{\bar{p}}{\bar{\rho}} - \frac{\bar{p}_\infty}{\bar{\rho}_\infty} \right) + \frac{1}{2} (\bar{U}^2 - \bar{M}_\infty^2) \right\} dy \right]$$

$f_{qw}$  goes to zero at the edge of the thermal boundary layer. But just before going to zero, it makes a small maximum as can be seen from Figure 8.6 for example. The point of this maximum is considered as the edge of thermal boundary layer. It is very unlikely that there is a grid point in the  $\zeta$  direction just at this point. So this location is obtained by interpolation.

## B.10 DETERMINATION OF THE FLOW PROPERTIES AT THE EDGE OF THERMAL BOUNDARY LAYER

Since, the flow variables are not constant between the edge of the boundary layer and the shock, determination of the boundary layer edge requires special care. Thermal boundary layer is thicker than the momentum boundary layer and edge variables ( $U_e$ ,  $T_e$ ,  $M_e$ ,  $p_e$ ,  $\rho_e$ ) are obtained at the thermal boundary layer edge.

The Local Reynolds number at the edge of the thermal boundary layer is defined as

$$\text{Re}_{x,e} = \frac{U_e \rho_e x}{\mu_e} \quad (\text{B.29})$$

It is very unlikely that there is a grid point in the  $\zeta$  direction just at the edge point. So edge values of the flow variables are obtained by linear interpolation.

## B.11 CALCULATION OF $\delta/L$ , $\delta^*/L$ , $\theta/L$ , $H$

Boundary layer thickness,  $\delta$ , is the normal distance from the surface to the point where

$$\frac{U}{U_e} = 0.99 \quad (\text{B.26})$$

Displacement thickness,  $\delta^*/L$ , is

$$\delta^* \equiv \int_0^{\epsilon} \left( 1 - \frac{\rho U}{\rho_e U_e} \right) dy$$

$$\frac{\delta^*}{L} = \int_0^{\epsilon} \left( 1 - \frac{\rho U}{\rho_e U_e} \right) d\left(\frac{y}{L}\right)$$

or

$$\frac{\delta^*}{L} = \int_0^{\epsilon} \left(1 - \frac{\rho U}{\rho_e U_e}\right) d\left(\frac{y}{L}\right) \quad (\text{B.27})$$

Displacement thickness,  $\theta/L$ , is

$$\theta \equiv \int_0^{\epsilon} \left(1 - \frac{U}{U_e}\right) \frac{\rho U}{\rho_e U_e} dy$$

$$\frac{\theta}{L} = \int_0^{\epsilon} \left(1 - \frac{U}{U_e}\right) \frac{\rho U}{\rho_e U_e} d\left(\frac{y}{L}\right)$$

or

$$\frac{\theta}{L} = \int_0^{\epsilon} \left(1 - \frac{U}{U_e}\right) \frac{\rho U}{\rho_e U_e} d\left(\frac{y}{L}\right) \quad (\text{B.28})$$

The shape factor,  $H$ , is

$$H = \frac{\delta^*}{\theta} \quad (\text{B.29})$$

## APPENDIX C

### SKIN FRICTION COEFFICIENT POST PROCESSING

#### C.1 DIFFERENTIAL POST PROCESSING

Non-dimensional form of the skin friction coefficient ( $C_f$ ) is

$$C_f = \frac{\tau_w}{\frac{1}{2}\rho_e U_e^2} \quad (\text{C.1})$$

where

$$\tau_w = \mu_w \left. \frac{\partial U}{\partial y} \right)_w \quad (\text{C.2})$$

Non-dimensional form of  $\tau_w$  is

$$\bar{\tau}_w = \frac{\mu_w}{\mu_\infty} \left. \frac{\partial \left( \frac{U}{U_\infty} \right)}{\partial \left( \frac{y}{L} \right)} \right)_w \quad (\text{C.3})$$

$C_f$  becomes

$$C_f = 2 \left. \frac{\mu_\infty}{\rho_\infty L U_\infty} \frac{\bar{\mu}_w}{\bar{\rho}_e} \frac{1}{\bar{U}_e^2} \frac{\partial \bar{U}}{\partial \bar{y}} \right)_w \quad (\text{C.4})$$

where

$$\text{Re}_{L,\infty} = \frac{\rho_\infty U_\infty L}{\mu_\infty}$$

Finally;

$$C_f = \frac{2}{\text{Re}_{L,\infty}} \left. \frac{\bar{\mu}_w}{\bar{\rho}_e} \frac{1}{\bar{U}_e^2} \frac{\partial \bar{U}}{\partial \bar{y}} \right)_w \quad (\text{C.5})$$



where

$$\tau_w = -\frac{d}{dx}(F_{v,x}) \quad (C.10)$$

$$\tau_w = -\frac{d}{dx} \left[ \int_{CS} u \rho \vec{V} \cdot dA + \int_{CS} p dA_x + \right]$$

$$\tau_w = -\frac{d}{dx} \left[ - \int_{CS1} u \rho u dz + \int_{CS2} u \rho u dz + \int_{CS3} u \rho (-u dz + w dx) - \int_{CS1} p dz + \int_{CS2} p dz - \int_{CS3} p dz \right]$$

$$\tau_w = -\frac{d}{dx} \left[ \int_{CS} (u \rho u - U_\infty \rho_\infty U_\infty + p - p_\infty) dz \right] - U_\infty \rho_\infty w_\infty \quad (C.11)$$

where

$$f_{\tau_w} = \left[ \frac{\rho}{\rho_\infty} \left( \frac{U}{U_\infty} \right)^2 - \left( \frac{\rho_\infty}{\rho_\infty} \right) \left( \frac{U_\infty}{U_\infty} \right)^2 + \frac{p}{\rho_\infty U_\infty^2} - \frac{p_\infty}{\rho_\infty U_\infty^2} \right]$$

$$F_{\tau_w} = \int_0^\infty f_{\tau_w} d\left(\frac{z}{L}\right) = \int_0^\infty \left[ \frac{\rho}{\rho_\infty} \left( \frac{U}{U_\infty} \right)^2 - 1 + \frac{p}{\rho_\infty U_\infty^2} - \frac{p_\infty}{\rho_\infty U_\infty^2} \right] d\bar{z}$$

Non-dimensional form of  $\tau_w$  is

$$\frac{\tau_w}{\rho_\infty U_\infty^2} = -\frac{d}{d\left(\frac{x}{L}\right)} (F_{\tau_w}) \quad (C.12)$$

Finally  $C_f$  becomes

$$C_f = \frac{\frac{\tau_w}{\rho_\infty U_\infty^2}}{\frac{1}{2} \frac{\rho_e}{\rho_\infty} \left( \frac{U_e}{U_\infty} \right)^2} = \frac{-\frac{d}{d\left(\frac{x}{L}\right)} (F_{\tau_w})}{\frac{1}{2} \frac{\rho_e}{\rho_\infty} \left( \frac{U_e}{U_\infty} \right)^2} = \frac{-\frac{d}{d\bar{x}} \left( \int_0^\infty \left[ \frac{\rho}{\rho_\infty} \left( \frac{U}{U_\infty} \right)^2 - 1 + \frac{p}{\rho_\infty U_\infty^2} - \frac{p_\infty}{\rho_\infty U_\infty^2} \right] d\bar{z} \right)}{\frac{1}{2} \frac{\rho_e}{\rho_\infty} \left( \frac{U_e}{U_\infty} \right)^2} \quad (C.14)$$

## APPENDIX D

### STANTON NUMBER POST PROCESSING

#### D.1 DIFFERENTIAL POST PROCESSING

A non-dimensional heat transfer coefficient presented as the Stanton number (St) based on edge variables [8];

$$St = \frac{q_w}{\rho_e U_e (h_r - h_w)} \quad (D.1)$$

where

$$q_w = \left[ k \frac{\partial T}{\partial n} \right]_w \quad (D.2)$$

$$h_r = h_0 + 0.5(\text{Pr}^{*1/2} - 1)U_e^2 \quad (D.3)$$

The non-dimensional form of heat transfer rate to the wall,  $q_w$ , is

$$\frac{q_w}{\rho_\infty a_\infty^3} = \frac{M_\infty}{\text{Pr}(\gamma-1)\text{Re}_\infty} \bar{\mu}_w \left( \frac{\partial \bar{T}}{\partial \bar{n}} \right)_w \quad (D.4)$$

To get non-dimensional form of this definition, divide by  $a_\infty^2$ ;

$$\bar{h}_r = \bar{h}_0 + 0.5(\text{Pr}^{*1/2} - 1)\bar{U}_e^2 \quad (D.5)$$

$h_w$  can be defined as;

$$h_w = C_p T_w = \frac{\gamma}{\gamma-1} \frac{p_w}{\rho_w}$$

Non-dimensional form of this equation is

$$\bar{h}_w = \frac{\gamma}{\gamma-1} \frac{\bar{p}_w}{\bar{\rho}_w} \quad (\text{D.6})$$

Put equations (D.5) and (D.6) into  $(\bar{h}_r - \bar{h}_w)$ ,

$$(\bar{h}_r - \bar{h}_w) = \bar{h}_0 + 0.5(\text{Pr}^{*1/2} - 1)U_e^2 - \frac{\gamma}{\gamma-1} \frac{\bar{p}_w}{\bar{\rho}_w}$$

where  $\bar{h}_0 = h_\infty + 0.5U_\infty^2$ . Non-dimensional form of this equation is

$$\bar{h}_0 = \bar{h}_\infty + 0.5M_\infty^2 = \frac{\gamma}{\gamma-1} \frac{\bar{p}_\infty}{\bar{\rho}_\infty} + 0.5M_\infty^2$$

And final form of  $(\bar{h}_r - \bar{h}_w)$

$$\begin{aligned} (\bar{h}_r - \bar{h}_w) &= \frac{\gamma}{\gamma-1} \left( \frac{\bar{p}_\infty}{\bar{\rho}_\infty} - \frac{\bar{p}_w}{\bar{\rho}_w} \right) + 0.5(\text{Pr}^{*1/2} - 1)U_e^2 + 0.5M_\infty^2 \\ (\bar{h}_r - \bar{h}_w) &= \frac{\gamma}{\gamma-1} \left( \frac{\bar{p}_\infty}{\bar{\rho}_\infty} - \frac{\bar{p}_w}{\bar{\rho}_w} \right) + 0.5 \left[ M_\infty^2 + (\text{Pr}^{*1/2} - 1)U_e^2 \right] \end{aligned} \quad (\text{D.7})$$

$$\text{where } \bar{\rho}_\infty = \frac{\rho_\infty}{\rho_\infty} = 1 \quad \text{and} \quad \bar{p}_\infty = \frac{p_\infty}{\rho_\infty a_\infty^2} = \frac{p_\infty}{\rho_\infty \gamma R T_\infty} = \frac{p_\infty}{\rho_\infty \gamma} = \frac{1}{\gamma}$$

When the expression (D.4) and (D.7) is inserted into equation (D.10), final form of St based on edge variables is

$$\begin{aligned} St_\infty &= \frac{\frac{q_w}{\rho_\infty a_\infty^3}}{\frac{\rho_e U_e}{\rho_\infty a_\infty} (\bar{h}_r - \bar{h}_w)} \\ St &= \frac{M_\infty \bar{\mu}_\infty \left( \frac{\partial \bar{T}}{\partial \bar{n}} \right)_w}{\text{Pr}(\gamma-1) \text{Re}_\infty \bar{\rho}_e \bar{U}_e \left( \frac{\gamma}{\gamma-1} \left( \frac{\bar{p}_\infty}{\bar{\rho}_\infty} - \frac{\bar{p}_w}{\bar{\rho}_w} \right) + 0.5 \left[ M_\infty^2 + (\text{Pr}^{*1/2} - 1)U_e^2 \right] \right)} \end{aligned} \quad (\text{D.8})$$

## D.2 INTEGRAL POST PROCESSING

A non-dimensional heat transfer coefficient presented as the Stanton number (St) based on edge variables [8];

$$St = \frac{q_w}{\rho_e U_e (h_r - h_w)} = \frac{\frac{d}{dx}(f(x))}{g(x)} \quad (D.9)$$

where  $f(x)$  is

$$f(x) = \left[ \int_0^\infty \bar{\rho} \bar{U} \left\{ \left( \frac{\gamma}{\gamma-1} \right) \left( \frac{\bar{p}}{\bar{\rho}} - \frac{\bar{p}_\infty}{\bar{\rho}_\infty} \right) + \frac{1}{2} (\bar{U}^2 - \bar{M}_\infty^2) \right\} dy \right]$$

$(\bar{h}_r - \bar{h}_w)$  is same with (D.7).

$$(\bar{h}_r - \bar{h}_w) = \frac{\gamma}{\gamma-1} \left( \frac{\bar{p}_\infty}{\bar{\rho}_\infty} - \frac{\bar{p}_w}{\bar{\rho}_w} \right) + 0.5 \left[ M_\infty^2 + (\text{Pr}^{*1/2} - 1) \bar{U}_e^2 \right]$$

St number becomes

$$St_\infty = \frac{\frac{q_w}{\rho_\infty a_\infty^3}}{\bar{\rho}_e \bar{U}_e (\bar{h}_r - \bar{h}_w)} \quad (D.10)$$

$$St_\infty = \frac{\frac{d}{dx}(f(x))}{g(x)} = \frac{\frac{d}{dx} \left[ \int_0^\infty \bar{\rho} \bar{U} \left\{ \left( \frac{\gamma}{\gamma-1} \right) \left( \frac{\bar{p}}{\bar{\rho}} - \frac{\bar{p}_\infty}{\bar{\rho}_\infty} \right) + \frac{1}{2} (\bar{U}^2 - \bar{M}_\infty^2) \right\} dy \right]}{\bar{\rho}_e \bar{U}_e \left[ \frac{\gamma}{\gamma-1} \left( \frac{\bar{p}_\infty}{\bar{\rho}_\infty} - \frac{\bar{p}_w}{\bar{\rho}_w} \right) + 0.5 (M_\infty^2 + (\text{Pr}^{*1/2} - 1) \bar{U}_e^2) \right]}$$

where

$$g(x) = \bar{\rho}_e \bar{U}_e \left[ \frac{\gamma}{\gamma-1} \left( \frac{\bar{p}_\infty}{\bar{\rho}_\infty} - \frac{\bar{p}_w}{\bar{\rho}_w} \right) + 0.5 (M_\infty^2 + (\text{Pr}^{*1/2} - 1) \bar{U}_e^2) \right]$$

## CURRICULUM VITAE

### PERSONAL INFORMATION

Surname, Name: Aziz, Şaduman  
Nationality: Turkish (TC)  
Date and Place of Birth: 26 February 1974 , Eskişehir  
Marital Status: Married  
Phone: +90 312 475 42 29  
email: sdogrusoz@ssm.gov.tr

### EDUCATION

Degree	Institution	Year of Graduation
MS	METU Aeronautical Engineering	1999
BS	METU Aeronautical Engineering	1996

### WORK EXPERIENCE

Year	Place	Enrollment
2001- Present	MSB Savunma Sanayi	Technical Manager
1996-2001	METU Aeronautical Engineering	Teaching Assistance

### FOREIGN LANGUAGES

English

### PUBLICATIONS

1. Aziz, Ş., Kavsaoglu, M. Ş., Kaynak, Ü., "Effects of Wall to Stagnation Temperature Ratio on Hypersonic Corner Flows", 35<sup>th</sup> AIAA Fluid Dynamics Conference and Exhibit, 6-9 June 2005, Toronto, Toronto, Ontario Canada.
2. Doğrusöz, Ş., Kavsaoglu, M. Ş., Kaynak, Ü., "Numerical Solution of Hypersonic High Temperature Flows over a Flat Plate", International Conference "High-Speed Flow: Fundamental Problems, Zhukovsky, Moscow region, Russia, September 21-24, 2004.
3. Doğrusöz, Ş., Kavsaoglu, M. Ş., Kaynak, Ü., "Numerical Solution of Hypersonic Compression Corner Flows", 10<sup>th</sup> AIAA/NAL/NASDA/ISAS, International Space Planes and Hypersonic Systems and Technologies Conference, April 24-27, 2001 Kyoto, JAPAN, AIAA 01-1750
4. Doğrusöz, Ş., Kavsaoglu, M. Ş., "Euler Solution of A Hypersonic Compression Corner Flow", AIA'98, 2<sup>nd</sup> Ankara International Aerospace, Conference, September 9-11, 1998, Ankara, Turkey.